Università degli Studi di Napoli Federico II
Facoltà di Ingegneria

Giovanni Lanzano

PHYSICAL AND ANALYTICAL MODELLING OF TUNNELS UNDER DYNAMIC LOADINGS

Tesi di Dottorato
XXI ciclo

Il Coordinatore
Prof. Ing. Federico M. MAZZOLANI

Dottorato di Ricerca in Ingegneria delle Costruzioni

List of symbol

a_i	peak ground acceleration
$a_{max,b}$	peak ground acceleration on bedrock
$a_{max,s}$	peak ground acceleration on surface
A	area of cross-section
α	relative stiffness ratio (Penzien, 2000)
α_R	Rayleigh coefficient alfa
α_N	Newmark coefficient alfa
β_R	Rayleigh coefficient beta
β_N	Newmark coefficient beta
C_i	propagation velocity
C	compressibility ratio (Wang, 1993)
$[C]$	Damping matrix
ξ	damping ratio
d	tunnel diameter
d_{eq}	equivalent thickness (Plaxis 8.0)
δt	Time step (Plaxis 8.0)
D	wave amplitude
D_0	Damping
Δ	diameter change
Δt	Dynamic step (Plaxis 8.0)
E_s	Young's modulus of soil
E_t	Young's modulus of tunnel
E_{oed}	Oedometric modulus of soil
ε_l	longitudinal strain
ε_n	normal strain
η	Viscosity
f	wave frequency
F	flexibility ratio (Wang, 1993)
$\{F\}$	Displacement vector
ϕ	angle of incidence
ϕ_s	friction angle of soil
G_s	shear modulus of soil

γ	shear strain
γ_{max}	maximum free-field shear strain
γ_s	soil unit weight
γ_N	Dissipation parameter
H	soil layer thickness
I	inertia modulus of cross-section
I_p	plasticity index
K_j	spring constant
$[K]$	Stiffness matrix
l	tunnel length
L	wavelength of sinusoidal wave
m	mass of lining for unit length
M	Bending moment
$[M]$	Mass matrix
N	Hoop load
ν_s	Poisson's ratio of soil
ν_t	Poisson's ratio of tunnel
p	interface soil/tunnel stresses
r	tunnel radius
r_d	reduction factor for acceleration
R	reduction factor for forces
R_{ck}	cubic concrete strength
ρ	radius of curvature
ρ_s	soil density
S	site amplification factor
S_V	design velocity of response spectrum
σ_j	normal stress
t	time variable
t_t	tunnel thickness
T	shear forces
T_s	fundamental period of soil deposit
τ_j	shear stress
θ	circular tunnel cross-section angle
u_j	tunnel displacement
u_x	soil displacement along the tunnel axis

u_y	soil displacement in the cross-section
V_i	peak ground velocity
x	direction along the tunnel axis
z	depth of soil deposit

Index $i = C, S, R$ is referred to compression, shear and Rayleigh waves
Index $j = a, t, h, v$ is referred to axial and transversal components or horizontal and vertical components

Introduction

RESEARCH OBJECTIVES

The main goal of this work is the study of the behaviour of the tunnels in soils under seismic motions. Many cases of earthquake damage to underground structures are reported in literature (Owen and Scholl, 1981; Sharma & Judd, 1991; Power et al., 1998). In particular, during the Hyogoken-Nambu earthquake (Kobe 17.I.1995, M_w=7.2), an intense damage distribution was observed at the metro transportation system, especially for the Daikai station and the tunnel lining (Yoshida, 1999).

The damage surveys show that the underground structures, particularly the tunnels, can be considered safer than the above-ground structures with reference to collapse limit states. Nevertheless, in the urban areas the serviceability of underground networks (like roadway, railway, water and gas pipelines) were severely interrupted and limited after strong earthquakes. The need to preserve their serviceability during and after the seismic events incremented the engineering interest on the seismic behaviour of the tunnels, especially in order to update the codes prescriptions for the design of these structures.

Experimental observation made by Okamoto et al. (1973), showed that the behaviour of the tunnels during seismic motion is governed by the kinematic response of the surrounding soil rather than by inertial forces

arising in the structure. Therefore, in the closed-form analytical solutions applicable, the seismic increments of internal forces depend mostly on the maximum shear strain of the soil in free-field conditions (e.g. Hashash et al., 2001). Also, the lining forces increments are usually function of the stiffness ratio between the soil and the tunnel (e.g. Penzien & Wu, 1998).

The closed-form expressions support a kind of simplified design procedures, called 'uncoupled methods', which lead to evaluate the internal forces in two different steps: first, the calculation of the maximum free-field strain and, second, the evaluation of the maximum increments of the internal forces. These analyses are often over-conservative with respect to more complex analyses, calculating the lining forces through an unique soil-structure interaction model.

In Italy, an extended research project was launched in the April 2003, called **ReLUIS** (*Rete dei Laboratori Universitari di Ingegneria Sismica – Network of University Laboratory of Seismic Engineering,* www.reluis.it). The scope of this project was to support the development of up-to-date seismic design procedures through the experimental validation of the computational methods.

The ReLUIS project is divided into 10 research lines. The 6th line is dedicated to geotechnical systems and is entitled '*Innovative methods for design of retaining structures and for assessment of slope stability*'. This line is subdivided into 4 sub-line projects. The first sub-line project regards the study of the behaviour of urban tunnels and retaining structures under seismic loading.

A number of centrifuge tests on physical models of retaining walls and tunnels under seismic conditions has been planned in the framework of the sub-line project. The tests were carried out to provide experimental data to calibrate numerical analyses and were not meant to model directly real structures or earthquakes.

A contractual agreement between the ReLUIS consortium and the Cambridge University (CUTS) was set up to perform a set of centrifuge tests at the Schofield Centre. This University structure is equipped with geotechnical centrifuges to run dynamic tests. The testing programme

included 4 tunnel tests and 8 retaining wall tests; all the models aimed to reproduce plane strain conditions. The sequence of construction phases was not realistically reproduced, but the procedures to create the models was specified in order to include them in the numerical simulations of the experiments.

For such problems, the physical modelling constitutes maybe the unique experimental tool available, since field-instrumented test sites are very costly and can give reliable results only along extended observation periods. In other words, the centrifuge tests are ‘artificial case histories’. although very idealised with respect to actual tunnel-soil systems. Since in the centrifuge tests the stress conditions of the real size structures are correctly reproduced, the results can be used to calibrate and assess simple to advanced numerical prediction models.

From the above premises, this work developed through three different stages, approximately lasting one year each:

1. Collection and study of the reference literature for the most important research topics:
   - damage case histories occurred in underground structures (including tunnels and pipelines) during strong-motion earthquakes;
   - pseudo-static methods for the calculation of the seismic increments of the internal forces in the tunnel lining, both in the cross section and along the longitudinal axis;
   - physical modelling of the soil/tunnel interaction through small scale centrifuge tests.
2. Numerical analysis of the dynamic behaviour of subsoil, both in free-field conditions and including the tunnel in the calculation domain.
3. Centrifuge testing and interpretation, in close co-operation with the hosting Cambridge University and other research groups involved in the same ReLUIS project sub-line.

TEXT ORGANIZATION AND SUMMARY

The text was structured in seven chapters, corresponding to distinct theoretical, numerical and experimental aspects of the research.

After Chapter 1, summarising the engineering issues of the problem, two chapters of the thesis (Chapters 2, 3) were dedicated to the explanation and use of analytical methods to predict the behaviour of circular tunnels during an earthquake, comparing analyses of different complexity levels. The core part of the text (Chapters 4, 5, 6) describes the execution and interpretation of centrifuge tests on sand models, in which a circular aluminium tunnel was placed. The calculation methods previously illustrated were finally used in order to simulate the experimental tests in centrifuge (Chapter 7).

In *Chapter 1*, a set of case histories of damage occurred in the underground structures during recent earthquakes are widely described. The observed cases were subdivided considering different worldwide areas, which suffered severe earthquakes (Japan, California, China, Greece, Turkey and Italy). All the literature cases were classified using different criteria, based on the damage entity, structure and crack type. At the end of the chapter, some protection methods to avoid structural cracks in the lining during a seismic event are briefly described.

Chapter 2 explains the analytical solutions formulated to compute the internal forces in the lining due to a seismic event. This topic is introduced by a description of the multi-level approach for the seismic analysis of geotechnical structures. Such methods involved the use of analytical formulas or computer codes with increasing complexity, in order to perform reliable and conservative analyses of the seismic soil/structure interaction. The behaviour of a circular tunnel can be studied separating the analysis of the transversal section from that along the longitudinal axis. From the existing literature, several simplified closed-form expressions are available to calculate the increments of internal forces due to shear wave propagation across the transversal tunnel section. These expressions require the knowledge of the maximum shear strain, evaluated at the tunnel depth but in free-field conditions, and the soil/structure stiffness ratio. Such

approaches typically rely upon the hypotheses of plane strain and linear elastic homogeneous materials for both subsoil and tunnel lining.

In *Chapter 3*, the main features of the calculation codes used to perform dynamic analyses are described. The *EERA* code (Bardet et al. 2000) was used to carry out 1D seismic site response analyses on ideal subsoil models, which represented different classes of soils in terms of stiffness profiles (gravel, sand and clay). The same soil profiles and recorded accelerograms were assumed in 2D dynamic analyses using the FE calculation code *Plaxis 8.0* (Brinkegreve 2002). The FE analyses were performed considering both free-field conditions and the full tunnel/soil interaction problem. Preliminary linear FE analyses without the structure were carried out in order to calibrate the performance of the FE code against that of *EERA*. The calibrations allowed to optimise the model used in the subsequent interaction analyses, namely: the maximum mesh size, the characteristic parameters of the lateral absorbing boundaries, those affecting the viscous (Rayleigh) damping, and the factors controlling the numerical (Newmark) integration in the time domain. To model the soil non-linear behaviour, a hybrid EERA-Plaxis procedure was followed, with a fictitious introduction in the linear analyses of the degradation of shear stiffness and damping ratio. Some FE numerical analyses were performed considering a sinusoidal time history of acceleration as input motion, in order to give preliminary indications on how to optimise the centrifuge experiments.

Chapter 4 describes the advantages and the critical aspects in the use of the centrifuge tests for the study of geotechnical seismic engineering problems. The difference between the centrifuge small scale tests and the 1g shaking table tests are discussed, as well as the criteria of comparison with the field prototype behaviour. The scaling factors for dynamic tests are explained, showing the possible errors which may occur in the centrifuge modelling at high “g” levels (Bilotta & Taylor 2005). The level of advanced technology to perform dynamic tests was considered, describing the equipments of the most important laboratories. The main important laboratory equipments required to carry out dynamic centrifuge tests are a large geotechnical centrifuge, a seismic actuator and a special container to simulate the soil shaking (Kutter 1995). Some cases of centrifuge tests on

tunnels and pipelines, which are available in literature, were widely described, showing the results of the experiments.

In *Chapter 5* the centrifuge tests carried out at the Schofield Centre are described in detail. The operations of the geotechnical centrifuge were reported (Schofield 1980), including all the equipments employed as the beam-like centrifuge, the dynamic actuator (SAM) and the Laminar box. The centrifuge models were realized using dry sand deposits and a small alloy tube, in order to simulate the tunnel. Pseudo-harmonic horizontal loads were applied at the base of the container, in order to simulate the shear wave propagation through the model. The materials used to build the sample models, i.e. the Leighton Buzzard sand and the aluminium used for the tunnel model, were characterised. The measuring instrumentation consisted in accelerometers placed in the models a different depths, the LVDT to measure the displacements of the sand surface and strain gauges, applied on the lining to obtain direct measurements of the internal forces in the dynamic phase. The instruments calibration procedures were explained in detail, especially for the strain gauges, which were subjected to diverse calibrations in order to obtain reliable calibration factors. The model and centrifuge preparation procedures were described step by step. The four tests performed were described, considering all the earthquakes fired and the layout of the transducers. At the end of the chapter, the post-flight observations are reported, both when the model was unloaded from the centrifuge arm and the box was emptied.

In *Chapter 6*, the measurements of the instruments installed were reported. The LVDT results were showed for 3 out of the total 4 tests, considering both the swing-up and dynamic phase displacements. The digital data records were checked with manual readings made during and after the test phases. The horizontal acceleration records were taken along three instrumented alignments, two located inside the model and one on the external side of the box. An external base accelerometer was used to obtain the input motions of each fired earthquake. The profiles were compared considering different verticals, earthquakes and models. The acceleration time histories were also processed in order to obtain back-analysed values of soil parameters. The amplification function of the base/top accelerometers yielded a value of the mobilised shear stiffness and damping

ratio, along different depth ranges. The stress-strain loops provided alternative estimates of the shear stiffness profiles, which were compared with those resulting from the amplification functions. The strain gauges recordings were reported both in the swing-up and during the earthquakes. The time histories were plotted in sequence, in order to recognize the static and the dynamic components of the internal forces obtained by the measurements. The results were compared for the two instrumented sections in the different models. The dynamic increments of internal forces were compared with analytical predictions of the bending moment and hoop forces using the closed-form expressions by Wang (1993).

In *Chapter 7*, an example of numerical interpretation of a centrifuge test is described. Also in this case the EERA and Plaxis 8.0 codes were used, in order to perform dynamic analyses with a pseudo-nonlinear behaviour of the sand. In a kind of 'blind prediction' (class A), the soil properties were assumed from laboratory tests on the same sand, carried out in the framework of the same research project. The soil was characterised with a vertical profile of initial shear stiffness and damping ratio, and the degradation curves of shear stiffness and damping ratio with the shear strain level. An other set of 'back-analyses' (class C predictions) was carried out using the mobilized value of shear stiffness and damping ratio obtained from the interpretation of the experimental centrifuge results. The results of the 'Class A' and 'Class C' analyses were compared to the experimental data and the results of pseudo-static predictions.

REFERENCE

Bardet J. P., Ichii K., Lin C. H. (2000). EERA a Computer Program for Equivalent-linear Earthquake site Response Analyses of Layered Soil Deposits. Univ. of Southern California, Dep. of Civil Eng.

Bilotta E., Taylor N., 2005, Modellazione geotecnica in centrifuga. Argomenti di Ingegneria Geotecnica. Hevelius Ed. (in Italian).

Brinkgreve R.B.J., Plaxis 2D version8. A.A. Balkema Publisher, Lisse, 2002NTC, 2008Castellani et al. 2006

Hashash, Y.M.A., Hook, J.J., Schmidt, B., Yao, J.I-C. (2001), *Seismic design and analysis of underground structures*. Tunnelling and Underground Space Technology, 16, 247-293.

Kutter B.L., (1995), *Recent advances in centrifuge modelling of seismic shaking (state of art),* Proceedings of Third International Conference on Recent Advance in Geotechnical Earthquake Engineering and Soil Dynamics, April 2-7, 1995, VolII, St.Louis, Missouri

Okamato S., Tamura C., Kato K., Hamada M., (1973), *Behaviours of submerged tunnels during earthquakes*, Proceedings of the Fifth World Conference on Earthquake Engineering, vol.1, Rome, Italy, pp. 544-553.

Owen G.N., Scholl R.E., (1981), *Earthquake engineering of large underground structures*, Report no. FHWA/RD-80/195. Federal Highway Administration and National Science Foundation.

Penzien J., Wu C., (1998), Stresses in linings of bored tunnels, International Journal of Earthquake Engineering and Structural Dynamics, v.27, 1998.

Power M.S., Rosidi D., Kaneshiro J.Y., (1998), *Seismic vulnerability of tunnels and underground structures revisited*, Proceedings of North American Tunneling ’98, Newport Beach, CA, Balkema Rotterdam, p. 243-250.

Schofield A.N., (1980), *Cambridge Geotechnical Centrifuge Operations*, Geotechnique 30, No.3, 227-268

Sharma S.W.R., Judd, (1991), *Underground opening damage from earthquakes*, Engineering Geology, vol.30, p. 263-276.

Yoshida N., (1999), *Underground and buried structure*, Earthquake Geotechnical Engineering, Seco e Pinto (ed.) 1999 Balkema, Rotterdam, ISBN 90 5.

Wang J., (1993), *Seismic Design of Tunnels: A Simple State-of-the-art Design Approach*, Monograph 7, Parsons, Brinckerhoff, Quade and Douglas Inc, New York.

www.reluis.it

Chapter 1

Damage case histories and protection methods

1.1 INTRODUCTION

For a long time has been general belief that earthquake effects on underground structures is not very important. This is because these structures have generally experienced a low level of damage in comparison to the surface engineering works. Nevertheless, some underground facilities were significantly damaged during recent strong earthquakes (Hashash *et al*. 2001). In modern urban areas, underground space has been used to store a wide range of under-ground structures. Most underground structures are essential to human life and include many utilizations: pipelines for water, sewage, gas, electricity and telecommunication; subways; underground roads. For these reason it is very important to study how tunnels are damaged during earthquakes to protect the human life and the service efficiency.

1.2 CASE HISTORIES COLLECTION

Very few data are available concerning damages to underground structures and tunnels after earthquakes before 70’s. Damages and failures were accurately documented only after strong earthquakes: after San Fernando

earthquake (1971), ASCE (1974) published some data about damages to underground structures in the Los Angeles area. Moreover in many cases an accurate monitoring of lining cracks existing before the earthquake was missing. Therefore the real damage suffered by structures during the earthquake was unknown. After 1974 a systematic data collection of tunnel damages concerning different earthquakes was carried out, for the purpose of recognizing common features and similar causes:

- **Dowding & Rozen** (1978) collected 71 cases of damage concerning both American (7) and Japanese (6) earthquakes. Such a database includes both railway and roadway tunnels and water pipelines. Most of the cases are in compact rock (12), other in fractured rock (11) and only 3 cases regard tunnel in soil.
- **Owen & Scholl** (1981) updated the work by Dowding & Rozen, collecting 127 cases of damage to underground structures. An important adding was from the cut-and-cover tunnels, damaged during the San Francisco (1906) and San Fernando (1971) earthquakes. These structures were shallow and generally constructed in poor soil.
- **Sharma & Judd** (1991) enlarged the collection of the previous Authors reaching a total number of 192 cases for 85 different earthquakes. To correlate seismic vulnerability of a tunnel to some relevant factors, six parameters were examined: tunnel cover, subsoil type, peak ground acceleration, magnitude of the earthquake, distance from the epicentre and type of lining support. Most of the damages (60%) occurred in the shallow tunnels (depth lower than 100m); some cases (42%) are from unlined tunnels in rock.
- **Power *et al.*** (1996) added to the data collected by Sharma & Judd (1991), the cases of damages to underground structures after Kobe (1995) and Northridge (1995) earthquakes. They collected 217 cases of bored tunnels only. Most of the data are from the tunnel damaged during the extremely severe earthquake of Kobe (1995).
- **Corigliano** (2006) completed the database of the tunnel damage occurred during the recent earthquakes, adding the data concerning the Chi-Chi (1999) (Taiwan) and Niigata (2004) (Japan) events. A total of 345 cases was collected for 35 earthquakes, considering

only the very strong events (Mw>7). Kobe (1995) & Chi-Chi (1999) events provided more than the half of the total cases.

1.3 EXAMPLES OF DAMAGE TO UNDERGROUND STRUCTURES

As observed from the collected cases, some worldwide areas suffered severe damage due to strong earthquakes. The areas subjected to the strongest earthquakes are located on the west coast of the American Continent (Alaska, Canada, California, Mexico), on the east side of the Asian Continent (China, Japan, Taiwan, India) and along the coasts of the Mediterranean countries (Italy, Turkey, Greece). Following this consideration, the cases of the damage, suffered by underground structures, were showed for some of these hard-hit countries (Hashash *et al.* 2001).

California

From 1900 to 2004, six severe earthquakes occurred in California. At the beginning of the 20th century was the catastrophic earthquake of San Francisco (1906) with moment magnitude Mw=7.8. This event destroyed completely the city of San Francisco, causing over 3000 deaths. More recently three severe earthquakes occurred in five years only: Loma Prieta in 1989 (Mw=7.1), Petrolia in 1992 (Mw=6.9) and Northridge in 1994 (Mw=6.7). Power et al. (1998) reports many cases of damages occurred during these earthquakes (64 cases).

In order to reduce the vulnerability of tunnels during the earthquakes, many studies have been carried out in California for both static and seismic design of these structures. For instance for the construction of the Bay Area Rapid Transit (BART) and the Los Angeles Metro special seismic joints had been designed to permit differential displacements limiting the in-crease of stresses in the lining.

During the Loma Prieta (1989) event such joints had a good performance, because the subway structures had no damages (Hashash et al. 2001). On the contrary many tubes of the water supply system suffered severe damages. Schmidt & Hashash (1999) account for the structural damages of the Alameda

Tubes, two submarine tunnels of 12m diameter: they were extremely cracked due to liquefaction phenomena occurred in the marine sand.

Bardet & Davis (1999) report many cases (61) of steel tubes, which were strongly dam-aged during the Northridge (1994) earthquake. In Fig.1.1 some drawings show the deformation of the tubes after the seismic event. They show mechanisms of deformation which are peculiar of thin steel tubes: in most cases they underwent a kind of shrivelling due to lateral buckling for lack of confinement.

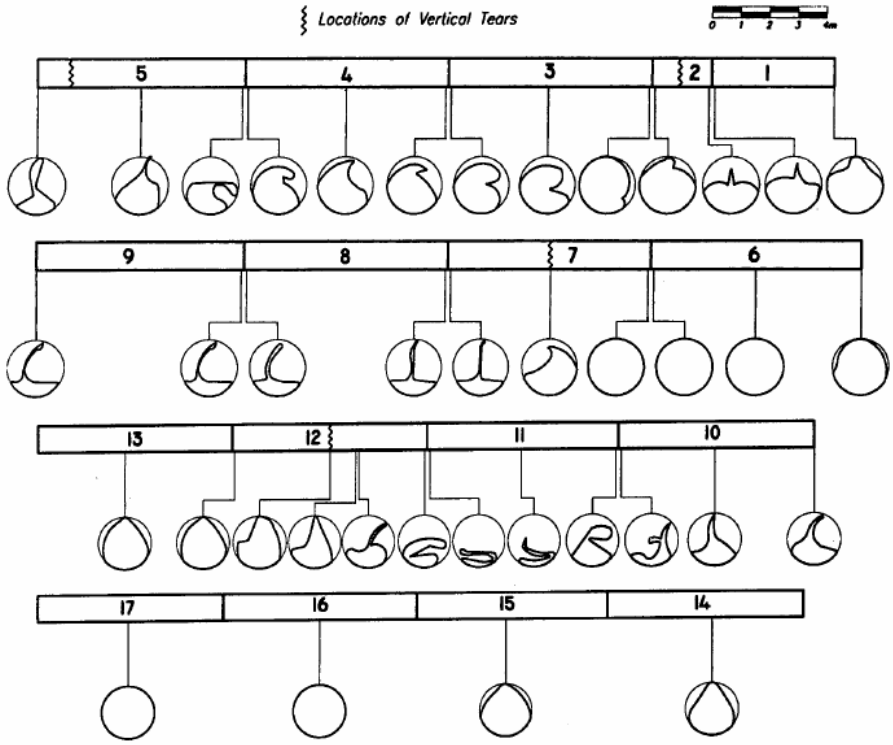

Fig.1.1: Drawing of damaged tubes during Northridge earthquake (1994) (Bardet & Davis, 1999)

Japan

The extremely strong earthquakes occurred in Japan caused millions of dead people and hundreds of crashed buildings. The high seismic vulnerability, the living density and sustained industry of Japan are the crucial patterns that make this geographic area one of the country with highest seismic risk in the world. During severe earthquakes, many above-ground and

under-ground structures have suffered enormous damage, even if buried structures are generally considered safer. In 1995, the catastrophic event of Hyogoken-Nambu caused many damages to the city of Kobe, located near the earthquake epicentre. The main shock, with magnitude moment Mw=6.9 and duration of 20s caused the death of 5100 people and the collapse of bridges, buildings and other civil structures. The whole Kobe metro system was damaged, forcing the service to stop.

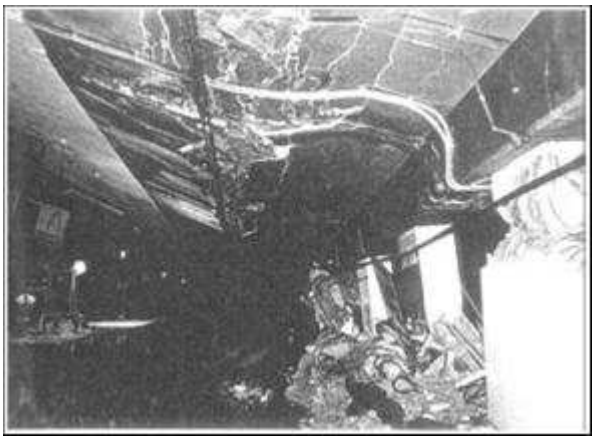

Fig.1.2a: Damage to the Daikai Station during the Kobe earthquake (1995) (Yoshida, 1999)

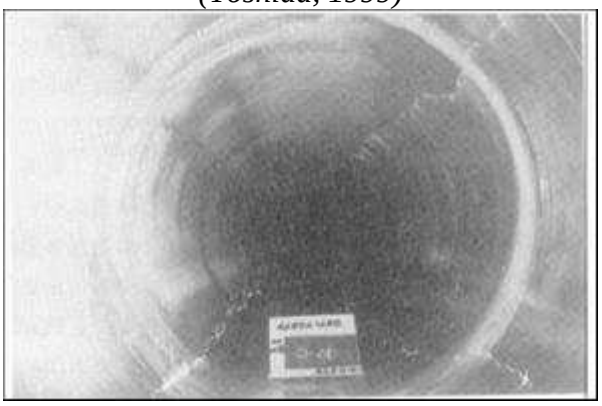

Fig.1.2b: Damage to metro tunnel segments during the Kobe earthquake (1995) (Yoshida, 1999)

Power et al. (1996) produced a database of observed cases after the Kobe earthquake (around 110), considering only bored tunnels. This is an important information to understand the impact of this event on metro and roadway

tunnels. Iida et al. (1996) and Yoshida (1999) have shown (Fig. 1.2a) the damage suffered by the metro station of Daikai: just above the station platforms the ceiling collapsed as some supporting columns buckled. Yoshida (1999) reports also the damage occurred in the metro lining (Fig.1.2b): they consisted mainly in longitudinal cracks, up to 250mm wide, located at $\theta=\pi/4+n\pi/2$(n=0,1,2,3) along the section.

Taiwan

In 1999 a very strong earthquake occurred in the island of Taiwan, causing destructive consequences in the near Popular Republic of China too. The Chi-Chi earthquake, from the name of the city placed near the epicentre, occurred on September 21st at 01:47 AM, with a magnitude moment Mw=7.6.

Miyajima & Hashimoto (1999) studied the data relative to the damages suffered by the water supply system during this earthquake: cracking affected around 0.14Km of transmission pipelines and around 4.56Km of service pipelines. The Water Works Association of the Chinese Republic estimated that around 50% of cracking was caused by soil shaking, and the other 50% was due to slopes failure and liquefaction occurred near the tubes.

Turkey

In the same year of the Chi-Chi earthquake in Taiwan (i.e. 1999), two strong earthquakes occurred in the Turkish region. The first one happened on the 7th August (Mw=7.4) and was named Kocaeli; instead the second one, occurred in the 12th November (Mw=7.2), had name **Duzce,** by the name of the city near the epicentre. During the last event, some damages to tunnel was observed by 0'Rourke *et al.* (2001): they showed the case of the Bolu tunnel, 3260 Km roadway structure which connected the city of Ankara to the city of Istanbul. The internal radius was 7m and the tunnel was built following the New Austrian Method (NATM). During the earthquake the tunnel was under construction. The earthquake epicentre was located 40Km west to the construction site. Most of the damage was observed in the Ankara side (farer from the epicentre) and consisted in collapse of the tunnel entrance and cracks along the lining. All the damaged sections were under construction and had a temporary structure of *spriz-beton*. Higher damage (cracks and collapses) occurred in the lining sections located in soft clay.

Italy

In order to find and to report a case of seismic damage to a tunnel in Italy, the strong earthquake which happened in the Irpinia region on 23rd November 1980 was considered. The event had Conza della Campania (Av) as epicentre and moment magnitude Mw=6.9, causing a total of almost 3000 deaths. Cotecchia *et al.* (1986) showed some cases of lining cracks and structural collapse, occurred during this earthquake. The water supply tunnel Pavoncelli, a large diameter structure used to transport water from Campania to Puglia, suffered damages in many sections (fig.1.3). The structural collapse occurred when the tunnel passed between two material of different lythology. Moreover the high energy of the earthquake caused fault reactivation along the long trail.

Fig.1.3: Collapsed sections of Pavoncelli Tunnel during the Irpinia earthquake (1980)(Cotecchia 1986)

1.4 DAMAGE CLASSIFICATION CRITERION

The collection work by Power *et al.* (1998) provides a relatively wide database of damages observed in tunnels which underwent seismic loads. The database is very heterogeneous, as very different cases can be distinguished for type of cracks, damage level, soil and lining type.

In order to classify the behaviour of tunnels during earthquake, some criterions were chosen from the literature.

Power et al. (1996) recognized three types of buried structures that behave differently during the earthquakes:

- *Bored tunnels*

- *Cut-and-cover structures*
- *Steel and plastic pipelines*

The database should be then subdivided according to such categories.

Also the damages need to be classified as Dowding & Rozen (1978) did for the first time. They noticed three different patterns of cracking or failure in a tunnel, which can be also found combined:

- *Ground failure*, such as liquefaction or landslides at tunnel portals;
- *Fault displacement*;
- *Ground shaking* or *ground vibrations*;

Particular lythological conditions cause the onset of damage of the first and second type: in the first case it is necessary that the tunnel entrance is near a slope; in the second case the lining needs to pass through an active fault. A prudent siting can avoid these conditions. Ground shaking occurs when the tunnel crosses very poor ground. In this case a wide cracking appears on the lining for long stretches.

Dowding & Rozen (1978) divided their database using the damage level as a criterion. They considered three damage classes (no damage, minor damage, damage). Huang *et al.* 1999 and Wang *et al.* 2001 added a damage level to such classification, subdividing the second group in two classes (slight and moderate).

Following the approach of Dowding & Rozen (1978), the three damage levels are defined by using the crack width (W) and length (L), the tunnel functionality and the need of restoration after earthquakes:

- *Class A*: Slight damage. L<5m W<3mm. Perfect functionality. No restoration needed. No service stop;
- *Class B*: Moderate damage. L>5m W>3mm. Differential displacements cause deep cracks, spalling and exposed reinforcement. Compromised functionality. Service interruption until the complete restoration with a-seismic expedients;
- *Class C*: Severe damage. Landslide and liquefaction. Structural collapse of the lining. Service stop without any possible restoration;

Corigliano (2007) more recently subdivided 230 worldwide cases from 35 different earthquakes in these three classes: severe damage occurred only for 6 seismic events.

1.5 SEISMIC PARAMETERS AFFECTING THE DAMAGE

Once the database is classified, it is possible to highlight the dependency of the tunnel damages on some significant variables (earthquake parameters or soil/structure characteristics).

Dowding & Rozen (1978) tried to correlate the damage level with the peak ground acceleration and the peak ground velocity of the seismic signal at surface above the tunnel. The acceleration and velocity values, as computed by using attenuation laws, were plotted in a graph (Fig.1.4) along the ordinal number of the case observed. For each case they used different indicators to distinguish the damage levels.

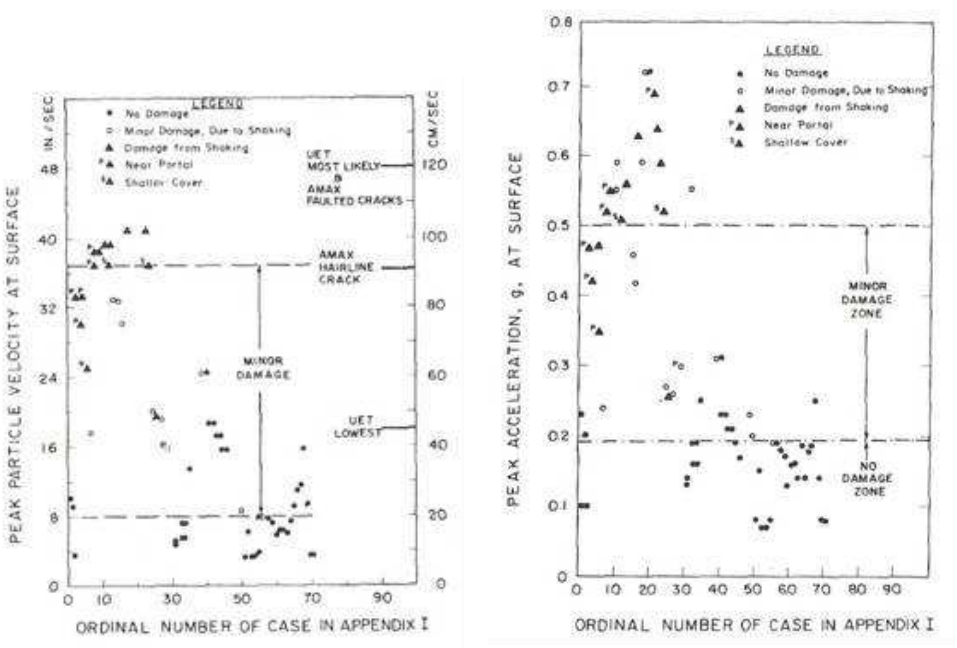

(a) (b)

Fig.1.4: PGA (a) and PGV (b) against damage level (Dowding & Rozen, 1978)

Two PGA thresholds can be recognized in the graph of Fig.4: the first at 0.2g, which separates the cases of slight damage (Class A) from the cases of moderate damage (Class B); the second at 0.5g, used to distinguish the cases of moderate damage (Class B) from the cases of severe damage (Class C).

This important information was confirmed by following Authors, showing that severe damage occurred only for particularly strong earthquakes. In fact the 0.5g limit is very high compared to the values that cause damage to above-ground structures. This notice confirms the intuitive point which the underground structures are generally safer than the above-ground structures: obviously, the tunnel confinement limits considerably the structure displacements due to seismic shaking.

Sharma & Judd (1991) extended the work of Dowding & Rozen (1978) to other parameters which they considered crucial for the tunnel behaviour. Beyond the PGA, they took into account the epicentral distance, the magnitude, the tunnel depth, the ground type and the lining support. In Fig. 1.5 the six histograms concerning these six variables are shown, where. the distribution of the 4 levels of damage (no damage, slight damage, moderate damage and severe damage) can be quantified.

It is important noticing that the deeper the tunnel, the lower the damages (Fig. 1.5a). This different behaviour is likely due both to the degree of confinement and to the improvement of the ground characteristics with depth. During the earthquake the shallow tunnels suffer larger deformations and subsequently higher stresses.

The graphs relative to rock type (Fig. 1.5b) and lining support (Fig. 1.5c) suggest that higher damage occurs in compact rock and for concrete linings without reinforcements. Nevertheless, such graphs do not clarify the influence of the relative stiffness between soil and lining.

The graphs of PGA (Fig. 1.5f), epicentral distance (Fig. 1.5d) and magnitude (Fig. 1.5e) confirm that the damaging effects increase with the earthquake magnitude and reduces as the epicentral distance increases. It is also confirmed that only severe earthquakes can cause severe damages to the underground structures.

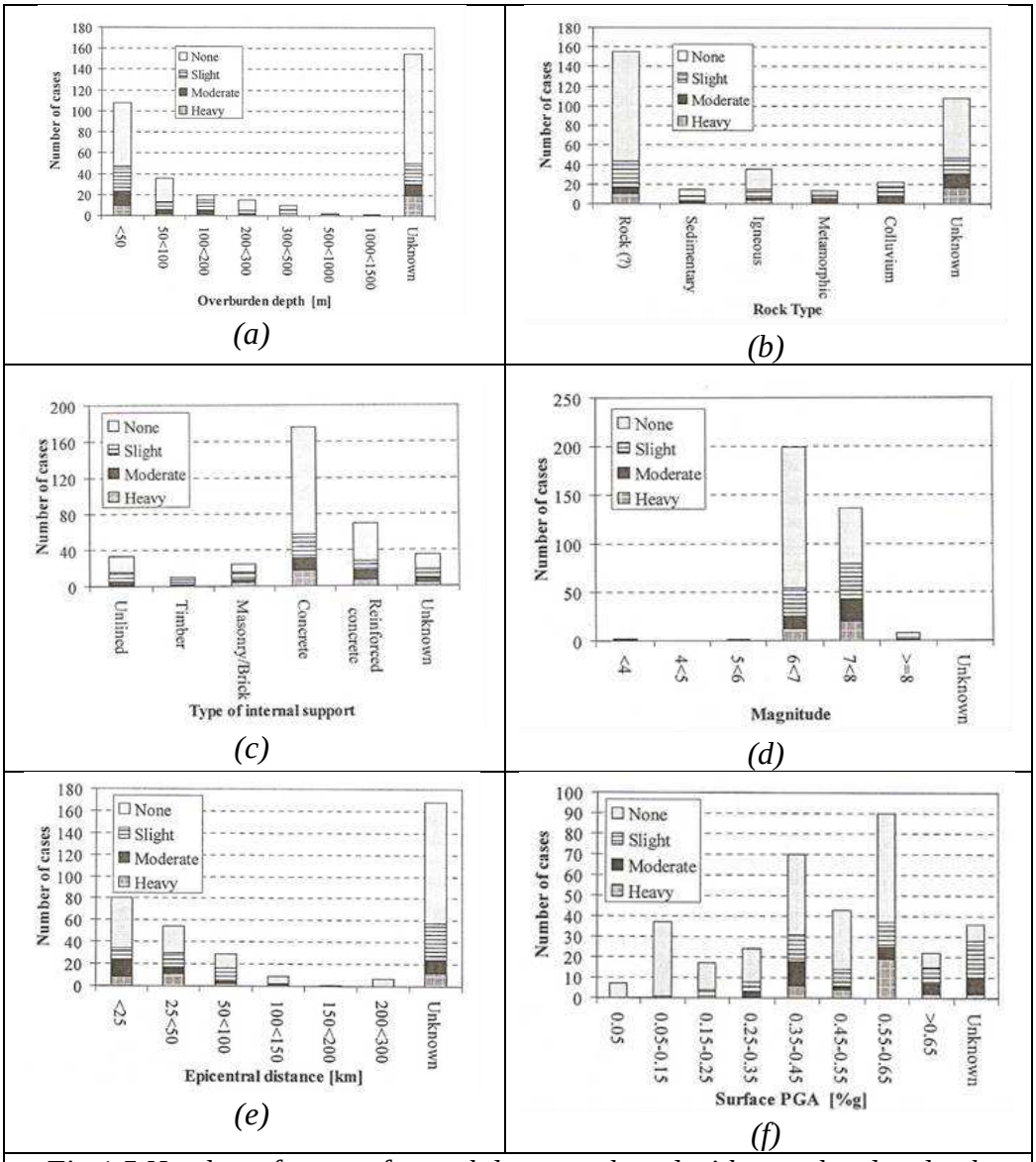

Fig.1.5 Number of cases of tunnel damage plotted with: overburden depth (a); rock type (b); type of internal support (c); magnitude (d); epicental distance (e); PGA (f) (Sharma & Judd, 1991)

1.6 CRACK DISTRIBUTION ALONG THE TUNNEL LINING

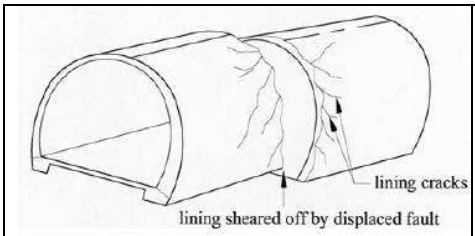

(a)

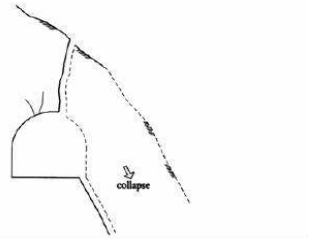

(b)

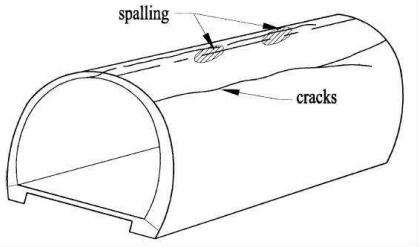

(c)

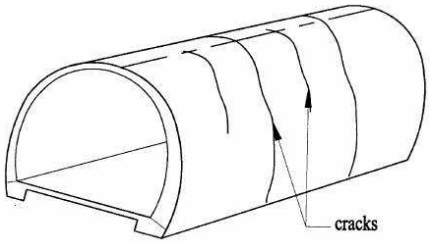

(d)

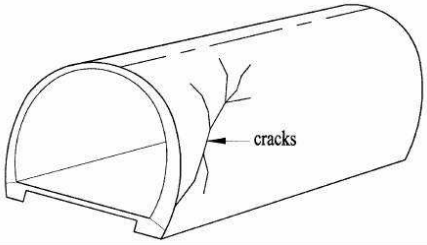

(e)

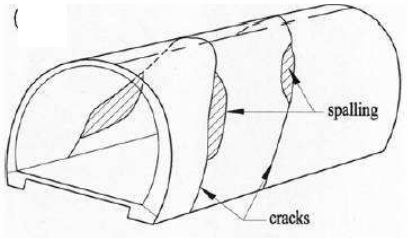

(f)

(g)

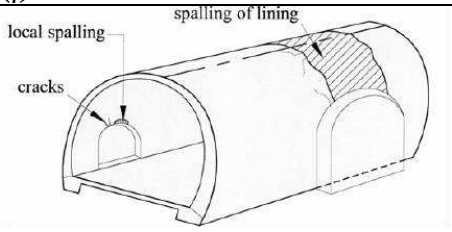

(h)

Fig.1.6: Types of damage: sheared off lining (a); slopes failure (b); longitudinal cracks (c); transverse cracks (d); inclined cracks (e); extended cracks (f); wall deformation (g); spalling of lining (h). (Wang et al. 2001)

Wang *et al.* (2001) suggest several patterns of cracking induced into the tunnel lining during an earthquake The eight patterns are (Fig.1.6):

a) *Sheared off lining*: it occurs for tunnel passing through active faults;
b) *Slopes failure induced tunnel collapse*: it occurs when the tunnel runs parallel to slopes generating landslides passing through the lining;
c) *Longitudinal cracks*: it occurs when the tunnel is subjected to higher deformations due to surrounding ground;
d) *Traverse cracks*: it occurs when the tunnel has weak joint;
e) *Inclined cracks*: it occurs for a combination of longitudinal and transversal cracks;
f) *Extended cracks*: it occurs when there is the partial collapse of linings for seismic intense deformation;
g) *Wall deformation*: it occurs when there is a transverse reduction due to the invert collapse;
h) *Spalling of lining*: it occurs when the transversal section completely collapses.

Table 1.1: Links between possible factors and cracks types

Possibile factors	**a**	**b**	**c**	**d**	**e**	**f**	**g**	**h**
Passing through fault zones	*							
Unfavourable ground conditions				°		*		
Interface hard-soft ground						*		
Nearby slope surface and portals		*		*	*	*		
Collapse during construction			°		°		°	
Lining cracks before earthquake			°	°				
Poor structural arrangements				°	°			*
Unreinforced concrete lining	°	°		°	°	°	°	*
Deteriorated lining material			°	°				
Cavity existed behind lining			*		°			

* decisive link ° weak link (Wang *et al.* 2001)

In Tab.1.1 the possible links between causes (geological, geotechnical and structural factors) and effects (type of damage according to Fig.1.6) are reported, showing when the influence is weak or decisive.

1.7 DESIGN ISSUE

In order to summarize some considerations about the seismic damage to tunnels, Yoshida (1999) gives a schematic drawing of typical conditions inducing cracking and collapse on the lining during an earthquake (Fig. 1.7), only referred to seismic ground shaking.

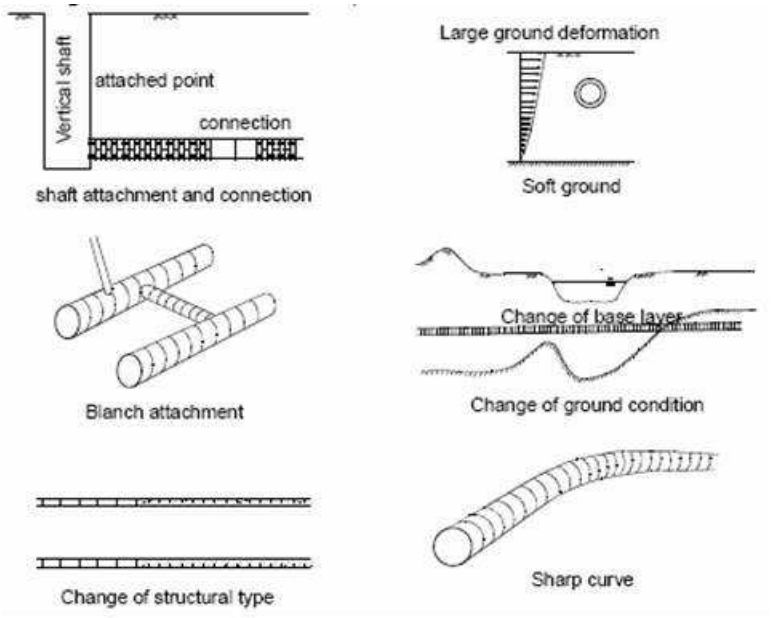

Fig.1.7: typical conditions which induce tunnel damage due to earthquakes (Yoshida 1999)

A structural or lythological modification determines unfavourable conditions and causes lining cracking and collapse. When there is no external or internal variations along the tunnel longitudinal axis, the damage can occur for tunnel buried in soft soils. In such cases the most frequent cracking pattern consists in longitudinal cracks developed longitudinally at $\theta=\pi/4+n\pi/2$ (n=0,1,2,3) positions along the transverse

section, sometimes symmetric, sometimes anti-symmetric, as shown by Wang *et al.* (2001), reporting some observations of damaged tunnels during the Chi-Chi earthquake (Fig.1.8).

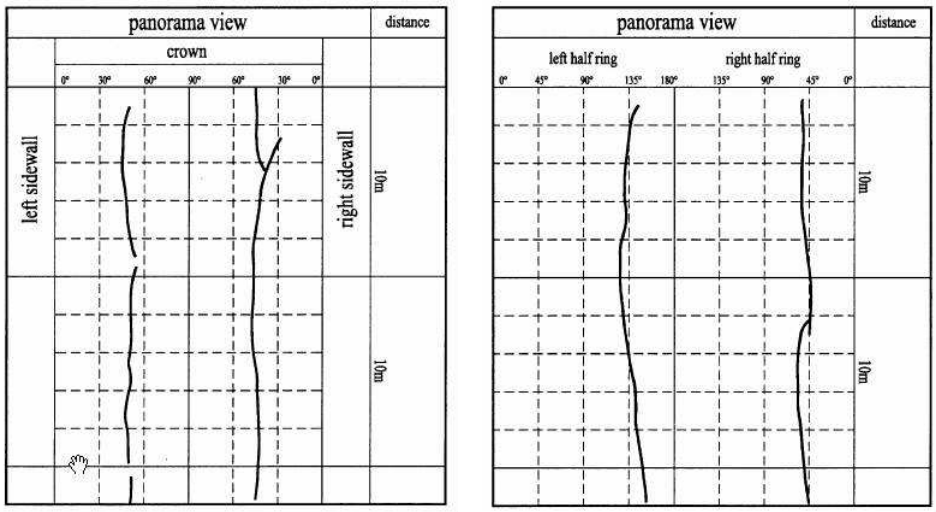

Fig.1.8: Longitudinal cracks: symmetric (a) or anti-symmetric (b) (Wang et al.2001)

After considering several cases of damage to underground structures, it is possible to summarize as follows:

1. During an earthquake underground structures suffer minor damage compared to above-ground structures. All the cracks and collapses take place only for severe earthquakes, with high magnitude and without special a-seismic expedients. Generally for moderate earthquakes, the static design is enough to protect structures from seismic motion;
2. Deep tunnels are safer compared to shallow tunnels;
3. All the structures buried in soft soils suffers higher damage compare to structure in rock;
4. Some seismic parameters have crucial influence on the stresses arising in the structure:: peak ground acceleration, frequency content and duration;
5. Damage degree increases with magnitude and decreases with epicentral distance;

6. Tunnels running across active faults may suffer severe damage due to differential displacements. Wherever it is possible, the tunnel should not pass through active faults;
7. Some damage occurs at portals due to landslide near the entrance. As for the active fault, the tunnel should not pass near provisional slopes;
8. Ground motion may be amplified upon incidence with a tunnel if wavelengths are between one and four times the tunnel diameter. This observation shows that high frequencies can be more dangerous than lower ones, but such frequencies are generally outside the range of a typical earthquake energy content;
9. Water and gas supply system are more vulnerable compared to metro and road tunnels, as steel tubes have a thickness/diameter ratio lower than concrete tunnels. Most of the damage of such lines occurs in saturated sand due to liquefaction;
10. Most of the metro lines and roadway tunnels are only damaged by extremely severe earthquakes. Some authors (Iida *et al.*,1996; Yoshida, 1999), describing the damage of the metro line of the city of Kobe during the earthquake of 1995, show that many sections suffered cracks and collapses for the absence of a-seismic expedients. On the other hand some American metro lines had good performance during the Loma Prieta earthquake (1989), thanks to special seismic joints used in the tunnel design.

1.8 SEISMIC PROTECTION OF TUNNEL

Protective measures against seismic actions are particularly important for underground structures having abrupt changes in structural stiffness or ground conditions (Fig.1.7) as occurs for:

- connections between tunnels and buildings or transit stations;
- junctions of tunnels of different structural material;
- passing through distinct geologic media of varying stiffness;
- local restraint on tunnels from movements of any type.

At these locations, stiffness difference may subject the structure to differential movements and generate stress concentration.

In order to avoid this stress increase the most common solution is to follow differential displacements by means of seismic flexible joints, that usually consist of bended steel plates and rubber. The joints have three important goals: allowing differential movements in longitudinal and transverse directions and relative rotation; resisting to static and dynamic earth and water loads; water tightness.

Joints are particularly useful at tunnel portals. In fact tunnel portal has a different behaviour compared to tunnel lining. Yeh (1974) and Hetenyi (1976) develop methods to calculate additional stresses due to the tunnel-portal stiffness change. But the seismic design of this structure has usually to account also for the inertial effects due to the above-ground structure. For the design of the Alameda Tubes (Schmidt *et al.* 1998) two dynamic analyses were carried out both for the running tunnel and the portal structure. Therefore the tunnel is assumed to move independently from portal station. The allowed displacement of the joint design is the difference between the two time histories (tunnel and portal). Generally the longitudinal differential displacement is higher than the transverse displacement.

Kawashima (2000) proposes, beyond the seismic joint solution, an extended isolation of tunnel from the surrounding ground when the structure passes through two different soil (in terms of stiffness) (Fig. 1.9). If a soft layer between the underground structure and the surrounding medium is placed, the transmission of seismic deformation may be mitigated., reducing the forces in the tunnel.

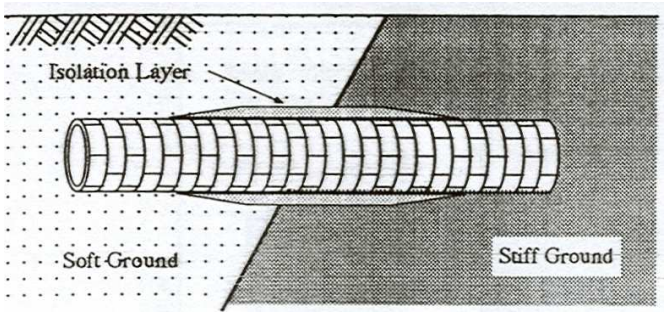

Fig.1.9: Isolation for a shield tunnel (Kawashima, 2000)

As an example, a 10m diameter tunnel is considered that intersects a discontinuity between soft and stiff soil (Fig. 1.10). A 200mm thick elastic

material was provided around the tunnel. The elastic modulus of the isolation material was lower than that of the stiffer soil by a factor of $1.5 \cdot 10^{-3}$.

Fig. 1.10b shows how the computed bending moment decreases in accordance with tunnel isolation, and has negligible increments beyond 40m from the discontinuity. The material used for seismic isolation need to be stable to settlements and long-term use.

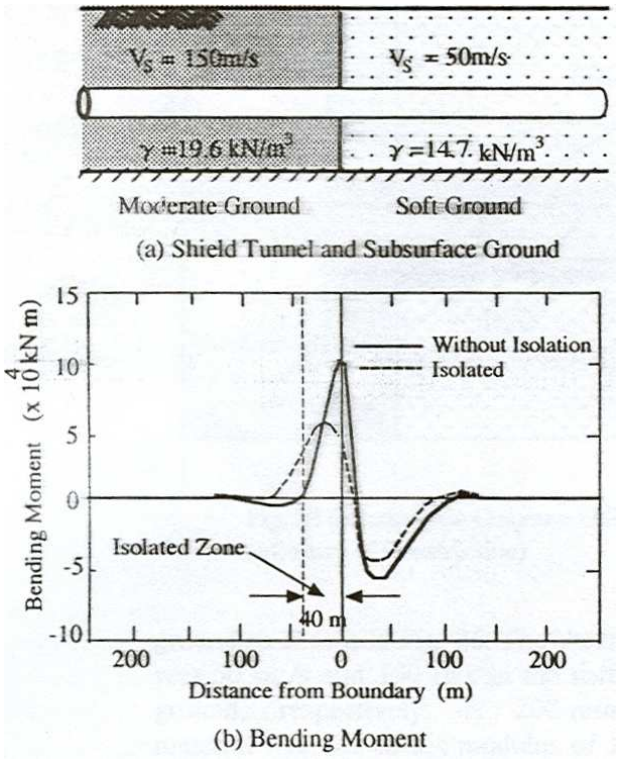

Fig1.10: Effect of seismic isolation: case of study (a); bending moment decreasing (b) (Kawashima, 2000).

In order to protect existing structures from ground shaking, an accurate investigation of soil/lining contact is required, through sampling and geophysical techniques. If the tunnel is in poor condition some restoration interventions are needed. Full restoration would require replacing the tunnel and adding steel reinforcements. Lining thickness increase is not a good solution, as it increases the structural stiffness and hence the internal forces in the lining.

Structure protection against ground failure, i.e. large permanent ground deformations, is not easy to design. For construction of a new tunnel the lining can be simply relocated. Otherwise, design strategies include ground stabilization, drainage, soil reinforcement, grouting or earth retaining systems. Protection from structure flotation is required in liquefiable soils: a structure buried in liquefiable soil during an earthquake tends to move up, developing high deformations. Schmidt and Hashash (1999) proposed the use of cut-off walls made by sheet pile walls, stone or jet grout columns (Fig.1.11).

Barrier walls reduce the rise of excess pore water pressure in the ground under the tunnel: adding the wall makes the underground structure wider and the uplift more difficult. This expedient should be used combined with flexible joints to allow differential displacements.

In order to protect underground structures against landslide the potential of slope instability need to be reduced: in fact, tunnels cannot accommodate irreversible displacements due to slope failure (Power *et al.* 1996).

Design strategies for tunnels crossing active faults depend on the magnitude and displacement of expected earthquake. If the deformations are concentrated in a narrow zone, common retrofit design is to enlarge the tunnel across and beyond the displacements zone. The reason of this solution is to give a wide gap to permit roads or rails restoration when the tunnel has high differential translations in the active fault lining section.

San Francisco BART and Los Angeles Metro rapid-transit tunnel systems were designed according to this philosophy (Hashash *et al.* 2001). Moreover for BART tunnels concrete-encased steel ribs were adopted to provide sufficient ductility. Under axial fault displacements, the tunnel compressions are more damaging than tensions, causing water inflow. One more time, flexible joints are the adequate solution (Wang 1993).

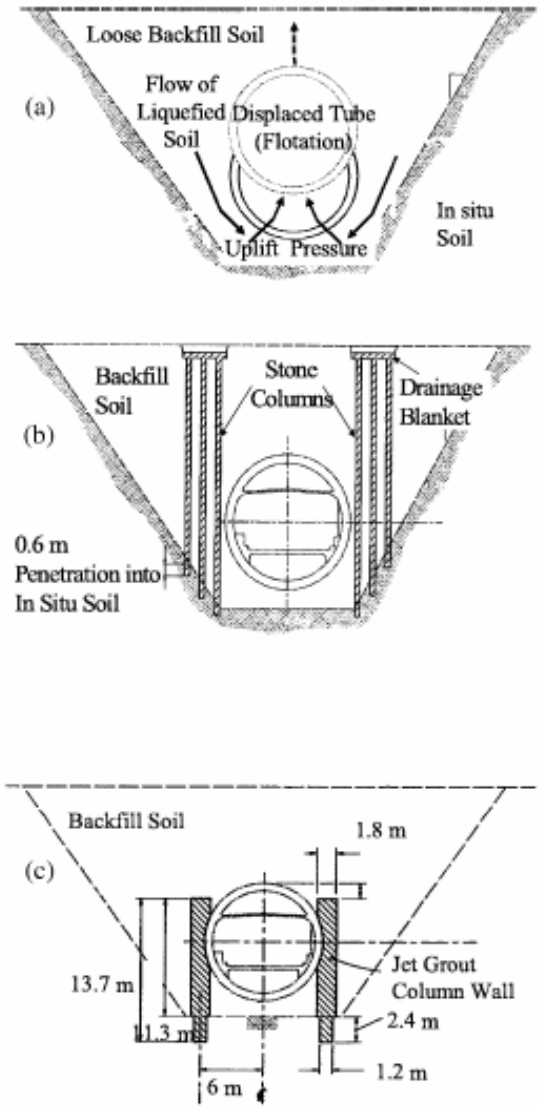

Fig.1.11: Tunnel flotation due to liquefaction: flotation mechanism (a); isolation with stone column (b); isolation with jet grout (c) (Schmidt & Hashash, 1999)

1.9 FINAL REMARKS

In the past most of the underground structures were designed without seismic considerations, because generally the tunnels had a good performance during the earthquakes compared to above-ground structures behaviour. In other cases, the design of buried structures was carried out with the same seismic considerations of above-ground structures. In order to optimize the tunnel seismic design, a correct evaluation of stresses under seismic waves is needed.

Performace-based seismic design should be aimed both to maintain in operation the tunnels during the more frequent events (of lower intensity) and to avoid human life losses for exceptional earthquakes (of higher intensity), according to the local seismic hazard predictions. In some cases, and almost always in presence of ground discontinuity, structural discontinuity or high potential of ground failure, protecting measures need to be designed.

REFERENCE

AFPS/AFTES, (2001), *Earthquake design and protection of underground structures*.

ASCE, (1974), *Earthquake damage evaluation and design considerations for underground structures*, Febbraio, American Society of Civil Engineers, Los Angeles Section.

Bardet J.P., Davis C.A., 1999, *Response of large-diameter buried pipes to earthquakes*, Earthquake Geotechnical Engineering.

Clough R.W., Penzien J. (1993), *Dynamics of structures,*. McGraw-Hill, New York.

Corigliano M., (2006), *Seismic response of deep tunnel in near-fault conditions*, Tesi di Dottorato in Ingegneria Geotecnica, Politecnico di Torino

Cotecchia 1986, *Ground deformations and slope instability produced by the earthquake of 23 November 1980 in Campania e Basilicata.* Geol. Appl. Idrogeol. 21 (5), 31-100.

Dowding C.H., Rozen A., (1978), *Damage to rock tunnels from earthquake shaking,* American Society of Civil Engineers, Journal of Geotechnical Engineering Division, Vol.104, p. 175-191.

EN 1998-1 (2003), *Eurocode 8: Design of structure for earthquake resistance,*. Part 1: General rules, seismic actions and rules for buildings. CEN European Committee for Standardisation, Bruxelles, Belgium.

Hashash Y.M.A., Tseng W.S., Krimotat A., 1998, *Seismic soil-structure interaction analysis for immersed tube tunnels retrofit,* Geotech. Earthquake Eng. Soil Mech. III 2, 1380-1391. ASCE Special publication n°75.

Hashash, Y.M.A., Hook, J.J., Schmidt, B., Yao, J.I-C. (2001), *Seismic design and analysis of underground structures*. Tunnelling and Underground Space Technology, 16, 247-293.

Hetenyi M., 1976, *Beam on elastic foundation,* University of Michigan Press.

Huang T.H., Ho T.Y., Chang C.T., Yao X.L., Chang Q.D., Lee H.C., 1999, *Quick investigation and assessment on tunnel structure after earthquake, and the relevant reinforced methods.* Report for Public Construction Commission, Taipei, Taiwan.

Iida H., Hiroto T., Yoshida N., Iwafuji M., (1996), *Damage to Daikai subway station,* Soils and Foundations, Japanese Geotechnical Society, Special issue on geotechnical aspects of the 17 January 1995 Hyogoken-Nambu Earthquake, p. 283-300.

Kawashima K., (2000), *Seismic design of underground structures in soft ground: a review,* Geotechnical Aspects of Underground Construction in Soft Ground, Kusakabe, Fujita & Miyazaki (eds). Balkema, Rotterdam, ISBN 90 5809 1 066.

Kramer S.L., (1996), *Geotechnical Earthquake Engineering,*. 653 pp., Prentice-Hall, New Jersey.

Miyajima M., Hashimoto T.; (2001), *Damage to water supply system and surface rupture due to fault movement during the 1999 Ji-Ji earthquake in Taiwan*, Proceedings Fourth International Conference on Recent Advances in Geotechnical Earthquake Engineering, San Diego, California, Marzo 2001.

O'Rourke T.D., Goh S.H., Menkiti C.O., Mair R.J., (2001), *Highway tunnel performance during the 1999 Duzce earthquake*, Proceedings of the Fifteenth International Conference on Soil Mechanics and Geotechnical Engineering, 27-31 Agosto 2000, Instanbul, Turchia.

Okamato S., Tamura C., Kato K., Hamada M., (1973), *Behaviours of submerged tunnels during earthquakes*, Proceedings of the Fifth World Conference on Earthquake Engineering, vol.1, Rome, Italy, pp. 544-553.

Owen G.N., Scholl R.E., (1981), *Earthquake engineering of large underground structures*, Report no. FHWA/RD-80/195. Federal Highway Administration and National Science Foundation.

Power M.S., Rosidi D., Kaneshiro J.Y., (1998), *Seismic vulnerability of tunnels and underground structures revisited*, Proceedings of North American Tunneling '98, Newport Beach, CA, Balkema Rotterdam, p. 243-250.

Rampello S.(2005), *Costruzioni in sotterraneo e scavi a cielo aperto,*. Linee guida AGI: Aspetti geotecnici della progettazione sismica, Parte III: Opere geotecniche, Capitolo 15, pag. 213-225

Russo M., Amberg W., (2001), *Gallerie profonde in zone sismiche, recenti sviluppi*, X Congresso Nazionale "L'ingegneria Sismica in Italia" (ANIDIS), Potenza-Matera 9-13 Settembre 2001

Schmidt B., Hashash Y., (1999), *Preventing tunnel flotation due to liquefaction*, Proceedings of the Second International Conferce on Earthquake

Geothecnical Engineering, June 21-25. Lisboa, Portugal, pp. 509-512

Sharma S.W.R., Judd, (1991), *Underground opening damage from earthquakes*, Engineering Geology, vol.30, p. 263-276.

St.John C.M., Zahrah T.F. (1987), *Aseismic design of underground structures*, Tunneling and Underground Space Technology, 2 (2), 165-197

Vanzi I., (2000), *Elastic and inelastic response of tunnels under longitudinal earthquake excitation*, Journal of Earthquake Engineering, Imperial College Press, United Kingdom, vol.4(2), Aprile 2000.

Wang J., (1993), *Seismic Design of Tunnels: A Simple State-of-the-art Design Approach*, Monograph 7, Parsons, Brinckerhoff, Quade and Douglas Inc, New York.

Wang W.L., Wang T.T., Su J.J., Lin C.H., Seng C.R., Huang T.H., (2001), *Assesment of damage in mountain tunnels due to the Taiwan Chi-Chi earthquake*, Tunneling and Underground Space Technology, 16, p.133-150.

Yeh G.C.K., 1974, *Seismic analysis of slender buried beams*, Bull.Seismol. Soc. Am. 64,5 pp.1551-1562.

Yoshida N., (1999), *Underground and buried structure*, Earthquake Geotechnical Engineering, Seco e Pinto (ed.) 1999 Balkema, Rotterdam, ISBN 90 5.

Chapter 2

Design of shallow tunnel under seismic loadings

2.1 INTRODUCTION

Towns are commonly interested by the construction of underground structures: among them urban tunnels are often excavated in soft ground and at a relatively shallow depth, compared to deeper tunnels crossing mountain districts.

In seismic areas the increments of stress arising under seismic waves need to be considered during design. The tunnel behaviour under earthquake loadings is usually studied by considering separately the performance of the transverse section and that in longitudinal direction.

In the following paragraphs, a review of the more common methods used to calculate the seismic stresses and strains in a circular tunnel is shown. The attention will be focused on pseudo-static methods used at the first stages of design to calculate deformations and forces through simple closed-form equations based on synthetic parameters of the potential seismic event.

2.2 SEISMIC DESIGN METHODS FOR GEOTECHNICAL STRUCTURES

2.2.1 Performance based design

The codes approach considers a seismic design based on conventional evaluation of the seismic action, assumed constant with time (pseudo-static). Moreover the assessment criteria for the collapse conditions are based on the use of a global safety factor.

The performance based design needs to evaluate the seismic response of the system under earthquakes of different magnitude. Generally a double verification is required, referred to two different seismic events:

- **Standard** Earthquake (level L1): intensity of the motion with extremely high probability of overflow during the lifetime of the system under examination. For this earthquake the structure must have a “good” performance, equivalent to the condition in which the functionality of the system is preserved;
- **Severe** Earthquake (level L2): intensity of the motion with extremely low overflow probability during the lifetime of the system under examination. For this earthquake the human lives must be protected and the performance of the structures must be satisfied concerning the collapse.

Also for the underground structures, and the tunnel in particular, different design criteria could be defined, following the indication of the recent codes (EN 1998-1 2003, OPCM 3274). For the tunnels, the two design levels (Wang 1993, Hashash et al 2001) were called as ‘maximum design earthquake’(**MDE**) and ‘operational design earthquake’ (**ODE**). Carrying out a probabilistic analysis, the MDE level can be defined using a seismic event which have an overflow probability of 3-5% during the structure lifetime; instead the event required for the ODE level has an overflow probability of 40-50%, equivalent to the half part of the verifiable earthquakes during the structure lifetime. The synthetic parameters used to defined a design earthquake are the signal amplitude (PGA), the frequency content and the seismic event duration.

The choice of the design earthquake is carried out through an analysis of seismic hazard. The methods used in order to estimate the synthetic parameter and response spectra are (Kramer 1996, Silvestri 2005):

- **The Deterministic Methods**: in these methods the earthquake, which could produce the maximum amplitude of the ground motion in the site under examination, is searched;
- **The Probabilistic Methods**: the goal of this methods is the determination of the motion features based on the overflow probability of the interesting magnitudes.

2.2.3 Levels of seismic analysis

Different methods of analysis generally exist in order to solve a problem; each methods have a different level of complexity and different reliability of the results. The problems concerning the seismic engineering applied to the geotechnical works could be studied defining three types of analysis of increasing complexity degree (Silvestri & Simonelli 2003):

- Pseudo-static analysis
- Simplified dynamic analysis
- Full dynamic analysis

In the next paragraphs the three analysis methods will be nested only in two classes: simplified and full dynamic analysis. First class includes the analysis methods which calculate the seismic stress and strain on the structure in two phases: in the first phase a site response analysis is carried out, considering *free-field* motion condition; in the second phase, using synthetic free-field parameters or maximum values depth distributions obtained in the previous step, the seismic effects on the structure (stress and strain) are calculated using analytical formulas or methods that simulate the soil as an elasto-plastic springs bed of different stiffness. For this reason the simplified method could be generally called "**uncoupled**" and includes both the pseudo-static and the simplified dynamic analyses. Instead the full dynamic analyses belong at the second methods class, in order to include the so called "**coupled**" methods: the seismic effects on the structure are obtained in an unique calculation step.

The **pseudo-static** methods are approximate approaches to obtain the seismic response, but should be generally preventive, because the soil behaviour is assumed as simplified, defining synthetic parameters as input value. The input magnitude used to represent the seismic motion is the peak ground acceleration (PGA - $a_{max,r}$) expected on a rigid bedrock. The value of PGA is dependent from the seismic level of the region in which the structure is located. The ground shaking is estimated through a simplified analysis of the site response, in which the results are expressed in terms of maximum acceleration expected on soil surface ($a_{max,s}$), obtainable through the use of amplification coefficients (S) of the bedrock value $a_{max,r}$

In the recent codes (EN 1998-1 2003, OPCM 3274), the input parameters, in order to calculate the previous values, are available based on qualitative and quantitative characteristics of the deposit. The parameter generally used in order to define and quantify the soil layer behaviour is the apparent shear wave velocity *Cs*. Without direct determination of this parameter (for example through down-hole tests), other parameters were used in order to correlate to *Cs* (for example CPT resistance, undrained shear strength, etc). Some authors (Pitilakis *et al.,* 2006; Bouckovalas *et al.,* 2006) showed that the values of the coefficients proposed by the codes (EN 1998-1 2003) are lower compared to the values obtained from more complex analyses: in some soil types the earthquake effects could be underestimated following the codes.

Table 2.1: Amplification factors for soil types

Subsoil class	**S** EC8	**S** (Ausilio *et al.* 2007)
A1	1	1
A2	1.25	$1.468 \cdot a_{r,max}^{-0.1251}$
B	1.3	$1.0177 \cdot a_{r,max}^{-0.2017}$
C	1.15	$1.0624 \cdot a_{r,max}^{-0.2362}$
D	1.1	$0.539 \cdot a_{r,max}^{-0.4171}$
E	1.35	$1.2274 \cdot a_{r,max}^{-0.2052}$

In order to obtain a reasonable evaluation of the amplification factor *S*,

Ausilio *et al.* (2007), through site response analyses deducted mathematical expressions of the factor S, as a power function of the peak ground acceleration on bedrock In the table 2.1 the values for each subsoil class are reported (EN 1998-1 2003, OPCM 3274).

The S values are generally higher than 1, except for the soil class D with bedrock acceleration higher than 0.23g. In most of the cases such values are lower than the S value obtained from Eurocode8.

Pseudo-static analyses evaluated the total inertial effects through an equivalent value of acceleration, in order to take account of the acceleration variability with space and time. In the common design, the seismic analyses of soil/structure interaction are carried out almost only using pseudo-static methods: the definition of a design procedure, therefore, has a remarkable importance, in order to carry out analyses which are correct and largely validated by the engineering experience.

For the **simplified dynamic** analyses the seismic actions are defined as a set of time histories of acceleration recorded on a bedrock base ($a_r(t)$). Using these input motions an analysis of the seismic response of the site (without the structure) is carried out, in order to obtain the seismic output signal on surface or generally at the structure depth. The SSR analyses must be carried out through numerical codes in order to simulate the waves propagation from the bedrock to the desired depth. For this reason a more reliable estimation of the values of maximum total stresses, strain and acceleration with depth is given. These analyses permit an accurate evaluation of the input parameters for the soil/structure interaction analyses. Once the site seismic response is given, a second phase of the simplified analysis is carried out, like for the pseudo-static analysis, in order to evaluate the maximum seismic effects on the structure.

The **full dynamic** analysis is the most complete and detailed analysis level, but at the same time the most intuitive: this method needs, as input parameters, a set of acceleration time histories on rigid bedrock and carries out a seismic waves propagation analysis, solving the motion equations, including the geometry and the stiffness of the structure in the analysis domain. In order to carry out the full dynamic analyses, some numerical codes (Plaxis 8.0, FLAC, ABAQUS, etc) could be used. Some of these software solve the propagation equations in the time domain, updating step by step the stress-

strain relationship, in order to take account of the non-linearity of the soil medium. These calculation instruments are particularly sensitive to many factors: for this reason the numerical analysis must be validate through theoretical formulas, life sized structures observation and physical models tests.

2.3 DESIGN METHODS FOR TUNNELS IN SEISMIC ZONES

2.3.1 Seismic behaviour of underground structures

Approaching the surface, seismic waves induce several effects in the ground which can be divided into three categories:

- fault displacements;
- ground failure such as liquefaction and slope instability;
- ground shaking.

Accordingly, the effects of the earthquake on tunnels and underground structures are different, as discussed in the previous chapter. Most of the damages on tunnels in soft ground occurs for ground shaking caused by the propagation of the shear waves.

The major factors influencing the damage from shaking include:

- the shape, size and depth of the structure;
- the properties of the surrounding ground;
- the properties of the structure;
- the severity of ground shaking.

For most underground structures, the inertia of the surrounding soil is large compared to the inertia of the structure. The measurements made by Okamoto *et al.* (1973) of seismic response of an immersed tube tunnel during several earthquakes show that the response of a tunnel is dominated by the surrounding ground response and not by the inertial properties of the tunnel structures itself.

The seismic design of underground structures is therefore based on the prediction of the ground displacement field and the analysis of its interaction with the structure. The emphasis on displacement is in contrast to the design of surface structures, which focuses on inertial effects of the structures itself.

Following this criterion, some design methods for tunnels under seismic loadings were developed, like the '**Seismic Deformation Method**' (Kawashima, 1999), which will be illustrated later. The behaviour of a tunnel is usually approximated to that of an elastic beam subjected to deformations imposed by surrounding ground. Three types of deformations (Owen & Scholl, 1981) express the response of underground structures to seismic motions (Fig.2.1):

- Axial compression/extension
- Longitudinal bending
- Ovalling/racking

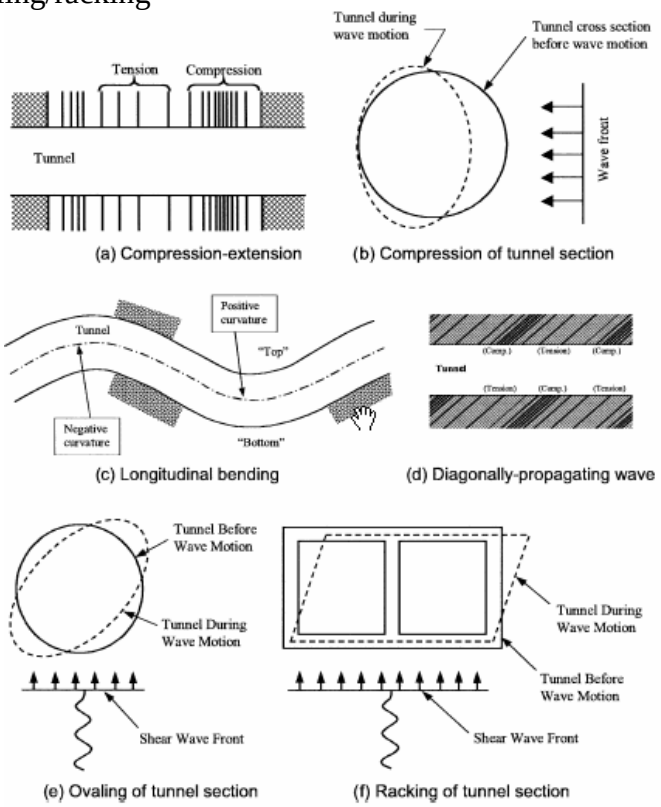

Figure 2.1: Types of tunnel deformations during a seismic event (Owen & Scholl, 1981)

Axial deformations in tunnels are generated by the components of seismic waves that produce motions parallel to the axis of the tunnel and cause alternating compression and tension. Bending deformations are caused by the

components of seismic waves producing particle motions perpendicular to the longitudinal axis. Ovaling or racking deformations develop when shear waves propagate normally, or nearly, to the tunnel axis, resulting in a distortion of the cross-sectional shape of the tunnel lining.

The longitudinal and transverse deformation of a tunnel will be discussed separately.

2.4 ANALYSIS OF THE LONGITUDINAL BEHAVIOUR OF A TUNNEL

For the seismic analysis of longitudinally extended underground structures, like tunnels, the horizontal propagation of surface and body waves produces a spatial incoherence of the seismic motion. Therefore different segments of a long underground structure are not subjected to the same motion condition at the same instant. Named C the propagation velocity along the tunnel axis of length l, ϕ the incidence angle and L the wavelength of the plane waves, the condition causing the motion phase displacement on the structure is $l>L = C/f$. This condition shows that the effect of longitudinal propagation is remarkable for lower propagation velocity and is not negligible for lower frequencies (Rampello, 2005).

In order to simplify the effects of seismic loads along the tunnel axis, it is possible assuming a completely coherent seismic signal; in other terms different spatial segments of tunnel are subjected to the same signal with different arrival time.

Consider a planar wave front advancing with speed C and impinging on the tunnel axis with an angle ϕ. The sinusoidal signal is used to represent an accelerogram with an equivalent energy content. The apparent velocity of the waves on the tunnel axis is $C_x = C/\cos\phi$. Compression P waves travelling in the ϕ direction with amplitude D_p cause, along the tunnel axis, both a train of compression waves, with amplitude $D_{pp}=D_p\cos\phi$, and a train of shear waves with amplitude $D_{ps}=D_p\text{sen}\phi$. Shear S waves with amplitude D_s can be decomposed similarly: they produce both compression waves with amplitude $D_{sp}=D_s\text{sen}\phi$, along the tunnel axis, and shear waves with amplitude $D_{ss}=D_s\cos\phi$, acting transversally. Finally the stresses are coupled unless the incidence angle is 0° or 90° (Fig. 2.2).

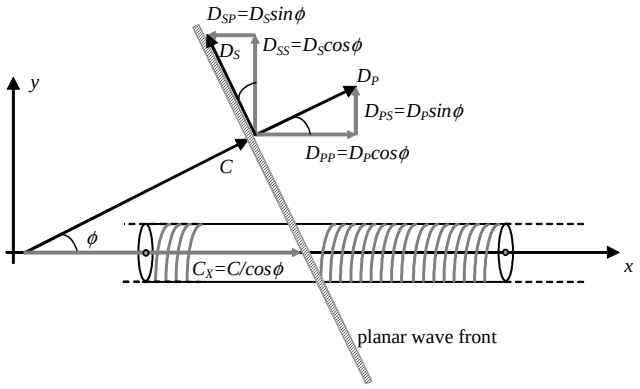

Figure 2.2. Geometry of the problem (Vanzi, 2000)

2.4.1 Free-field motion

The first step to calculate the stresses on tunnel due to travelling seismic waves, is the evaluation of the *free-field* deformation. The term *free-field* refers to soil strains caused by seismic waves in the absence of structures and excavations. This deformation is computed ignoring the interaction between the underground structure and the surrounding ground, providing a first-order estimate of the structure deformation. This approach may overestimate or underestimate the tunnel deformation due to the different structure stiffness compared to surrounding medium.

Closed-form expressions exist in literature which simply estimate the tunnel strains and stresses arising in the tunnel lining. The seismic wave field is modelled as a plane wave with the same amplitude in every tunnel segment, differing only in their arrival time (coherence). Wave scattering and three dimensional propagation are neglected, even if these phenomena can determine a variation of stress and strain along the tunnel axis.

St. John and Zahrah (1987), using the approach of Newmark (1968) for wave propagation, develop *free-field* solutions for three wave types (compression P, shear S and Rayleigh waves) impinging the tunnel. The starting point of the analytical procedure is the equation of planar wave propagation in *x* direction through a homogeneous medium:

$$u(x,t) = f(x - Ct) \tag{2.1}$$

In (2.1), *t* is the time and *C* is the wave propagation speed in the medium. In

order to calculate the curvature and strain in the wave propagation direction, the $u(x,t)$ is derived to x:

$$\frac{\partial u}{\partial x} = -\frac{1}{C}\frac{\partial u}{\partial t} \tag{2.2a}$$

$$\frac{\partial^2 u}{\partial x^2} = -\frac{1}{C^2}\frac{\partial^2 u}{\partial t^2} \tag{2.2b}$$

Using the equations (2.2) the strain and curvature in free-field conditions are calculated for the three different types of waves (P, S, and Rayleigh waves). For example, for the compression P wave, the maximum longitudinal strain value is:

$$\varepsilon_{lm} = \frac{V_p}{C_p} \tag{2.3}$$

where V_p is the peak ground velocity of seismic signal (amplitude for sinusoidal waves) and C_p is the propagation velocity for the compression waves. If the maximum curvature for shear waves S is considered, the expression will be:

$$\frac{1}{\rho_m} = \frac{a_s}{C_s^2} \tag{2.4}$$

a_s is the peak ground acceleration of the seismic signal (amplitude for sinusoidal waves) and C_s is the propagation speed for shear waves. In the general case, the P, S and Rayleigh waves propagate in the medium with a generic angle of incidence on the underground structure. In Table 2.2, the components of deformation and curvature relevant to the different wave types, their maximum values and the angles of incidence for which the maximum occurs are shown (the P, S or R notation is relative to compression, shear and Rayleigh waves).

The axial and bending deformations are combined in order to calculate the total longitudinal strain. The values relative to compression waves P and shear waves S are:

$$\varepsilon_{ap} = \frac{V_p}{C_p}\cos^2\phi + r\frac{a_p}{C_p^2}\sin\phi\cos^2\phi \tag{2.5a}$$

$$\varepsilon_{as} = \frac{V_s}{C_s}\sin\phi\cos\phi + r\frac{a_s}{C_s^2}\cos^3\phi \tag{2.5b}$$

Sometimes it is difficult to evaluate which wave is crucial for the tunnel design, but the Rayleigh waves are significant only for shallow tunnel very far from the seismic source.

Table 2.2: strain and curvature due to body and surface waves (St.John & Zahrah 1987)

Wave Type	Longitudinal strain	Normal strain	Shear strain	Curvature
P waves	$\varepsilon_l = \frac{V_p}{C_p}\cos^2\phi$ $\varepsilon_{lm} = \frac{V_p}{C_p}$ *(for $\phi = 0°$)*	$\varepsilon_n = \frac{V_p}{C_p}\sin^2\phi$ $\varepsilon_{nm} = \frac{V_p}{C_p}$ *(for $\phi = 90°$)*	$\gamma = \frac{V_p}{C_p}\sin\phi\cos\phi$ $\gamma_m = \frac{V_p}{2C_p}$ *(for $\phi = 45°$)*	$\frac{1}{\rho} = \frac{a_p}{C_p^2}\sin\phi\cos^2\phi$ $\frac{1}{\rho_m} = 0.385\frac{a_p}{C_p^2}$ *(for $\phi \cong 35°$)*
S waves	$\varepsilon_l = \frac{V_s}{C_s}\sin\phi\cos\phi$ $\varepsilon_{lm} = \frac{V_s}{2C_s}$ *(for $\phi = 45°$)*	$\varepsilon_n = \frac{V_s}{C_s}\sin\phi\cos\phi$ $\varepsilon_{nm} = \frac{V_s}{2C_s}$ *(for $\phi = 45°$)*	$\gamma = \frac{V_s}{C_s}\cos^2\phi$ $\gamma_m = \frac{V_s}{2C_s}$ *(for $\phi = 0°$)*	$\frac{1}{\rho} = \frac{a_s}{C_s^2}\cos^3\phi$ $\frac{1}{\rho_m} = \frac{a_s}{C_s^2}$ *(for $\phi = 0°$)*
Rayleigh waves (compressional component)	$\varepsilon_l = \frac{V_{RP}}{C_R}\cos^2\phi$ $\varepsilon_{lm} = \frac{V_{RP}}{C_R}$ *(for $\phi = 0°$)*	$\varepsilon_n = \frac{V_{RP}}{C_R}\sin^2\phi$ $\varepsilon_{nm} = \frac{V_{RP}}{C_R}$ *(for $\phi = 0°$)*	$\gamma = \frac{V_{RP}}{C_R}\sin\phi\cos\phi$ $\gamma_m = \frac{V_{RP}}{2C_R}$ *(for $\phi = 45°$)*	$\frac{1}{\rho} = \frac{a_{RP}}{C_R^2}\sin\phi\cos^2\phi$ $\frac{1}{\rho_m} = 0.385\frac{a_{RP}}{C_R^2}$ *(for $\phi \cong 35°$)*
Rayleigh waves (shear component)		$\varepsilon_n = \frac{V_{RS}}{C_R}\sin\phi$ $\varepsilon_{nm} = \frac{V_{RS}}{C_R}$ *(for $\phi = 90°$)*	$\gamma = \frac{V_{RS}}{C_R}\cos\phi$ $\gamma_m = \frac{V_{RS}}{C_R}$ *(for $\phi = 0°$)*	$\frac{1}{\rho} = \frac{a_{RS}}{C_R^2}\cos^2\phi$ $\frac{1}{\rho_m} = \frac{a_{RS}}{C_R^2}$ *(for $\phi = 0°$)*
The Poisson's ratio and dynamic modulus of a deposit can be computed from measured P and S waves propagation velocities in an elastic medium: $\nu_s = \frac{1}{2}\frac{(C_p/C_s)^2 - 2}{(C_p/C_s)^2 - 1}$ or $C_p = \sqrt{\frac{1}{(1-2\nu_s)}}C_s$; $E_s = \rho_s C_p^2\frac{(1+\nu_s)(1-2\nu_s)}{(1-\nu_s)}$				

2.4.2 Analytical solutions (St.John & Zahrah, 1987)

In order to obtain closed-form equations to evaluate the soil/structure seismic interaction, the tunnel is considered like an elastic beam surrounded by an elastic medium (St.John & Zahrah, 1987). The analytical solutions are obtained using a quasi-static representation of the seismic actions and neglecting the dynamic effects of the soil/structure interaction.

In the followings, only the shear wave S is considered; the analytical procedures are formally the same also for compression waves P but, as some Authors observed (St.John & Zahrah, 1987, Hashash *et al.*, 2001), the corresponding seismic strains are lower in comparison.

Considering a tunnel subjected to a sinusoidal wave S with wavelength L and amplitude D the displacements values are (Fig. 2.3):

$$u_y = D\cos\phi\sin\left(\frac{2\pi x}{L/\cos\phi}\right) \tag{2.6a}$$

$$u_x = D\sin\phi\sin\left(\frac{2\pi x}{L/\cos\phi}\right) \tag{2.6b}$$

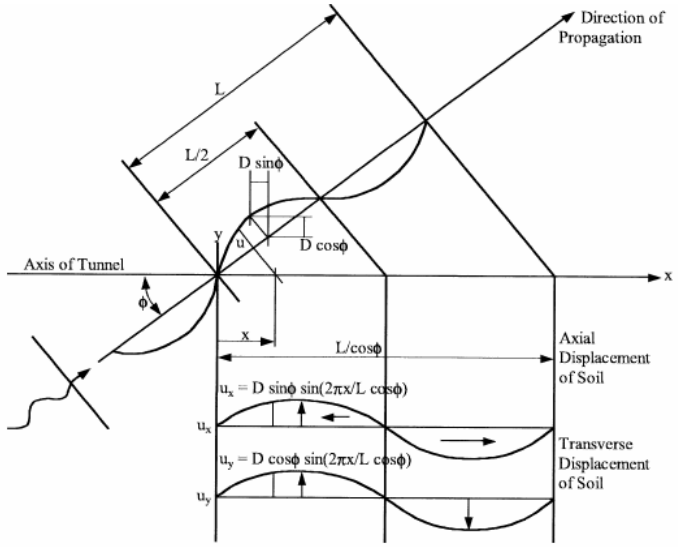

Figure 2.3. Displacements due to a sinusoidal shear wave.

The wavelength parameter L of the ideal sinusoidal signal representing the earthquake action is defined as $L = T_s C_s$ (Wang, 1993), where T_s is the fundamental period of the deposit, which can be calculated for instance according to Idriss and Seed (1968), and C_s is the propagation speed of the shear waves.

The sinusoidal wave amplitude D comes from specific site conditions. Generally the parameter D can be computed according to the following expressions (Hashash *et al.*, 2001), in which it is the only unknown quantity, by equalling the deformations values in free-field conditions (2.7) and the

structure strain of an elastic beam:

- for axial free-field deformations: $\frac{2\pi D}{L} = \frac{V_S}{C_S}\sin\phi\cos\phi$ (2.7a)
- for bending free-field deformations: $\frac{4\pi^2 D}{L^2} = \frac{a_S}{C_S}\cos^3\phi$ (2.7b)

Once obtained all the wave parameters, the following expressions of the seismic internal forces in the tunnel lining can be computed (St.John & Zahrah, 1987):

$$N = \left(\frac{2\pi}{L}\right)\sin\phi\cos\phi E_t AD\cos\left(\frac{2\pi x}{L/\cos\phi}\right) \quad (2.8a)$$

$$T = \left(\frac{2\pi}{L}\right)^3\cos^4\phi E_t IA\cos\left(\frac{2\pi x}{L/\cos\phi}\right) \quad (2.8b)$$

$$M = \left(\frac{2\pi}{L}\right)^2\cos^3\phi E_t IA\sin\left(\frac{2\pi x}{L/\cos\phi}\right) \quad (2.8c)$$

where E_t is the Young's modulus of the structure, I is the second moment of area, A is the area of the transverse section. The expressions (2.8) were obtained without considering the dynamic soil-structure interaction. Therefore, if the structure is stiffer than the surrounding ground it distorts less, as a consequence of the interaction.

If the structure is considered as an elastic beam on an elastic soil, the static interaction is considered and the equation to solve is:

$$E_t I\frac{d^4 u_t}{dx^4} = p \quad (2.9)$$

where u_t is the structure deformation and p is the interface stress. The contact action at the interface between the soil and the structure is modelled through a bed of linearly elastic springs:

$$p = K_t(u_y - u_t) \quad (2.10)$$

Substituting the (2.10) in the (2.9) the tunnel curvature obtained is lower than the value of the previous calculation.. A reduction parameter can be used to take into account this difference:

$$R_1 = \frac{1}{1 + \frac{E_t I}{K_t}\left(\frac{2\pi}{L}\right)^4 \cos^4 \phi} \tag{2.11}$$

Shear forces and bending moments must be reduced using the *R* factor in order to obtain correct solutions. The same approach is used to find the expression of the axial force from the equation:

$$E_t A \frac{d^2 u_a}{dx^2} = K_a (u_a - u_x) \tag{2.12}$$

A reduction factor is obtained to be multiplied by the previous expression (2.8a) for axial forces:

$$R_2 = \frac{1}{1 + \frac{E_t A}{K_a}\left(\frac{2\pi}{L}\right)^2 \cos^2 \phi} \tag{2.13}$$

According to Eqs (2.8) and (2.11), the angle that maximizes bending moments and shear forces is ϕ=0°. On the other hand the condition of maximum axial force does not follow straightforward from Eqs. (2.8) and (2.13), but it is common assumption in design that the maximum axial force can be computed for ϕ=45°, which corresponds to the exact maximum condition when the soil-structure interaction is neglected (Eq.2.8).

In soft soil the structure modifies the deformation of the surrounding ground, therefore Eqs (2.11) and (2.13), which accounts for interaction, should be used; on the other hand, in rock and stiff soil the use of the free-field expressions (2.8) is usually enough accurate due to the high contrast of stiffness between the tunnel and the ground.

According to Eqs. (2.8), as structural stiffness increases due to tunnel lining reinforcements, this generally determines an increase of the seismic loads in the lining. In order to avoid this, flexible joints can be designed.

When the use of Eqs. (2.11) and (2.13) is needed, the spring constants K_t and K_a shall be determined. They represent the ratios between the interface soil-structure interaction loads and the corresponding displacements. Literature values for this constants (Wang, 1993) are a function of the wavelength of incident wave:

$$K_t = K_a = \frac{16\pi G_s (1 - \nu_s)}{(3 - 4\nu_s)} \frac{d}{L} \tag{2.14}$$

where G_s and ν_s are the shear stiffness modulus and Poisson ratio for the medium and d is the diameter of the circular tunnel.

This elastic coefficients must be representative of the dynamic behaviour and the cyclic load of the sinusoidal wave.

2.4.3 Seismic deformation method (Kawashima, 1999)

A new quasi-static method was used in Japan for the design of underground fuel pipelines from the Chiba Port to the International Airport of Marita (JRA, 1976): in this method the seismic deformation of the ground is the assumed as the seismic action on the pipelines. In the following years the method was improved until it became the main design method in Japan for all the underground structures under seismic conditions, known as 'Seismic Deformation Method'.

According to the method a long tunnel is modelled as an elastic beam in elastic soil. The equations of motion in the longitudinal and transverse directions are expressed as:

$$m\frac{\partial^2 u_a(x,t)}{\partial t^2} + E_t A\frac{\partial^2 u_a(x,t)}{\partial x^2} = K_a\{u_x(x,t) - u_a(x,t)\} \tag{2.15}$$

$$m\frac{\partial^2 u_t(x,t)}{\partial t^2} + E_t I\frac{\partial^4 u_t(x,t)}{\partial x^4} = K_t\{u_y(x,t) - u_t(x,t)\} \tag{2.16}$$

where m is the mass of lining for unit length, E_tA and E_tI are the axial and bending stiffness of the tunnel section; u_a and u_t are the longitudinal and transversal displacements of section x at the time t; u_x and u_y are the displacements at the same instant t of the soil surrounding the same section x, K_a and K_t, are the elastic constants of the springs modelling the soil reaction in the longitudinal and transversal direction. As the inertial effects can be in most cases neglected, the (2.15) and (2.16) can be simplified to the Eqs. (2.9-2.10) and (2.12).

To use the above formulas in design, the soil displacements u_x and $u_{y.}$ are computed in the method by assuming an ideal soil deformation of sinusoidal shape having wavelength L (Fig.2.4).

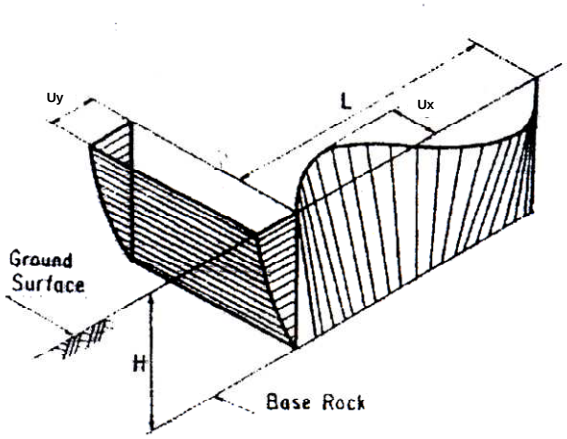

Figure 2.4: Ideal displacements of tunnel axis (Kawashima 1999)

The *free-field* deformation of the soil surrounding the tunnel is the result of different components due to the non homogeneous subsoil characteristics, the thickness of soft soil layers, and the signal variation compared to the bedrock registration. In order to take into account such a variability, the wavelength *L* of the ideal *free-field* displacement function is not the simple wavelength of the wave passing through the medium but rather an equivalent value that give a good agreement of the six seismic deformation components. The *L* adopted value is:

$$L = \frac{2L_1 L_2}{L_1 + L_2}; L_1 = V_S T_S; L_2 = V_{SB} T_S \tag{2.19}$$

V_S and V_{SB} are the propagation velocity of the shear waves in the soil and in the bedrock respectively. T_S is the fundamental period of soil layer, calculated as:

$$T_S = 1.25 \sum_i \frac{4H_i}{V_{Si}} \tag{2.20}$$

H_i and V_{Si} are the thickness and the shear waves propagation velocity of the i-th sub-layer, that is for each sub-layer in which the soil is divided. Once the wavelength L is defined, the design value of the soil displacement both in longitudinal and transversal direction is given by the following expression:

$$u(x,t) = u_h \cos\left(\frac{\pi z}{2H}\right) \sin\left(\frac{2\pi x}{L}\right) \tag{2.21}$$

u_h is the horizontal displacement at surface and is obtained, in the hypothesis of homogeneous soil, as:

$$u_h = \frac{2}{\pi^2} S_V T_S \tag{2.22}$$

where S_V is the design peak ground velocity of the bedrock response spectrum.

By substituting Eq. (2.21) in the (2.17) and (2.18), the differential equation can be solved and the axial forces and bending moments on the structure are given as:

$$N_h = c_{ta} c_{ja} \frac{\pi E_t A}{L} \tilde{u}_h \tag{2.23}$$

$$N_v = c_{ta} c_{ja} \frac{\pi E_t A}{L} \frac{\tilde{u}_h + \tilde{u}_v}{2} \tag{2.24}$$

$$M_h = c_{tt} c_{jt} \frac{4\pi^2 E_t I_h}{L^2} \tilde{u}_h \tag{2.25}$$

$$M_v = c_{tv} c_{jv} \frac{4\pi^2 E_t I_v}{L^2} \tilde{u}_v \tag{2.26}$$

In these expressions N_h and N_v represent the axial forces in the horizontal and vertical direction; M_h and M_v are the bending moments in the horizontal and the vertical plane containing the tunnel axis. Other terms appear in the Eqs. (2.23-2.26): $\tilde{u}_h$ and $\tilde{u}_v$ are the displacements at the tunnel depth, in the horizontal and vertical direction; c_{ta}, c_{tt} and c_{tv} are the transmission factors of displacements from the soil to the structure, in the axial and transversal components direction; finally c_{ja}, c_{jt} and c_{jv} are the modification factors due to the contours conditions of the longitudinal element.

The transmission factors are:

$$c_{ta} = \frac{1}{1 + \left(\frac{2\pi}{\lambda_a L'} \right)^2}; \ \lambda_a = \sqrt{\frac{K_a}{EA}}; \ L' = \sqrt{2} L \tag{2.27}$$

$$c_{tt} = \frac{1}{1 + \left(\frac{2\pi}{\lambda_h L} \right)^4}; \ \lambda_t = \sqrt[4]{\frac{K_t}{EI_h}} \tag{2.28}$$

$$c_{tv} = \frac{1}{1+\left(\frac{2\pi}{\lambda_v L}\right)^4};\ \lambda_v = \sqrt[4]{\frac{K_v}{EI_v}} \tag{2.29}$$

where K are the spring stiffness in which the soil is modelled. The axial force (2.23) and the bending moment (2.25) expressions, combined with static loads, are used in the design of the underground Japanese structures.

2.5 ANALYSIS OF THE TRANSVERSE SECTION OF A TUNNEL

When a shear wave propagates perpendicularly to the tunnel axis the transverse section of the tunnel is deformed: circular tunnels undergo ovalisation, rectangular sections undergo racking. A common approach to design is neglecting the asynchronous effects in the longitudinal direction and considering the cross section of the tunnel under plane strain. In the followings the attention will be focused on circular tunnels only.

The dynamic interaction between the ground and the lining is neglected and the maximum distortional deformation due to the shear waves is calculated in the *free-field* conditions (fig.2.5). The maximum diameter change of an ideal circle in the elastic medium and in the *free-field* conditions, is (Hashash *et al.* 2001):

$$\frac{\Delta}{d} = \pm\frac{\gamma_{\max}}{2} \tag{2.30}$$

If the circular unlined perforation is considered, the diameter change is dependent on the Poisson ratio of the medium:

$$\frac{\Delta}{d} = \pm 2\gamma_{\max}(1-\nu_s) \tag{2.31}$$

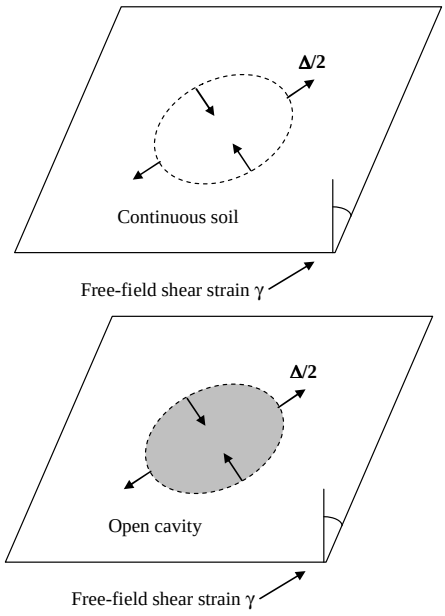

Figure 2.5: Shear strains of free-field and perforated soil (Hashash et al. 2001)

The perforated medium undergoes higher distortion (Eq. 2.31) compared to the intact medium (Eq. 2.30), about three times larger. When the lining is also considered, the maximum distortion is dependent on the soil/structure relative stiffness: if the tunnel stiffness is lower than the surrounding soil, then the condition is similar to a perforated ground (Eq. 2.31); if the soil and structure stiffness are comparable, the dynamic interaction gives values similar to the *free-field* condition (Eq. 2.30); finally, if the tunnel is stiffer than surrounding medium the distortion is lower than Eq (2.30).

As the presence of a lined cavity (i.e. the tunnel) affects the deformation field compared to the *free-field* conditions, such the interaction should be taken into account when computing the stresses in the lining.

2.5.1 Maximum free-field shear strain

The maximum shear strain in the *free-field* conditions at the tunnel depth is

the input parameter for the pseudo-static calculation of the internal forces in the tunnel lining. Wang (1993) suggests to calculate such a strain simply as the ratio between peak ground velocity at tunnel depth and the shear wave velocity of the soil layer, according to the wave propagation theory in an elastic, homogenous and isotropic medium. Penzien and Wu (1998) suggest to start from a displacement profile at the time t, in which the shear distortion is maximum and calculate the maximum shear strain as:

$$\gamma_{max} = \frac{u(-d/2,t) - u(d/2,t)}{d} \tag{2.32}$$

Kawashima (1999) suggests an even simpler horizontal *free-field* displacements distribution that has a quarter sinusoidal shape (§ 2.4.3 (2.22)).

A slightly more accurate procedure, in order to calculate the maximum shear strain, was proposed in some recently published works of conference proceedings (Bilotta *et al.* 2007, Bilotta *et al.* 2007). The γ_{max} values were evaluated as the ratio between the maximum shear stresses τ_{max} and the elastic shear moduli G.

The shear stress profile was computed through two different approaches .The first approach uses the following expression:

$$\tau_{max}(z) = r_d(z)\frac{a_{max,s}}{g}\sigma_v(z) \tag{2.33}$$

as used in simplified approaches of the liquefaction potential (Santucci de Magistris 2005). Beyond the vertical stress σ_v, the other factors are the peak ground acceleration on surface $a_{max,s}$ and reductive coefficient r_d which takes into account the soil stiffness and can be computed for instance according to the formula by Iwasaki et al (1978):

$$r_d(z) = 1\text{-}0.015z \quad (z \text{ in m}) \tag{2.34}$$

The peak ground acceleration at surface $a_{max,s}$ can be simply obtained from the peak ground acceleration at the bedrock, $a_{max,b}$, multiplied for the site amplification factor *S* (EN 1998-1 2003, NTC, 2008).

In the second approach, the shear strain $\tau_{max}(z)$ is calculated through the horizontal equilibrium of a soil column, between the surface and the depth *z*, as:

$$\tau_{\max}(z) = \int_0^z \rho_s a_{\max}(z) dz \tag{2.35}$$

where ρ is the soil density. In the simplest application the profile of maximum acceleration can be assumed linear from $a_{max,b}$ at bedrock to $S \cdot a_{max,b}$ at surface.

Using the pseudo-static approaches, linear and linear-equivalent analyses were carried out, adopting a visco-elastic behaviour for the investigated soil. In the linear analyses, the shear modulus G was assumed as the small strain modulus G_0; in the linear equivalent analyses G was referred to a degradation curve $G(\gamma)/G_0$, depending on shear strain level. In order to evaluate the maximum strain of the soil of the linear equivalent analyses, the Ramberg & Osgood (1943) model was considered, in which the shear strain was correlated with the maximum shear stress, using the expression:

$$\gamma_{\max}(z) = \frac{\tau_{\max}(z)}{G_0} + C\left[\frac{\tau_{\max}(z)}{G_0}\right]^R \tag{2.36}$$

In the (2.36), C and R are parameters depending on the particular subsoil considered, which can be calculated by fitting the degradation curve $G(\gamma)/G_0$. The second addend of the equation (2.36) represented the increment of shear stain due to non-linearity of the soils.

2.5.2 Formulae for seismic increments of internal forces in the lining

Some Authors have suggested formulae for the calculation of the increments of the internal forces in the lining due to the ground shear strain γ around the tunnel; they consider the relative stiffness between the soil and the structure.

According to **Wang (1993)** the relative stiffness between the structure and the surrounding medium is represented with two dimensionless parameters:

$$C = \frac{E_s(1-\nu_t^2)r}{E_t t_t (1+\nu_s)(1-2\nu_s)} \tag{2.37}$$

$$F = \frac{E_s(1-\nu_t^2)r^3}{6E_t I(1+\nu_s)} \tag{2.38}$$

where t_t is the lining thickness, I is the second moment of the area of the lining section, E_t and ν_t are the elasticity Young's modulus and Poisson ratio

of the structure, and E_s and ν_s the corresponding quantities of the surrounding ground. Assuming full-slip conditions at the interface between the soil and the lining, the diameter change, and the maximum increments of bending moments and hoop forces are:

$$\frac{\Delta d}{d} = \pm \frac{1}{3} K_1 F \gamma_{\max} \tag{2.39}$$

$$N_{\max} = \pm \frac{1}{6} K_1 \frac{E_s}{(1+\nu_s)} r \gamma_{\max} \tag{2.40}$$

$$M_{\max} = \pm \frac{1}{6} K_1 \frac{E_s}{(1+\nu_s)} r^2 \gamma_{\max} \tag{2.41}$$

in which:

$$K_1 = \frac{12(1-\nu_s)}{2F + 5 - 6\nu_s} \tag{2.42}$$

It is generally assumed that the full slippage between the soil and the lining occurs for very strong earthquakes (Maximum Design Earthquakes). For more frequent seismic events (Operational Design Eathquakes) it is generally assumed that some friction can be developed between tunnel and soil. If the slippage does not occur at all, the expression of hoop force modifies as follows:

$$N_{\max} = \pm K_2 \tau_{\max} r = \pm K_2 \frac{E_s}{2(1+\nu_s)} r \gamma_{\max} \tag{2.43a}$$

$$K_2 = 1 + \frac{F\left[(1-2\nu_s) - (1-2\nu_s)C\right] - \frac{1}{2}(1-2\nu_s)^2 + 2}{F\left[(3-2\nu_s) + (1-2\nu_s)C\right] + C\left[\frac{5}{2} - 8\nu_s + 6\nu_s^2\right] + 6 - 8\nu_s} \tag{2.43b}$$

A quantitative assessment of the tunnel flexibility can be calculate as the ratio between the diameter changes with and without (*free-field*) the tunnel. The value is:

$$\frac{\Delta_t}{\Delta_{ff}} = \frac{2}{3} K_1 F \tag{2.44}$$

According to **Penzien & Wu (1998)** and **Penzien (2000)**, the increments of internal forces in the circular tunnel lining, at the generic angle θ, can be calculated from the maximum diameter change Δ during the earthquake

(Tab.2.3):

Table 2.3: Seismic force (Penzien 2000)

	Full slippage	**No slippage**
M (θ)	$-\frac{6E_t I\Delta_1}{d^2(1-\nu_t^2)}\cos 2\left(\theta+\frac{\pi}{4}\right)$	$-\frac{6E_t I\Delta_2}{d^2(1-\nu_t^2)}\cos 2\left(\theta+\frac{\pi}{4}\right)$
N (θ)	$-\frac{12E_t I\Delta_1}{d^3(1-\nu_t^2)}\cos 2\left(\theta+\frac{\pi}{4}\right)$	$-\frac{24E_t I\Delta_2}{d^3(1-\nu_t^2)}\cos 2\left(\theta+\frac{\pi}{4}\right)$
T (θ)	$-\frac{24E_t I\Delta_1}{d^3(1-\nu_t^2)}sen2\left(\theta+\frac{\pi}{4}\right)$	$-\frac{24E_t I\Delta_2}{d^3(1-\nu_t^2)}sen2\left(\theta+\frac{\pi}{4}\right)$

The Authors calculate the diameter change as:

$$\Delta_i = R\Delta_{ff} = \pm\frac{4(1-\nu_s)}{(\alpha_i+1)}\cdot\frac{d}{2}\gamma_{ff} \tag{2.45}$$

(i=1,2 for full or no slippage conditions)

In this formula the diameter change Δ depends on the maximum *free-field* shear strain γ_{ff} at the tunnel depth and on the parameter α. This is representative of the relative stiffness between the structure and the ground and has two different expressions, in the case of the full slip or no slippage conditions:

$$\alpha_1 = \frac{12E_t I_t(5-6\nu_s)}{d^3 G_s(1-\nu_t^2)} \text{ (full slippage)} \tag{2.46a}$$

$$\alpha_2 = \frac{24E_t I_t(3-4\nu_s)}{d^3 G_s(1-\nu_t^2)} \text{ (no slippage)} \tag{2.46b}$$

According to the formulae in Tab. 2.3 the maximum for the bending moment and for the hoop force in the tunnel lining occur at θ=45°.

It can be noted that the formulae proposed by **Penzien & Wu (1998)** and **Penzien (2000)** depend on the same parameters of those proposed by Wang (1993). Hashash *et al.* (2005) compared the two analytical formulations in a typical problem of a circular tunnel with *d* = 6m at a depth 15m in a homogeneous elastic layer 30m thick.: the characteristics of the structure are shown in the Tab.2.4; in Tab. 2.5 the characteristics of the ground are shown for three typical cases.

Table 2.4: Input lining data (Hashash et al. 2005)

Lining parameter	**Value**
Young's modulus (E_t)	24,800,000 kN/m^2
Area (per unit width)	0.3 m^2/m
Moment of inertia (I)	0.00225 m^4/m
Lining thickness	0.3 m
Weight	0
Poisson's ratio (ν_t)	0.2

Table 2.5: Input soil data (Hashash et al. 2005)

Soil parameter	**Value**	
Case 1	Young's modulus (E_s)	312,000 kN/m^2
	Poisson ratio (ν_s)	0.3
Case 2	Young's modulus (E_s)	312,000 kN/m^2
	Poisson ratio (ν_s)	0.49
Case 3	Young's modulus (E_s)	185,400 kN/m^2
	Poisson ratio (ν_s)	0.49

Using a finite element code (Plaxis v.8.0), a set of analysis was carried to obtain a numerical solution as a reference for the same problem. The conditions were: plain strain; linear elastic lining and surrounding medium; absence of weight; no-slip interface. In order to simulate the pseudo-static action on the lining, a horizontal load distribution was applied on the top boundary. The results are plotted in Fig. 2.6.

For full slip conditions, the bending moments, hoops and shear forces computed by the analytical expressions are very similar for both formulation, whereas for the no-slip conditions the maximum hoop forces by Penzien (2000) (Fig.2.6a) are much lower compared than those computed by formula of Wang (1993). The hoop values computed according to Wang (1993) are similar to the results of the finite element code. For the bending moment and the shear force the solutions are the same (Fig.2.6b). Furthermore for the bending moments the agreement between the two solutions proposed by Wang (1993) and Penzien (2000) is rather satisfactory.

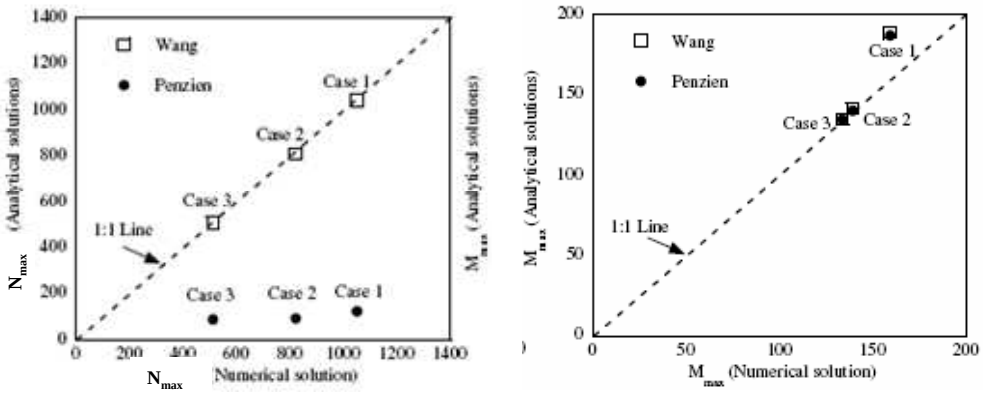

(a) (b)

Figure 2.6: Comparison of calculated forces of numerical solution (x axis) and analytical solution (y axis) in no slippage conditions: thrust force (a) and bending moment (b) (Hashash et al. 2005)

2.6 FINAL CONSIDERATIONS

The chapter reviews the available pseudo-static methods to evaluate the increments of internal forces in a tunnel lining, both in the longitudinal direction and along the cross section, during an earthquake. Some issues should be highlighted:

- the inertia of the surrounding soil is much larger than that of the lining; the tunnel seismic response is in fact dominated by the dynamic response of the surrounding ground.
- for the seismic analysis in the longitudinal direction, the horizontal propagation produces a spatial incoherence of the seismic motion; in common practice a completely coherent seismic signal is assumed;
- the usual design strategy requires evaluating the *free-field* motion in terms of the maximum displacements and the application of them to the structure in a quasi-static analysis aimed to evaluate dynamic interaction forces;
- St.John & Zahrah (1987) and Kawashima (2000) give the expressions of the internal forces arising along the longitudinal axis of a tunnel subjected to seismic loads: they study the tunnel in longitudinal direction as an elastic beam surrounded by elastic springs;

- the most important deformation pattern of the cross section of a circular tunnel is the ovalisation due to the shear waves propagating in the same plane;
- Wang (1993), Penzien & Wu (1998) and Penzien (2000) give the expressions of the internal forces arising in the tunnel cross section, depending on the relative stiffness between the soil and the structure and the maximum *free-field* shear strain;
- Solutions by Penzien (2000) underestimates the hoop forces compared to Wang (1993) in the conditions of no slippage at the interface. Using FEM solutions as a benchmark it appears that solutions by Penzien (2000) may be wrong.

REFERENCE

AFPS/AFTES, (2001), Earthquake design and protection of underground structures.

Ausilio E., Silvestri F., Troncone A., Tropeano G., Seismic displacement analysis of homogeneous slopes: a review of existing simplified methods with reference to Italian seismicity, IV ICEGE, Thessaloniki, 2007

Bilotta E., Lanzano G., Russo G., Santucci de Magistris F., Aiello V., Conte E., Silvestri F., Valentino M., 2007, Pseu-do-static and dynamic analyses of tunnels in transversal and longitudinal direction, Proceedings of Fourth International Conference on Earthquake Geotechnical Engineering, June 25-28, Thessaloniki Greece.

Bilotta E., Lanzano G., Russo G., Santucci de Magistris F., Silvestri F., 2007, Methods for the seismic analysis of trans-verse section of circular tunnels in soft ground, ISSMGE-ERTC12 Workshop at XIV ECSMGE, Geotechnical Aspects of EC8, Chapter 22, Madrid Spain.

Bouckovalas G.D., Papadimitriou A.G., Karamitros D. (2006). Compatibility of EC-8 ground types and site effects with 1-D wave propagation theory. Proceedings ETC-12 Workshop, NTUA Athens.

Clough R.W., Penzien J. (1993), Dynamics of structures,. McGraw-Hill, New York.

Corigliano M., Scandella L., Barla G., Lai C.G., Paolucci R., (2007), Seismic analysis of deep tunnels in weak rock: a case study in Southern Italy, Proceedings of Fourth Interna-tional Conference on Earthquake Geotechnical Engineering, June 25-28, Thessaloniki Greece

EN 1998-1 (2003), Eurocode 8: Design of structure for earthquake resistance,. Part 1: General rules, seismic actions and rules for buildings. CEN European Committee for Standardisation, Bruxelles, Belgium.

Fu P.C., Wang G., Zhang J.M., Analytical approaches for underground structures subjected to longitudinally propagating waves, Proceedings of Third International Conference on Earthquake Geotechnical Engineering, 2004

Hashash, Y.M.A., Hook, J.J., Schmidt, B., Yao, J.I-C. (2001), Seismic design and analysis of underground structures. Tunnelling and Underground Space Technology, 16, 247-293.

Hashash, Y.M.A., Park D., Yao J.I-C., (2005), Ovaling de-formations of circular tunnels under seismic loading, an up-date on seismic design and analyses of underground structures, Tunnelling and Underground Space Technology, 20, 435-441.

Iwasaki T., Tatsuoka F., Tokida KI:, Yasuda S. (1978), A practical method for assessing soil liquefaction potential based on case studies at variuos sites in Japan, Proceedings of the Second International Conference on Microzonational, San Francisco, p. 885-896.

Kawashima K., (1999), Seismic design of underground structures in soft ground: a review, Geotechnical Aspects of Underground Construction in Soft Ground, Kusakabe, Fujita & Miyazaki (eds). Balkema, Rotterdam, ISBN 90 5809 1 066.

Kramer S.L., (1996), Geotechnical Earthquake Engineer-ing,. 653 pp., Prentice-Hall, New Jersey.

NTC, 2008 norme tecniche costruzioni ITA (in Italian)

Okamato S., Tamura C., Kato K., Hamada M., (1973), Behaviours of submerged tunnels during earthquakes, Proceedings of the Fifth World Conference on Earthquake Engineering, vol.1, Rome, Italy, pp. 544-553.

Owen G.N., Scholl R.E., (1981), Earthquake engineering of large underground structures, Report no. FHWA/RD-80/195. Federal Highway Administration and National Science Foundation.

Penzien J., Wu C., (1998), Stresses in linings of bored tunnels, International Journal of Earthquake Engineering and Structural Dynamics, v.27, 1998.

Penzien J., (2000), Seismically induced racking of tunnel linings, International Journal of Earthquake Engineering and Structural Dynamics, 29, 683-691.

Pitilakis K., Gazepis Ch, Anastasiadis A.(2006), Design response spectra and soil classification for seismic code provisions,. Proceedings ETC-12 Workshop, NTUA Athens.

Power M.S., Rosidi D., Kaneshiro J.Y., (1998), Seismic vulnerability of tunnels and underground structures re-visited, Proceedings of North American Tunneling ’98, Newport Beach, CA, Balkema Rotterdam, p. 243-250.

Ramberg W., Osgood W.R. (1943). Description of stress strain curves by three parameters. Technical Note 902, National Advisory Committee for Aeronautics, Washington, D.C.

Rampello S.(2005), Costruzioni in sotterraneo e scavi a cielo aperto,. Linee guida AGI: Aspetti geotecnici della pro-gettazione sismica, Parte III: Opere geotecniche, Capitolo 15, pag. 213-225 (in Italian)

Santucci de Magistris F., 2005, Valutazione della suscettibilità alla liquefazione mediante metodi semplificati, Linee guida AGI: Aspetti geotecnici della progettazione sismica, Appendice E (in Italian).

Silvestri F., Simonelli A.L., 2003, Principi di progettazione e metodologie di analisi, Linee Guida AGI – Aspetti geotecnici delle progettazione in zone sismiche (in Italian).

Silvestri F, 2005, Appendice C – Caratteri dei moti sismici ed analisi di pericolosità, Linee Guida AGI – Aspetti geotecnici delle progettazione in zone sismiche (in Italian).

St.John C.M., Zahrah T.F. (1987), Aseismic design of underground structures, Tunnelling and Underground Space Technology, 2 (2), 165-197

Vanzi I., (2000), Elastic and inelastic response of tunnels under longitudinal earthquake excitation, Journal of Earth-quake Engineering, Imperial College Press, United Kingdom, vol.4(2), Aprile 2000.

Wang J., (1993), Seismic Design of Tunnels: A Simple State-of-the-art Design Approach, Monograph 7, Parsons, Brinckerhoff, Quade and Douglas Inc, New York.

Yoshida N., (1999), Underground and buried structure, Earthquake Geotechnical Engineering, Seco e Pinto (ed.) 1999 Balkema, Rotterdam, ISBN 90

Chapter 3

Numerical modelling of soil/tunnel interaction

3.1 INTRODUCTION

The most complex level of analysis for the problems of seismic soil/structure interaction is the full dynamic analysis. These type of analyses are generally numerical analyses, performed through calculation codes which implement the finite element method or the finite difference method. In order to give reliable results to the user, the input parameters, both geotechnical and seismic, should be reasonably obtained from a calibration analysis of the calculation domain. Moreover the advanced constitutive models should describe the sufficiently approximated mechanical behaviour of the medium: in the seismic problems the constitutive model of the soil should incorporate a variation law of the stiffness G and damping ratio D_0 with the shear strain γ.

In this chapter the results of dynamic interaction of the soil/tunnel system are explained and discussed. The basic operations of the codes used to perform dynamic analyses are reported, clarifying the limitations and the carried out procedure to perform reliable analyses. The features of tunnel dynamic analyses under sinusoidal input or recordings of Italian earthquakes are accurately described, showing the results in terms of maximum internal forces compared with the values of parallel simplified analyses.

3.2 BACKGROUND OF TUNNEL FULL DYNAMIC ANALYSES

Pakbaz & Yareevand (2005) carried out some numerical analyses using the codes *CA2*, in order to study the effect of the earthquake on the circular tunnels, in an elasto-plastic bi-dimensional medium. The input signal used for the analyses was the acceleration time histories recorded during the Naghan Fars earthquake (Mw=7; a_{max}=0.7g), applied at the bottom of the calculation domain. The tunnel is modelled as an elastic beam and the effect of structure construction was not accounted; moreover the tunnel axis was at 20m depth and has a 4m diameter. Two set of parametric analyses were carried out, in order to show the maximum stresses variation with the peak ground acceleration and with the *flexibility ratio* F (Wang, 1993). Moreover the numerical analyses were compared with the results of theoretical formulas in order to show similarity and difference. In the fig.3.1 the results were reported, using condition of no slippage between soil and tunnel

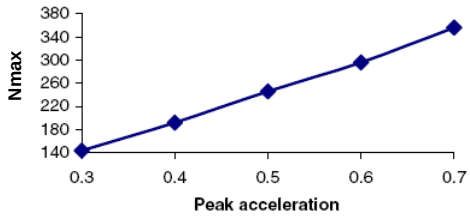

Figura 3.1 a) a_{max} vs. N_{max}

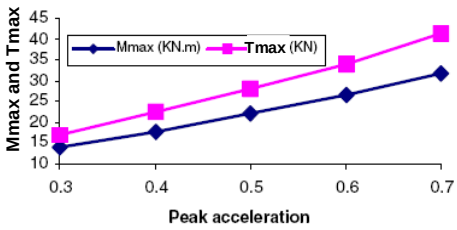

Figura 3.1 b) a_{max} vs. M_{max} e T_{max}

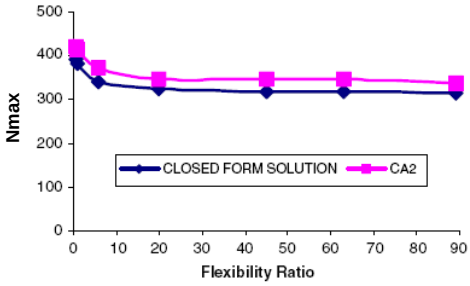

Figura 3.1 c) F vs. N_{max}

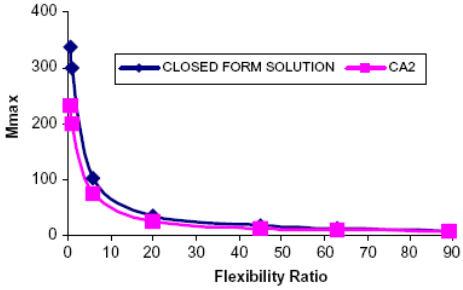

Figura 3.1 d) F vs. M_{max}

In the fig 3.1a) and b), the internal forces of the tunnel varied linearly with the maximum acceleration. In the fig 3.1c) and d) the comparison between

numerical analyses and closed-form equations of Wang (1993) were reported: firstly the numerical internal forces were consistent with the analytical values; secondly the internal forces decreased with the increase of ratio F. In particular the maximum bending moment (fig 3.1d) reduced substantially its value, until almost zero values; instead the maximum hoop load (fig 3.1c) was clearly constant for F>10. From this observation on dependency of M_{max} and N_{max} from the ratio F, the Authors proposed a modification of the formulas of Wang (1993):

$$\begin{aligned} F < 20 \quad & M_{\max} = \pm\left(\frac{1}{6}\right) K_1 \frac{E_m}{(1+\nu_m)} R^2 \gamma_{\max} \\ F > 20 \quad & M_{\max} = \pm\left(\frac{1}{10}\right) K_1 \frac{E_m}{(1+\nu_m)} R^2 \gamma_{\max} \end{aligned} \tag{3.1}$$

In the existing literature, some numerical procedures were reported in order to carry out full dynamic analyses. Bielak *et al.* (2003) developed a procedure called "**Domain Reduction Method**" (DRM). The main idea of the DRM was the division of the initial problem in two successive numerical phases. The calculation domain was reduced to a narrow zone near the structure, separating an external domain from an internal domain. The first calculation phase consisted in the substitution of the internal domain with an equivalent *free-field* domain. An acceleration time histories was applied at the base of the model and the wave propagation was evaluate also in the substituted zone. In the second phase only the reduced domain was considered, applying at the boundaries a distribution of stresses equal to the values obtained in the extended domain *free-field* in the same points.

Corigliano *et al.*(2007) improved this procedure in order to carry out numerical analyses on a rock tunnel near an active fault. In the fig. 3.2 the calculation domain used in the numerical analyses was showed: in the first phase a tri-dimensional domain was considered, including the earthquake generation mechanism at the source; in the second phase a reduced bi-dimensional domain was considered, applying at the lateral boundaries a force distribution evaluate in the previous step in the same points.

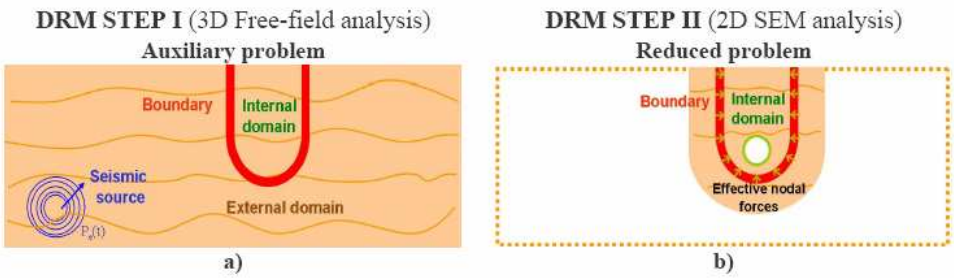

Figura 3.2: Domain Reduction Method (Corigliano et al. 2007)

The internal forces values, calculated in the full dynamic analyses, was then compared with the expression suggested by Corigliano *et al.* (2006): the equations were deduced from the formulas of Einstein & Schwartz (1979), solving the case of a shear strain applied in a quasi-static way to a soil/tunnel system. The expression was obtained using the same approach of Wang (1993) and Penzien (2000). The comparison showed a good agreement between numerical analyses and closed-form solutions (fig.3.3); both for maximum hoop load and bending moment.

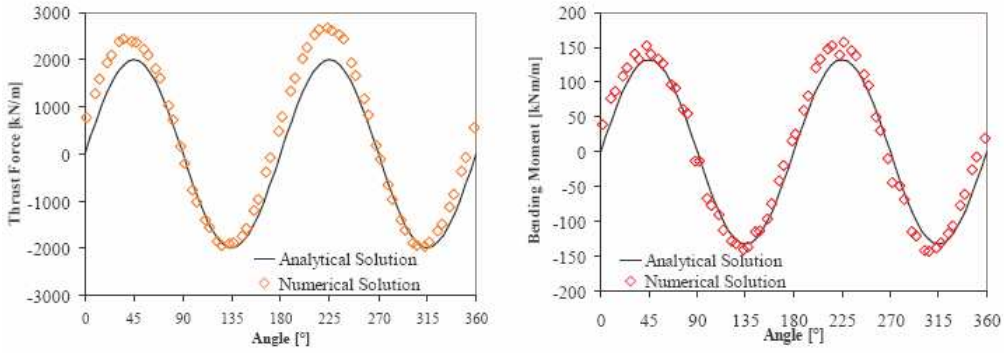

Figura 3.3: Comparison between M e N calculated from the numerical analyses and the closed-form solutions (Corigliano et al. 2007)

3.3 OVERVIEW OF THE NUMERICAL CODES FOR DYNAMIC TESTS

Lanzo (2005) briefly reported the characteristics of some numerical codes, which could perform dynamic analyses: the software listed in the table 3.1 have important difference about the solution of motion equation, the

constitutive models implementation, the damping calculation and the effect of the lateral adsorbent boundaries. Moreover only a restricted part of the software list was constituted by numerical codes able to perform soil/structure interaction analyses (Plaxis 8.0, FLAC 4.0, etc). In order to calculate reliable internal forces due to seismic shaking, for these codes a calibration of the calculation domain features should be performed. In the table 3.1, then, the codes used for the numerical analyses described in this chapter is made in evidence: the characteristics of EERA and Plaxis 8.0 are reported in the next sections.

Table 3.1 Numerical codes for dynamic analyses (Lanzo 2005)

Geometry	Commercial codes	Analysis type		Interface
1-D	SHAKE	TS	LE	DOS
	SHAKE91			
	PROSHAKE			Windows
	SHAKE2000			
	EERA			
	DESRA 2	ES	NL	DOS
	DESRAMOD			
	D-MOD 2			
	SUMDES			
	NERA	TS		Windows
	DEEPSOIL			
	CYBERQUAKE	ES		
2-D/3-D	QUAD4	TS	LE	DOS
	QUAD4M			
	FLUSH			
	QUAKE/W 5.0			Windows
	DYNAFLOW	ES	NL	DOS
	GEFDYN			
	TARA-3			
	FLAC 4.0			Windows
	PLAXIS 8.0			
TS=total stresses; ES=effective stresses; LE=linear equivalent; NL=non linear				

3.2.1 EERA (Bardet et al.2000)

The software EERA (*Equivalent-linear Earthquake site Response Analysis*) is an implementation of the equivalent-linear earthquake site response

analysis, which was previously implemented in the original and subsequent versions of SHAKE (Schnabel et al., 1972; and Idriss and Sun, 1991). EERA evaluates the seismic site response (SSR) of a soil deposit: the medium is modelled as a system of continuous horizontal layer, which are homogeneous, isotropic and visco-elastic, based on a uniform half-space (fig.3.4).

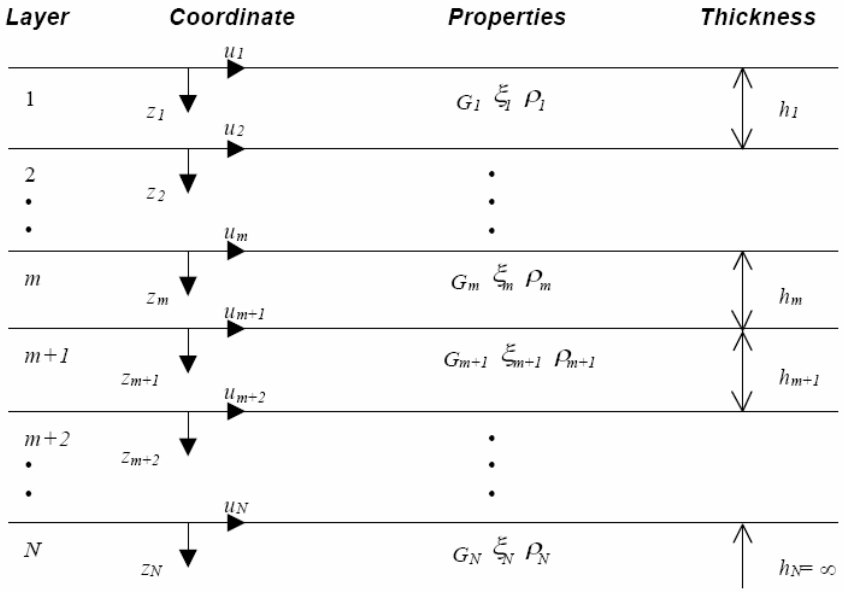

Fig 3.4: One-dimensional layered soil deposit system (Bardet et al.2000)

The one-dimensional equation of motion for vertically propagating shear waves is:

$$\frac{\partial \tau}{\partial z} = \rho \frac{\partial^2 u}{\partial t^2} = G \frac{\partial^2 u}{\partial z^2} + \eta \frac{\partial^3 u}{\partial z^2 \partial t} \tag{3.2}$$

in which h_i, G_i, ρ_i, η_i and ξ_i are respectively the layer thickness, the shear modulus, the unit mass, the viscosity and the damping ratio for each layer. The viscosity and the damping ratio are linearly dependent through the expression:

$$\xi_i = \frac{\eta_i \omega}{2G_i} \tag{3.3}$$

The soil deposit is crossed by shear waves, incident vertically to the surface between the layers. All the numerical models are in *free-field* conditions. EERA implements the SHAKE processor in a Microsoft Excel file, which is composed by the sequent worksheets:

- *Earthquake*
- *Profile*
- *Mat1, Mat2, Mat3, etc.*
- *Iteration*
- *Acceleration, Strain, Ampli, Fourier, Spectra*

In the worksheet "**Earthquake**" the input signal can be loaded in order to perform the ground shaking. Before the earthquake is loaded, in the worksheet was definable five entries (recognizable in blue): the earthquake name; the time step ΔT, which is the time interval between the evenly spaced data points of the time history of input ground motion; the desired maximum acceleration, in order to scale the input values; the maximum frequency cut-off in order to eliminate the annoying high frequencies; the NFFT number of the points of the Fast Fourier Transform, which is larger than the earthquake points. The input earthquake data are imported from a text file using the command "*Process earthquake data*".

The characteristics of the soil deposit are showed in the section "**Profile**", in which the geometry and the properties are defined layer by layer. The user can be choose the type of the analysis to perform: visco-elastic linear or non linear. When a linear visco-elastic analysis is performed, each layer is defined by the thickness h, the maximum shear stiffness G_0, the value of the initial damping D_0, the volume unit weight γ_S, and the apparent shear wave velocity C_S (linearly dependent from the others parameters). When a non linear analysis is carried out, all the previous parameters was defined, except for the damping ratio, which was directly defined by the $D(\gamma)$ law (initial value). Therefore for each soil layer can be defined a different variation curve (in the worksheets **Mat1**, **Mat2**, etc.) for the shear stiffness $G(\gamma)/G_0$ and the damping $D(\gamma)$. The non linear analysis consists in an equivalent visco-elastic analysis: a set of linear analyses are performed sequentially, updating for each step the value of the shear stiffness $G(\gamma)$ and the damping ratio $D(\gamma)$, depending by the convergence on shear strain reached. The location and type of earthquake

motion is defined by specifying *Outcrop* for an outcropping rock motion, or *Inside* for a non outcropping motion (fig 3.5). In the case of *Inside* motion the acceleration time histories is directly applied at the soil layered base; instead a *Outcrop* motion corresponds to a acceleration time history applied on the soil surface and reported at the base through a deconvolution analysis.

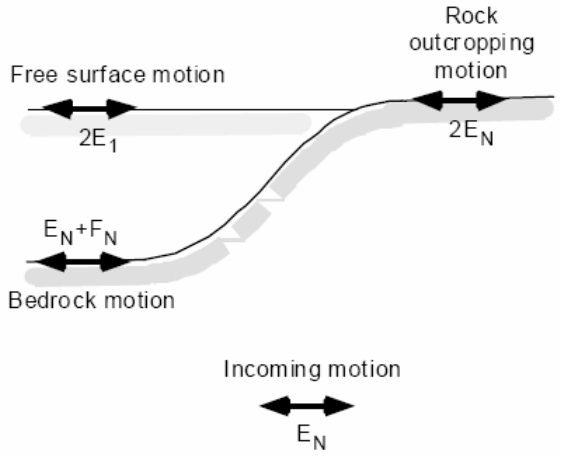

Fig 3.5: Outcrop or inside input motion (Bardet et al.2000)

In the **Iteration** worksheet the motion equations are solved in the frequencies domain. Three option for the calculation are included in this section: the number of iterations, which can be increased depending by the convergence of the calculation; the ratio of equivalent uniform strain R_γ for the effects of earthquake duration, which is typically between 0.4 and 0.75 depending on earthquake magnitude; the type of linear equivalent model (SHAKE or SHAKE91). The calculation starts clicking on the command "*Calculate Compatible Strain*". The iteration procedure for equivalent linear approach in each layer is as follows (fig. 3.6):

- Initialize the values of G_i and ξ_i at their small strain values
- Compute the ground response, and get the amplitudes of maximum shear strain γ_{max} from the time histories of shear strain in each layer
- Determine the effective shear strain γ_{eff} from γ_{max} as:
  $$\gamma_{eff} = R_\gamma \gamma_{max} \qquad (3.4)$$

where R_γ is the ratio of the effective shear strain to maximum shear strain. R_γ is specified in input and is the same for all layers.

- Calculate the new equivalent linear values G_{i+1} and ξ_{i+1} corresponding to the effective shear strain γ_{eff}.
- Repeat the steps until the differences between the computed values of shear modulus and damping ratio in two successive iterations fall below some predetermined value in all layers.

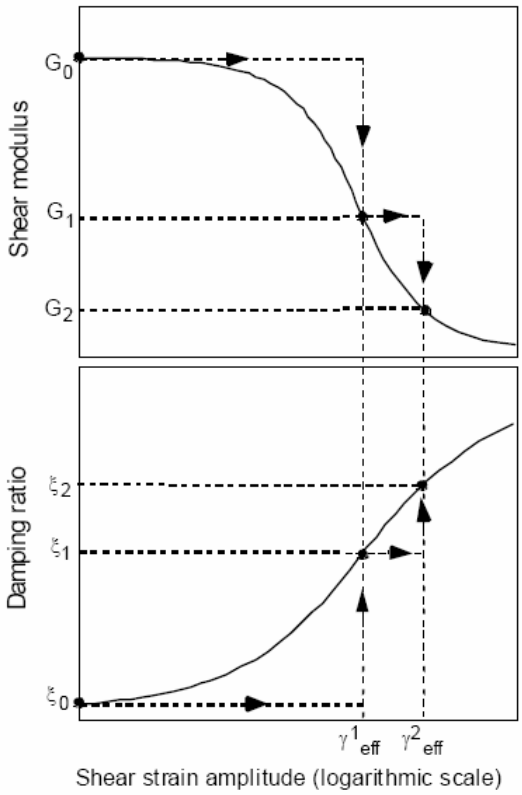

Fig 3.6: Iteration of shear modulus and damping ratio with shear strain in equivalent linear analysis (Bardet et al.2000)

After the calculation is performed, the results were showed as table for each iteration, and as graphs for the profiles of maximum shear stress, shear strain and acceleration. Moreover the distribution with depth of the mobilized G and D were graphically reported.

In the Output worksheets the results of the calculation were reported as time histories or through signals transform in the frequency domain at specific layers: the **Acceleration** and **Strain** worksheets give the time histories of acceleration, velocity and displacement or of shear stress and strain corresponding to a specific layer (outcrop or inside); in the **Fourier** and **Spectra** worksheets the spectrum of Fast Fourier Transform and the response spectrum are evaluated; in the **Ampli** worksheet the amplification function is obtained as a ratio between the Fourier spectra in two different layers. The worksheet can be duplicated in order to obtain the output data in different layers. Once in all the worksheet the soil layer number and the type of layer (inside or outcrop) are specified, the results are given clicking on the command "*Calculate Output*" and "*All of the Above*".

3.2.2 Plaxis 8.0 (Brinkgreve, 2002)

3.2.2.1 General features

The software **Plaxis 8.0** is a finite element (FE) calculation code for stability and deformation analysis. These commercial code is very versatile and largely used for the classical geotechnical problems. The software models real or ideal conditions having one-dimensional or bi-dimensional domain, corresponding to axi-symmetric or plane strains. The software is divided in 4 modulus, which correspond to different phases of the numerical analysis. The Plaxis modulus are:

1. **Input**
2. **Calculation**
3. **Output**
4. **Curves**

In order perform a FE analysis using Plaxis 8.0, the user have to create the model domain, assign the material properties and fix the boundaries condition. In the **Input** software modulus the geometry of the model is created, the mesh is generated and the initial condition was set. The mesh is composed by triangular elements, which can have 6 or 15 nodes, in order to model the volume clusters. The 15 nodes triangle gives a 4^{th} order interpolation for the displacements and 12 Gauss points for the numerical integration; instead the 6

nodes triangle has only a 2nd order integration and 3 Gauss points. In the section *General Settings* the name and the description of the project, the nodes number and the acceleration value are defined; moreover the fundamental dimension were fixed (distance, weight and time). The limit of the model area can be assigned according to the domain extension.

The FE numerical model generation starts from the geometric domain generation, which is the graphical representation of the problem under examination. A geometric model is composed by points, lines and clusters. Despite of this basic element, structural objects can be create, modelling the geometry and the mechanical properties, in order to perform the soil/structure interaction and calculate the internal forces on the element (tunnels, plates, etc.). Once the problem is drawn, the boundary conditions can be assigned by the user, according to the library constraints, or choosing the standard fixities, which is applied automatically according to the analysis type, which can be static or dynamic. Once the geometric and structural settings are defined, distributed (constant or linear) or concentrated loads or displacements, applied in the created internal or external points, can be introduced in the calculation domain. In the *Material* section the mechanical properties of the soil layers are fixable: the assignable values are the unit weight, the permeability and the stiffness-strength parameters, which are the elastic modulus *E*, the Poisson ratio ν, the friction angle ϕ and the cohesion *c*. Moreover the stiffness parameters can be defined as linearly variable with depth. For each soil material created can be assigned a constitutive model and the soil behaviour, assignable between drained and un-drained. For each material the interface soil/structure behaviour is defined through the parameter R, which has 1 as a default value, but can be reduced to values almost null. When an interface element is located between the soil layer and a structure, a material type is assigned at the interface element and the R represents the reduction factor applied at the elastic stiffness E. If the R=1, the interface condition are “no slip”; if the R=0.1, the interface conditions tend to “full slip”.

The Plaxis 8.0 software implements 6 constitutive models, in order to perform different soil behaviour. Some of the available models are:

- *Linear Elastic Model*
- *Mohr-Coulomb Model*
- *Hardening Soil*

Each cluster of material can be pasted in a permanent folders in order to use the same materials in other analyses.

Also the structural elements are defined in the *Material* section, assigning the properties of the element *Plate*, used both for panels and tunnel structure type. The most important input parameters are the flexural rigidity EI and the axial stiffness EA. From these two parameters, the thickness of the structural element is obtained from the expression:

$$d_{eq} = \sqrt{12\frac{EI}{EA}} \tag{3.5}$$

Once the model features are assigned for each layer and structural element and before the calculation step, the domain is divided in finite elements: the software automatically generates the mesh, without an ordinate structure. In order to get better performance on the analysis results, where the stress variations are very high, the mesh can be more dense, around a model point, line or in a selected region. At the end of Input phase the initial condition is created, performing the generation of pore pressure and effective initial stresses. The initial stress is calculated starting from the K_0 ratio, evaluate from the famous Jaky's (1944) relationship $K_0=1\text{-}sen\phi$ or manually fixed by the user; the lithostatic conditions can be also generated in the Calculation phase, carrying out a plastic analysis without any loads, displacements and structures activated.

After the FE model generation, the effective calculation is carried out, defining the type of analysis required. In the **Calculation** modulus is assigned the analysis phase, the structures and the soil layers are switched on or off, and the loads and the displacements are activated. The calculation is performed, solving a system of equilibrium and congruence equations in the mesh nodes. The Plaxis code permits the execution of 4 types of FE analysis:

- *Plastic*
- *Consolidation*
- *Phi-c reduction*
- *Dynamic*

The *Plastic* option is an elasto-plastic deformation analysis; the *Consolidation* option considers the dissipation with time of pore pressure increments; the *Phi-c reduction* option carries out a stability analysis reducing the strength parameters in order to evaluate a safety factor; the *Dynamic*

option consists in the application of time histories of loads or displacement, corresponding to a point or a line of the model. Before the analysis starting, some relevant mesh points can be selected, in order to know the variation of some parameters with non-geometric parameters. Each calculation phase is divided in steps, in order to carry out the specific analysis in progressive increments of the variable parameters. When the analysis phase is set, the analysis type, the starting phase, the number of steps, the iterative control parameters should be fixed. Once all the phase condition is defined, the calculation process is started; the analysis is performed in sequence, until the soil does not collapse. In the *Iteration* window, some information of calculation process are showed, including the evolution of the displacement in the selected point, in order to check that the analysis correctly goes forward.

Once a FE analysis phase is ended or stopped (manually or automatically due to soil collapse), the results of the calculation can be inspected in the **Output** modulus. The parameters, which can be displayed in the whole domain, are:

- Total or incremental displacements, velocity and acceleration;
- Total or incremental strain; Cartesian components of total or incremental strain;
- Effective or total stress; Cartesian components of total and effective stresses; total and increments of pore pressure;
- Loads or displacements, stress or strain in the structural elements.

The analysis results was given both as through graphical representation (vectors, contours or shadings) and table lists. The Plaxis user can create a section in the model domain, in order to display the previous listed parameters along the section line (in graph and table form). Concerning the structural elements, the software gives the values of model parameters, but moreover the internal forces in the last calculation steps (hoop load, shear force and bending moment) and the envelops of the previous ones.

The **Curves** modulus is used to obtain non-geometrical variation of the model output parameters (except for the internal forces). In this sub-programme the load or time-displacements curves, the stress-strain ones, the stress or strain paths and the time histories of displacement, velocity or acceleration of the calculation selected points can be displayed and listed. In the mesh nodes, the value of load, displacement, velocity and acceleration are

given; from the integration internal nodes the value of stress and strain are obtained. A total of 10 nodes and 10 integration points can be selected in the Calculation phase, which are an important code limitation on the required results.

3.2.2.2 Dynamic analyses

The procedure to perform dynamic analyses is formally similar to the other types of analyses, but needs some explanations about the additive parameters and conditions compared to the other analyses. Moreover the seismic analysis are particular dynamic analysis, in which the waves propagation due to an earthquake should be correctly modelled. The topics of the dynamic analyses, discussed in this section, are:

- *General settings of earthquakes problems* (**Input**)
  - Standard Earthquake boundaries
  - Prescribed displacements
  - Wave velocities
- *Integration of the motion equation* (**Calculation**)
  - Basic equation of the dynamic behaviour
  - Dynamic time, Time stepping and Dynamic sub-step
  - Boundary coefficients
  - Multipliers for time histories
- *Results of seismic analysis* (**Output** and **Curves**)
  - Envelopes of the internal forces
  - Time histories in the selected points

In order to perform the seismic shaking of a soil layer, the dynamic loads are applied at the bottom of a bi-dimensional model domain, causing the propagation of the shear waves until the surface of the soil layer. In the **Input** modulus the earthquakes problems can be performed, applying at the model, the "*Standard Earthquake Boundary*" (SEB), which includes the creation of adsorbent boundaries on the lateral surface of the domain and prescribed displacements at the bottom of the mesh. The SEB conditions always consider a rigid bedrock, because the adsorbent boundaries are not located on the model bottom and the surface is completely reflecting. Moreover the *Standard Fixities* are also generated in the SEB, in order to perform static analysis, but

in the dynamic analysis are neglected. Using the SF the general boundary constrains are $u_x=0$ for the lateral boundaries and $u_x=0$ and $u_y=0$ for the bottom of the model. The use of prescribed displacements permits the application of time histories of displacements, velocity or acceleration during the Calculation phase. In the prescribed displacement menu, the default conditions consider a dynamic displacement multiplier of $u_x=0.01$m and $u_y=0$m.

The stiffness properties of soil layer can be also defined using the value of compression and shear wave velocity as input parameter. Therefore the relationship between C_P and C_S and the maximum shear stiffness G_0 and the oedometric modulus E_{oed} are:

$$C_s = \sqrt{\frac{G}{\rho}}; \quad C_p = \sqrt{\frac{E_{oed}}{\rho}} \tag{3.6}$$

In the **Calculation** phase the equation of the wave propagation are solved in the time domain. The basic equation of the dynamic behaviour is:

$$[M]\{\ddot{u}\}+[C]\{\dot{u}\}+[K]\{u\}=\{F\} \tag{3.7}$$

in the (3.7), M is the mass matrix, C is the damping matrix, K is the stiffness matrix, F is the displacement vector and u is the displacement vector. The material damping of soil C in the calculation algorithm is implemented as the Rayleigh formulation. Therefore the damping matrix is calculated as linear combination of mass and stiffness matrices:

$$[C]=\alpha_R[M]+\beta_R[K] \tag{3.8}$$

where α_R and β_R are the Rayleigh coefficients. The damping ratio is associated to the j mode of vibration through the expression:

$$\xi_i = \frac{1}{2}\left(\frac{\alpha}{\omega_j}+\beta\omega_j\right) \tag{3.9}$$

The value of the damping ξ_i is not constant with the value of circular frequency $\omega=2\pi f$ (fig.3.7) and depends of the value of the Rayleigh coefficients.

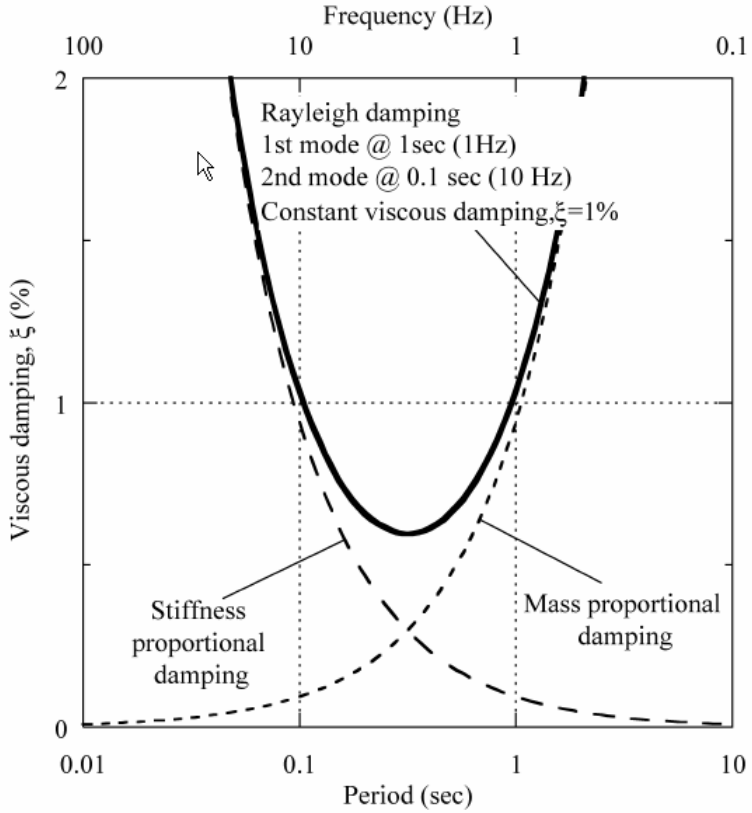

Fig.3.7 Viscous damping vs circular frequency (Hashash & Park 2002)

The value of α_R and β_R can be assigned in the material data sets, caring to use the value of realistic damping because these parameters largely affect the soil response. The default damping conditions are $\alpha_R = \beta_R = 0$, which should model a un-damped scheme.

In order to solve the motion equations, an implicit time integration method is used in the software dynamic implementation, according to the Newmark scheme. The expression of the displacement and velocity at the time t+Δt are:

$$u^{t+\Delta t} = u^t + \dot{u}^t \Delta t + \left[\left(\frac{1}{2} - \alpha_N\right)\ddot{u}^t + \alpha_N \ddot{u}^{t+\Delta t}\right]\Delta t^2$$
$$\dot{u}^{t+\Delta t} = \dot{u}^t + \left[(1-\beta_N)\ddot{u}^t + \beta_N \ddot{u}^{t+\Delta t}\right]\Delta t \qquad (3.10)$$

The values of the coefficients α_N and β_N can modify the accuracy of the numerical integration in the time domain. The Newmark coefficients cannot

be choose independently, but a precise condition is imposed, in order o obtain stable solution:

$$\beta_N \geq 0.5$$

$$\alpha_N \geq \frac{1}{4}\left(\frac{1}{2}+\beta_N\right)^2 \tag{3.11}$$

The default values for the Newmark coefficients are α_N= 0.3025 and β_N= 0.60, valid for a damped scheme. The default values of Rayleigh factors (α_R =β_R =0) and Newmark factors (α_N= 0.3025 and β_N= 0.60) are not coherent, because the null material damping is not concord with the damped scheme used to establish the integration coefficients.

In the Calculation modulus, some parameters should be accurately defined in each dynamic phase in order to perform a correct seismic analysis. Firstly the Dynamic Time, expressed in seconds, for each phase should be assigned; in this was the time step used in the dynamic loading is evaluated as:

$$\delta t = \frac{\Delta t}{n \cdot m} \tag{3.12}$$

where Δt is the Dynamic Time, n is the number of Additional Steps and m is the number of the Dynamic Sub-Step, which can be defined in the calculation menu. The maximum number of Additional Steps available in Plaxis is 1000 and corresponds to the numbers of Curves values for the time histories of the selected point. If the input signals has a number of values higher than 1000, the Plaxis increases the time step of the output data of the time-dependent parameters, in order to give always in output a total number of 1000 points for each dynamic phase. This filtering effect is greater depending on the value of the ratio between the input points and the additional steps and determines an information missing, especially for the high frequency, which are cut away over the 1/(Δt/1000) value. Despite this data missed in the graphical output getting, the integration of acceleration time history is correct if the product between the additional steps and the dynamic sub-step is equal or larger compared to the input motion points. If the time step δt obtained in the Plaxis calculation is different from the time step of the input signals, the software performs the interpolation of the data, in order to obtain an equivalent value for the acceleration. Of course the simplest way to obtain the whole time histories is to separate the input motion, each portion with a total of 1000 points, and apply the cut time history in sequence.

A severe limitation of the time step is directly connected with the mesh properties. Therefore if the time step is too large can give unreliable results and substantial deviation. The value of the limit time step, which is called "critical", is defined by the maximum frequency and by the coarseness of the FE mesh. The expression is:

$$\delta t_{critical} = \frac{B}{\alpha\sqrt{\frac{E(1-\nu)}{\rho(1+\nu)(1-2\nu)}}\sqrt{1+\frac{B^4}{4S^4}-\frac{B^2}{2S}\left[1+\frac{1-2\nu}{4}\frac{2S}{B^4}\right]}} \tag{3.13}$$

in which α is factor dependent by the element type (6 or 15 nodes); B and S are parameters directly connected to the mesh size. This time step is chosen to obtain that a wave during a single step does not move a distance larger than the minimum dimension of an element.

In the Input phase, the SEB procedure assigns adsorbent properties to the lateral boundaries. The use of a lateral adsorbent boundary is equivalent to apply a viscous damper where were the external fixities, in order to simulate the behaviour of a laterally infinite medium. A portion of the travelling wave energy is adsorbed by the dampers, and the rest returns to the calculation domain. Using the method described by Lysmer and Kuhlemayer (1969) the waves reflection in "narrow" calculation domain should be limited. The normal and shear components adsorbed by the damper in the horizontal direction are:

$$\begin{aligned}\sigma_n &= -c_1\rho C_P\dot{u}_x \\ \tau &= -c_2\rho C_S\dot{u}_y\end{aligned} \tag{3.14}$$

In absence of adsorbent boundaries the behaviour is equivalent to a condition in which the coefficients c_1=c_2=1. The Plaxis manual suggests, in order to obtain a reasonable waves adsorbing, the values for the parameters c_1=1 e c_2=0.25.

The seismic input can be applied through dynamic Multipliers, defined in the Input phase, which operate as scaling factors on the value of seismic input time histories:

Prescribed displacement (t) = Input motion (t) × dynamic multiplier (3.15)

In order to activate the input motion, the dynamic time histories should be loaded in the dynamic analysis menu of the Calculation modulus. In this window, the user can apply on the model bottom a harmonic load multiplier or

a generic time histories. When the harmonic load is selected, the user should be assigned amplitude, frequency and initial phase angle of the sinusoidal signal. When the generic time history is optioned, the input motion should be loaded from a file, specifying the input type (displacement, velocity or acceleration), only in two format: *SMC* and *ASCII* files. The *SMC* format is a standard format generated by the U.S. Geological Survey National Strong-motion Program, in order to create a database of earthquakes recordings. These files are available in the National Geophysical Data Center (NGDC) of the National Oceanic Atmospheric Administration (NOAA). The input data of the *SMC* files are accelerations, expressed in cm/s2. For this reason the dynamic multiplier for the prescribed displacement should be fixed to 0,01m in the Input phase. The *ASCII* file can be create by a text editor, generating two columns of data, separated by space: the first column is the time variable and the second one is the input motion, expressed as an history of acceleration, velocity or displacement. If the acceleration is defined as m/s the prescribed displacement u_x=1m, instead if the acceleration is expressed in g, the value u_x=9.81m. Once the file is chosen, the time histories can be visualized (*View* button), in order to ensure that the model correctly read the input motion.

The results of the dynamic analyses are obtained in the Output and Curves sections. The time histories of the node and internal points can be showed in the Curves section, if some points were selected in the calculation phase. The acceleration value are expressed in m/s^2 and the velocity in m/s. In the output section the value of some parameters (acceleration, velocity, displacements, stress, strain, etc.) can be observed relative to the last calculation step. The value of internal forces of a structural elements are also reported as envelopes of maximum and minimum values.

3.2.3 Comparison between the calculation codes

In order to summarize the dynamic performance of the considered software, the basic features of the calculation codes are briefly reported in the table 3.2.

Table 3.2: Comparison between EERA and Plaxis 8.0

Calculation code	**EERA**	**Plaxis 8.0**
Literature	Bardet et al.2000	Brienkgreve 2002
Meshing	Continuous layers	Finite elements
Equation integration	Frequency domain	Time domain
Solution type	Transfer function	Integration step by step
Soil material model	User G(γ)/G and D(γ)	Linear
Non linearity	Linear equivalent	None
Dynamic analysis	Free-field	Soil/Structure interaction
Boundaries	Indefinitely extended	Adsorbent boundaries
Material damping	Independent from ω	Rayleigh formulation

The two dynamic codes has wide difference, which involves many aspects from the soil modelling, the calculation algorithm, the materials model and the properties of the lateral frontiers and the damping ratio. The most important advantage of the FE element analysis consist in the possibility to study seismic interaction between the soil and the structure, which is not included in the EERA analyses. Therefore the Plaxis 8.0 software is used for a wide range of geotechnical application, from the consolidation to stability analysis. The main limit of the FE analysis is in the material model to perform dynamic analysis. The Hardening Soil model, which incorporate plastic deformation for small strain, is unable to reproduce a the degradation curves for the shear modulus and the damping ratio. In order to take account the non-linearity, a mixed procedure EERA-Plaxis was used to carry out full dynamic analyses. In the next section the procedure is described and applied for some cases of study.

3.4 FULL DYNAMIC TESTS

In this section a set of seismic analyses are explained, both in free-field and dynamic interaction conditions. Three types of soil, relative to different class of materials, and three earthquake recordings are used to perform the dynamic analyses. A comparison between different methods of analyses on the same soil types were reported. The analyses were carried out with the two calculation codes, showing all the characteristics of the analyses. All the results were reported in some scientific papers for International and Italian

conference (Bilotta et al.2007a; Bilotta et al. 2007b; Bilotta et al.2007c; Bilotta et al.2008).

3.4.1 Soil profiles types and input signals

The numerical simulations were carried out using three types of soil profile (Fig. 3.8): a 30m layer of soft clay, medium dense sand and gravel were considered, based on a half space of soft rock (C_s= 800m/s, γ_s=22kN/m^3, D_0=0.5%).

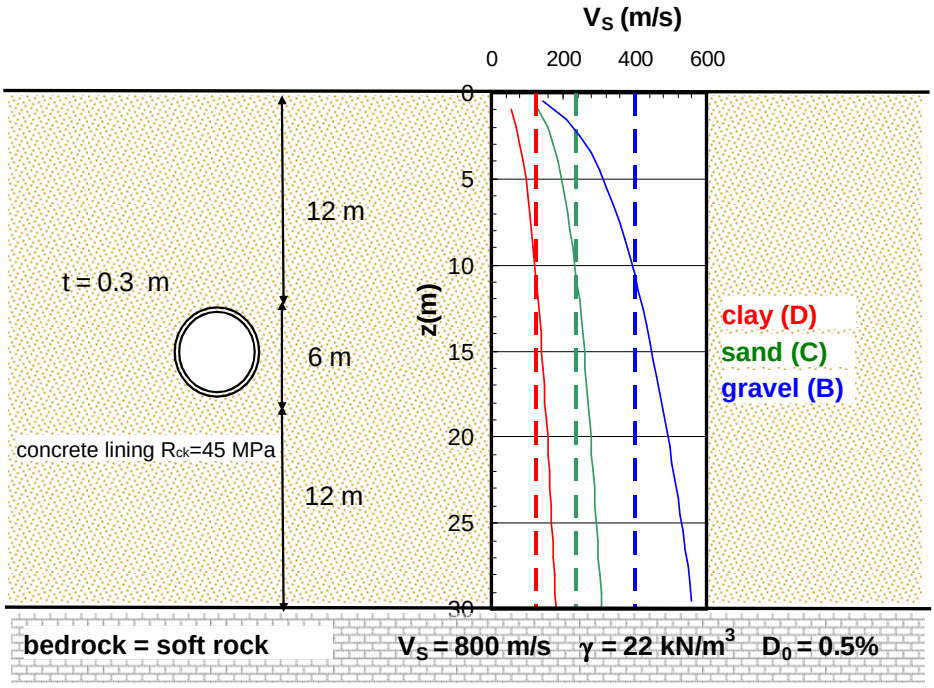

Figure 3.8: Subsoil profile

In the clay profiles of fig.3.8, the un-drained behaviour was not accounted, considering a one-phase material but having shear velocity values typical of a soft clay. The C_S profiles and the value of an "equivalent shear wave velocity" $C_{S,30}$ are reported for each type of subsoil in fig.. The value of $C_{S,30}$ was obtained from the expression:

$$C_{s,30} = \frac{30}{\sum_{i=1,n} h_i / C_{s,i}} \qquad (3.15)$$

The table 3.3 synthesizes the geotechnical parameters of the selected soils:

Table3.3 . Subsoil parameters and classification (NTC, 2008)

Soil	φ' [°]	I_P (%)	γ [kN/m^3]	D_0 (%)	$C_{S,30}$ [m/s]	Type
Clay	25	30	18	2.5	124	D
Sand	35	-	20	1.0	239	C
Gravel	44	-	21	1.0	401	B

For the dynamic analyses, the soil stiffness and damping curves, $G(\gamma)/G_0$ e $D(\gamma)$, depending on the shear strain level, γ, induced by the earthquake. In these cases literature empirical relationship was used in order to define $G(\gamma)/G_0$ e $D(\gamma)$. The fig.3.9 reports the curves adopted and given by:

- For the clay, the curves suggested by Vucetic & Dobry (1991) with I_P=30%;
- For the sand, the Seed & Idriss (1970) curves, implemented in EERA;
- For the gravel, the relation reported by Stokoe (2004) for a D_{50} = 10mm.

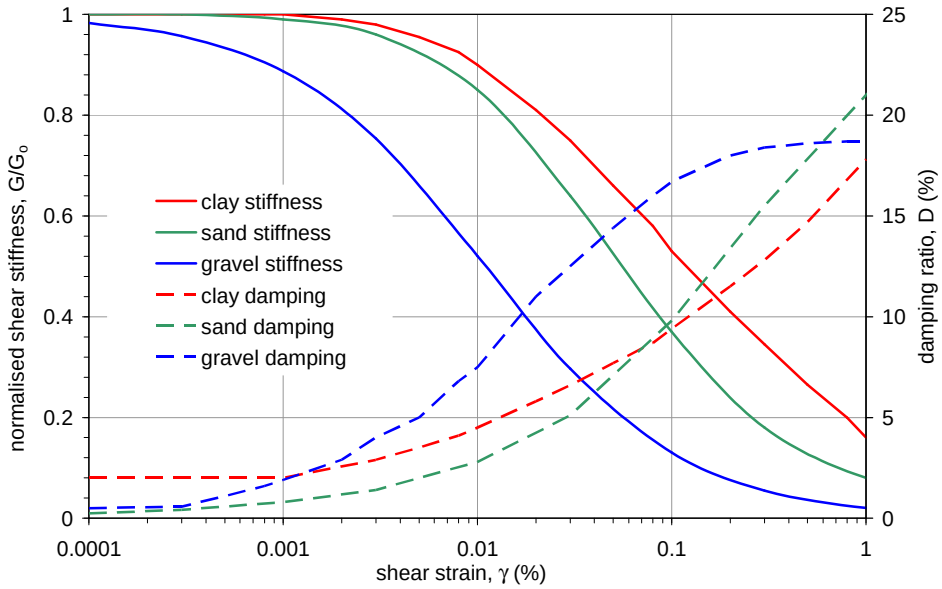

Fig.3.9 Shear stiffness and damping ratio degradation curves

As a input motion, three acceleration time histories was selected from an Italian recording database of seismic events (Scasserra 2008). The most severe

earthquakes was considered (PGA>0.3g) and the signals was scaled to 0.35g (comparable to the real maximum acceleration), corresponding to design earthquake of the seismic zone 1, according to seismic zonation of OPCM 3724 (2003) (fig.3.10). In the table 3.4 the recordings used in the dynamic analyses were reported:

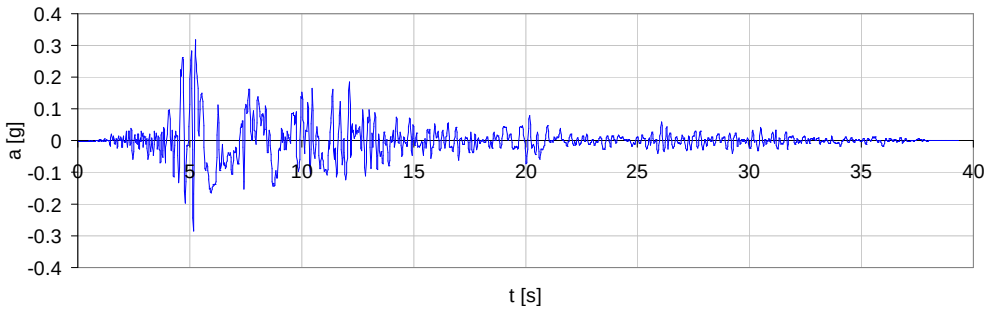

Sturno 270

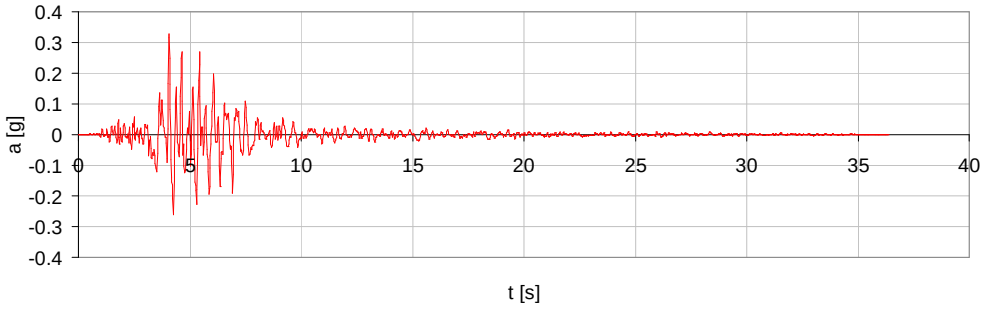

Tolmezzo 00

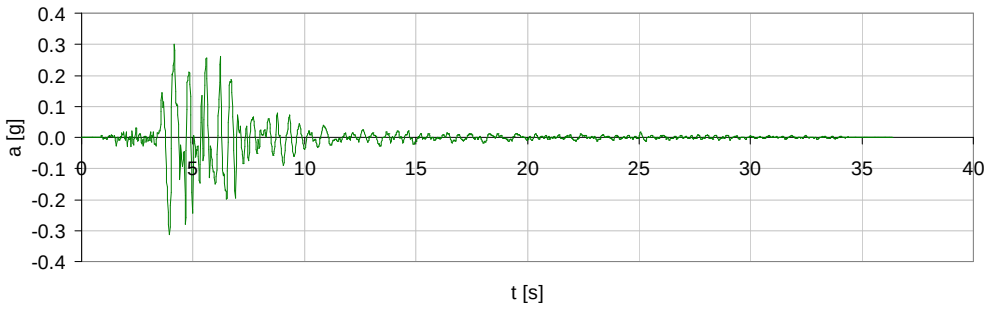

Tolmezzo 270

Fig. 3.10: Scaled recordings of the input earthquakes (Scasserra 2008)

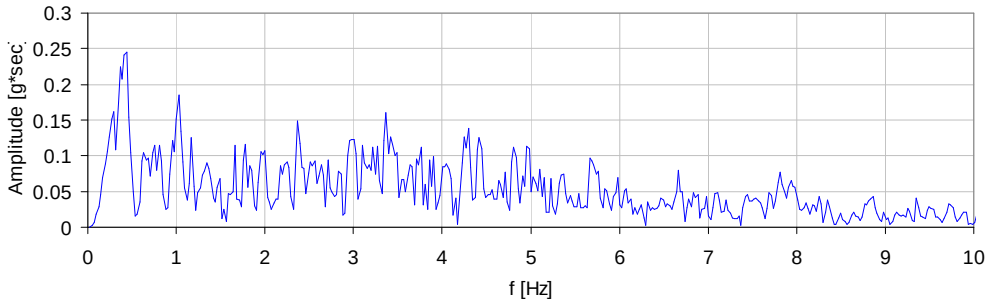

Sturno 270

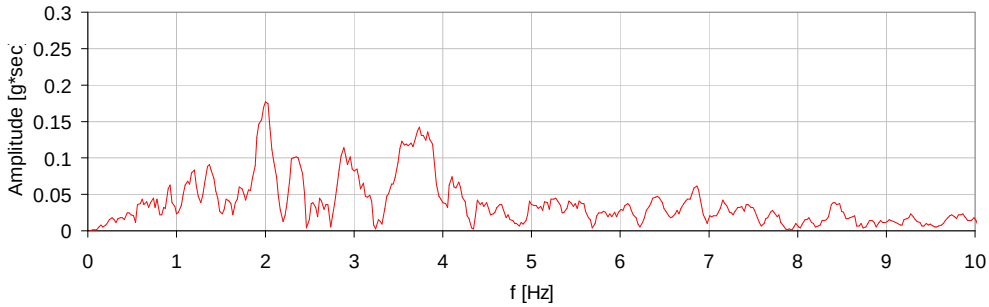

Tolmezzo 00

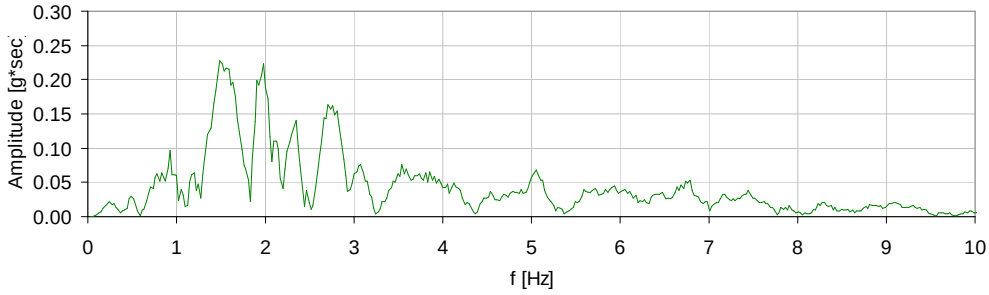

Tolmezzo 270

Fig. 3.11: Fourier spectra of the input earthquakes

The selected recordings were relative to very strong motion, corresponding to historical earthquakes. The frequency content was showed in the fig (3.11), showing that the main frequency is lower for the Sturno 270 signal (0.5Hz), compared to the Friuli (1976) recordings (2Hz and 1.5Hz). In all the

considered signal the energy content was negligible over the 10Hz.

Table 3.4: Acceleration time histories used in the dynamic analyses

Recording	***Earthquake***	***PGA [g]***	***Tp [s]***
Sturno 270	*Campano Lucano 1980*	*0.321*	*2.28*
Tolmezzo 00	*Friuli 1976*	*0.315*	*0.50*
Tolmezzo 270	*Friuli 1976*	*0.375*	*0.67*

The dynamic analyses were carried out using two different calculation code: EERA and Plaxis, which were briefly described in the previous sections. EERA carried out free-field one-dimensional analyses, in which is considered the non linear behaviour of the soil through a visco-elastic linear equivalent analyses. Plaxis 8.0 permitted to insert the tunnel in the calculation domain, carrying out bi-dimensional analyses in which were considered the tunnel behaviour in the transverse section (ovaling deformation).

3.4.2 EERA Analyses

The full dynamic analyses were carried out using a linear elastic model. In order to take account of the stiffness and damping ratio variation with the shear strain in the soil/structure interaction analyses, preliminary analyses were performed using EERA software. The soil profile of the fig.3.8 and the curves of the fig 3.9 were considered as input values in order to carry out the EERA non-linear analyses and give the input data for the full dynamic analyses (Amorosi et al. 2007). The stiffness and damping ratio assigned to the soil material in the Input phase of Plaxis 8.0, were the mobilized values corresponding to the maximum shear strain reached in each soil layer. The modified profiles of shear stiffness and damping ratio depend on the initial value of stiffness and damping, on the variation law adopted for the soil, on the problem geometry and on the seismic event features (peak ground acceleration, frequency content). The strategy of the procedure calibration of the analysis are divided in these steps:

- The initial shear stiffness and damping ratio, the curves of shear stiffness and damping ratio against the shear strain, the input acceleration time history were defined;

- A waves propagation analysis in one-dimensional *free-field* condition were performed using the calculation code EERA with a visco-elastic linear equivalent behaviour;
- In the last iteration step the EERA software gives back the profile of the mobilized shear stiffness and damping ratio;
- The value of G and D layer by layer were used as an input value for the linear visco-elastic analyses with the FE software;
- A set of free-field analyses using the FE bi-dimensional model with the modified parameters were performed in order to make a comparison with the EERA results;
- Once the comparison was coherent, the tunnel was inserted in the FE model with the same features of the free-field analyses.

The values of initial shear stiffness G_0 and damping ratio D_0 relative to the input parameters of SSR analyses and the output values of the corresponding G and D mobilized were showed in the figs.3.12 and 3.13. The G and D value were directly red from the degradation curves $G_0(\gamma)/G$ e $D_0(\gamma)$, for each soil type and earthquake fired. The input motion in EERA was applied at the base of the soil layer as an *Inside* recordings, which corresponded to a direct application of the time history without deconvolution from the surface. In this way the same acceleration time history was applied at the base of the FE model, in order to carry out analyses coherent with EERA.

The fig.3.12 showed a drastic reduction of the shear stiffness modulus, which was stronger for the stiffest material due to the shape of the gravel degradation curve, for which $G(\gamma)/G_0<1$ also for very small shear strains. The damping ratio values (fig.3.13) were subjected to a large increase, obtaining a D mobilized between 12% and 20% in most of the cases. As for the shear stiffness, the damping ratio increase was stronger for the gravel soils, due to the $D(\gamma)$ curve adopted for this material. The new value of G and D became input values for linear analyses using FE code Plaxis 8.0 both for free-field and full dynamic interaction.

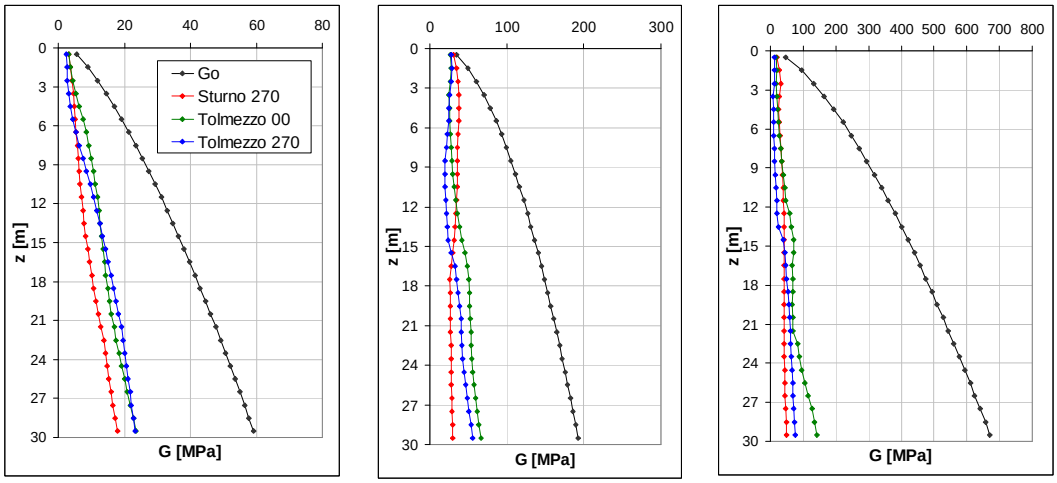

(a) *(b)* *(c)*

Fig 3.12: Shear modulus for the clay (a),sand (b) and gravel (c)

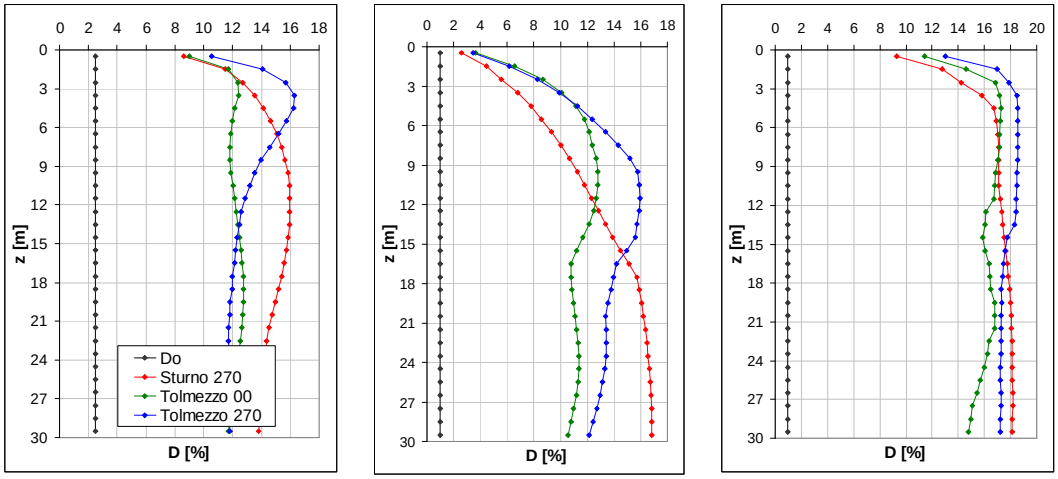

(a) *(b)* *(c)*

Fig 3.13: Damping ratio for the clay (a),sand (b) and gravel (c)

3.4.3 Plaxis 8.0 analyses

In order to correctly perform the FE numerical analyses, a calibration of the model domain were done, considering all the parameters which influenced the wave propagation through the mesh. These parameters can determined substantially the analysis results and were singly investigated. The calibration phase was carried out in free-field conditions, in order to make a comparison

using the EERA results and verify the good performance of the FE model. The parameters considered in the calibration analyses are:

- Layering of the soil profile;
- Extension of the model domain;
- Maximum mesh size;
- Rayleigh damping parameters;
- Newmark integration parameters;

The mobilized shear stiffness profile outputted in the SSR analyses are not constant with depth, but changed both for the initial soil profiles and the fired earthquake. Moreover also the value of the maximum shear stiffness G0 increased with depth, because in a homogeneous media, the stiffness properties are variable along the soil layer depending on the local lythostatic stress condition. Instead the initial damping ratio profile was fixed constant, as input data, but became variable and changed radically its value, when a profile of mobilized values was considered. In total for the 3 soil types and the 3 input motions, 9 different profiles of mobilized parameters were used to perform the FE numerical analyses. In order to respect the soil layering of the EERA analyses, which consisted in 30 layers of 1m thickness, the FE domain was subdivided in the same way, introducing, as input parameters of each layer, the values of mobilized G and D. In this way the comparison between the free-field results was coherent, accounting for the difference of the two commercial codes. The bedrock was simply considered rigid, neglecting the contribution of the base stiffness on the signal propagation along the soil layer. From a set of preliminary analyses performed by EERA with the input profiles, the profiles of maximum acceleration and shear strain, obtained with a bedrock of rigid and soft rock, were very similar.

The software Plaxis automatically generates the mesh in the calculation domain, but, considering the analysis to perform, the density of the triangular elements could be modified in some particular domain areas. For the static analyses the mesh is thickened in a control volume where the stress and strain variation is high (around the structural elements). In the dynamic analyses the whole soil thickness participate to the propagation of the shear waves in the domain. Kuhlemayer & Lysmer (1969) defined a upper limit for the mesh

dimension, in order to perform reliable FE analyses. The maximum size of the triangular elements is directly connect with the maximum frequency of the wave which correctly propagates in the meshed domain. Considering a multi-frequency signal, as a natural recording of an earthquake, the maximum frequency could be defined as a limit frequency between the significant and negligible values, in order to consider the great portion of the energy content of the signal. A simple rule in order to optimize the FE meshing was used in the domain preparation: a minimum number of 3-4 points was used in order to describe the half wavelength of an element of thickness H and shear wave velocity C_S. The expression of the maximum element size is (Lysmer & Kuhlemeyer, 1973):

$$d \leq \frac{\lambda_{\min}}{k} = \frac{C_{s30}}{k f_{\max}} \tag{3.16}$$

in which C_{s30} is the average value of the shear wave velocity and k is a experience range value between 4 and 10. The maximum frequency was fixed at 15Hz, obtaining a limit value for the element size equal to 1.22m for sand and gravel models; instead for the clay models the mesh was thickened in the first upper 10 soil layers until a mesh size of 0.63m. Adopting a thin layering of the soil bank, the refinining of the mesh, in order to respect the condition imposed by the eq. (3.16), was very simple because the mesh was forced by the points of the layering. Moreover when a structure was consider, a further refining was performed around the structural element.

The material damping in Plaxis is defined according to the Rayleigh formulation, and the damping matrix is considered as a linear combination of mass matrix and stiffness matrix through the coefficient α_R e β_R (eq.(3.8)). The values of the Rayleigh parameters was obtained using the method of the double frequency control: the two parameters were assumed in order to obtain constant damping in a range of frequency, significant for the content of the input signal. The damping factor was approximately constant in a range between two natural frequency of the soil layer (Hashash & Park 2002, Lanzo et al. 2004). The first frequency are generally the first resonance frequency; the second frequency was the second or higher resonant frequency, depending on the main frequency of the input signal (fig.3.14). In order to obtain a correct evaluation of the damping, the main earthquake frequency are included

in the range of the two control frequencies. If the signal frequency was lower than the first resonance frequency of the soil layer, the control frequencies are the first and the second natural frequencies. This method avoids that the damping ratio was overestimate in a frequency interval, significant for the earthquake frequency content.

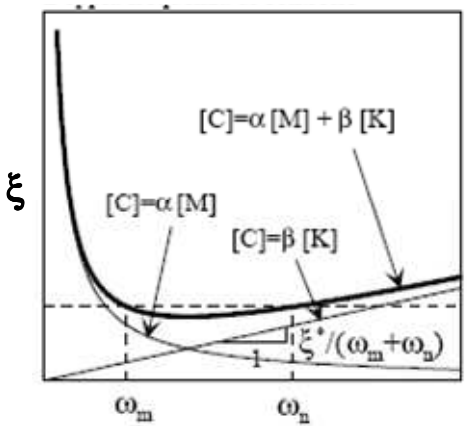

Fig.3.14 Double frequency control method (Lanzo et al. 2004)

Beside the viscous damping, an other artificial damping occurred during the dynamic analyses due to the integration of the equations of the waves propagation. As explained in the previous section, Plaxis 8.0 uses the Newmark method to perform the solution of the equations in the time domain. In the equation (3.10) α_N and β_N, which are parameters for the integration accuracy, were not assigned independently. In the default settings of Plaxis 8.0, the values of the Newmark coefficients are α_N=0.3025 and β_N=0.6, but this choice are reasonable for a damped scheme. Therefore these value determines an artificial damping, which can be evaluated introducing a dissipation parameter γ_N, linearly dependent from α_N and β_N:

$$\gamma_N = \beta_N - \frac{1}{2}; \quad \alpha_N = \frac{(1+\gamma_N)^2}{4} \tag{3.17}$$

The default values of Newmark coefficients give a value of γ_N=0.1. Visone (2009) proposed an evaluation of the total damping (viscous and integration) depending on γ_N:

$$\xi_i = \frac{1}{2}\left[\frac{\alpha_R}{\omega_n} + (\beta_R + \gamma_N \delta t)\omega_n\right] \tag{3.18}$$

Alternatively others values couples can be assigned to the Newmark coefficients, respecting the condition (3.11). The constant average acceleration method has γ_N =0 and subsequently α_N=0.25 e β_N=0.5. For moderately high values of the viscous damping the value of numerical damping is negligible and the Plaxis 8.0 default values can be used. In the case of low or null viscous damping ratio, a set of calibration analyses should be perform in order to find the couple of Newmark parameters, starting from the default ones, which limit the entity of numerical damping. Moreover the conditions of null total damping are impossible to model using the Newmark integration scheme.

The extension of the calculation domain is the most important topic in the calibration of a FE model. As described in the section, the lateral boundaries were modelled as a viscous dampers, using the Lysmer & Kuhlemeyer (1969) formulation. The lateral dampers should model a laterally infinite soil layer, in order to simulate the one dimensional propagation and make a comparison with EERA results. The default values of the relaxation parameters of the eq.(3.14) are c_1=1 e c_2=0.25, suggested by Plaxis in order to simulate a reasonable adsorption and reflection of the incident waves. This assumption was verified, making a comparison between the EERA and Plaxis results obtained in the mid-span vertical. The presence of lateral dampers highly influenced the motion field in the calculation domain, when different extensions of the FE model were considered. In order to obtain the better comparison between the one-dimensional and bi-dimensional analysis, the lateral boundaries were gradually fixed farer from the central vertical until the results were consistent.

A set of calibration analyses on the extension of the calculation domain were carried out. The boundaries, which was modelled using the viscous dampers of the adsorbent frontiers, were located at different distance from the central vertical. The input signal, used for the calibration of the FE domain, was the earthquake recordings of Tolmezzo 270 (Table 3.4; fig.3.10), scaled at 0.35g. The soil profile corresponded to the medium dense soil type of the fig.(3.8), considering all the initial soil characteristics. Also in this case the analyses performed were compared to corresponding EERA analyses, which

were carried out using a visco-elastic linear model. Both the analysed did not consider the soil non-linearity, because there were only a calibration analyses and did not model the real behaviour of the soil.

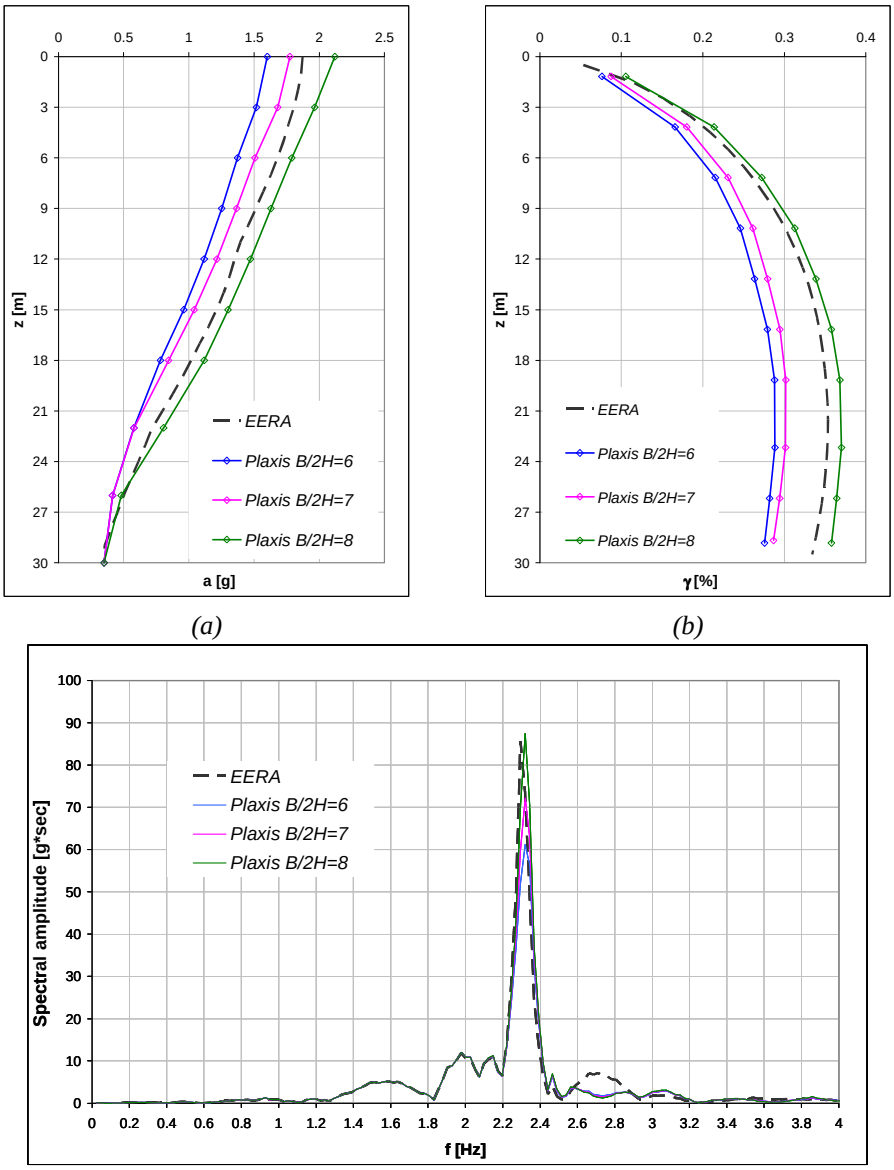

(a) *(b)*

(c)

Fig.3.15: Profiles of a_{max} (a) and γ_{max} (b); Fourier Spectra on surface (c)

In fig.(3.15) the comparison between the shear strain and acceleration profiles, and the Fourier spectra of the surface acceleration time history were showed. Different values of ratio between the half-length (B/2) and the depth (H) of the FE domain were considered, assigning the value of the damping ratio (D_0=1%) through the Rayleigh formulation. From the calibration analyses results, a good agreement, both in terms of profile of maximum values and surface Fourier spectrum, between the EERA and Plaxis analyses were reached for a ratio B/2H=8. In the fig.3.16 the calculation domain used for the free-field dynamic analyses was reported. The lateral boundaries were moved away until 8H from the central vertical. If the layer thickness H was equal to 30m, the total width of the calculation domain was L_{tot}=8H+8H=480m. The very extended FE model and the thick meshing on the whole domain determined a high increase of the computational burden.

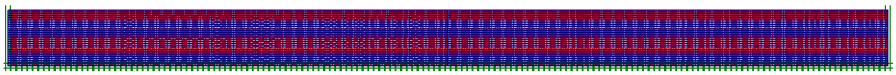

Fig.3.16: Extension of the free-field domain

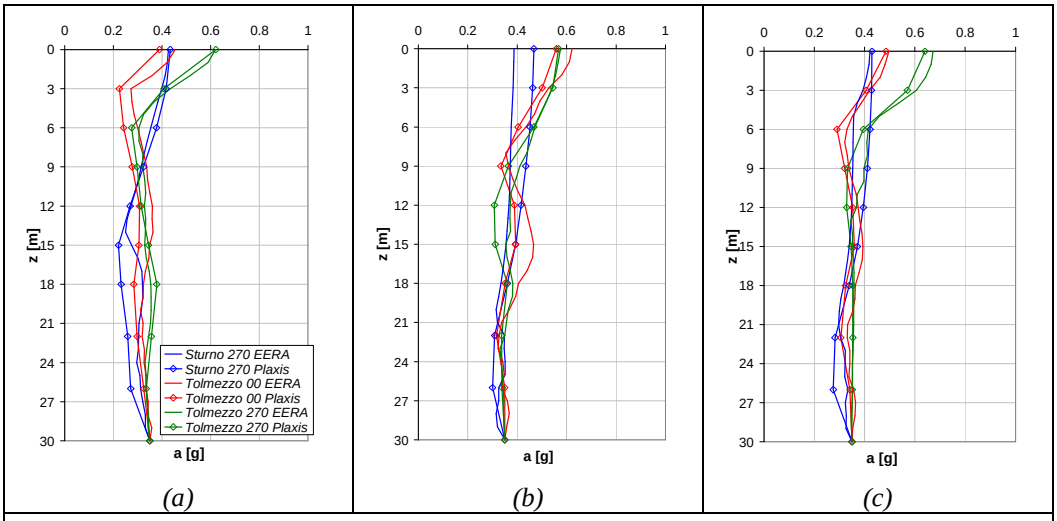

Fig.3.17: Maximum acceleration profiles for clay (a), sand (b)and gravel (c)

In the figs. (3.17) and (3.18) the comparison between the EERA and Plaxis profiles of maximum acceleration and maximum shear strain, in free-field conditions using the linear equivalent procedure, are showed. The FE input

profile of fig.(3.12) and (3.13), different both for soil type and earthquake input, were subjected in the Plaxis code to the corresponding acceleration time history.

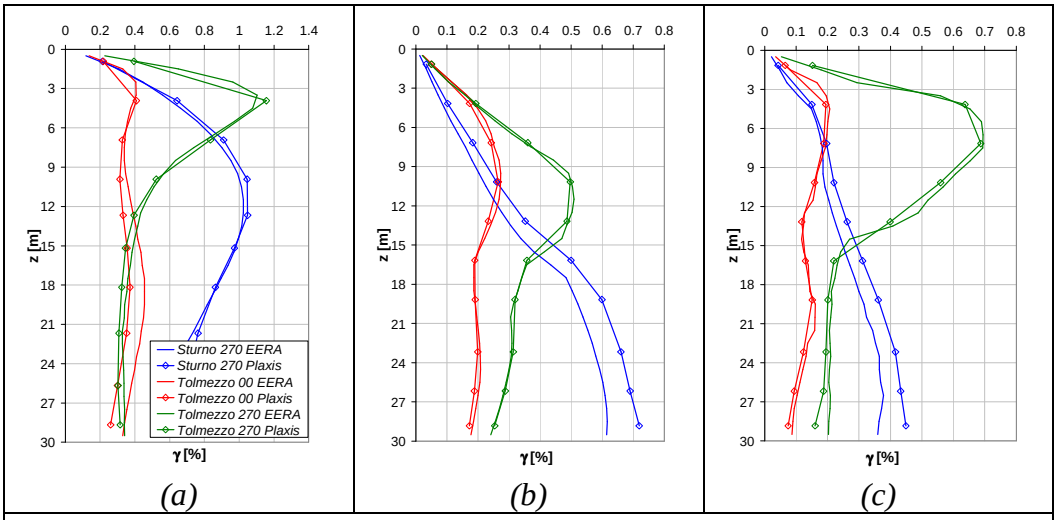

Fig.3.18: Maximum shear strain profile for clay (a),sand (b)and gravel (c)

The linear equivalent analyses performed by Plaxis showed a good agreement with the results of the EERA analyses, especially for the shear strain distributions. The profiles of the Tolmezzo 00 and Tolmezzo 270 time histories, obtained from the two software, was overlapped; in the case of Struno 270 the results of Plaxis were slightly different from EERA, but showing a similar behaviour. The good performance of the free-field FE analyses, using the mixed EERA/Plaxis procedure in order to carry out dynamic non linear analyses, showed the correctness of the model calibration.

Once the calculation domain was set and all the input parameters was introduced in the dynamic analyses, the soil/structure interaction analyses were performed. The tunnel, considering both its geometry and properties, was inserted in the mid-span of the model section. In the fig.(3.19) the mesh used for the full dynamic analyses, represented in a simplified way, was showed, observing that the mesh was thickened around the lining.

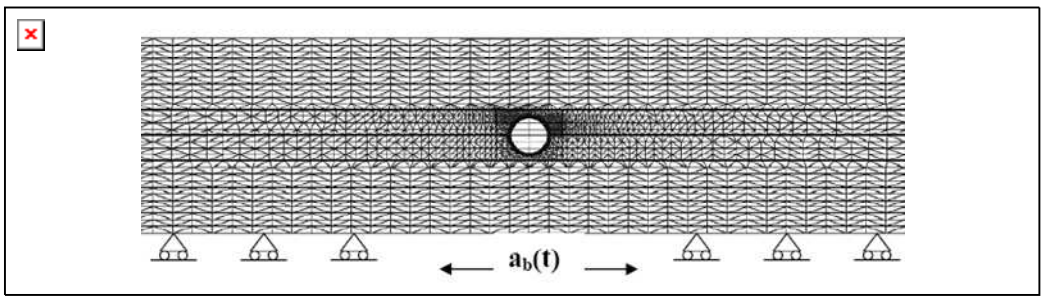

Fig.3.19: Extract of the full dynamic mesh

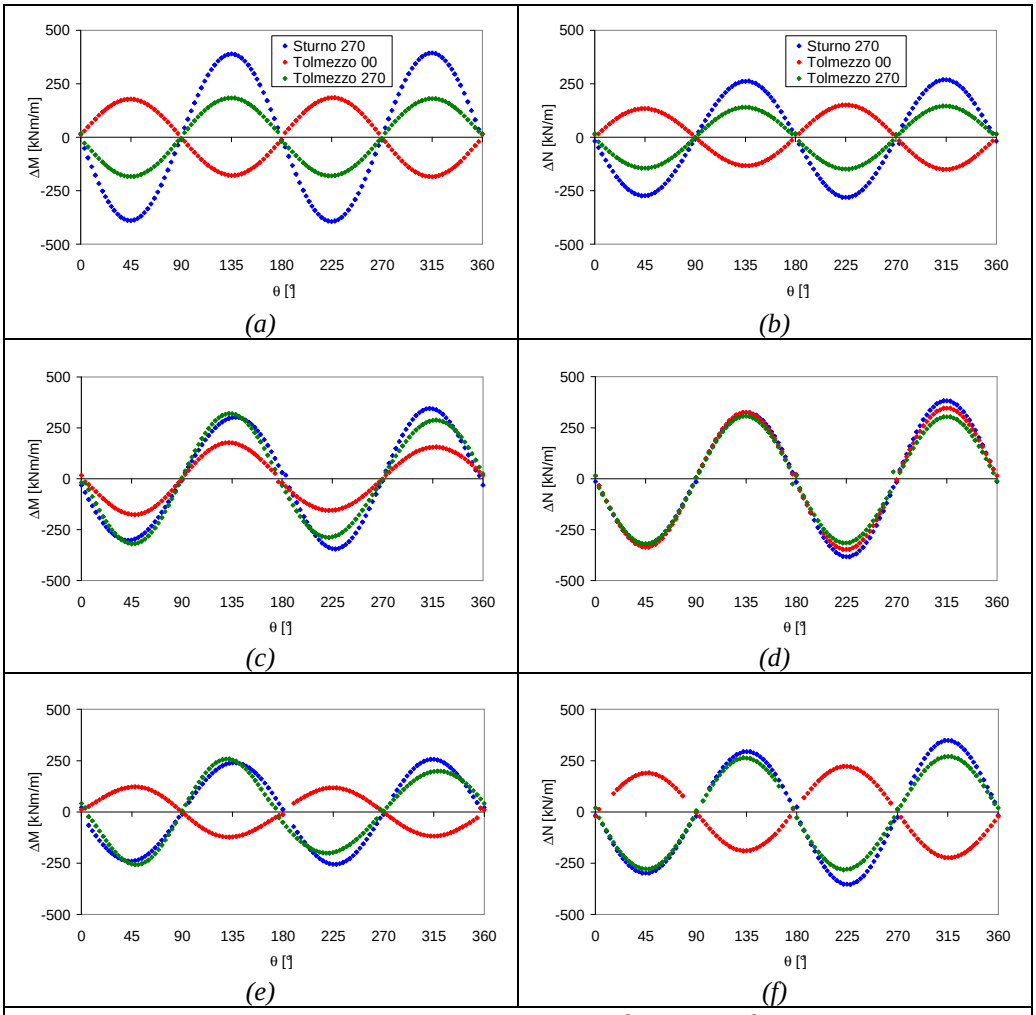

Fig.3.20: Dynamic increments of internal forces:
a) and b) clay; c) and d) sand; e) and f) gravel

The lining was modelled as plate element, 30cm thickness and 6m diameter, made of concrete with R_{ck}=45MPa. The distribution of the internal forces increments (bending moment and hoop force) with angle θ were showed in the fig.(3.20). The graphs are referred at the earthquake instant in which the deformation of the tunnel lining was maximum, and subsequently the internal forces increments registered the maximum absolute values.

The variation of the lining thickness was investigated in the case of Tolmezzo 00, considering different value between 10cm and 130cm, in order to consider a wide range of thickness, in which the most used values in the design were included. In the fig.(3.21) the variation of maximum internal forces increments versus the lining thickness is showed.

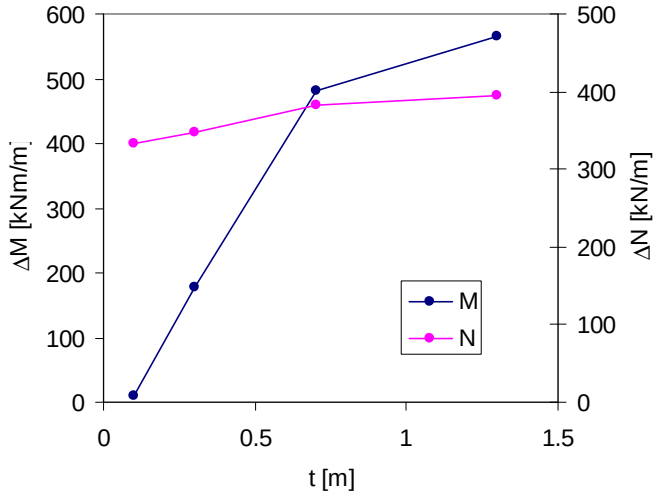

Fig.3.21: Increments of internal forces against lining thickness

The seismic increments of internal forces increase less than linear with the increasing thickness of the lining. The bending moments started from almost zero values for very thin lining, showing a significant increase (500kNm/m) until 1.3m. The hoop forces variation was lower, included in the range between 300-400kN/m.

3.4.4 Comparison with simplified analysis

A comparison between the seismic increments of internal forces calculated by means of the analytical formulation of Wang (1993) and the results of full

dynamic finite element analyses, also performed by Plaxis, were showed in this section. A summary of the considered methods of seismic analysis are reported in the tab (3.5).

Table 3.5: Overview of the seismic analysis methods performed

<table>
<tr><td rowspan="2">Analysis</td><td rowspan="2">Methods</td><td rowspan="2">$a_{max,b}$</td><td rowspan="2">$a_{max,s}$</td><td rowspan="2">τ_{max}</td><td>γ_{max}</td><td rowspan="2">M_{max}, N_{max}</td></tr>
<tr><td>Linear equivalent analysis</td></tr>
<tr><td rowspan="2">Pseudo-static</td><td>Down-up Method</td><td>a_g</td><td rowspan="2">S· a_g</td><td>$\tau_{max}(z)=\int_0^z \rho_s a_{max}(z)dz$</td><td rowspan="2">$\frac{\tau_{max}(z)}{G_0}+C\left[\frac{\tau_{max}(z)}{G_0}\right]^R$</td><td rowspan="2">$M_{max}=\pm\frac{1}{6}K_1\frac{E_s}{(1+\nu_s)}r^2\gamma_{max}$
$N_{max}=\pm K_2\frac{E_s}{2(1+\nu_s)}r\gamma_{max}$
no-slip conditions
(Wang 1993)</td></tr>
<tr><td>Up-down Method</td><td>(-)</td><td>$\tau_{max}(z)=r_d(z)\frac{a_{max,s}}{g}\sigma_v(z)$</td></tr>
<tr><td>Simplified dynamic</td><td>EERA Plaxis</td><td>a_g</td><td colspan="3">SSR analysis (free-field)</td></tr>
<tr><td>Full dynamic</td><td>Plaxis</td><td>a_g</td><td colspan="4">Envelopes of M_{max}, N_{max}</td></tr>
</table>

In order to carry out non-linear analyses using pseudo-static methods, the Ramberg & Osgood formulation (§2.5.1), was used to calculate the value of maximum shear strain. The C and R parameters of the Ramberg & Osgood model were evaluated from the degradation curves on the three subsoil types of the table, interpolating the G(γ)/G0 curves. The value of the parameters are showed in the table 3.6 (Valentino, 2006):

Table.3.6: Parameters of the Ramberg & Osgood model

Soil	**C**	**R**
Clay	12000	2.24
Sand	800000	2.63
Gravel	8000000	2.60

The simplified dynamic analysis was performed by using the Wang (1993) formulation for the no slippage conditions and assuming as input the *free-field* shear strain.γ computed in the finite element analysis. The pseudo-static analyses were performed used the method proposed in the §, in order to evaluate the maximum shear strain, and to obtain the maximum internal forces using the same Wang's expressions. The results in terms of maximum increments of the bending moment and the hoop force are shown in the Figs.3.22 and 3.23. The graphs shows a good agreement between the full

dynamic and the simplified dynamic analysis, in particular for the bending moment, with a slight overestimation using the simplified methods (Fig. 3.23).

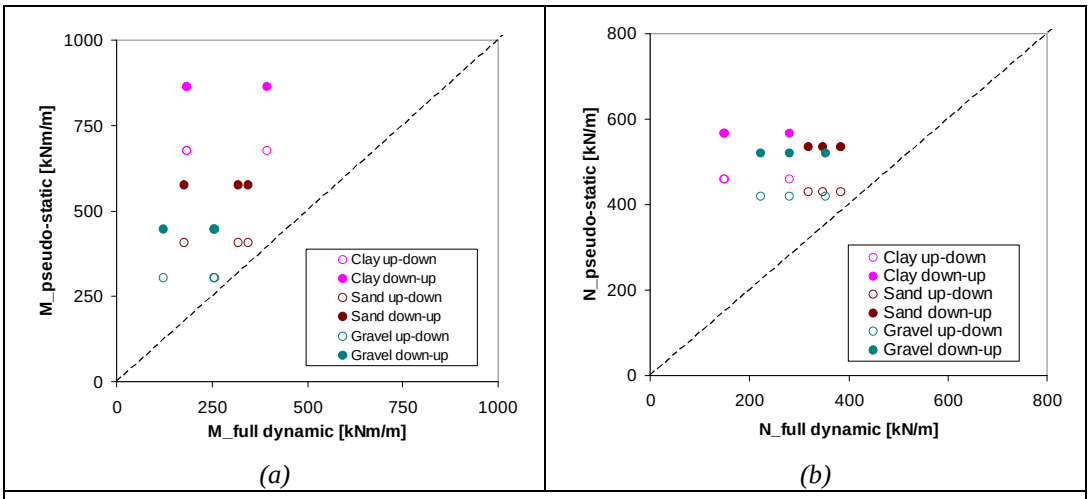

(a) *(b)*

Fig.3.22: comparison between the results of the numerical full dynamic analyses (x axis) and the equivalent pseudo-static computations (y axis): increments of bending moment (a) and hoop force in no slippage conditions (b)

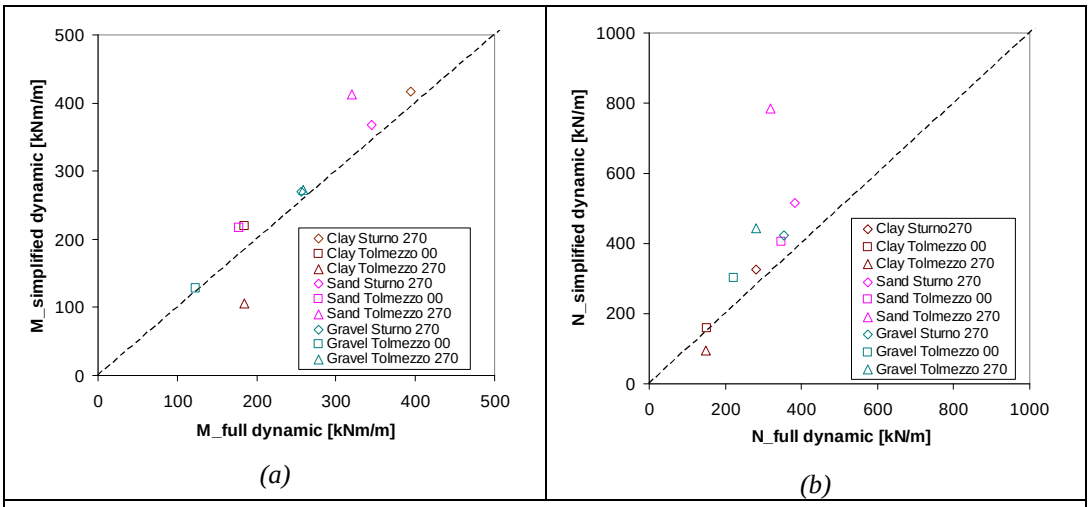

(a) *(b)*

Fig.3.23: comparison between the results of the numerical full dynamic analyses (x axis) and the equivalent simplified dynamic computations (y axis): increments of bending moment (a) and hoop force in no slippage conditions (b)

The pseudo-static approach tends to largely overestimate the values computed by the complete dynamic analyses. This suggests that effects of the kinematical interaction arise which cannot be considered by using the pseudo-static methods.

3.5 PARAMETRIC ANALYSES USING SINUSOIDAL INPUT

In order to programme the experimental activity, which is extensively described in the next chapters, a preliminary numerical study of a model under sinusoidal input motions was performed using the numerical codes EERA and Plaxis 8.0 (Bilotta et al. 2007). Performing these numerical analyses, the geometry and material properties of the centrifuge models were studied. Neglecting the scaling factors used for the centrifuge dynamic analyses (Bilotta & Taylor 2005), the performed analyses were carried out at the prototype scale.

The soil profile under examination was typical of a dry medium dense sand. The model thickness is 30m and the layer was base on a rigid bedrock. The soil stiffness properties were coincident with one of the soil profile used for the full dynamic analyses with natural acceleration time histories. The general features are briefly reported: the soil had a visco-elastic linear behaviour, with a constant value of the damping ratio D_0 and a power function distribution of the initial shear modulus G_0 with depth (fig.3.24). The value of the Poisson ratio was ν=0.25 and the average shear wave velocity C_{S30}=239m/s (Class C according to NTC, 2008).

Once the calculation domain was defined, a set of parametric analyses on a free-field model using both the EERA and the Plaxis 8.0 software were performed. Subsequently the Plaxis 8.0 code was used to generate numerical domains with a tunnel with axis depth of 15m and diameter of 6m. obtaining a coperture ratio C/D=2. The input signals were coherent with the acceleration time histories applied in the dynamic centrifuge tests, consisting in sinusoids of constant amplitude and frequency. The frequency range used for the analyses, between 1.5Hz and 4.5Hz, included the first resonant frequency of the soil layer, which is equal to 2.3Hz. The amplitude of the sinusoidal signals

was maintained constant in the different analyses and equal to 0.35g, as the event duration, which is 20s.

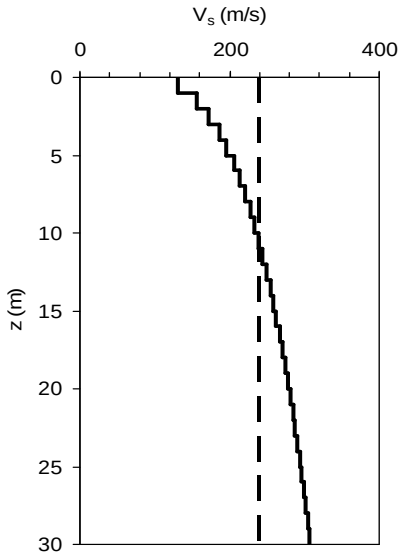

Fig.3.24: Profile of C_S and average value

The free-field comparison between the two numerical codes about the maximum acceleration on surface and the maximum shear strain at tunnel depth, showed a good agreement between EERA one-dimensional and Plaxis 8.0 bi-dimensional (fig.3.25). The FE analyses were carried out considering a damping ratio D_0=0, and a modified value for the Newmark parameters (α_N=0.25, β_N=0.5), in order to reduce the effect of the numerical damping.

Once the numerical model was calibrated using free-field analyses, the full dynamic analyses were carried out considering different values for the lining thickness (10cm; 30cm; 70cm). A concrete (R_{ck}=45MPa) tunnel was modelled considering an elastic modulus E=38GPa and a Poisson ratio ν=0.2. In the fig.3.26 the values of the maximum shear strain of the lining were showed, evaluated as:

$$\gamma(t) = \frac{u(t, D/2) - u(t, -D/2)}{D} \tag{3.20}$$

compared with the free-field shear strain at the same depth.

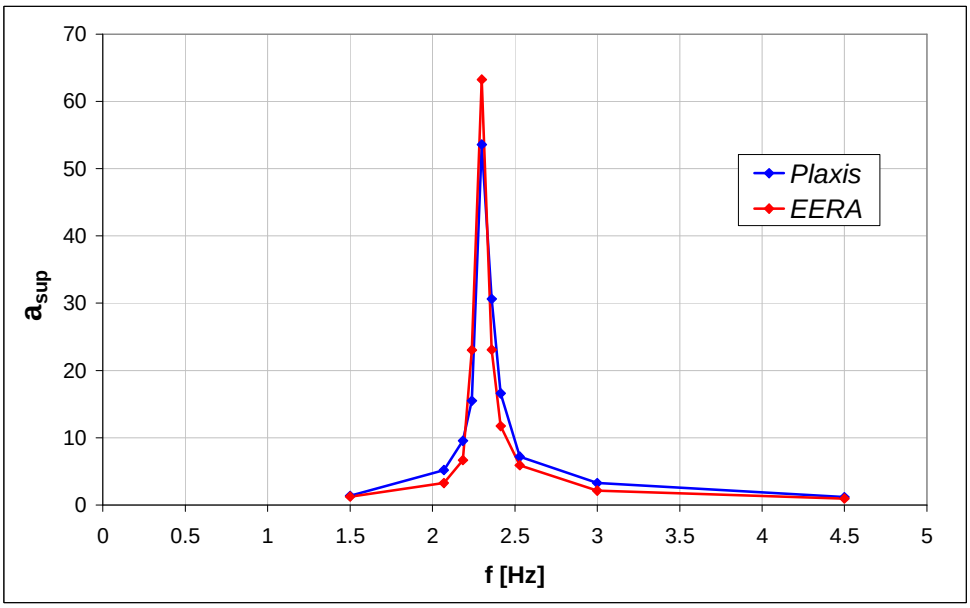

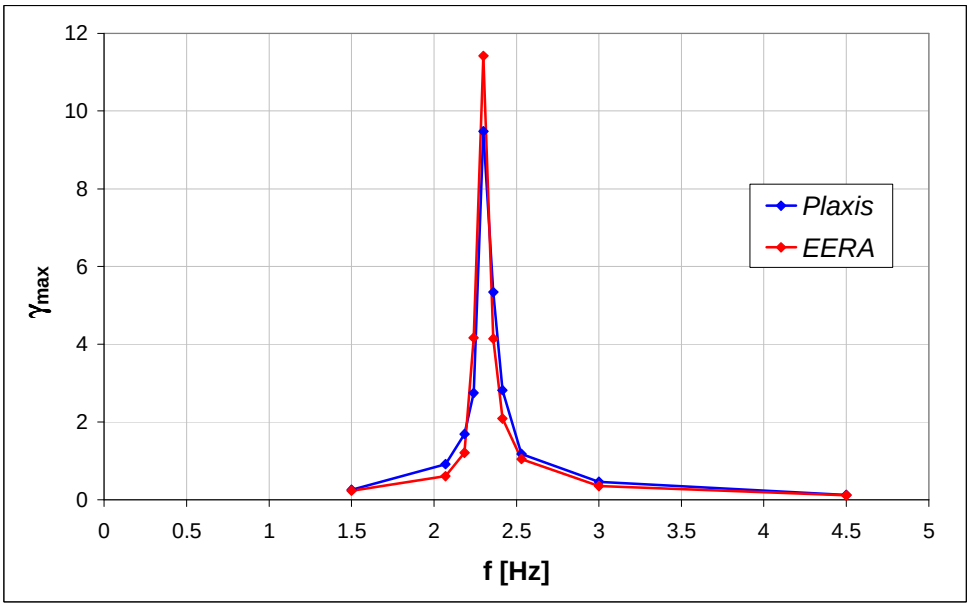

Fig.3.25 : Free-field acceleration a_{max} on surface (a) and shear strain γ_{max} at tunnel depth (b)

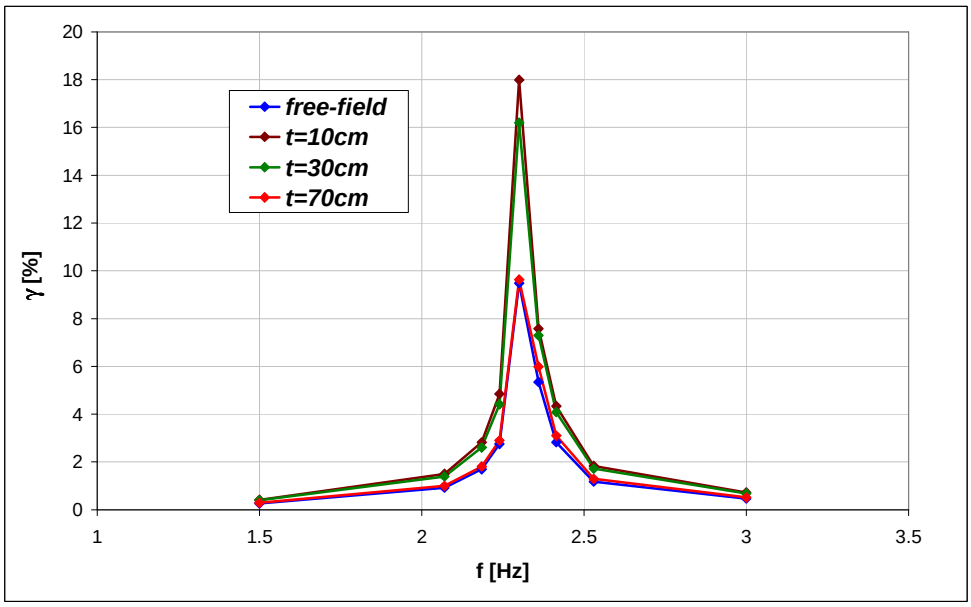

Fig.3.26: Maximum racking of tunnel lining

The tunnel did not modify the value of the first resonant frequency: the presence of an obstacle (covered cavity) did not determine a substantial variation of the dynamic features of the soil layer. Moreover the fig. shows that a particular value of the lining thickness reproduced exactly the free-field conditions: this thickness value corresponded to 70cm, which had a stiffness such as the lining and free-field shear strain were the same. This consideration permitted the recognizing of two different behaviour, depending on the relative soil/structure stiffness through the thickness tunnel parameter: the flexible lining are tunnel which have shear strain higher compared to free-field deformations; the tunnels have stiff lining on contrary. The numerical analyses results were considered in the definition of experimental programme of centrifuge tests.

FINAL REMARKS

The full dynamic analysis are a powerful tool in order to model seismic problems, especially when a structure was inserted in the calculation domain. These analyses are very complex, because many parameter must be

accurately defined. In order to summarize the performance and the results of numerical analyses, the final observation of this section are:

- The data of full numerical analyses carried out on tunnel in seismic conditions are very poor;
- Most of the authors observed that the full dynamic analyses suffered performance difficulties for the long time of the calculation and for the memory occupation of the output files;
- The code Plaxis 8.0 has the great advantage to include the tunnel in FE domain, but is unable to perform dynamic analysis in complete non-linearity, i.e. following a user degradation curve of the shear stiffness and damping ratio;
- The FE model needs an accurate calibration of the calculation domain, considering all the input parameter in a dynamic analyses;
- The calibration showed that the FE free-field model reproduces the one-dimensional behaviour when its width is extremely wide;
- The non-linearity was accounted in the full dynamic analysis, introducing mobilized parameters (from EERA analyses) as input parameters for linear visco-elastic analyses;
- Full dynamic analyses on soils type and earthquake recordings showed the effect of the kinematic interaction on the calculation of the internal forces. These are neglected when using the simplified (pseudo-static and simplified dynamic) approaches of design;
- The full dynamic analyses using sinusoidal input were performed in order to define the experimental programme of the centrifuge tests. The results showed the importance of the stiffness ratio between the soil and the structure.

REFERENCE

AGI. 2005. Aspetti geotecnici della progettazione in zona sismica, Patron, Bologna, (in Italian)

Aiello V., Silvestri F., 2002, Vibrazioni prodotte da infrastrutture di trasporto in ambiente urbano: una proposta metodologica applicata a un caso di studio. XXII Convegno Nazionale di Geotecnica, Palermo.

Amorosi A. Boldini D. 2007. Modellazione numerica del comportamento sismico trasversale di gallerie superficiali in terreni argillosi, Memorie in ricordo di Renato Ribacchi, pp.207-217.

Bardet J. P., Ichii K., Lin C. H. (2000). EERA a Computer Program for Equivalent-linear Earthquake site Response Analyses of Layered Soil Deposits. Univ. of Southern California, Dep. of Civil Eng.

Bielak J., Loukakis K., Hisada Y., Yoshimura C., *Domain reduction method for three-dimensional earthquake modelling in localized regions.* Part I: Theory, BSSA. 93 (2), 817-824, 2003.

Bilotta E., Taylor N., 2005, Modellazione geotecnica in centrifuga. Argomenti di Ingegneria Geotecnica. Hevelius Ed. (in Italian).

Bilotta E., Aiello V., Conte E., Lanzano G., Russo G., Santucci de Magistris F., Silvestri F. (2006), Sollecitazioni indotte da sisma in gallerie circolari interrate, Incontro Annuale dei Ricercatori di Geotecnica 2006–IARG 2006, Pisa, 26-28 Giugno 2006

Bilotta E., Lanzano G., Russo G., Santucci de Magistris F., Aiello V., Conte E., Silvestri F., Valentino M., 2007, Pseudo-static and dynamic analyses of tunnels in transversal and longitudinal direction, Proceedings of Fourth International Conference on Earthquake Geotechnical Engineering, June 25-28, Thessaloniki Greece.

Bilotta E., Lanzano G., Russo G. (2007). Analisi della sezione trasversale della galleria sottoposta a sollecitazioni dinamiche. Incontro Annuale dei Ricercatori Geotecnici IARG, Salerno 2007

Bilotta E., Lanzano G., Russo G., Santucci de Magistris F., Silvestri F., 2007, Methods for the seismic analysis of trans-verse section of circular tunnels in soft ground, ISSMGE-ERTC12 Workshop at XIV ECSMGE, Geotechnical Aspects of EC8, Chapter 22, Madrid Spain.

Bilotta E., Lanzano G., Russo G., Santucci de Magistris F., Silvestri F., AN EARLY-STAGE DESIGN PROCEDURE FOR CIRCULAR TUNNEL LINING UNDER SEISMIC ACTIONS. 14WCEE. Pechino 2008

Brinkgreve R.B.J., Plaxis 2D version8. A.A. Balkema Publisher, Lisse, 2002NTC, 2008Castellani et al. 2006

Corigliano M. 2007. Seismic response of deep tunnels in near-fault conditions, pHd Thesis Technical University of Turin.

Corigliano M., Scandella L., Barla G., Lai C.G., Paolucci R., (2007), Seismic analysis of deep tunnels in weak rock: a case study in Southern Italy, Proceedings of Fourth Interna-tional Conference on Earthquake Geotechnical Engineering, June 25-28, Thessaloniki Greece

Einstein H. H., Schwartz C. W. (1979), *Simplified analysis for tunnel support*, Journal of the geotechnical engineering division, 105 499-518, 1979.

EN 1998-1 (2003), Eurocode 8: Design of structure for earthquake resistance,. Part 1: General rules, seismic ac-tions and rules for buildings. CEN European Committee for Standardisation, Bruxelles, Belgium.

Hashash Y.M.A., Park D., 2002, Viscous damping formulation and high frequency motion propagation in non-linear site response analysis. Soil Dynamics and Earthquake Engineering 22 (2002) 611–624.

Jaky J. (1944), The coefficient of earth pressure at Rest. Journal of the Society of Hungarian Architects and Engineers, pp- 355-358.

Kramer S.L., (1996), Geotechnical Earthquake Engineer-ing,. 653 pp., Prentice-Hall, New Jersey.

Kuhlmeyer R.L, Lysmer J. (1973). Finite Element Method Accuracy for Wave Propagation Problems, Journal of the Soil Mechanics and Foundation Division, vol.99 n.5, pp. 421-427

Lanzo G., Silvestri F., 1999, Risposta sismica locale, Argomenti di Ingegneria Geotecnica n°10, Hevelius ed. (in Italian).

Lanzo G., Pagliaroli A., D'Elia B., 2004, Influenza della modellazione di Rayleigh dello smorzamento viscoso nelle analisi di risposta sismica locale, Atti dell'XI Conferenza Nazionale su "L'ingegneria Sismica in Italia".

Lanzo G. (2005), Risposta sismica locale, Linee guida AGI: Aspetti geotecnici della progettazione sismica, Parte II, Capitolo 6, pag. 83-98

Lanzo G. (2005), Soluzioni analitiche approssimate per il calcolo del moto sismico in superficie, Linee guida AGI: Aspetti geotecnici della progettazione sismica, Appendici, Appendice D, pag. 335-350

Lysmer J. Kuhlmeyer R.L, 1969, Finite dynamic model for infinite media, J. of Eng. Mech. Div., ASCE: 859-877.

NTC, 2008 norme tecniche costruzioni ITA (in Italian)

Pakbaz M., Yareevand A., (2005), 2-D analysis of circular tunnel against earthquake loading, Tunnelling and Under-ground Space Technology, 20, 411-417.

Penzien J., (2000), Seismically induced racking of tunnel linings, International Journal of Earthquake Engineering and Structural Dynamics, 29, 683-691.

Ramberg W., Osgood W.R. (1943). Description of stress strain curves by three parameters. Technical Note 902, National Advisory Committee for Aeronautics, Washington, D.C.

Scasserra G., Stewart J.P., Kayen R.E., Lanzo G., 2008, *Site characterization of Italian strong motion recordings stations*, Proceedings of Conference commemorating the 1908 Messina and Reggio Calabria earthquake. Vol.1020 pp.338-345

Seed H.B., Idriss I.M. (1970). Soil moduli and damping factors for dynamic response analysis. Report No. EERC70-10, Earthquake Engineering Research Center, Univ. of California, Berkeley, (California).

Stokoe K.H., 2004, Comparison of Linear and Nonlinear Dynamic Properties of Gravel, Sand, Silts and Clays, Proc. V ICSDEE & III ICEGE, Berkeley, USA.

Valentino M. (2006). Metodi dinamici e pseudostatici per l'analisi sismica di infrastrutture interrate. Tesi di Laurea Specialistica, Università della Calabria.

Visone C. 2008. Performance based design of embedded retaining walls. PdD Thesis, University of Naples "Federico II".

Vucetic M., Dobry R. (1991). Effects of the soil plasticity on cyclic response. Journal of Geotechnical Engineering, ASCE, 117(1):89-107.

Wang J., (1993), Seismic Design of Tunnels: A Simple State-of-the-art Design Approach, Monograph 7, Parsons, Brinckerhoff, Quade and Douglas Inc, New York.

Chapter 4

Centrifuge modelling of seismic actions on tunnels

4.1 INTRODUCTION

Physical modelling is an important tool in order to study the seismic geotechnical problems. In the last decade a number of published research works made use of geotechnical centrifuge to analyse issues concerning soil liquefaction and interaction between soil and structure during a dynamic event.

The usefulness of the small scale experiments derives from random features of seismic events because the earthquakes are not predictable with certainty. From the historical data of previous events some vulnerable worldwide areas are recognizable, but not knowing exactly when an earthquake occurs, an investment on field instrumentations could not give back useful data in short time. O'Rourke et al.(2001) gave data from an instrumented lining during the Duzce earthquake (1999), located near the epicentre. The tunnel was located near Bolu, in Turkey, and as it was under construction at the time of the seismic event, the monitoring system was active and recorded interesting data. They showed an ovaling deformation of the cross-section during the earthquake. Moreover a permanent increase of bending moment and hoop forces were observed, of about 17% of the values measured before the event..

Elgamal *et al.* (2007) computed about 15 geotechnical centrifuge equipped for dynamic tests only in Japan. Most of these equipments were installed after the disastrous earthquake of Kobe (1995). Other geotechnical centrifuges, in which dynamic tests were carried out, are available in USA and Europe. The United Kingdom (Cambridge University) and France (CEA-CESTA and LPCP) are equipped with dynamic actuators in order to shake the base of centrifuge model during the flight.

Some problems concerning dynamic centrifuge tests are briefly discussed in this chapter, focusing on the scaling laws and effects, types of earthquake actuators and special boxes used to accommodate horizontal movement. Moreover, some recent experimental works involving dynamic centrifuge tests on tunnels are presented.

4.2 SCALING LAWS

Both soil stiffness and strength are strongly dependent on the confining stress, then a realistic value of in situ stresses is needed to correctly evaluate the stress-strain behaviour of soil and the dynamic interaction between the structure and the surrounding ground.

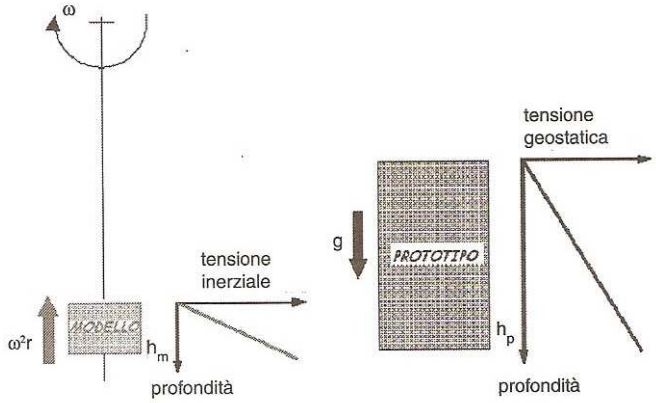

Fig.1 - Mechanical similitude between prototype and model (Bilotta & Taylor, 2005)

Many Authors discussed about the scaling laws and scaling effects, occurring during a centrifuge experiment (cf Schofield 1980, Taylor 1995,

Bilotta & Taylor 2005). The acceleration level reached during the swing up of the sample corresponds to a gravity field higher than the Earth's one. Therefore the vertical stresses, always zero at the model surface, change at depth to a value N times higher than in 1g conditions, in which N is the level of centrifugal acceleration. Therefore the stress at the generic depth h_m in the centrifuge model (at N g)is the same at the depth $h_p=Nh_m$ in the prototype (at 1g) (fig.4.1): the coincidence of stresses at the same depth in the model and the prototype is the major advantage in centrifuge modelling. All the scaling laws can be derived by means of dimensional analysis: in the table 4.1 the scaling factors for the most frequent quantities are showed.

Table 4.1: Scaling factors

Magnitude	**Scaling factors (model/prototype)**
Length	1/N
Acceleration	N
Velocity	1
Density	1
Stress	1
Strain	1
Frequency	N
Time (inertial effects)	1/N
Time (consolidation)	$1/N^2$

When a dynamic event is under examination, the specific scaling factors are derived from the equation of cyclic displacement, written at prototype scale:

$$u_p = A_p \sin\left(2\pi f_p t_p\right) \tag{4.1}$$

A_p is the motion amplitude and f_p is the signal frequency. In order to obtain velocity, the equation (4.1) is differentiated, giving:

$$\frac{du_p}{dt_p} = 2\pi f_p A_p \cos\left(2\pi f_p t_p\right) \tag{4.2}$$

And by further differentiating the equation (4.2), the acceleration is:

$$\frac{d^2 u_p}{dt_p^2} = -(2\pi f_p)^2 A_p \sin(2\pi f_p t_p) \tag{4.3}$$

Considering that the length and acceleration factor scale are N^{-1} and N respectively, the conversion factor for frequency must be N. Therefore using these scaling values:

- Max displacement: $u_p = A_p = NA_m = Nu_m$ (4.4a)
- Max velocity: $V_p = 2\pi f_p A_p = 2\pi \frac{f_m}{N} NA_m = 2\pi f_m A_m = V_m$ (4.4b)
- Max acceleration:

$$a_p = -(2\pi f_p)^2 A_p = -\left(2\pi \frac{f_m}{N}\right)^2 NA_m = \frac{-(2\pi f_m)^2 A_m}{N} = \frac{a_m}{N} \tag{4.4c}$$

As a consequence, there is no scaling factor for the velocity, which is the same in model and prototype. In contrast with scaling factors of consolidation time (N^{-2}), the dynamic time is scaled by N^{-1}: therefore during the test the dynamic duration is N time shorter compared to prototype model.

Kutter (1995) described some scaling effects generally occurred during centrifuge tests. In the dynamic tests two relevant effects are considered:

- *Conflict between dynamic time and consolidation time:*

In order to study liquefaction problems fine saturate sands are used in the centrifuge dynamic tests. During the induced earthquakes on flights, the dissipation of the pore over-pressure and the dynamic event are contemporaneous, due to relatively high permeability of the sand. Therefore in the clay the consolidation phenomena starts after the dynamic event due to low permeability of this ground type. In order to avoid unrealistic behaviour in the saturate sands, the filtration and dynamic time scale factor must be the same (Bilotta & Taylor 2005). A classical solution is the use of a pore fluid 100 times more viscous than water, but having the same density, like the silicon fluids. The permeability is 100 times smaller and at 100g level the scale factor for consolidation and dynamic events is the same.

- *Particle size effect:*

Following the length scale factor in the centrifuge test, a sandy model represent a gravel prototype. This simplistic consideration caused some

discussions on the validity of centrifuge results. Kutter (1995) clarified that inter-particle contact forces are the same in the model and in the prototype, if same soil is used. Therefore these forces depend on the numbers of inter-particle contacts per unit area, which are due to absolute particle size and not to gravity. Some geotechnical phenomena are influenced by particle size, as the thickness of the shear band in strain softening materials. In such cases suitable trial tests need to be performed in order to quantify the particle size effects on the problem.

Other scale effects are described in the centrifuge literature like strain rate effects (Kutter 1995) and errors due to rotation acceleration field (Schofield 1980). Kutter (1995) suggested to perform numerical analysis of the centrifuge models, in order to compare them with experimental data, at the model scale, and to quantify the modelling scale errors, because the model is never ever a perfect simulation of the prototype.

4.3 DYNAMIC ACTUATORS AND CONTAINERS

In the early 1980s centrifuge shaking tables were designed and developed; many actuators were built until today using different technologies. Piezoelectric, explosive and electromagnetic shakers were designed, but they had severe limitations in the control of input motion. Kutter (1995) explained the main disadvantage for each kind of shaker: piezoelectric shakers generate multi-frequency shaking but only with high values of frequency; explosive are not able to fire earthquakes with a specific time histories; electromagnetic shakers showed good performance, but economically they were not preferable compared to other technological solutions. The most powerful and versatile solution is an earthquake actuation through servo-hydraulic system. Only in the 1990s some small servo-hydraulic actuators were developed in Japan and US. They exhibited good performance and, afterward, an extended diffusion. These actuators were mounted underneath the shaking: the centre of the mass was located at a relative distance from the action line of the shaker, causing uncontrolled rocking movements of the model box. In order to avoid these annoying effects, “second generation” actuators were mounted behind the model box. Therefore the large geotechnical centrifuges permitted positioning

the shakers at the side of the shaking table. Most of the recent actuators were developed in order to limit external noise and rotation movements, as the SAM actuator, designed at Cambridge University. Most of these actuators apply an input motion at the base of the model box only in one horizontal direction; but a series of 2D shakers were recently built in order to perform more complex dynamic problems, as for the centrifuge of the Honk Kong University (Shen *et al.*, 1998), Tokyo Institute of Technology (Takemura *et al.*, 2002) and UC Davis (Kutter *et al.* 1994 & Wilson *et al.* 2004), in the United States.

Kutter (1995) explained the importance of the frequency content of the input signal in the design of a centrifuge shaker: a multi-frequency input signal gives many pieces of information on the soil deposit characteristics. Many laboratories are equipped with actuators which can fire only single frequency signals. The use of sinusoidal base motion is justified by a easier understanding of the soil response. Nonetheless, a constant amplitude can give false impression of importance of a particular soil response aspect. A great commitment is aimed in the technical development of dynamic actuators in order to perform multi-frequency input motion (Elgamal *et al.* (2007)).

Another important issue in dynamic centrifuge testing is the design of the model container. The kinematic conditions at the vertical boundaries of the soil model should permit to model the vertical propagation of shear waves in a laterally infinite soil layer. Therefore the following aspects should be considered (Kutter 1995):

1. *No normal strain in the horizontal direction:* the sides of the boxes should tend to deflect during the swing-up and the liquefaction phenomena due to horizontal stresses modifications. A small deflection could cause a modification of sample model (settlements and densification)
2. *No energy transfer between soil and container:* in order to permit the vertical propagation of shear waves the box sides should not be fixed. Rigid boundaries could cause the creation of undesirable P-waves in the model and the modification of the motion field.

3. *Complementary shear stresses at the end of the box:* the box should be designed in order to avoid rotation of the model during the dynamic phase.

Ko (1994) reported two solutions useful in order to allow horizontal movements of the box during the vertical propagation. Firstly a plastic compound called “Duxeal” was used in many models in order to adsorb the stress wave at the walls of a rigid box. This solution was useful to perform dynamic test having a strong-box with fixed sides. On the other hand some special boxes were designed in order to maintain a constant horizontal cross-section, to have zero mass and zero stiffness, and develop complementary shear stresses. Following these considerations, many strong-boxes were realized using a series of rectangular frame overlapped (laminations). In order to allow horizontal movements, a rubber layer or a ball bearing system was inserted between the laminations. To study liquefaction problems, the first rectangular laminar box was developed by Hushmand *et al.* (1988), using a ball bearing system to reduce friction between the laminations. Schofield & Zeng 1992 explained the seismic behaviour of the Equivalent Shear Beam container (ESB), built with alternating rectangular layer of aluminium and rubber (fig.4.2).

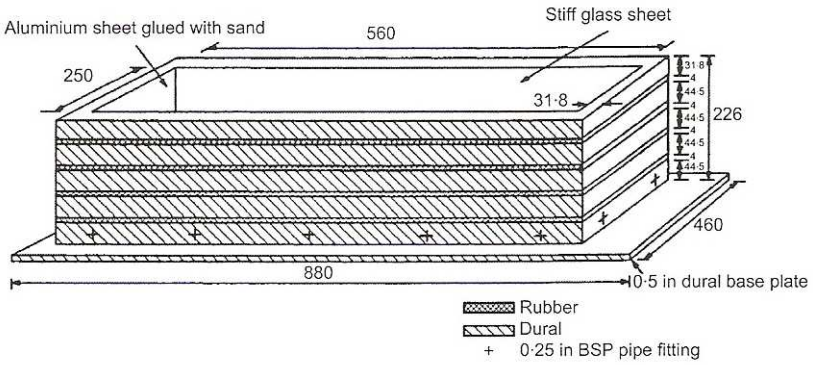

Fig.4.2 (Teymur & Madabushi, 2003)

The design philosophy of ESB was that the walls of the containers had the same deflection of and natural frequency of the soil inside the model. Fiegel *et al.* (1994) showed the comparison between different strong-boxes used during dynamic tests, including rigid box, laminar box (Hushmand et al. 1988), ESB

container (Schofield & Zeng 1992) and the Hinged Plate Container (HPC). The HPC was constructed with a series of hinges between the aluminium layers in order to permit the continuity of the displacements and avoid the stress concentrations at the laminations steps (fig.4.3).

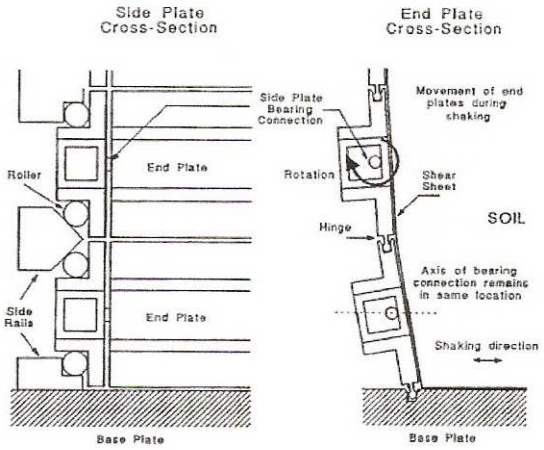

Fig.4.3 (Fiegel et al.1994; Kutter, 1995)

From the results, they observed that HPC and ESB had similar natural frequency, but the soil-container system of the Laminar Box had a natural period about 5% greater. The ESB box had smaller damping compared to HPC and Laminar Container. Fiegel et al. (1994) concluded that different boxes had different frequency and damping characteristics in order to analyze experimental results.

Some of the most interesting actuators and strong boxes widely used in the past and in the present are explained in the following.

Japan & Honk Kong

A very large number of geotechnical centrifuge were installed in Japan from the 1980s until today and some of them were equipped with in-flight dynamic actuator. Fujii (1991) described the operation of a small electro-magnetic earthquake simulator, used in the geotechnical centrifuge of the Chuo University in Tokyo. Matsuo *et al.* (1998) explained the features of the dynamic geotechnical centrifuge of the Public Works Research Institute (PWRI) of the Japan Construction Ministry, including an electro-hydraulic shaking table. Imamura *et al.*(1998) reported a detailed description of the

dynamic geotechnical centrifuge of the Nishimatsu Construction Society, focusing on the actuation system of an electro-hydraulic shaker. Takemura *et al.* (2002) detailed the preliminary dynamic tests in the geotechnical centrifuge of the Tokyo Institute of Technology (TITech), using a horizontal-vertical 2D in-flight shaker. Matsuda & Higuchi (2002) described the dynamic tests equipment used for the geotechnical centrifuge of the Technical Research Institute of Obayashi in Tokyo, including the servo-hydraulic shaker and the data acquisition system.

At the Hong Kong University of Science and Technology (HKUST) a large geotechnical centrifuge was developed in the 1998 (Schen *et al.* 1998). The centrifuge had an arm radius of 3.28m, a maximum acceleration of 150g for static tests and 75g for dynamic tests, and a payload capacity of 400g-tons (fig.4.4).

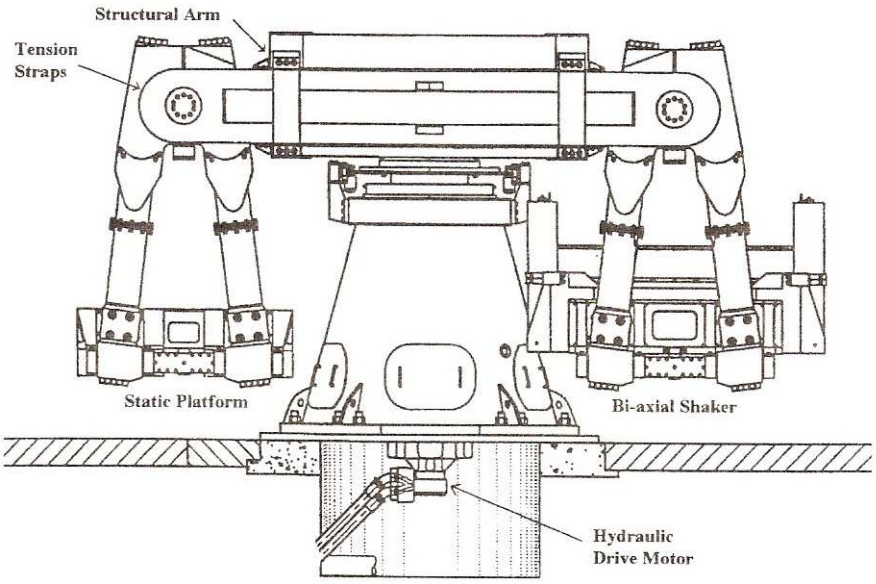

Fig.4.4 HKUST geotechnical centrifuge (Schen et al.)

The laboratory was equipped by three swinging platforms, two for static tests and one for dynamic tests, with the shaker on board. The shaker was designed in order to control the seismic motion in horizontal and vertical direction (2D) (fig.4.5). The actuator applied a sinusoidal base motion at the bottom of the model box, with shaking frequency between 0 and 350Hz.

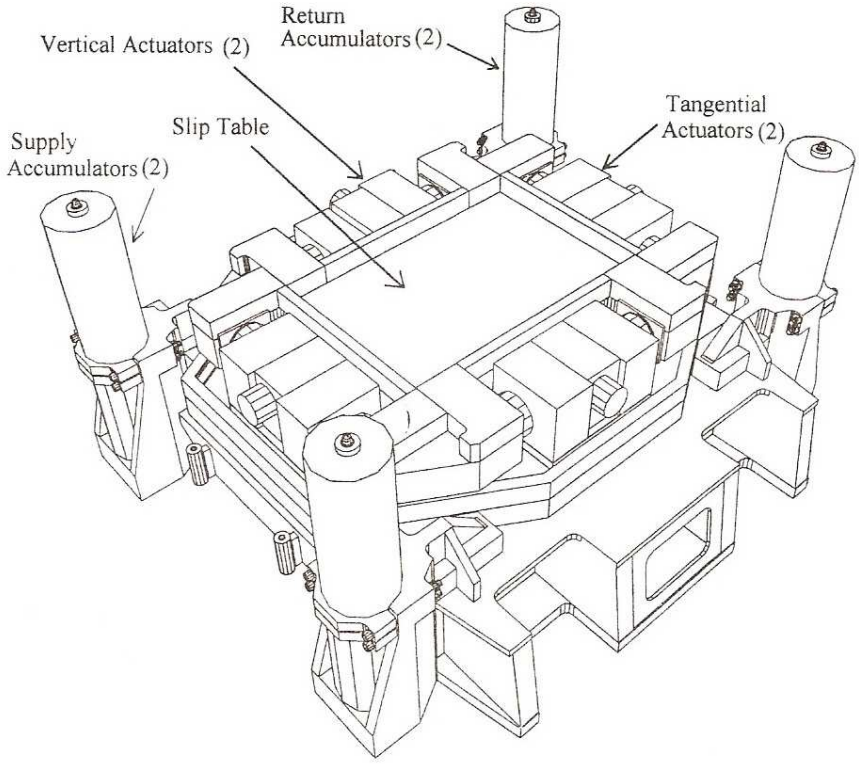

Fig.4.5 Seismic actuator at the HKUST (Schen et al.)

A laminar container was built with 52 aluminium rings separated by ball bearing in order to reduce friction between the laminations and accommodate the horizontal displacements of the model during the dynamic tests in flight.

USA

Some University Laboratories in USA are equipped with geotechnical centrifuges and are able to perform dynamic tests. Ketcham *et al.* (1991) described the electro-hydraulic shaker for small geotechnical centrifuge developed at the University of Colorado. Figueroa *et al.* (1998) explained the equipment of geotechnical centrifuge at Case Western Reserve University in Ohio. Van Laak *et al.* (1998) reported the features of the servo-hydraulic shaker for large centrifuge designed and built at Rensselar Polytechnic Institute (RPI). The Centre for Geotechnical Modelling at University of California Davis (UCD) was equipped since 1994 with a 9.1m radius

geotechnical centrifuge (Kutter *et al.,* 1991 1994). Moreover a servo-hydraulic bi-axial shaking table and a laminar box for the dynamic tests in the centrifuge were developed and currently used.

United Kingdom

Kutter (1982) described the features of the first actuator designed at Cambridge University, in the United Kingdom. This earthquake actuator, called *Bumpy Road*, was used for more than ten years, firing a very large amount of different earthquakes during its lifetime. In order to apply earthquake motion to the model, a curved track was mounted on the wall of the centrifuge and a cam roller followed this track. The model was shaken in circumferential direction through a crack and shaft, connected to the cam roller. The track was changeable but only two sinusoidal tracks were implemented. Madabhushi *et al.* (1998) showed the limits in the use of Bumpy Road Actuator. Therefore this shaker had a single frequency input signal and fixed duration; moreover the actuator had good performance when strong earthquakes were fired. The use of single frequency was a heavy limitations when it is considered the ground behaviour across the resonance frequency. Many papers were published using the data obtained by Bumpy Road: different problems were studied, from soil liquefaction (Schofield & Lee, 1988) to dynamic behaviour of walls (Zeng & Steedman, 1993). In order to avoid Bumpy Road limitations, a new actuator was designed at Cambridge University. This new shaker was called SAM (Stored Angular Momentum) and will be extensively explained in the §5.3.2.

The Schofield Centre of the Cambridge University was equipped with a set a different strong-boxes in order to carry out dynamic tests in flight. Madabhushi *et al.* (1994) described a set of centrifuge tests using a rigid box with adsorbent boundaries. Zeng & Schofield (1996) explained the design philosophy of the Equivalent Shear Box, used for many dynamic tests in centrifuge (Teymur & Madabhushi, 2003). Brennan *et al.* (2006) discussed about a new container developed at the Schofield Centre, suggested by the work of Van Laak *et al.* (1994), who built a light-weight laminar box at the RPI of the University of New York. The new container was called Laminar Box (LB) and was developed in order to have low mass and negligible inertia, but sufficient stiffness under high levels of gravity too. Brennan *et al.* (2006) compared the behaviour of the LB and the ESB : they carried out some tests

on dry sand models, placing a set of accelerometers along the central vertical and near the external wall. The comparison between the time histories was very good, showing similar acceleration at the box centre and near the wall, both for LB and ESB (fig.4.6).

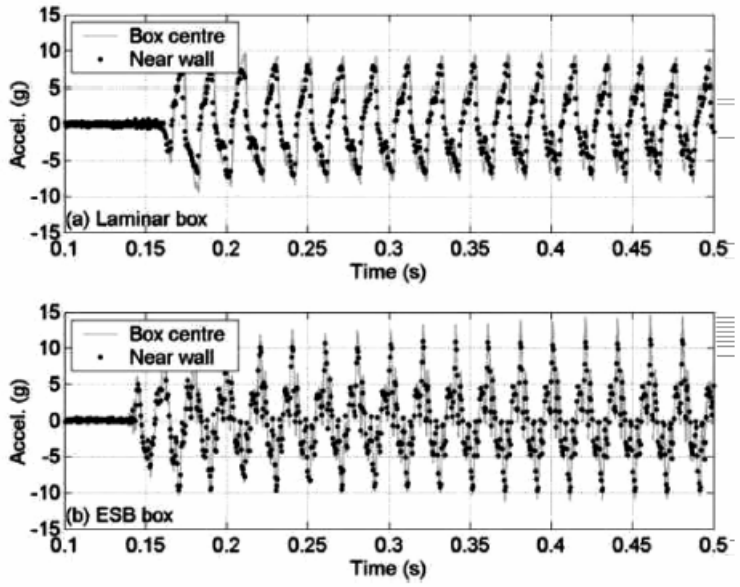

Fig.4.6: acceleration time histories recorded in LB and ESB boxes (Brennan et al.,2006)

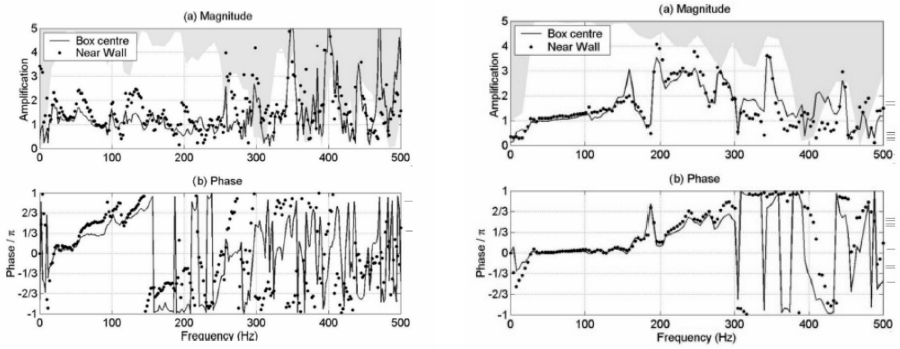

(a) Laminar Box (b) Equivalent Shear Box

Fig.4.7: Amplification fuction, coherency and phase angle in the ESB and LB boxes (Brennan et al.,2006)

Fig.4.7 showed the transfer function, plotted together with the coherence, and the phase angle. This comparison gave information on the multi-frequency content of the input signal at the base of the two boxes. In grey was plotted the coherence, which was an information on the reliability of the amplification data: a low value of coherence corresponded to external factors contemporaneous to dynamic motion, which made unreliable amplification data. At low frequency the coherence was generally high and the agreement between the central and the near wall vertical was reasonable. Laminar Box amplification function showed peaks at 20Hz, 50Hz and 120Hz in the near wall column, probably due to finite inertia of the container wall. In the ESB the comparison was reasonable, but until 160Hz the soil near the wall amplified less than the box centre soil. After 160Hz the opposite was true. In both cases the annoying effects were slights.

France

Derkx *et al.* (2006) explained the equipment of *Laboratoire Central des Ponts and Chaussées* (LPCP) in France, consisting in a geotechnical centrifuge, an earthquake actuator, a laminar box and a data acquisition system.

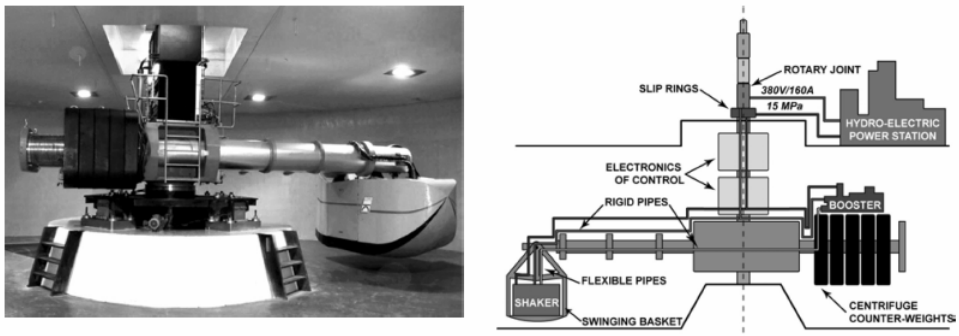

Fig.4.8: Centrifuge of the LPCP (Derkx et al.,2006)

The LPCP has a single arm centrifuge of 5,5m radius (fig.4.8), a maximum payload of 2 tons and a maximum centrifugal acceleration of 200g. The electro-hydraulic actuator is installed in the swinging basket and can fire single frequency signals in the frequency range 20-200 Hz, in a single direction (1D). In order to perform seismic experiments, simulating an infinitely extended soil layer, an equivalent shear beam box (ESB) was

developed and used at LPCP. The ESB box has an aluminium base-plate and is constituted by 15 overlapped aluminium frame, separated by rubber joints. In order to reduce deformation in the direction perpendicular to model shaking, two gantries for each side are installed (fig.4.9), including ball bearing between box and gantry to allow model movement in the shaking direction. On each frame two holes are made to pass sensor wires and measure the horizontal displacement during the tests.

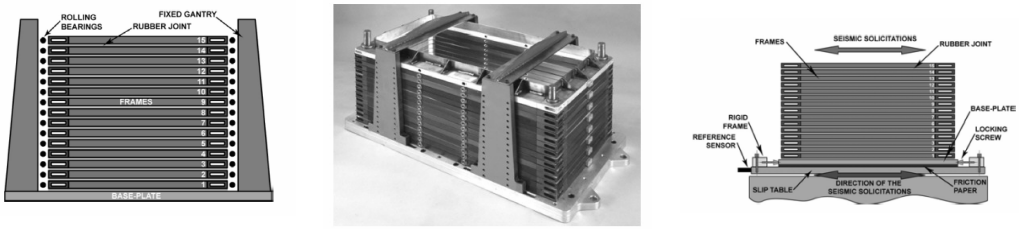

(a) (b) (c)

Fig.4.9: Laminar Box of the LPCP (Derkx et al.,2006)

Elgamal *et al.* (2007) briefly explained the features of geotechnical centrifuge, used in the *Centre du Commissariat à l'Energie Atomique – Centre d'Etude Scientifiques et techniques d'Aquitaine* (CEA – CESTA), located near Bordeaux. The centrifuge equipments are able to apply vertical and horizontal shocks, using a pneumatic system.

4.4 RESEARCH PROJECTS INVOLVING DYNAMIC CENTRIFUGE TESTS

In the 1980s a research project was funded, involving seven different university equipped with geotechnical centrifuge able to perform dynamic tests (Caltech, UC Davis, Cambridge University, RPI, University of Colorado, MIT and Princeton). The project was called **VELACS**, an acronym of Verification of Liquefaction Analysis by Centrifuge Studies. The first phase of the project consisted in a comparison between different experimental data on the same model, obtained from different centrifuge tests. The materials, the geometry and the boxes were the same, but the users, the shaker and the geotechnical centrifuge were different. The comparison showed a clear scatter between the tests: even if the model preparation procedure was standard, there

was a large difference in the input signals fired by the actuators and probably a difference in void ratio reached in the model. Despite the scatter, a set of dynamic tests involving soil liquefaction (fig.4.10) was carried out in order to compare the data results with numerical analysis.

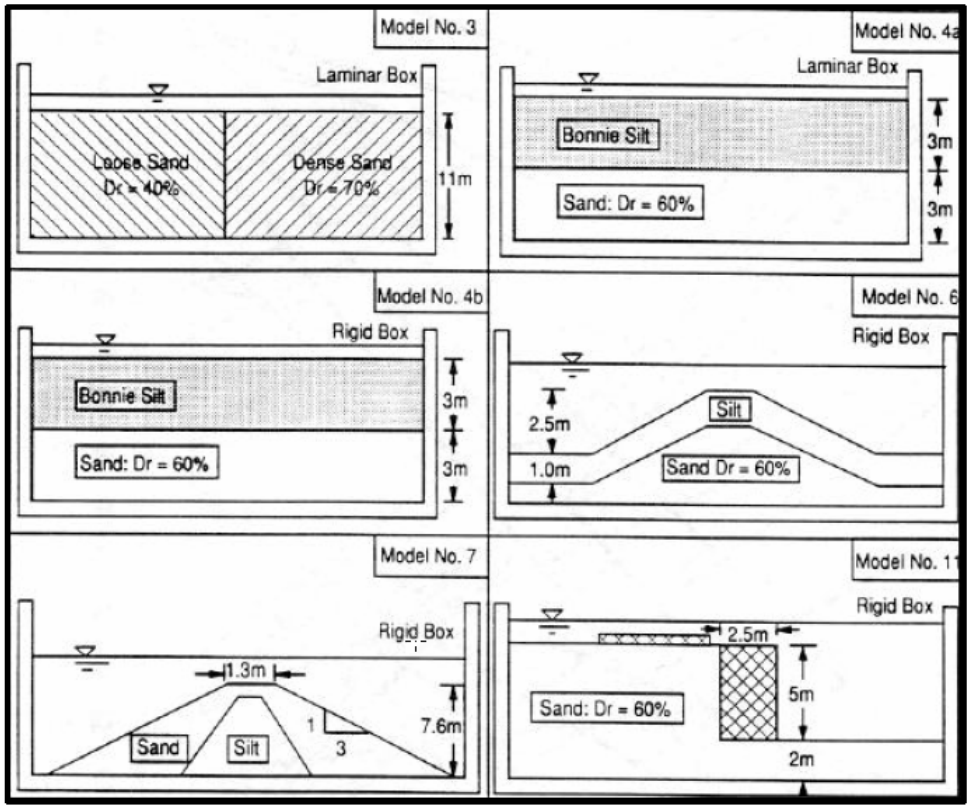

Fig.4.10: experimental models performed in the VELACS centrifuge tests

Moreover some laboratory test were carried out in order to obtain the soil characteristics at small strain (triaxial tests). All the experimental data were useful to produce “Class A” prediction of the experiments. The dynamic tests were repeated by two or more University in order to compare the results. A large scatter between the empirical data from different laboratories was found in the second phase, but this result was expected due to major complexity of the models. The conclusion was that each test was never ever a duplicate of an other test and was considered consistent by itself. The scatter between the empirical and numerical data, using SWANDYNE software, was smaller; the variability of experimental data was much lower than the variability of

analytical prediction methods. This project was very fruitful in order to understand how the centrifuge experiments could represent dynamic events and reproduce the seismic interaction, showing all the disadvantages and advantages of small scale dynamic modelling.

In North America an extended project was launched in the October 2000 called **NEES**, an acronym which means Network for Earthquake Engineering Simulation. NEES is a shared national network of 15 experimental facilities, collaborative tools, a centralized data repository, and earthquake simulation software, all linked by the Internet connections of NEESgrid. Together, these resources provide the means for collaboration and discovery in the form of more advanced research based on experimentation and computational simulations of the ways buildings, bridges, utility systems, coastal regions, and geo-materials perform during seismic events. Great investments were carried out in order to upgrade the equipments of the UC Davis and the RPI of the New York University.

4.5 PHYSICAL MODELLING OF TUNNEL BEHAVIOUR DURING AN EARTHQUAKE

Onoue *et al.* (1994; 1998) carried out a set of centrifuge tests on tunnels constructed using the “stacked-drift” method. This construction technique is used for large diameter tunnels and consists in a series of interlocking small diameter concrete filled tunnels, called drifts, constructed prior to excavating the interior soil. Beyond the static tests, carried out in order to evaluate the relationship between the earth pressures acting on the drifts and the contact pressures between drifts, a set of dynamic tests was conducted, with and without the tunnel. The models were instrumented with accelerometers placed along a vertical free-field line and load cells between the drifts. The g level used during the dynamic tests was 30g, and the input signal was a train of sinusoidal wave, with increasing frequency and amplitude. The transfer functions (fig.4.11) for a tunnel tests, measured in a free-field column, showed a resonant frequency smaller compared to the tests without the tunnel, having a maximum difference of 20%.

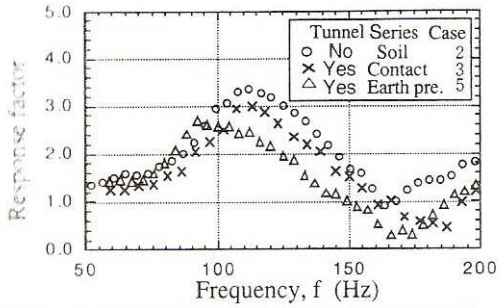

Fig.4.11 Surface-bottom transfer functions of the tests performed by Ounoue et al., 1998

The comparison between axial forces (fig.4.12) as calculated by analytical formulae and measured by load cells, showed generally a good agreement. The maximum axial value, obtained by measured values, was 80% of the analytical values, using a non-linear shear modulus of soil, given by the G-γ curve suggested by Iwasaki *et al.* (1978) for the Toyura sand.

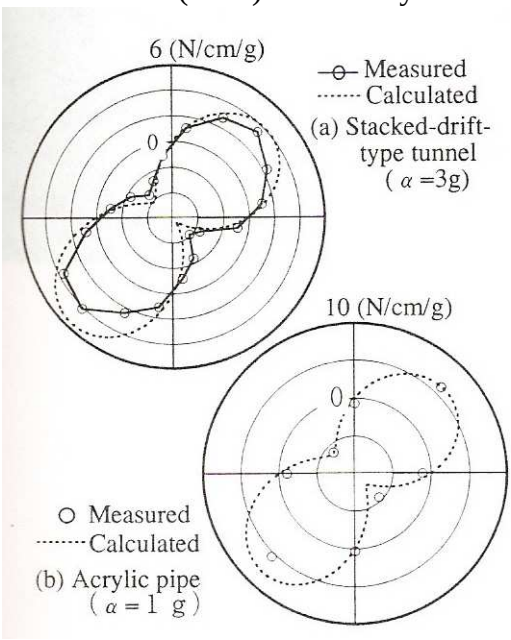

Fig.4.12 Comparison between measured and calculated hoop forces (Ounoue et al., 1998)

Yamada *et al.* (2002) used a shear box, made by overlapped laminations, in order to perform a quasi-static tests, through the application of lateral

displacement. They studied three different cases: a) single circular tunnel; b) single rectangular tunnel; c) triple-faced tunnel, made by a combination of the previous cases. The seismic loadings were applied using three actuators connected to three laminations. The models were manufactured by air pluviation of the Toyura sand in the shear box. The models layouts are in fig.4.13, including tunnel and instrumentation locations in the cross-section.

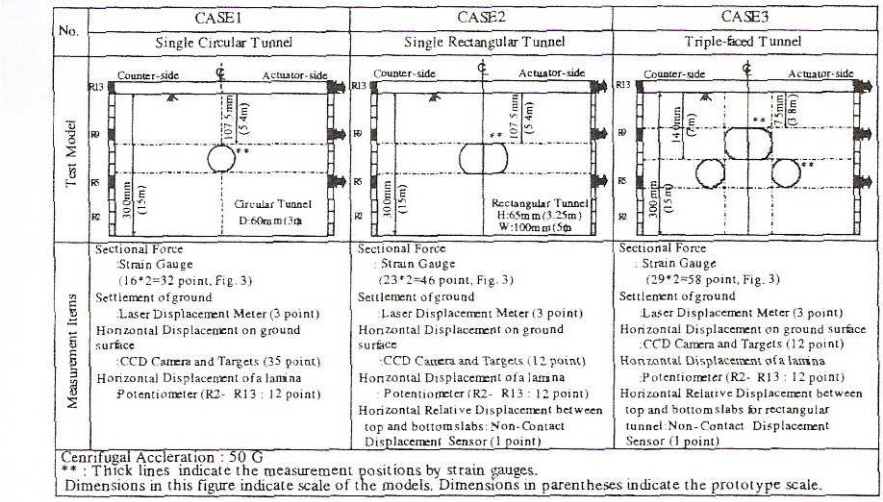

Figure 2. Test cases.

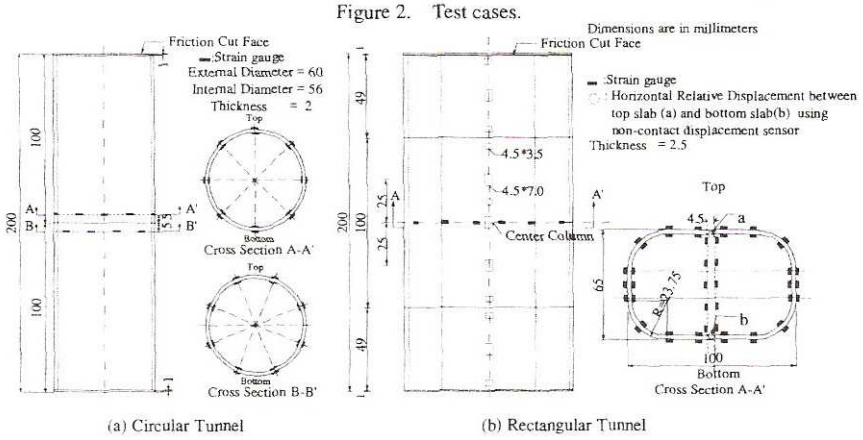

(a) Circular Tunnel (b) Rectangular Tunnel

Fig.4.13: Set-up of tests performed by Yamada et al., 2002

Also the aluminium tunnels features are reported in the fig.4.13, considering longitudinal and transverse dimensions and strain-gauges locations. All the tests were performed at 50g, and the input signals for

horizontal displacements were trains of sinusoidal waves of same frequency (200Hz at model scale) and different amplitude. In the table 4.2, the signals fired in the tests for each actuators are reported; the values of the input signals are referred to the maximum displacement (amplitude), considering for each step three cycles of loading.

Table 4.2: Displacements loading steps (Yamada et al., 2002)

Step	**1**	**2**	**3**	**4**	**5**	**6**	**7**	**8**
Lamina N° 13	0.050	0.100	0.200	0.400	0.800	1.600	3.200	6.400
Lamina N°9	0.033	0.067	0.133	0.267	0.533	1.067	2.133	4.267
Lamina N°5	0.017	0.033	0.067	0.133	0.267	0.533	1.067	2.133
Average shear strain (%)	0.015	0.031	0.062	0.123	0.246	0.492	0.985	1.969
Note	Input Wave: Sign wave (0.005Hz) – 3cycles/step Average shear strain = (Lamina N°13 displacement/Ground Height)							

In the table 4.2, there is also an estimation of average shear strain for each step. Beside the tunnel tests, some free-field tests were carried out, in order to evaluate the ground response to cyclic loadings.

The sectional forces obtained in the circular tunnel tests (fig.4.14) showed a higher value at $\pi/4$, as for the observed damage after the earthquakes (Yoshida 2000). Similar considerations were done for the rectangular tunnels, in which the maximum force value is at the tunnel corner and at the end of central column (in the case of bending moment). In fig.4.15 the relative horizontal displacements at tunnel depth were plotted against the maximum bending moment at the corner (rectangular tunnels): the bending moment seems to be non proportional to the relative displacements between two laminations on the box, while is almost proportional to the relative displacements between the top and the bottom of the tunnel. The results for triple-faced tunnels showed a general reduction of pseudo-static forces and relative horizontal displacements.

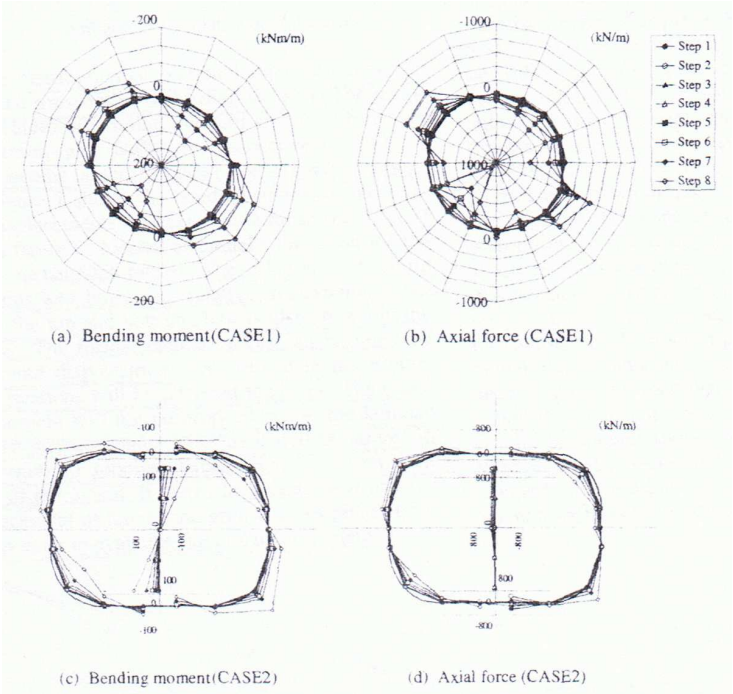

Fig.4.14: Behaviour of single tunnels (Yamada et al., 2002)

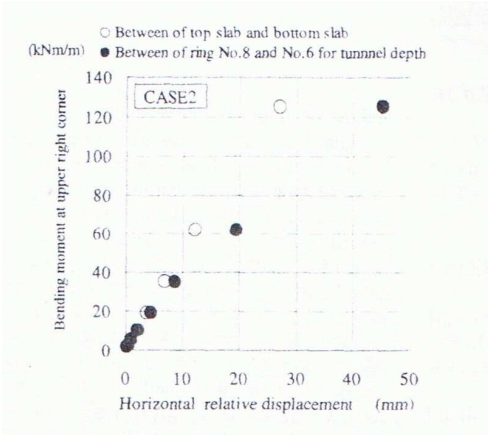

Fig.4.15: Bending moment vs horizontal displacements (Yamada et al., 2002)

Izawa *et al.* (2006) examined the seismic stability of rectangular tunnels through dynamic centrifuge tests. In order to investigate the seismic behaviour of large cross-section structure, two types of tests were carried out:

a) *Centrifuge pseudo-static tests*: the seismic loading was applied to a shear box through three actuators connected to three rings of the box. These actuators transmitted to the box a displacement distribution, linear with depth and variable with time according to a sinusoidal law.

b) *Centrifuge dynamic tests*: at the base of the model four sinusoidal waves were applied, in order to have a similar excitation compared to the pseudo-static case.

Both the tests were carried out at 50g, using the Toyura sand as a model material. The aim of this comparison was to evaluate the applicability of the Seismic Deformation Method (Kawashima, 2000) to rectangular underground structures, verifying if the inertia forces arising in the structure during dynamic tests are negligible, as postulated by the design method. The tunnel model was made by 2mm thick aluminium lining, in order to clearly measure the stress on the lining.

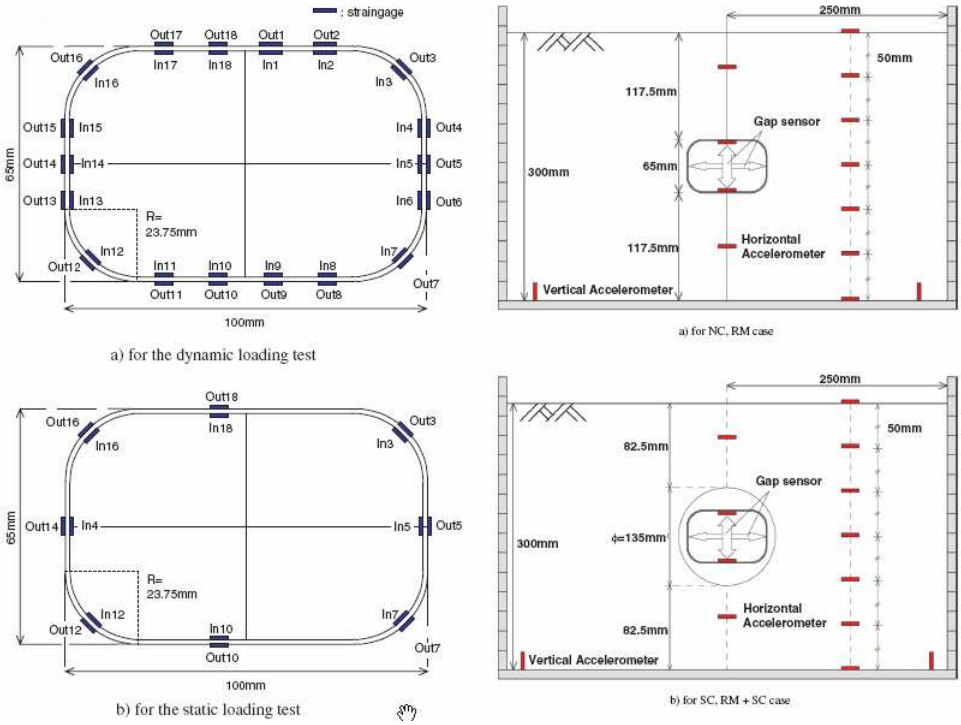

Fig.4.16 Set-up of the tests performed by Izawa et al, (2006)

In fig.4.16 a drawing of strain-gauges location is represented, for both the tests. Bending moment and axial force from pseudo-static and dynamic tests are shown in the fig.4.17.

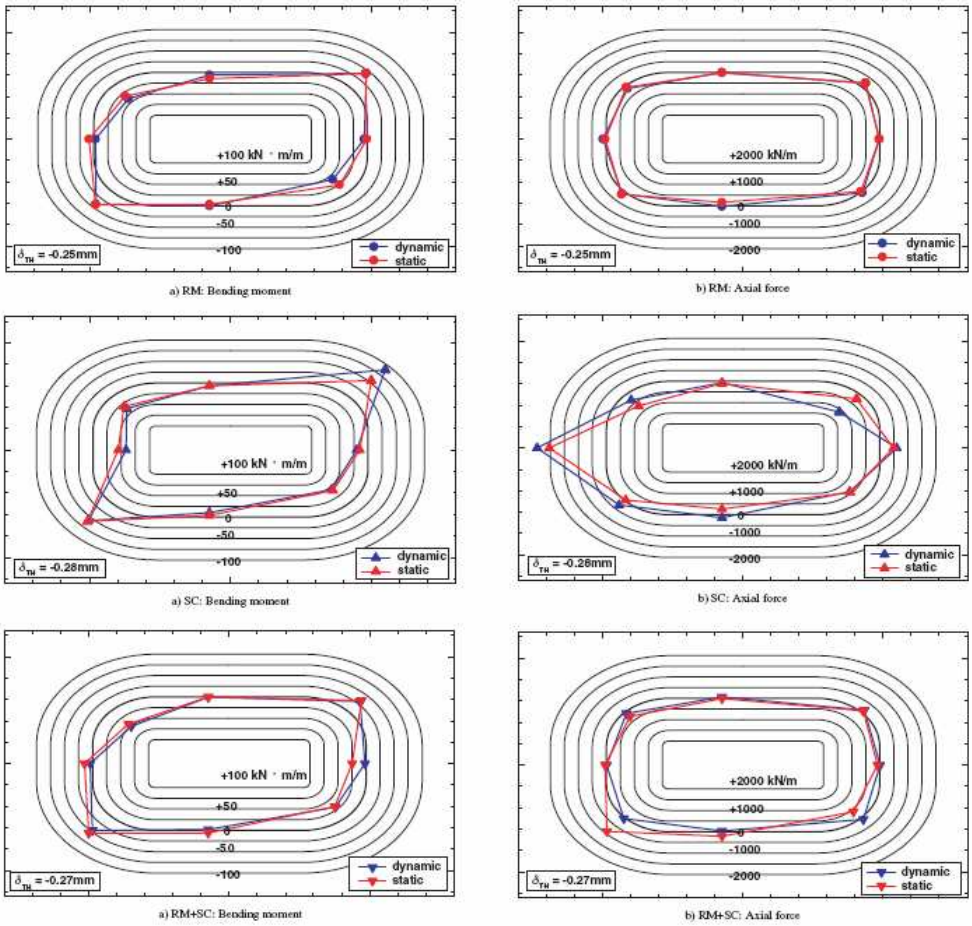

Fig.4.17 Distribution of hoop forces and bending moments (Izawa et al., 2006)

Provided that the lateral movement in both dynamic and pseudo-static tests was the same, the distribution of internal forces was almost the same in every test carried out. The Authors concluded that the inertia forces were effectively negligible and that the SDM is successfully applicable for rectangular tunnels.

Tohda *et al.* (2006) discussed the results of fourteen dynamic centrifuge tests on pipelines. Two pipeline models were prepared in order to model

different flexibility, using the same material (aluminium alloy) and diameter (9cm) for the pipe, but changing its thickness (0.095cm for flexible pipe and 0.35cm for rigid pipe). The tests were carried out at centrifugal acceleration of 30g, in order to perform the typical geometry of the pipelines at the prototype scale. The small tunnels were instrumented with load cells and strain gauges (fig.4.18).

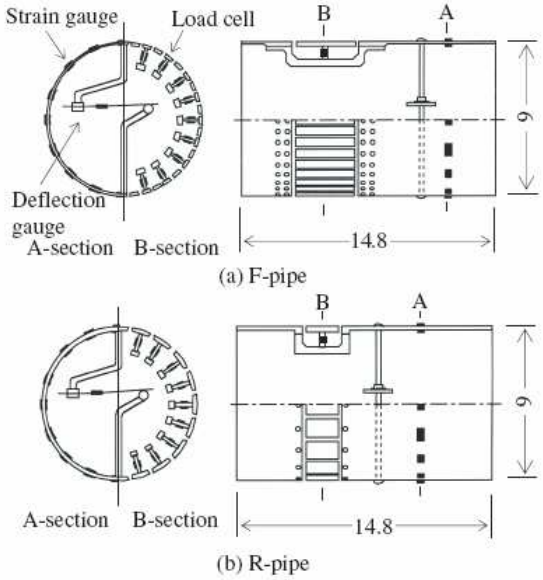

Fig.4.18: Instrumented pipes used in the tests performed by Tohda et al. (2006)

The structure was divided longitudinally in two parts: the first part was divided in 40 (F-pipe) or 20 (R-pipe) segments in the cross section in order to install a load cell for each segment and measure the normal earth pressure; on the second part strain gauges were stuck on the lining in order to measure bending strain. The models were prepared using dry sand, considering dense and loose ground conditions. Besides the stress transducers, thirteen accelerometers were placed in the model ground for each test (fig.4.19).

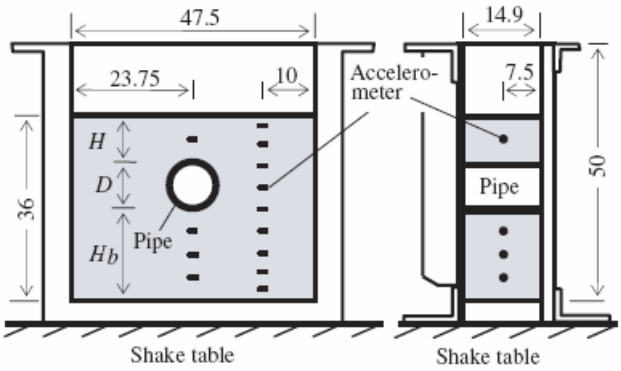

Fig.4.19: Set-up of the tests performed by Tohda et al. (2006)

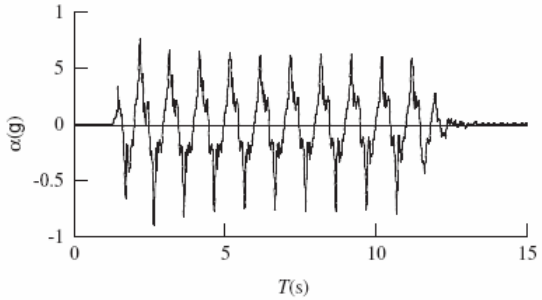

Fig.4.20: Typical input motion in tests by Tohda et al. (2006)

The input motion was similar to a sinusoid with 12 cycles, 0.8g peak ground acceleration and 1Hz frequency (fig.4.20). In the fourteen tests some parameters were changed: pipe flexibility; ground density; pipe ground cover (H); distance from the box bottom (H_b). In the fig.4.21 the typical measurements for a flexible pipe (F-pipe) and for a rigid pipe (R-pipe) were reported: on the left the distributions with depth of acceleration (α), shear stress (τ) and horizontal displacement (x) were shown; on the right the distributions along the tunnel lining of the maximum increments of bending strain ($\Delta\varepsilon$) and normal earth pressure ($\Delta\sigma$) were reported. Peak values of dynamic increments of stress and strain were located generally at +/- 45°, as found from field damage observations after earthquakes (Yoshida 1999).

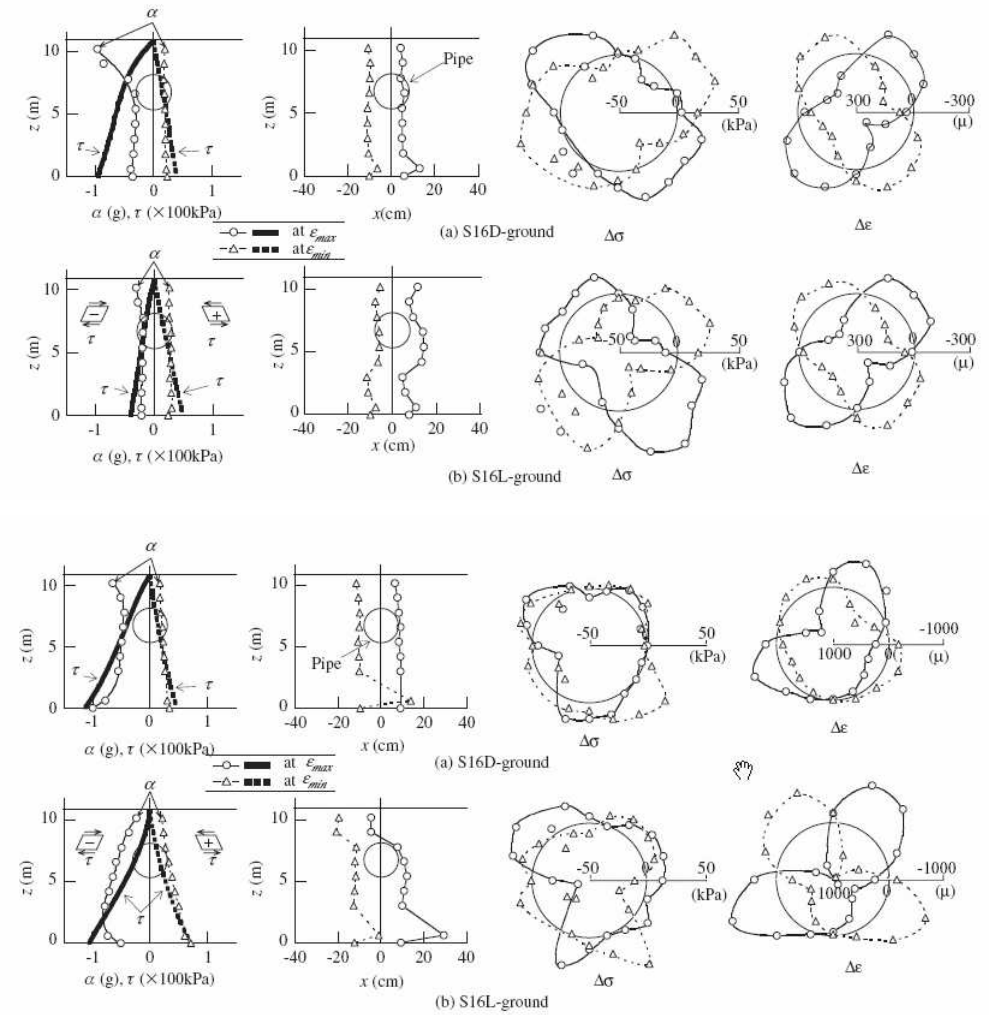

Fig.4.21 Main results of the tests by Tohda et al. (2006)

REFERENCE

Bilotta E., Taylor N., (2005), *Modellazione geotecnica in centrifuga,* Collana Argomenti di Ingegneria Geotecnica n°20, Hevelius ed.

Coelho P.A., (2007), *In situ densification as a liquefaction resistance measure for bridge foundations,* PhD Thesis, University of Cambridge.

Derkx F., Thorel L., Chazelas J.L., Escoffier S., Rault G., Buttigieg S., Cottineau L.M., Garnier J., (2006), *Dynamic tests and simulation of earthquakes in the LCPC's centrifuge,* Phisical Modelling in Geotechincs ICPMG '06, pp.181-186.

Elgamal A., Pitilakis K., Raptakis D., Garnier J., Madabhushi S.P.G., Pinto A., Steidl J., Stewart H.E., Stokoe K.H., Taucer F., Tokimatsu K., Wallace J.W., (2007), *A review of large-scale testing facilities in geotechnical earthquake engineering,* Earthquake Geotechnical Engineering, Chapter 5, pp.93-129.

Fiegel G.L., Hudson M., Idriss I.M., Kutter B.L., Zeng X., (1994), *Effect of Model Containers on Dynamic Soil Response,* Proceedings of Centrifuge '94.

Figeroa J.L., Saada A.S., Dief H., Dietz C.P., (1998), *Development of geotechnical centrifuge at Case Western Reserve University,* Centrifuge '98, pp.3-8.

Hushmand B., Scott R.F., Crouse C.B., (1988), *Centrifuge Liquefaction Tests in a Laminar Box,* Geotechnique, n°38, pp.253-262.

Izawa J., Kusakabe O., Nagatani H., Yamada T., Ohbo N., (2006), *Centrifuge modelling on seismic behaviour of rectangular tunnels,* Physical Modelling in Geotechnics – ICPMG '06, pp.1163-1169.

Jeyatharan, K., (1991), *Partial liquefaction of sand fill in a mobile arctic caisson under ice loading,* PhD Thesis, University of Cambridge

Ketcham S.A., Ko Hon-Yim, Sture S., (1991), *Performance of an earthquake motion simulator for small geotechnical centrifuge,* Centrifuge '91, pp. 361-368.

Ko Hon-Yim, (1994), *Modeling seismic problems in centrifuges,* Proceedings of the Centrifuge '94, pp.3-10.

Kutter B.L., (1995), *Recent advances in centrifuge modelling of seismic shaking (state of art),* Proceedings of Third International Conference on

Recent Advance in Geotechnical Earthquake Engineering and Soil Dynamics, April 2-7, 1995, VolII, St.Louis, Missouri.

Madabhushi S.P.G., Schofield A.N., Lesley S., (1998), *A new Stored Angular Momentum (SAM) based earthquake actuator,* Centrifuge 98, Balkema, Rotterdam

Madabhushi S.P.G., Houghton N.E., Haigh S.K., (2006), *A new automatic sand pourer for model preparation at University of Cambridge,* Physical Modelling in Geotechnics – 6ICPMG'06

Onoue A., Kazama H., Hotta H, Kimura T., Takemura J, (1994); *Behaviour of stacked-drift-type tunnels,* Centrifuge '94, pp.687-692.

Onoue A., Kazama H., Hotta H., (1998); *Seismic response of a stacked-drift-type tunnel in dry sand,* Centrifuge '98, pp.237-242.

O'Rourke T.D., Goh S.H., Menkiti C.O., Mair R.J., (2001), *Highway tunnel performance during the 1999 Duzce earthquake,* pp. 1365-1368.

Schofield A.N., (1980), *Cambridge Geotechnical Centrifuge Operations,* Geotechnique 30, No.3, 227-268

Schofield A.N., Zeng X., (1992), *Design and Performance of an Equivalent Shear Beam Container for Earthquake Centrifuge Modeling,* Cambridge University Internal Report.

Taylor R.N. (1995), *Centrifuges in modelling: principles and scale effects*. In: Geotechnical centrifuge technology, cap. 2, 19-33. Blackie Academic & Professional, Glasgow.

Timoshenko S.P., (1961), *Theory of elastic stability*, McGraw-Hill, chap.7 pp.278-313.

Tohda J., Nakamura Y., Inoue Y., Yoshimura H., Ko H.Y., Ohsugi A., (2006), *Dynamic response of sewer pipes rehabilitated by CIPP through*

centrifuge model tests, Phisical Modelling on Geotechnics, ICPMG ’06, pp.759-764.

Van Laak P.A., Adalier K., Dobry R., Elgamal A. W., (1998), *Design of RPI’s large servo-hydraulic centrifuge shaker,* Centrifuge ’98, pp.105-110.

Yamada T., Nagatani H., Igarashi H., Takahashi A., (2002), *Centrifuge model tests on circular and rectangular tunnels subjected to large earthquake-induced deformation,* Geotechnical Aspects of Underground Construction in Soft Ground, pp.673-678.

Zhao Y., Gafar K., Elshafie M.Z.E.B., Deeks A.D., Knappett J.A., Madabhushi S.P.G., (2006), *Calibration and use of a new automatic sand pourer,* Physical Modelling in Geotechnics – 6ICPMG’06

Zeng X., (1992), *Dynamic Centrifuge tests on Quay Wall Models,* Internal Report, University of Cambridge.

Chapter 5
Centrifuge tests

5.1 INTRODUCTION

In this chapter the centrifuge tests carried out at the Schofield centre, the geotechnical laboratory of the Cambridge University Engineering Department (CUED) were extensively explained. The equipment used to perform the test was described including the geotechnical centrifuge, the earthquake actuator and the strong box used for the models preparation. The instrumentation located in the model included accelerometers placed in the soil, strain gauges stacked on the tunnel and LVDTs for the surface settlements measurement. Moreover the calibration of the instruments was described, especially for the strain gauges, for which many trials loadings were performed in order to obtain a reliable calibration factor from the readings. The characteristics of the sand used for the model were briefly described, referring the physical properties and the small strain behaviour. The procedure for the model preparation were explained, including the pouring techniques to obtain the desired density. Many pictures are showed, concerning the tunnel and accelerometers placement in the model, according to the test layout. Once the models were ready the centrifuge loading and flight procedure were reported, including the signals fired in each test. The visual observation after the tests were reported, measuring the new position of sand surface and of all instruments. The interpretation of the accelerometers output data were reported, including the procedure to

filter the signal, evaluate the shear modulus G and calculate the stress-strain loops. The data given by the strain gauges was compared with the analytical results in order to quantify the kinematical effect on the stress calculation. In this chapter all the data will be accounted at the model scale.

5.2 TEST PROGRAMME

The four tunnel tests are being carried out on models made of dry sand at two different values of relative density, according to the table1, in the laminar box (500x250x300 mm^3) and at 80 g and 40g. In the table 5.1 the programme is shown:

Table 5.1: Centrifuge tunnel tests

model	*D* [mm]	*C* [mm]	D_r	*N*
T1	75	75	~75%	80-40
T2	75	75	~40%	80-40
T3	75	150	~75%	80-40
T4	75	150	~40%	80-40

In the table, D is the diameter of the tunnel, C is the cover, D_r is the relative density and N is the level of g.

5.3 FACILITIES

5.3.1 Philip Turner Centrifuge

Centrifuge experiments at Schofield centre are mostly carried out in a 10m beam centrifuge, named from the engineer, P.W. Turner, who designed this facility in the early 1970's (Schofield, 1980). The centrifuge consists essentially of a beam-like structure (fig 5.1c), which rotates about a central vertical axis. The sample can be carried at both the ends of the arm. In the tests performed only one model at one end is placed (fig 5.1b). At the other end a counterweight is provided (fig 5.1a). A swinging platform carrying the model and the actuator is installed on the blue end of the beam

(fig 5.1d) and the required counterweight on the red end. Dynamic tests are carried out at centrifuge acceleration in the range of 40 to 100g.

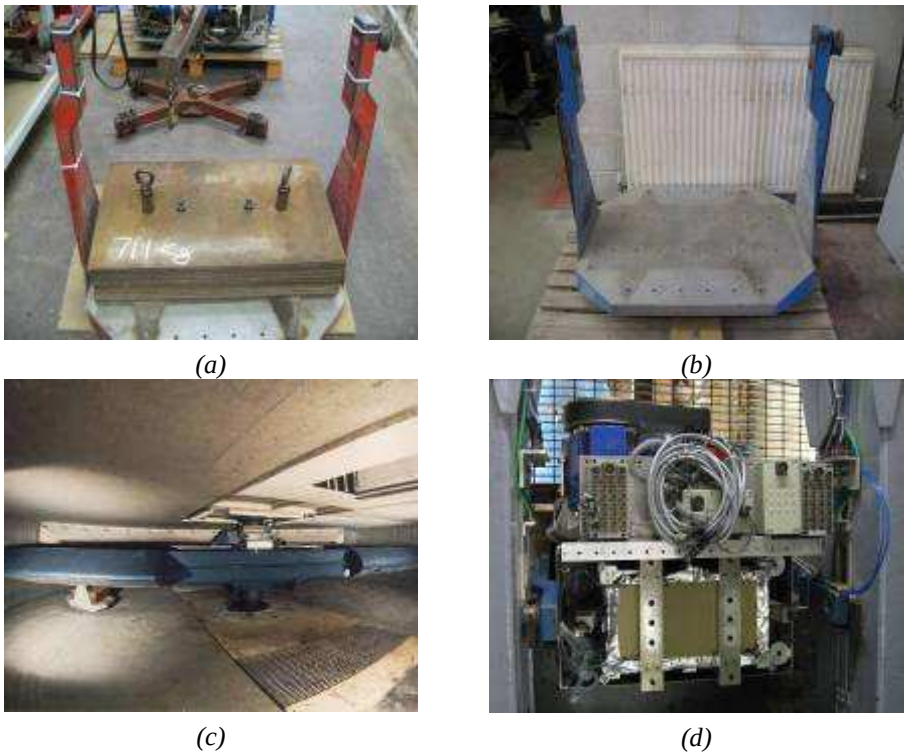

(a) *(b)*

(c) *(d)*

Fig.5.1: Philip Turner Centrifuge; a) Red end for counterweight; b) Blue end for the SAM and the model; c) Beam-like centrifuge structure; d) The model loaded on the centrifuge

5.3.2 SAM actuator

The Stored Angular Momentum (SAM) is an earthquake actuator developed at Cambridge University (Madabhushi *et al.*1998). The SAM actuator is a powerful tool and allows performing strong earthquakes at high g level. In the past many problems were studied using Bumpy Road Actuator, which had an essentially single frequency and a fixed duration.

The SAM actuator can fire successive earthquakes at different frequencies, duration and g level (fig 5.3). Very high levels of energy can be stored in a fly wheel spinning at high angular velocities. Madabhushi

(1998) described the SAM operation: a scheme of SAM is showed in the fig. 5.2.

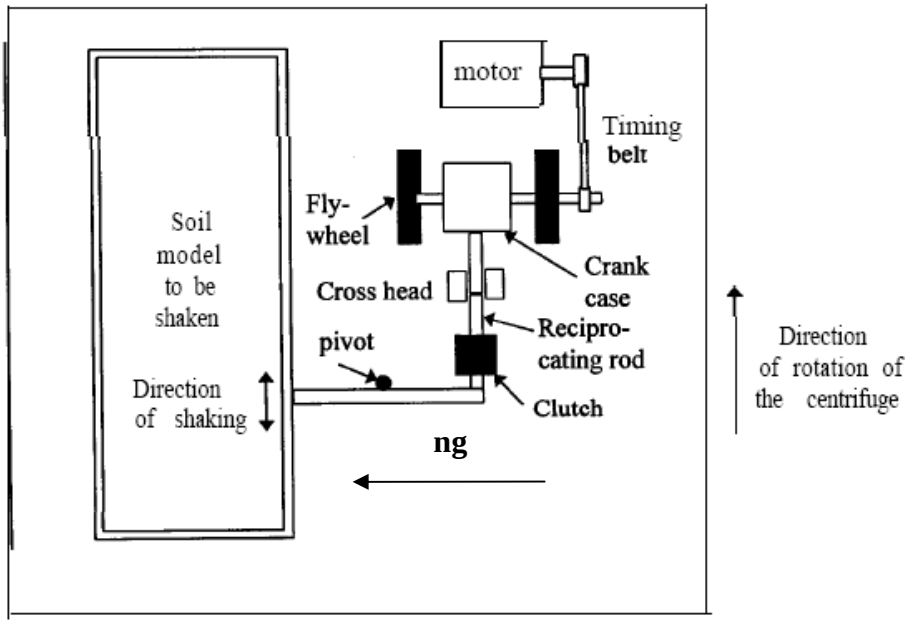

Fig.5.2: SAM operation scheme (Madabhushi et al.1998)

The energy stored in the fly wheel may be used to subject a centrifuge model to earthquakes. The angular velocity of the fly wheel determines the frequency of the earthquake. The duration of the earthquake is controlled by a fast acting clutch which starts and ends the earthquake. The strength of the earthquake can be controlled by altering the pivot point of the lever. The soil model is shaken in the direction of centrifuge flight and the fly wheels rotation in the plane of rotation of the centrifuge arms. The variables that can be changed during the tests are:

- Frequency
- Level of '*g*'
- Earthquake strength
- Duration

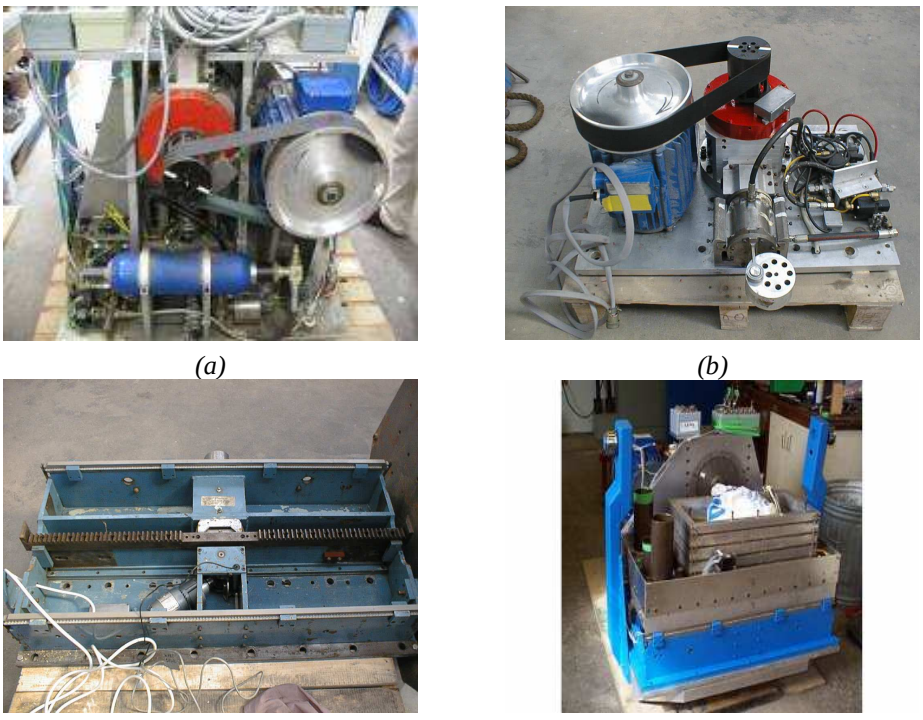

(a) *(b)*

(c) *(d)*

Fig.5.3: SAM Actuator; a) Loaded on the Blue End; b)Unloaded; c) Horizontal track for applying the signals; d) Model mounted on the SAM

5.3.2 Laminar Box

The tests are performed using a Laminar Box. This box is made by a series of rectangular overlapped frames (laminations) and connected by ball bearing (fig.5.4a). This solution is useful to minimize the friction between the laminations and to allow the horizontal movements of the whole box. The model container has inside dimensions of 500x250x300 and has a weight of 93.5 kg. A plate is put at the base of the box to connect the container with the SAM actuator and fire the earthquake on the model (fig.5.4b). The weight of the plate is 58 kg.

(a) *(b)*

Fig.5.4:Laminar Box; a) Free horizontal displacements; b)Strongbox and base plate

5.4 MATERIALS

5.4.1 Sand

The models will be made using dry Leighton Buzzard sand (grade E) reconstituted at two different relative densities (about 40% and 75%). The properties of the sand used in the models (fig 5.5a)was largely known from the existing literature (Jeyataran 1991, Tan 1990) and is reported in the table 5.2:

Table 5.2: Physical properties of Leighton Buzzard sand (Tan 1990 & Jeyataran 1991)

Sand	G_s	e_{max}	e_{min}	γ_{max} [kN/m^3]	γ_{min} [kN/m^3]	d_{max} [μm]	d_{min} [μm]	ϕ [°]
Leighton Buzzard (fract.E)	2,65	1,014	0,613	16,11	12,90	150	90	32

In which G_s is the specific gravity, e is the void ratio, γ_S is the unit weigh, d is the particle diameter and ϕ is the friction angle. The relative density for cohesion-less soil was evaluated from the expression:

$$D_r = \frac{e_{max} - e}{e_{max} - e_{min}} \qquad (5.1)$$

in which the void ratio e was calculated from the equation:

$$e = \left(\frac{G_S \cdot m_S}{Vol_S} \right) - 1 \qquad (5.2)$$

where m_s is the weight of the sand poured in the box (measured at the end of model preparation) and Vol_s is the internal volume of the box, extracting the tunnel volume. The total internal value was obtained empting the box with water until the same depth reached in the sand pouring and designed in the test layout: therefore the model thickness is lower (290mm) than maximum value (300mm). The internal volume measured was $3,47*10^7$ and was lower than the theoretical value obtained as $500x250x290=3,63*10^7$ due to the internal silicon junction that reduced the internal volume. The useful volume was obtained subtraction the tunnel volume ($0,08*10^7$) from the measured volume, giving the value of $3,39*10^7$.

5.4.2 Alloy (Dural)

The tunnel lining will be modelled using an aluminium tube having an external diameter D = 75mm and a thickness t = 0.5mm (fig. 5.5b). The unit weight of aluminium is 2770kg/m3. The mechanical properties are not unambiguous, because the elastic and yielding behaviour depends on the alloy type: the principal alloying constituents of the duralumin is the copper (4.4%), manganese (1.5%) and magnesium (0.6%). The typical properties of an alloy aluminium-copper are written in the table 5.4:

Table 5.4: Mechanical properties of the Aluminium alloy

Material	**E [GPa]**	**ν**	**f_{yk} [MPa]**	**f_{bk} [MPa]**
Al-Cu alloy	70	0.33	500	600

The aluminium tunnel thickness is equivalent to a very flexible concrete lining (0,06m): the use of these small dimension for the lining was justified by a better resolution of strain gauges instruments during the dynamic step.

5.5 INSTRUMENTATION

5.5.1 Accelerometers

In the centrifuge tests on tunnels miniature piezoelectric accelerometers manufactured by D.J. Birchall Ldt are used to measure acceleration in the soil and on the model container during earthquakes (fig. 5.5c). The device has a resonant frequency of about 50 kHz and maximum error of 5%. The weight of the transducer is about 5 grams.

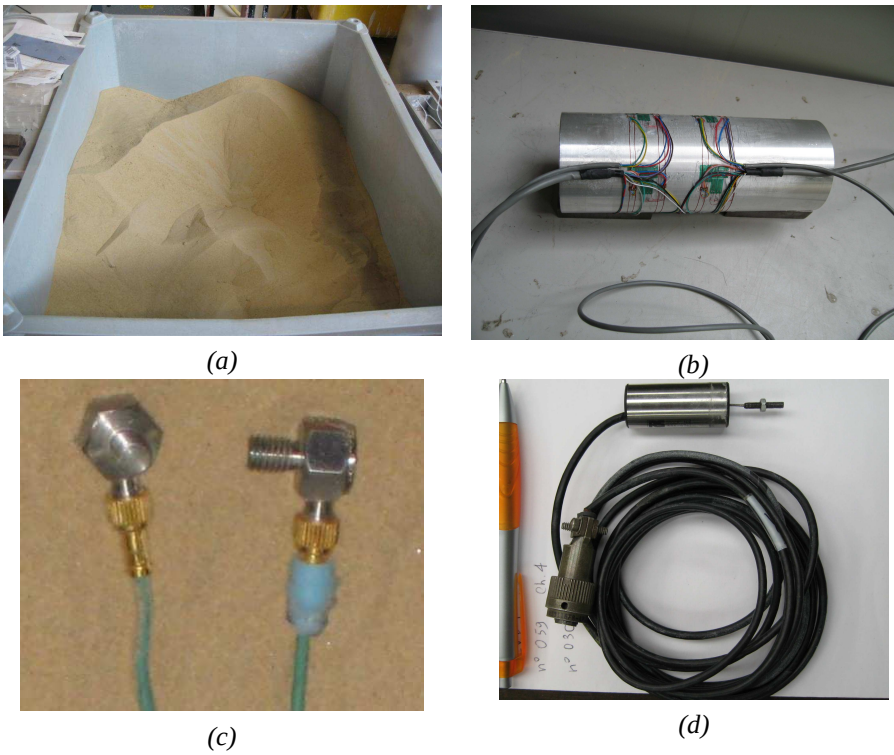

(a) *(b)* *(c)* *(d)*

Fig.5.5:Test materials :a)Leighton buzzard sand; b) Aluminium tube; Instrumentation: c) Accelerometers; d) LVDT

5.5.2 Strain Gauges

The tube has been instrumented in order to measure bending moments BM and hoop stresses HS at 4 locations along 2 transverse sections

(fig.5.6). It has been decided that the main instrumented section will be located at the mid-span of the tube and a second section at 50mm aside. This second section is needed for two reasons: checking the plane strain behaviour of the tunnel model (BM and HS at corresponding locations of different sections should be the same) and for redundancy of experimental data. In total 16 Wheatstone bridges have been attached to the tube and wired (4 locations x 2 sections x 2 force measurements).

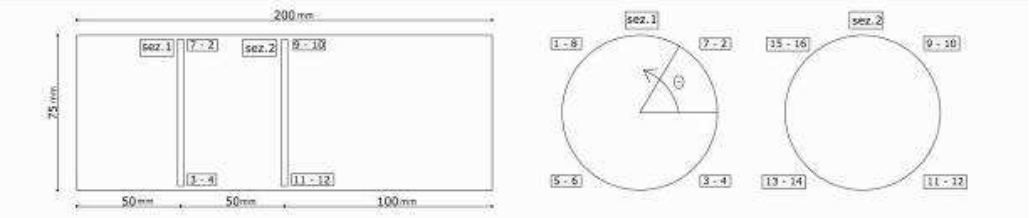

Fig.5.6: Strain gauges layout

The Wheatstone bridge is a system to obtain a measurement of a voltage variation connected to a deformation of the structure. This bridge system is constituted by 4 strain gauges, electrically located as in the fig.5.7. In the A and B points the bridge is connected to external power, whereas the C and D points are connected to a galvanometer, measuring the voltage. Starting from the input applied voltage V, the voltage variation measured by the galvanometer is proportional to an average deformation of the instruments:

$$\frac{\Delta V_{CD}}{V_{AB}} = \frac{K}{4}\varepsilon_m = \frac{K}{4}\left(\varepsilon_1 - \varepsilon_2 - \varepsilon_3 + \varepsilon_4\right) \tag{5.3}$$

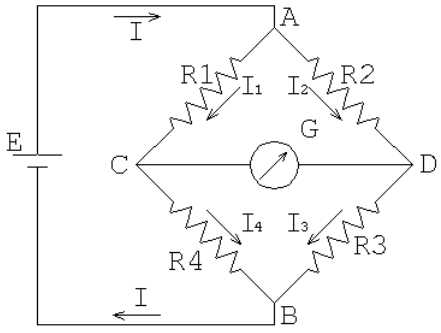

Fig.5.7: Wheatstone bridge

In the equation (5.3), K is the calibration factor, given by the strain gauge manufacturer (TML Tokyo Sokki Kenkyujo) and equal to 2,15, ε_m is the average deformation and ε_i is the deformation of each transducer. In fig.5.6 the layout of the strain gauges is reported: the bending moment transducers were located both in the internal and on the external tube surface at ($\theta=\pi/4+n\pi/2$; n=0,1,2,3). The *R1* and *R4* resistances were stuck on the external surface, whereas the *R2* and *R3* resistances were located on the internal side in the same position. The axial strain value from the elastic theory is:

$$\begin{cases} \varepsilon_1 = \varepsilon_4 = \dfrac{N(\theta_0)}{EA} + \dfrac{M(\theta_0)}{EI}\dfrac{t}{2} \\ \varepsilon_2 = \varepsilon_3 = \dfrac{N(\theta_0)}{EA} - \dfrac{M(\theta_0)}{EI}\dfrac{t}{2} \end{cases} \tag{5.4}$$

Substituting the equations (5.4) in the (5.3), the voltage variation is:

$$\left[\frac{\Delta V_{CD}}{V_{AB}}\right]_{BM} = K\frac{M(\theta_0)}{EI}\frac{t}{2} = K_{BM}M(\theta_0) \tag{5.5}$$

The measured variation ΔV_{CD} is directly proportional to bending moment through a factor. The “hoop stress” transducers were both located on the external surface: the *R2* and *R3* resistances were stacked beside the bending transducers, but had a different orientation. Therefore this couple of strain gauges measured the deformation longitudinally, and not in transverse direction, and was affected by the factor -ν. The *R1* and *R4* resistance, instead, were stuck at 20 degrees from the theoretically measuring point. From these considerations the value of total strain is given by:

$$\begin{cases} \varepsilon_1 = \varepsilon_4 = \dfrac{N(\theta_0+\Delta\theta)}{EA} + \dfrac{M(\theta_0+\Delta\theta)}{EI}\dfrac{t}{2} \\ \varepsilon_2 = \varepsilon_3 = -\nu\left(\dfrac{N(\theta_0)}{EA} + \dfrac{M(\theta_0)}{EI}\dfrac{t}{2}\right) \end{cases} \tag{5.6}$$

Substituting the equations (5.6) in the (5.3), the voltage variation is:

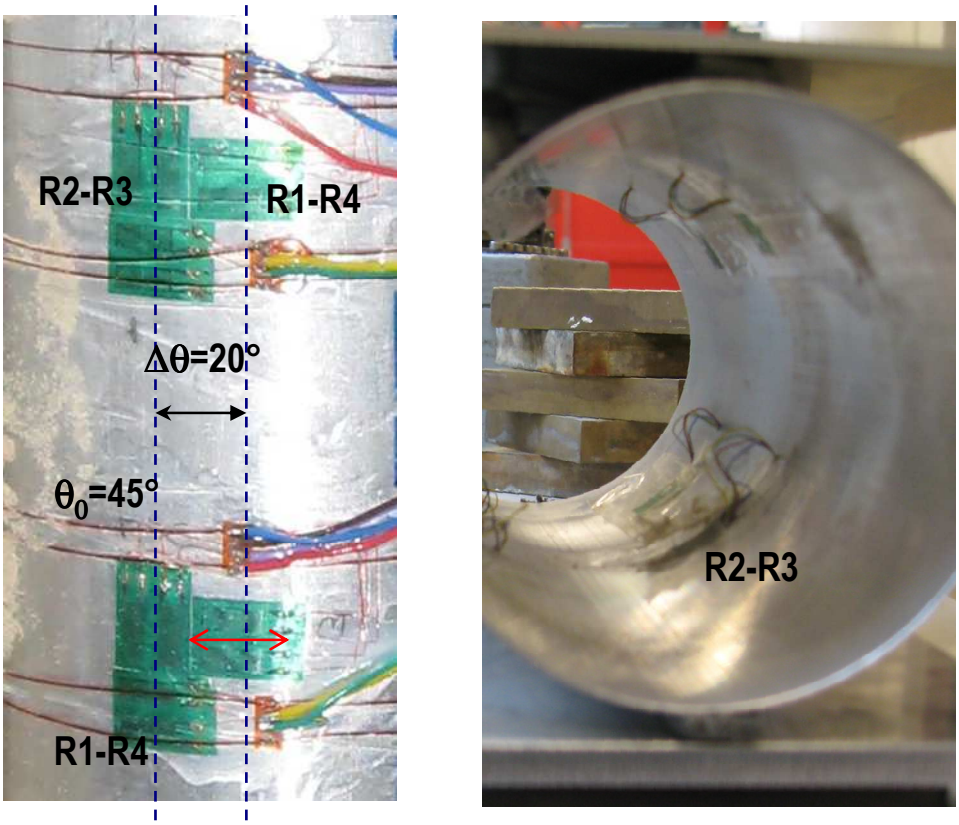

Fig 5.8: Position of the transducers: a) external and b) internal surface

$$\left[\frac{\Delta V_{CD}}{V_{AB}}\right]_{HS} = \nu\frac{K}{2}\left(\frac{N(\theta_0)}{EA}+\frac{M(\theta_0)}{EI}\frac{t}{2}\right)+\frac{K}{2}\left(\frac{N(\theta_0+\Delta\theta_0)}{EA}+\frac{M(\theta_0+\Delta\theta_0)}{EI}\frac{t}{2}\right) \quad (5.7)$$

In this case the voltage variation measured by the galvanometer was not directly proportional to hoop load, but was dependent both from hoop load and bending moment. In order to evaluate the normal stress, the hoop load was evaluated from the equation (5.7) but using the readings of bending moment for each transducers in the same position. The (5.7) can be written as:

$$\left[\frac{\Delta V_{CD}}{V_{AB}}\right]_{HS} = \nu\frac{K}{2}\frac{N(\theta_0)}{EA}+\nu\frac{K}{2}\frac{M(\theta_0)}{EI}\frac{t}{2}+\frac{K}{2}\frac{\alpha_{HS}N(\theta_0)}{EA}+\frac{K}{2}\frac{\alpha_{BM}M(\theta_0)}{EA}\frac{t}{2} \quad (5.8)$$

α_{BM} and α_{HS} are:

$$\begin{cases} \alpha_{BM} = \dfrac{M(\theta_0 + \Delta\theta_0)}{M(\theta_0)} \\ \alpha_{HS} = \dfrac{N(\theta_0 + \Delta\theta_0)}{N(\theta_0)} \end{cases} \tag{5.9}$$

These factors have a constant value for each loading condition applied on the tube. The bending moment addends are translated at first term:

$$\left[\frac{\Delta V_{CD}}{V_{AB}}\right]_{HS} - \frac{K}{2}\frac{M(\theta_0)}{EI}\frac{t}{2}(\nu + \alpha_{BM}) = \frac{K}{2}\frac{N(\theta_0)}{EA}(\nu + \alpha_{HS}) \tag{5.10}$$

Substituting the equation (5.5) in the (5.10), the result is:

$$\left[\frac{\Delta V_{CD}}{V_{AB}}\right]_{HS} - \frac{(\nu + \alpha_{BM})}{2}\left[\frac{\Delta V_{CD}}{V_{AB}}\right]_{BM} = \frac{K}{2}\frac{N(\theta_0)}{EA}(\nu + \alpha_{HS}) \tag{5.11}$$

and dividing by ($\nu+\alpha_{HS}$):

$$\frac{\left[\dfrac{\Delta V_{CD}}{V_{AB}}\right]_{HS} - \dfrac{(\nu + \alpha_{BM})}{2}\left[\dfrac{\Delta V_{CD}}{V_{AB}}\right]_{BM}}{(\nu + \alpha_{HS})} = \frac{K}{2}\frac{N(\theta_0)}{EA} \tag{5.12}$$

The hoop load is not directly proportional to the readings but through the bending moment readings and is dependent from ν and α_i (i=BM; HS), which are dependent from loading condition.

5.5.3 Displacements measuring device (LVDT)

The displacement of the surface during centrifuge tests is measured by linear variable differential transformers (LVDTs) manufactured by Sangamo. The transducers were constituted by a cylindrical body and by a thin metallic stick (fig.5.5d) that moved coaxially to the cylinder that was

fixed. Every stick movement corresponded to a voltage variation recorded by the acquisition system. Each transducer weighs about 36grams. LVDTs are placed in two gantries put longitudinally above the model.

5.6 CALIBRATION OF THE INSTRUMENTS

All the instruments are calibrated using a data logger with the software Dasylab 9.0. During the calibration, and subsequently during the tests, two different Junction boxes are used: one for the accelerometers and the other for strain gauges and LVDTs.

5.6.1 Accelerometers

The accelerometers are calibrated using a calibrator, which excites the instruments with a sinusoidal input having acceleration amplitude of +/-1 g.

Table5.5 : Accelerometers calibration factor

Layout name	*Calibration factors*			
	T-1	***T-2***	***T-3***	***T-4***
ACC1	9.447	8.942	9.183	9.021
ACC3	8.145	8.287	8.221	8.287
ACC4	4.823	4.877	4.854	4.797
ACC5	7.146	7.042	7.230	7.153
ACC6	8.495	8.254	8.495	8.459
ACC7	7.207	7.217	7.334	7.334
ACC8	7.917	7.737	7.933	7.872
ACC9	8.227	8.106	8.090	8.188
ACC10	7.033	7.006	7.030	7.104
ACC11	8.188	8.220	8.188	8.287
ACC12	6.853	6.876	6.864	7.781
ACC13	7.878	7.664	6.493	6.982
ACC14	8.106	8.058	8.122	8.090
ACC15	6.511	6.482	7.752	6.513
ACC16	4.581	4.486	4.541	4.551

A constant calibration factor is obtained assuming a linear response for the relevant acceleration range. The calibration factor was calculated before each test using the expression:

$$CF = \frac{1}{\left\{0{,}981\left[V_{\max} - \left(\frac{V_{\max} - V_{\min}}{2}\right)\right]\right\}} \tag{5.13}$$

In which Vmin and Vmax were the maximum and minimum voltage given from the calibration readings. All the calibration factor used test by test was reported in the table.5.5 The values were generally similar and were variable between 4.5 and 9.5.

5.6.2 Strain Gauges

5.6.2.1 Cambridge calibration

For the strain gauges calibration it is necessary to refer to a simple load case of which the closed form solution of bending moment and hoop load is known. Timoshenko (1961) gives the values of bending moment and hoop stress depending from the angle theta for some load cases. The θ angle is considered positive clockwise from the tunnel top and is limited in the interval 0-π, because is symmetric from π to 2π. The formulas are referred to a ring of radius R compressed by two forces P acting along a diameter:

$$M = PR\left[\left(1 - \frac{I}{AR^2}\right)\frac{1}{\pi} - \frac{\sin\theta}{2}\right] \tag{5.14}$$

$$H = -\frac{P}{2}\sin\vartheta \tag{5.15}$$

The theoretical loading conditions were recreated through an aluminium frame with a fixed lower plate and a mobile upper plate on which the load is put. The tunnel is placed in the frame (fig.5.9a) and is loaded and unloaded with a constant load increment. During calibration the tube is located into the loading frame both with the same orientation which it has

in the model (0 degrees or ‘vertical’) and rotated of +10 degrees from the ‘vertical’ position. Four different series of measurements (table 5.6) have been performed to minimize the differences between the theoretical model and real case (imperfect contact between the upper plate and the tunnel due to linings (fig.5.9b); contact between tunnel and lateral columns at the end of the frame during the load).

Table 5.6: Measurement series

Load series	*Duxeal Plate/ tunnel*	*Check contact with lateral columns*	*Load increment*	*Maximum load*
1	No	No	0.125kg	2kg
2	Yes	No	0.64kg	3.2kg
3	Yes	Yes *(no contact)*	0.64kg	3.2kg
4	Yes	Yes *(no contact)*	0.64kg	3.2kg

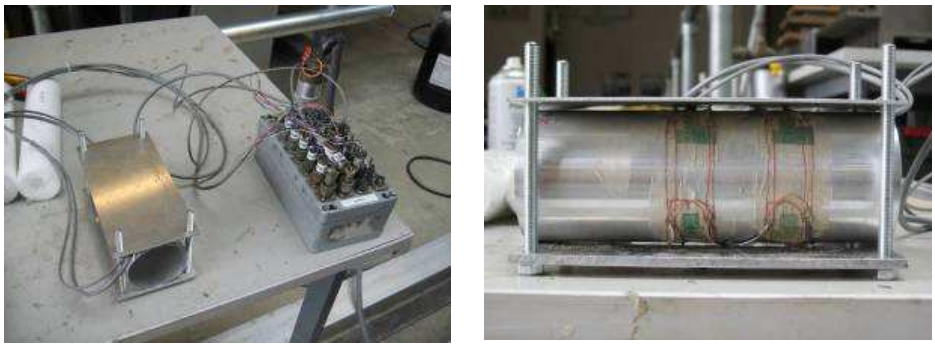

(a) *(b)*

Fig.5.9. Cambridge calibration: a) Frame for calibration; b) Imperfect contact tube/frame

5.6.2.2 Naples calibration

After the calibration at Cambridge University, a new calibration measurements was made at Naples University: the reason of the new calibration was that in some cases the calibration series performed at Cambridge University didn’t give an unambiguous factor. For the new calibration a new load layout was considered in order to maximize the stresses; a higher value of the maximum load was chosen to check the

linear behaviour of lining stresses in a larger field of load. A metallic frame was built in order to apply longitudinally on the lining a line of load (fig.5.10a). To avoid the imperfect contact between the frame and the lining due to the cables around the tube, some steel engravings were made on the internal side of the frame (fig.5.10b).

(a)

(b)

(c)

Fig.5.10: Naples calibration: a) metallic frame; b) steel engravings; c) load track for condition 2

Two different load conditions were applied on the lining, in order to extend the stress field and give a safer calibration factor:

1. *Load condition 1*: the tunnel was subjected to a load similar to Cambridge calibration, relative to 0 degrees, using the frame as a line of load, directly applied on the top of the tube. The transducers position was exactly the same position used during the centrifuge tests ($\theta=\pi/4+n\pi/2$; n=0,1,2,3). The equations for the calculation of bending moments and hoop loads are the (5.14) and (5.15)
2. *Load condition 2*: a small piece of aluminium channel (fig.5.10c) was used in order to perform a different loading condition (fig.5.11). The channel created two loading lines on the top and two ones on the bottom of the lining, with an aperture angle referred to the tunnel centre of around 60 degrees. The strain gauges position was rotated of 45 degrees compared to test position, in order to have the maximum values of bending moment and hoop stress.

The loading field in both the loading cases was larger than in Cambridge calibration: the maximum load was around 6kg, and the loading steps were not constant. In fig.5.11 the layout of the two kind of tests carried out was reported, and some pictures during the calibration phase in Naples:

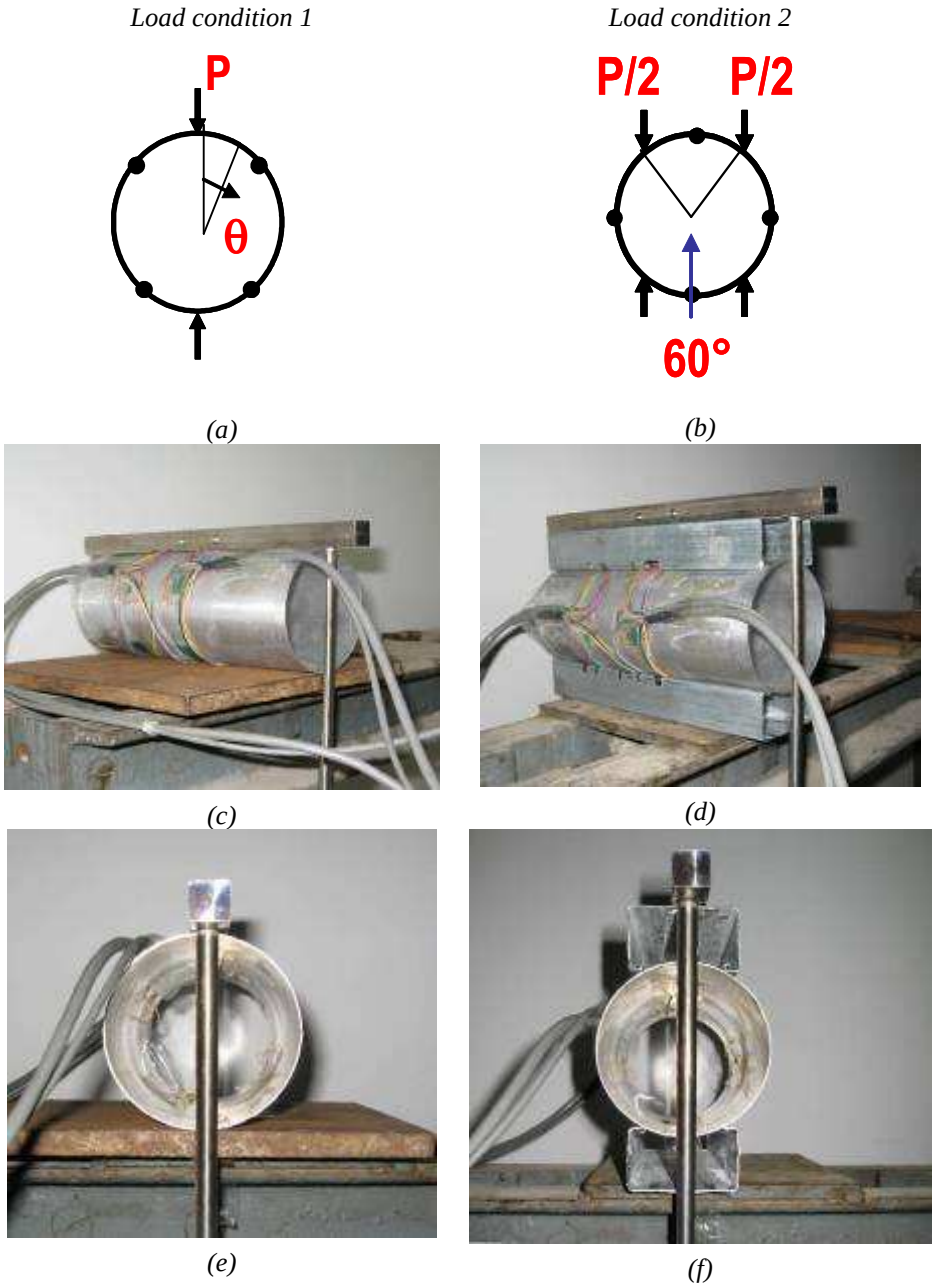

Fig.5.11: Calibration phases in Naples

The different load geometry and transducers position generated two different stress field applied on the lining. This stress distributions were got by the superimposition of simple cases of loading (fig.5.12), obtained by the Timoshenko's theory (1961) and directly given by the Roark's formulas (2002).

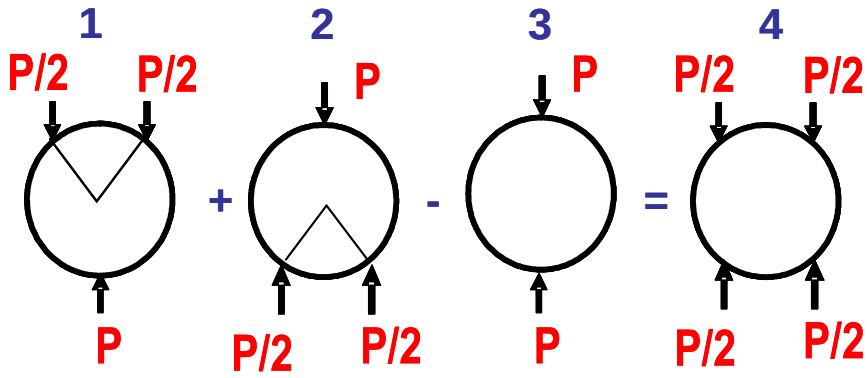

Fig.5.12: Superimposition of the simple load cases to obtain load condition2

The formulas for bending moment and hoop load relative to the load layout 1 of the fig.5.12 are (Roark, 2002):

$$M = PR\left\{\left[\sin\frac{\varphi}{2}\left(\sin\frac{\varphi}{2}-\pi+\frac{\varphi}{2}\right)+1-\frac{I}{AR^2}\left(1+\cos\frac{\varphi}{2}\right)\right]+\sin^2\frac{\varphi}{2}(1-\cos\theta)-\left(\sin\theta-\sin\frac{\varphi}{2}\right)\left\langle\theta-\frac{\varphi}{2}\right\rangle^0\right\} \quad (5.16)$$

$$N = P\left(\frac{\sin\frac{\varphi}{2}}{\pi}-\sin\theta\left\langle\theta-\frac{\varphi}{2}\right\rangle^0\right) \quad (5.17)$$

$$\begin{cases}\left\langle\theta-\frac{\varphi}{2}\right\rangle^0=0 & \theta<\frac{\varphi}{2}\\ \left\langle\theta-\frac{\varphi}{2}\right\rangle^0=1 & \theta>\frac{\varphi}{2}\end{cases} \quad (5.18)$$

In the (5.16) and (5.17) φ is the angle between the two loading point at P/2, I is the inertia moment, A is the area of cross section and R is the radius of the tube. In the fig.5.13 the bending moment and hoop load distributions around the tunnel for a unity external force were reported. The measurements points in the load condition 1 were at 45 degrees and 135 degrees, and for these locations the bending moment was close to zero (fig.5.13a) . Instead in the load condition 2 the location were at 0 degrees and 180 degrees, in which the bending moments reached the maximum value (fig.5.13b). The hoop load in the condition 1 had values which were around the half of maximum value (fig. 5.13c), whereas in the condition 2 the hoop load was zero at 0 degrees and gave the maximum value at 180 degrees (fig.5.13d).

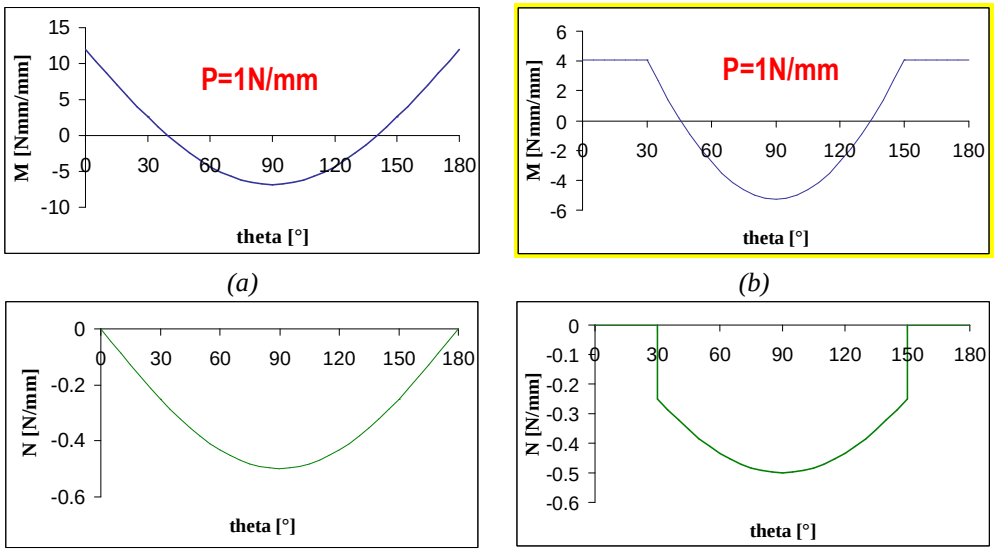

Fig.5.13 Load distribution around the tunnel: bending moment a) load condition 1 and b) load condition 2; hoop load c) load condition 1 and d) load condition 2

Bending moment were calculated from for every load step and strain gauges position (θ angle), considering both the calibration procedures. These values are plotted in an x-y graph against the voltage readings to obtain the linear fitting equation and R^2 value for every transducer. All load series curves for every strain gauge are introduced in a graph to get a single

calibration factor. Some load series have been not considered to obtain a correlation with $R^2 > 0.80$. The calibration factor values are written in the table 5.7. All the graphs are plotted in the fig.5.14.

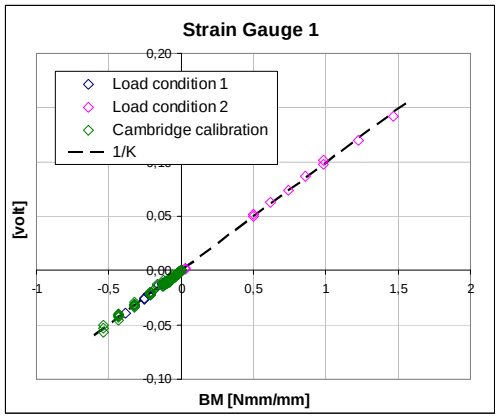

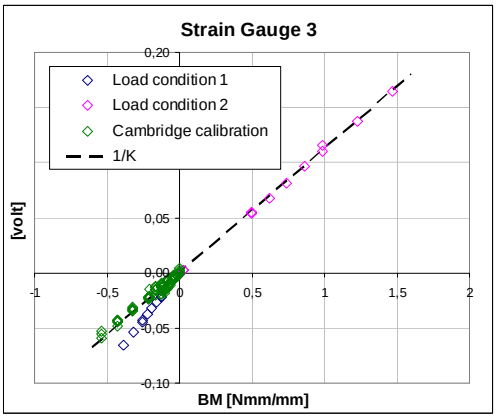

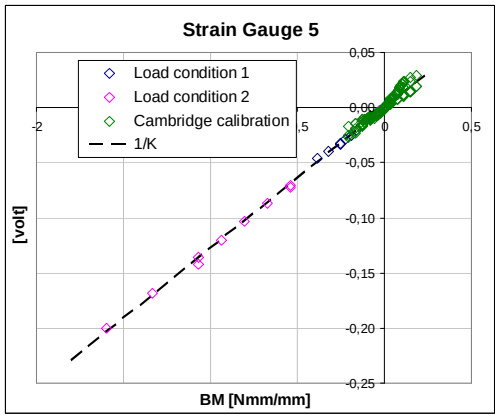

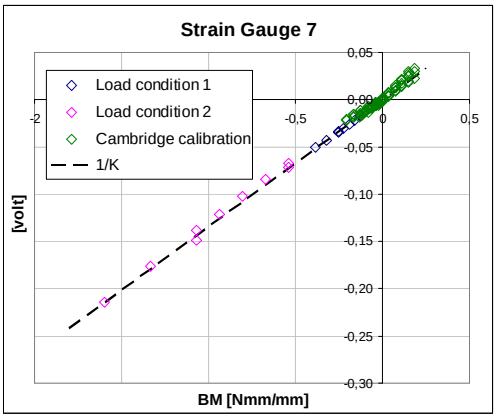

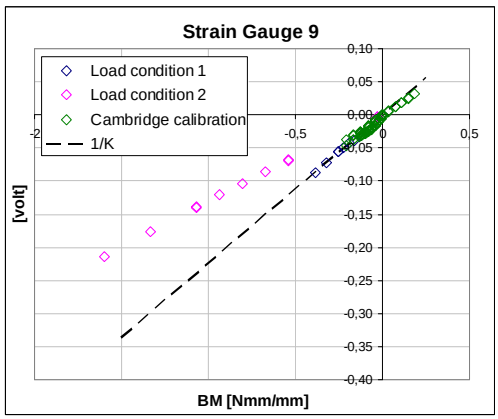

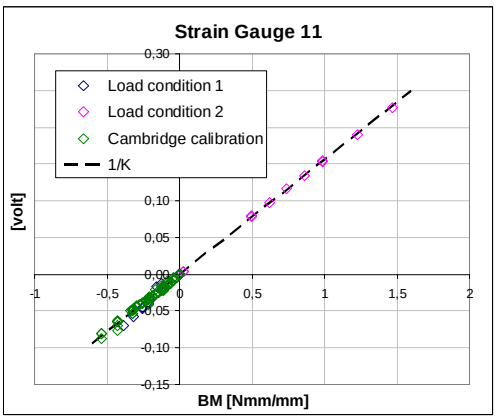

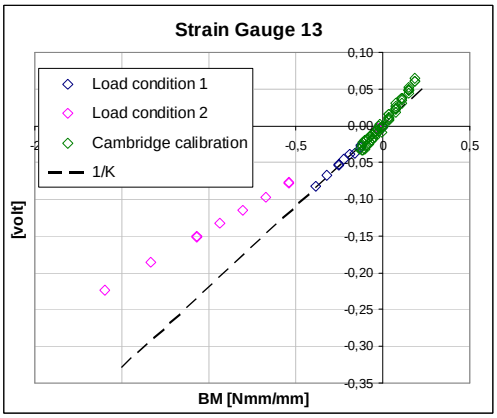

Strain gauge 15
MALFUNCTION

Fig.5.14 Bending moment vs calibration readings

Table 5.7: Calibration factors for bending moment transducers

Transducers number	*Section*	*Calibration factor*
1	1	10.1
3	1	9.24
5	1	7.87
7	1	7.51
9	2	4.44
11	2	6.19
13	2	4.56
15	2	?

For the hoop load, a same comparison between the Cambridge calibration data and the Naples calibration data was done, in order to obtain a reliable factor, using the equation (5.12). The calibration factor values are written in the table 5.8. All the graphs are plotted in the fig. 5.15.

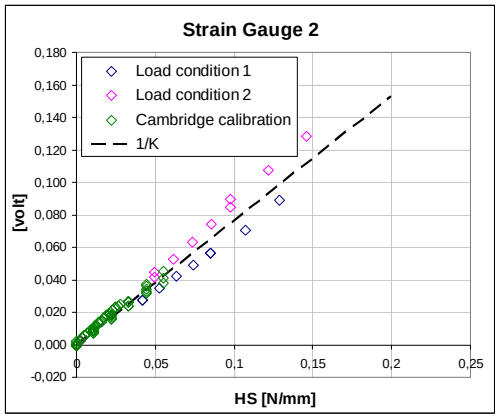
Strain Gauge 2
Load condition 1
Load condition 2
Cambridge calibration
1/K
[volt]
HS [N/mm]

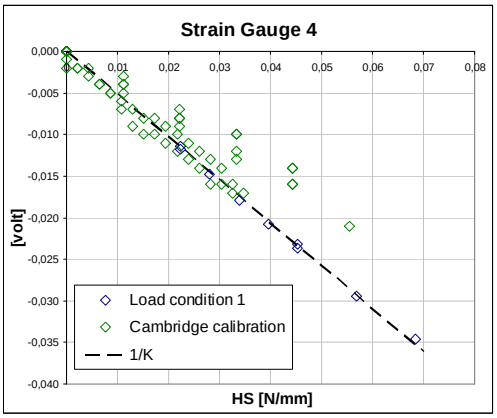
Strain Gauge 4
Load condition 1
Cambridge calibration
1/K
[volt]
HS [N/mm]

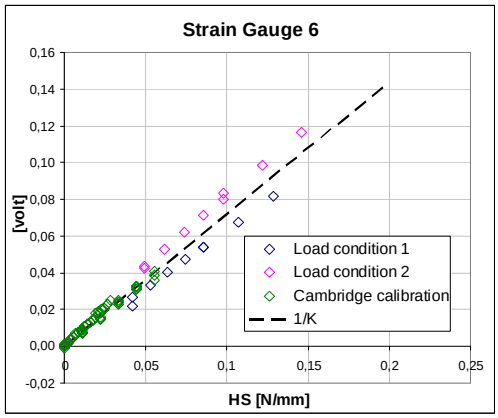
Strain Gauge 6
Load condition 1
Load condition 2
Cambridge calibration
1/K
[volt]
HS [N/mm]

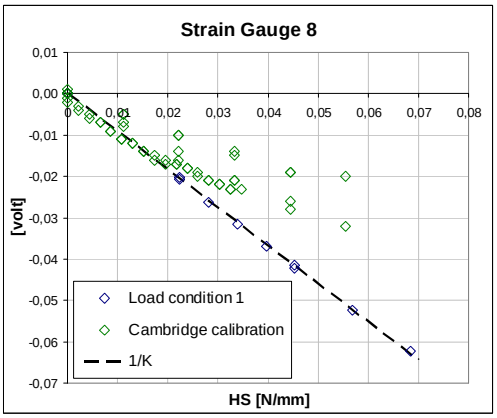
Strain Gauge 8
Load condition 1
Cambridge calibration
1/K
[volt]
HS [N/mm]

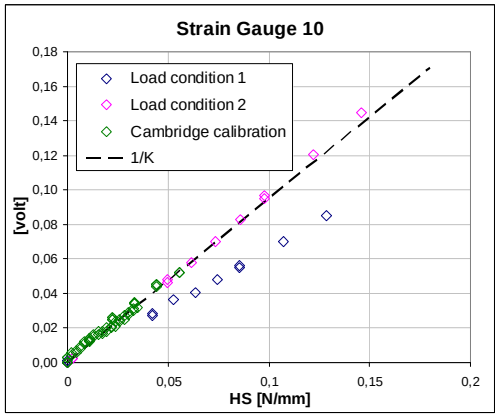
Strain Gauge 10
Load condition 1
Load condition 2
Cambridge calibration
1/K
[volt]
HS [N/mm]

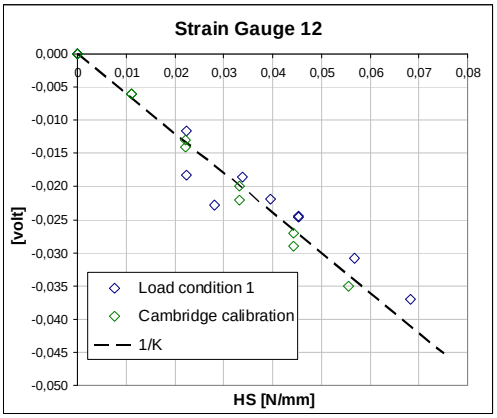
Strain Gauge 12
Load condition 1
Cambridge calibration
1/K
[volt]
HS [N/mm]

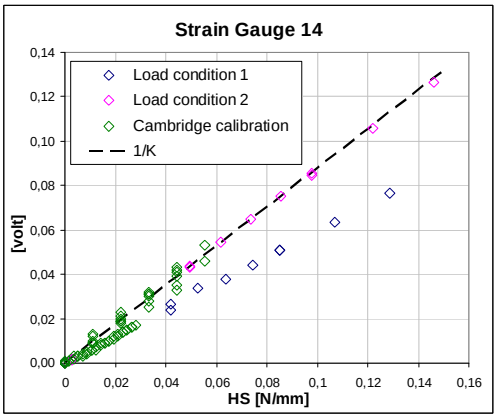

Strain gauge 16
MALFUNCTION

Fig.5.15 Hoop load vs calibration readings

Table 5.8: Calibration factors for hoop stress transducers

Transducers number	*Section*	*Calibration factor*
2	1	1.31
4	1	-1.94
6	1	1.39
8	1	-1,09
10	2	1,05
12	2	-1,66
14	2	1,14
16	2	?

5.6.3 LVDT

The LVDT's were calibrated using a device in which there was a calliper connected with a small platform vertically movable. The cylindrical body of the LDVT's was blocked, instead the metallic stick touched the mini platform and moved with itself. For every measured movement of the platform, a different reading was given by the instruments. The displacements versus the readings were put in a graph in order to find a reliable calibration factor. In the fig the graphs for the LVDT 045 and 059 were showed: all the data were interpolated with a linear equation, showed in each graph with the R^2 value. Both the LVDT's data gave an

unambiguous calibration factor because R^2>0,99, and the values was reported in fig. 5.16.

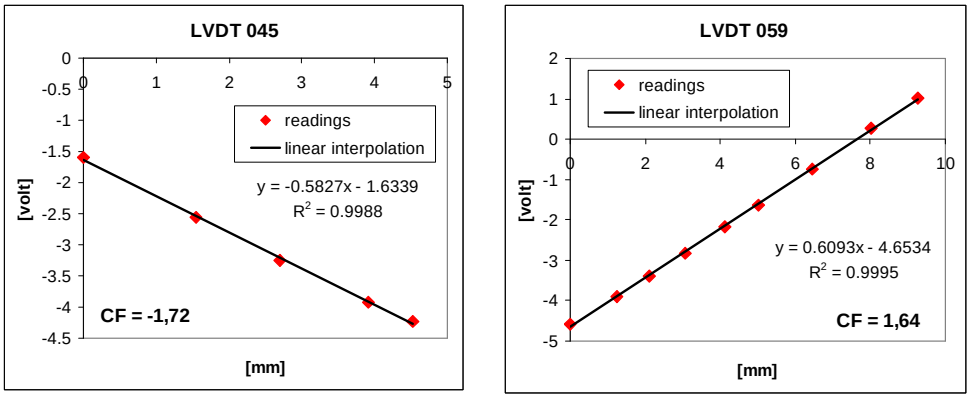

Fig. 5.16: Readings for LVDT's calibration

5.7 MODEL PREPARATION TECNIQUES

5.7.1 Container preparation

Firstly the Laminar Box is cleaned from the remains of previous test. The container is blocked with little columns at the corners of the box to prevent the movements during the model preparation, transportation and assembly. The grease layer between the box and internal rubber is removed and a new layer is replaced and is separated by the rubber with a cellophane coat. The internal rubber is stretched and is fixed at the box by aluminium tape (fig.5.17a). The lodging for the external accelerometers is placed by superglue on the lateral surface of the box. A paper ruler is stuck on the internal wall to control the level of the sand during the pouring phase. Before pouring the sand, the external walls of the box are protected by black plastic liners that are removed at the end of the deposition (fig. 5.17b). Photographs are taken during every step of the model container preparation.

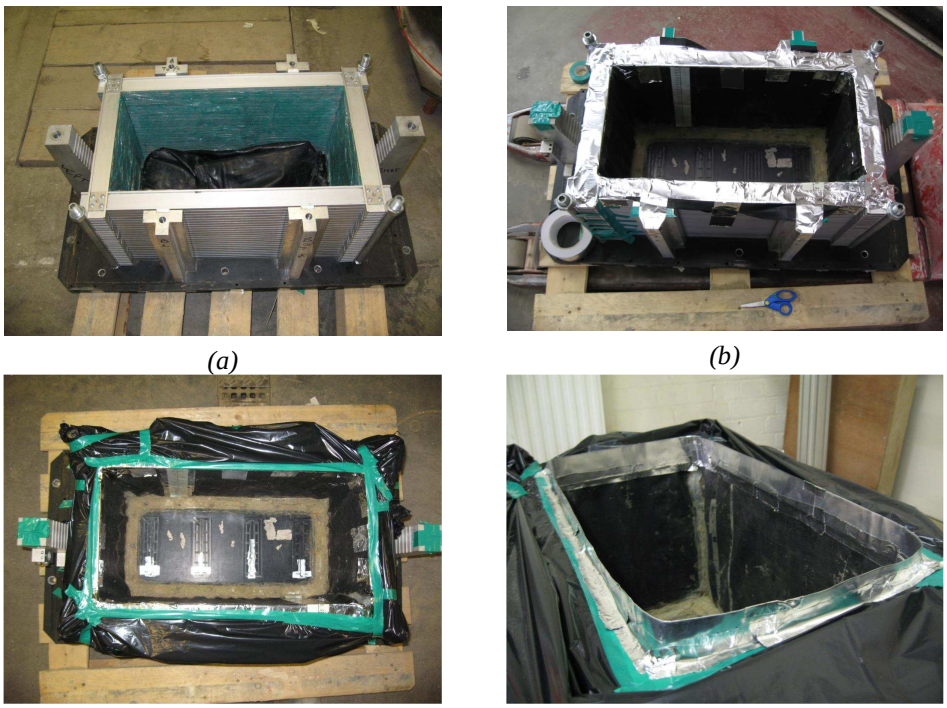

(a) *(b)*

(c) *(d)*

Fig.5.17: Container preparation;
a) greased internal laminar surface; b)internal rubber fixed at the box; c) black plastic pouring protection; d) box border protection for dense model

5.7.2 Sand pouring

The sand is poured into the strongbox through a hopper system, for the "loose sand models" (fig. 5.18a). The void ratio is therefore controlled by the height of the hopper and the opening of the slot at the bottom that control the rate of sand's flow. Trial test were performed in advance to calibrate these values. After the required height of sand layer had been achieved, the surface of sand is levelled by a modified vacuum cleaner. After the model is ready, the profile of the model is also measured.

The sand is poured into the strongbox through an automatic hopper system, for "dense sand models" (fig. 5.18b). The pouring of the sand is controlled by a computer, with whom the user can change the position of the hopper along 3 axes (2 horizontal and 1 vertical) and open or close the

nozzle. The parameters that play a crucial role in order to obtain the desired density are the drop height and the aperture diameter. To control the sand's flow, some trial tests were performed. Once the drop height and the aperture diameter are fixed, it's necessary to find the input coordinates of the container and then start the pouring. During every step the sand is poured first longitudinally and then transversally with an offset of 15mm. At the end of the step the hopper is lifted up by one layer (the height that corresponds to the thickness of the layer poured in every step). In order to obtain the desired density two solutions were performed during the pouring phase: firstly two small sieves are put on a muzzle under the aperture to spread the concentrated jet of sand exiting the nozzle over a wider area; second a thick aluminium barrier is fixed around the top of the box in the internal side in order to prevent the accumulation of the sand on the box borders (fig.5.17d). Once the model is ready, the profile of the model is also measured.

(a) *(b)*

Fig.5.18: Sand pouring:
a) hopper for loose sand models; b) automatic sand pourer

5.7.3 Accelerometers and tunnel placement

A layout drawing of the model is done for each test. In this drawing the position and the direction of every accelerometer is shown. According to the indications of the layout, the accelerometers are placed in the model and photographs are taken for every level (fig. 5.19c, e & f). According to layout drawing, the tunnel is placed in the model at the tube bottom depth (fig. 5.19d). A little square plate is placed at each end of the tunnel (fig. 5.19b) to avoid sand to enter during the test (the tunnel tube is shorter than the box width by 50 mm). A black plastic liner patch is inserted between the tunnel and the plate with a layer of grease to avoid any side friction (fig. 5.19a).

5.8 CENTRIFUGE PREPARATION

5.8.1 Balance calculation

When the sand pouring is finished, the total weight of the used sand is measured, in order to calculate an accurate balance of the centrifuge arm. It includes a list of all the masses and centre of masses for every component of the centrifuge package obtaining the necessary counterweight to put in the centrifuge. The tests are only carried out if the total mass of the package, which is checked just before loading, to confirm the calculations.

5.8.2 Pre-flight operation

Firstly the counterweight is loaded onto the centrifuge on the red end (fig. 5.20a). Secondly the SAM actuator without the model is installed on the beam on the blue end. Then the model is put in the SAM (fig. 5.20b) and every cable is connected to the Junction boxes, checking that all the transducers are in the right position and the cable is firmly tied. Once the model is in the centrifuge, the data acquisition and triggering system and the pressure in the accumulator required to activate SAM fast-acting clutch is checked before starting test.

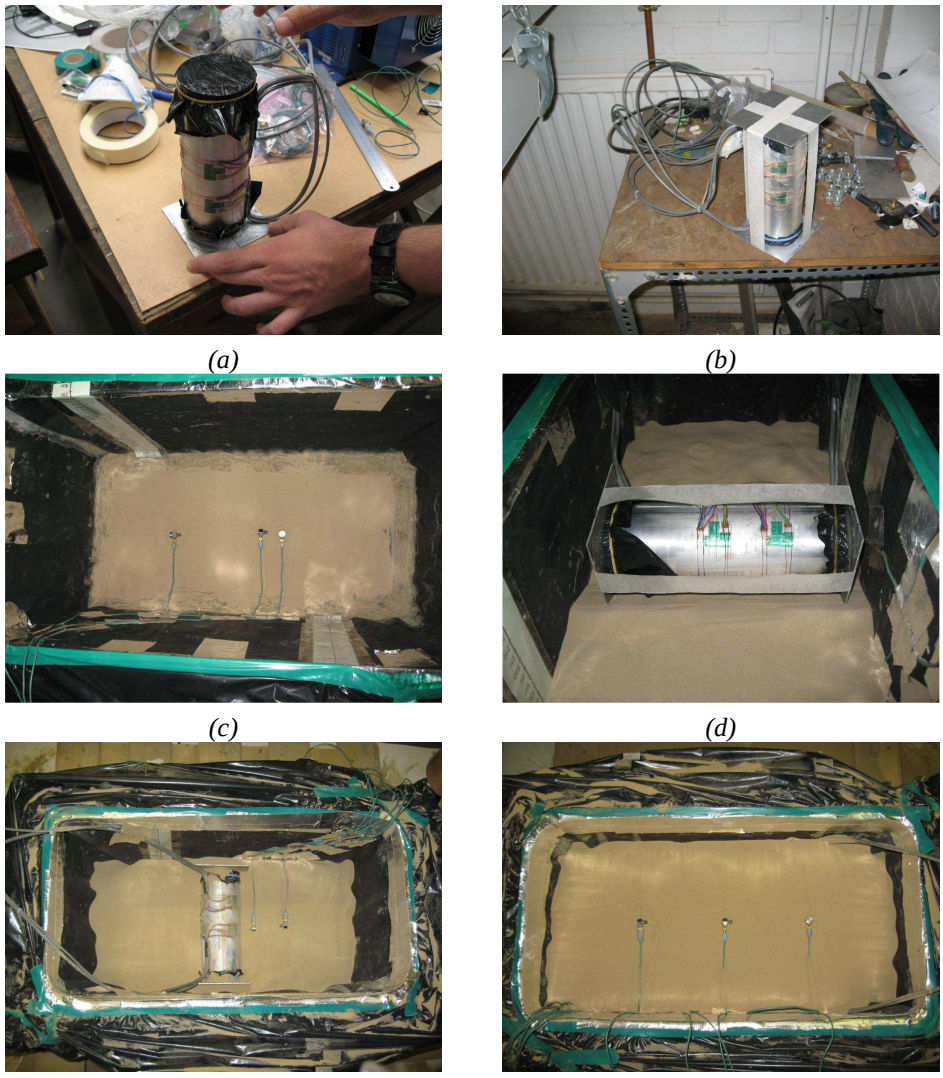

(a) *(b)*

(c) *(d)*

(e) *(f)*

Fig.5.19 Model preparation.
Tunnel preparation: a) black plastic and grease layer, b) protection plates; Instruments placement: c) first accelerometers level, d) tunnel placement, e) accelerometer level at tunnel depth, f) last accelerometers level

(a) *(b)*

Fig.5.20: Centrifuge loading of a) the counterweight and b) the model

5.8.3 Test procedure

Before starting the flight the corner columns are removed. When the test started the centrifuge is swung up in steps of 10g, 20g, 30g, 40g, 50g, 60g, 70g and 80g. At each stage the readings of strain gauges transducers are noted. Then the first earthquake is fired. After 4 earthquakes at 80g, the centrifuge is slowed down at 40g to fire other earthquakes. The model is permanently monitored through a camera installed on the beam. When the test is finished the model container is taken out of the pit and the profile of the model is measured again. The channels for the measurements are 32 in all: 16 for the accelerometers and 16 for strain gauges or LVDTs. Data is plotted out channel by channel and recorded in a text file for every earthquake and for the swing up phase.

All the data is acquired using the software CDAQS (Centrifuge Data AcQuisition System), a system that minimizes the noise derived by electrical interference of SAM system. The earthquake data has a sampling rate of 4 kHz.

5.9 MODELS DESCRIPTION

In order to carry out all the test programme at Schofield Centre, five months were necessary, from July 2007 to November2007. A timing of the work during this period is reported in the tab.5.9:

Table 5.9 : Timing of the centrifuge work

Month (2007)	**Operation**
July	1. Preparation T-2 model 2. Accelerometers calibration (T-2)
August	3. T-2 test execution 4. Tunnel calibration (Load series 1)
September	5. Preparation T-4 model 6. Accelerometers calibration (T-4) 7. LVDT calibration 8. Tunnel calibration (Load series 2 and 3) 9. T-4 test execution
October	10. Preparation T-3 model 11. Accelerometers calibration (T-3) 12. Tunnel calibration (Load series 4) 13. T-3 test execution
November	14. Preparation T-1 model 15. Accelerometers calibration (T-1) 16. T-1 test execution

The tests executions are not chronological, as from the programme, therefore the LVDT's was used only from the second test. A brief description of the models characteristics are reported in the following paragraphs.

5.9.1 Centrifuge test T-1

A model of dense sand and shallow tunnel is chosen for the fourth and last test. Model layout is plotted in fig.. The internal available volume of the box (without the volume of the tunnel) is $3.385*10^7$ mm^3 and the weight of the used sand is 52.4kg. These values give a void ratio of 0.712 and a relative density of 75.3%. A total of 31 transducers are used in this test: 16 accelerometers, 13 strain gauges and 2 LVDTs. The accelerometers layout is shown in the fig.5.21. The model was swung up two times: in the first time the model was accelerated to 80g, but was slowed down because the SAM didn't work; when the dynamic actuator was repaired, the model

was swung up for the second time and all the earthquake were performed. Four earthquakes are fired at 80g and one at 40g. All earthquakes features are written in the table 5.10.

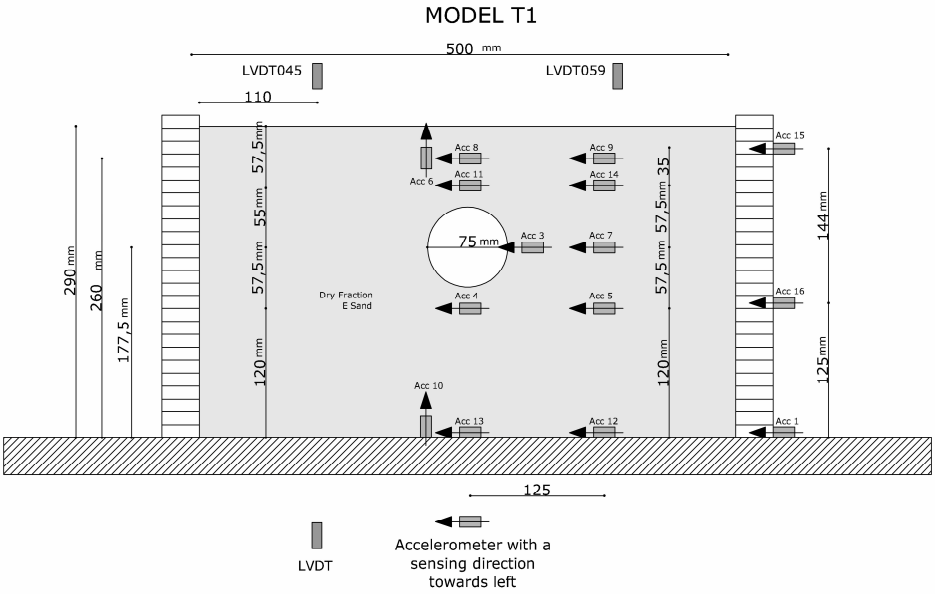

Fig.5.21: Centrifuge model T-1

Table 5.10: Earthquakes fired in the T-1 test

Earthquake	*G level*	*frequency*	*time*	*offset*
1	80	30 Hz	0.4 s	0.5 V
2	80	40 Hz	0.4 s	1 V
3	80	50 Hz	0.4 s	1.2 V
4	80	60 Hz	0.4 s	1.5 V
5	40	50 Hz	0.4 s	1.5 V

5.9.2 Centrifuge test T-2

A model of loose sand and shallow tunnel is chosen for the first test. Model layout is plotted in fig.. The internal available volume of the box (without the volume of the tunnel) is $3.39*10^7$ mm^3 and the weight of the used sand is 48.52 kg. These values give a void ratio of 0.849 and a relative density of 41.2%. A total of 31 transducers are used in this test: 15 accelerometers and 16 strain gauges. The accelerometers layout is shown in

the fig.5.22. Four earthquakes are fired at 80g and one at 40g. All earthquakes features are written in the table 5.11.

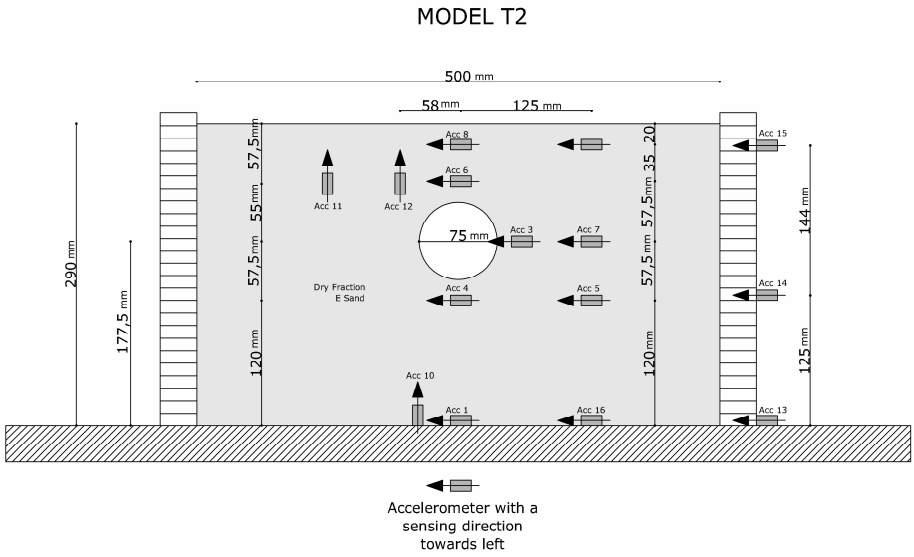

Fig.5.22: Centrifuge model T-2

Table 5.11: Earthquakes fired in the T-2 test

Earthquake	*G level*	*frequency*	*time*	*offset*
1	80	30 Hz	0.4 s	0.5 V
2	80	40 Hz	0.4 s	1 V
3	80	50 Hz	0.4 s	1.2 V
4	80	60 Hz	0.4 s	1.5 V
5	40	50 Hz	0.4 s	1.5 V

5.9.3 Centrifuge test T-3

A model of dense sand and deep tunnel is chosen for the third test. Model layout is plotted in fig.. The internal available volume of the box (without the volume of the tunnel) is $3.32*10^7$ mm^3 and the weight of the used sand is 51.5 kg. These values give a void ratio of 0.71 and a relative density of 75.9%. A total of 31 transducers are used in this test: 16 accelerometers, 13 strain gauges and 2 LVDTs. The accelerometers layout

is shown in the fig.5.23. Four earthquakes are fired at 80g and one at 40g. All earthquakes features are written in the table 5.12.

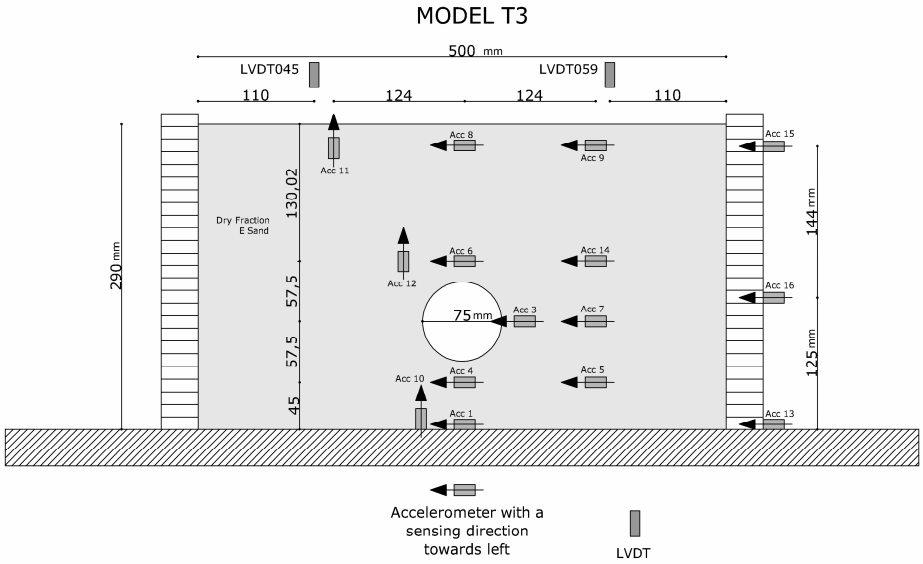

Fig.5.23: Centrifuge model T-3

Table 5.12: Earthquakes fired in the T-3 test

Earthquake	*G level*	*frequency*	*time*	*offset*
1	80	30 Hz	0.4 s	0.5 V
2	80	40 Hz	0.4 s	1 V
3	80	50 Hz	0.4 s	1.2 V
4	80	60 Hz	0.4 s	1.5 V
5	40	50 Hz	0.4 s	1.5 V

5.9.4 Centrifuge test T-4

A model of loose sand and deep tunnel is chosen for the second test. Model layout is plotted in fig.. The internal available volume of the box (without the volume of the tunnel) is $3.39*10^7$ mm^3 and the weight of the used sand is 48.48 kg. These values give a void ratio of 0.850 and a relative density of 40.8%. A total of 31 transducers are used in this test: 15 accelerometers, 13 strain gauges and 2 LVDTs. The accelerometers and

LVDTs layout is shown in the fig. 5.24. Four earthquakes are fired at 80g and two at 40g in two different flights: in the first flight 4 earthquake at 80g and 1 at 40g were fired, instead in the second flight only one earthquake at 40g was performed. All earthquakes features are written in the table 5.13.

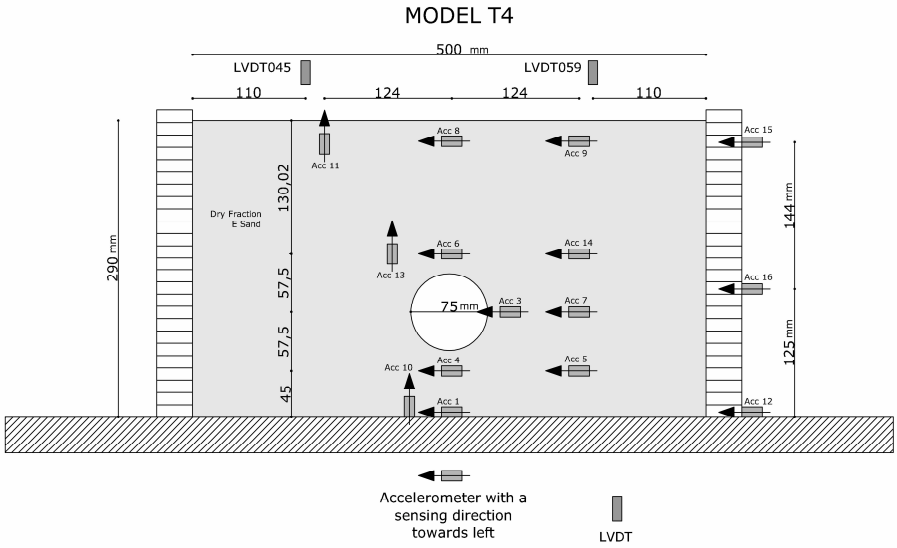

Fig.5.24: Centrifuge model T-4

Table 5.13: Earthquakes fired in the T-4 test

Earthquake	*flights*	*G level*	*frequency*	*time*	*offset*
1	1	80	30 Hz	0.4 s	0.5 V
2	1	80	40 Hz	0.4 s	1 V
3	1	80	50 Hz	0.4 s	1.2 V
4	1	80	60 Hz	0.4 s	1.5 V
5	2	40	50 Hz	0.4 s	1.5 V
6	2	40	40 Hz	0.4 s	1.25 V

5.10 POST-FLIGHT OBSERVATION

When the flight is ended the model was unloaded from the centrifuge arm. The sand surface was clearly settled in each tests as it was observed visually. In the fig. 5.25 the sand surface after the flight is showed for every

test, clarifying that the soil exhibited a larger displacement near the box boundary, especially at the model side where the strain gauges cables are located. Probably during the pouring phase the cables created an obstacle for the sand's flow, causing a shadow zone in which the sand had a lower density. Therefore this effects were clearer in the dense models, because the sand jet coming from the automatic pourer is only vertical and the obstacles cannot be avoided, compared to manual deposition.

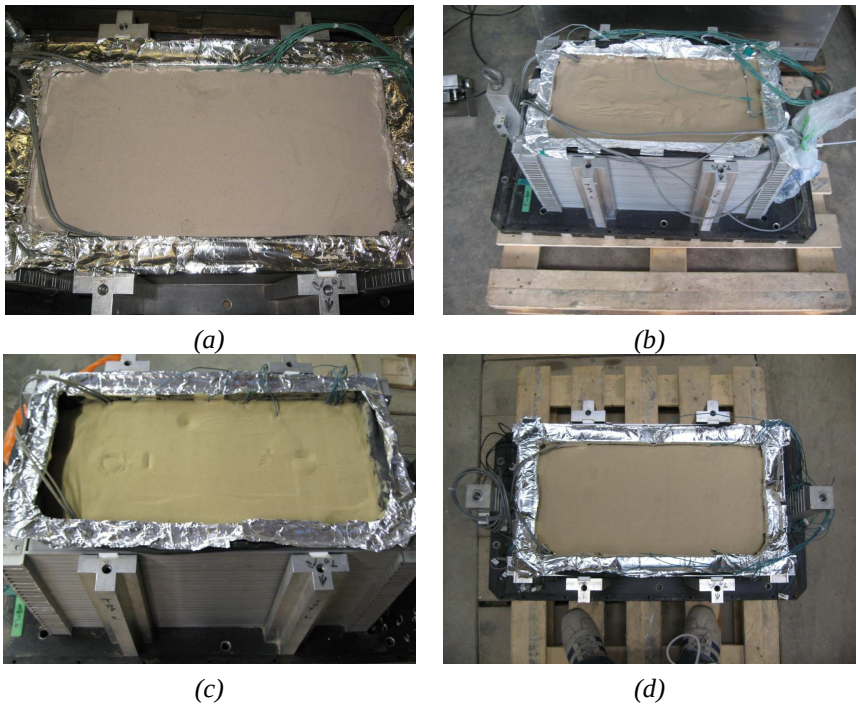

(a) *(b)*

(c) *(d)*

Fig.5.25: Sand surface after the test: a) T-1; b) T-2; c) T-3; d) T-4

Moreover both the dense models showed a larger displacement in a particular zone, located near the back of the box, above the tunnel (fig.5.26a,b). This point corresponded to the tunnel end, in which the lining was closed using a plastic liner and a small plate. Successively when the box was empted from the model sand, it was observed that a little amount of sand passed between the plastic liner and the plate, but not inside the cavity (fig.5.26c,d). Using a ruler the settlement was measured along two parallel longitudinal lines. The average value of the displacements,

compared to initial sand surface depth, was showed for every test in the fig..

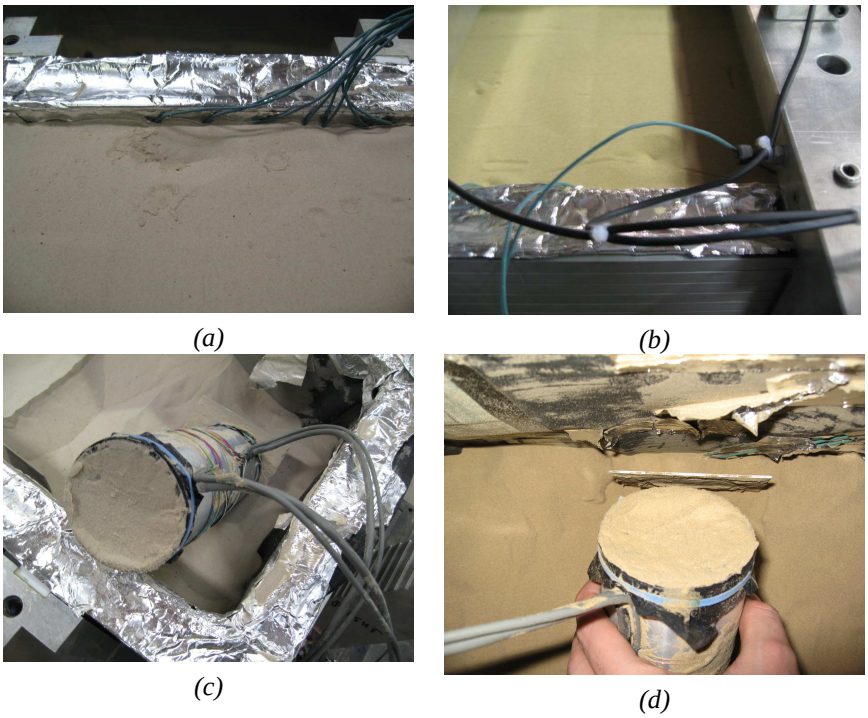

(a) *(b)* *(c)* *(d)*

Fig.5.26: Particular of sand surface of dense tests: a) T-1; b) T-2

Using a ruler the settlement was measured along two parallel longitudinal lines. The average value of the displacements, compared to initial sand surface depth, was showed for every test in the fig.5.27. Calculating an average value of the sand displacement, the relative density variation could be evaluated from the variation of the sand volume, considering no loosing sand mass during the flight. In the table 5.14 an estimation of void ratio and unit weight at the end of the flight was showed.

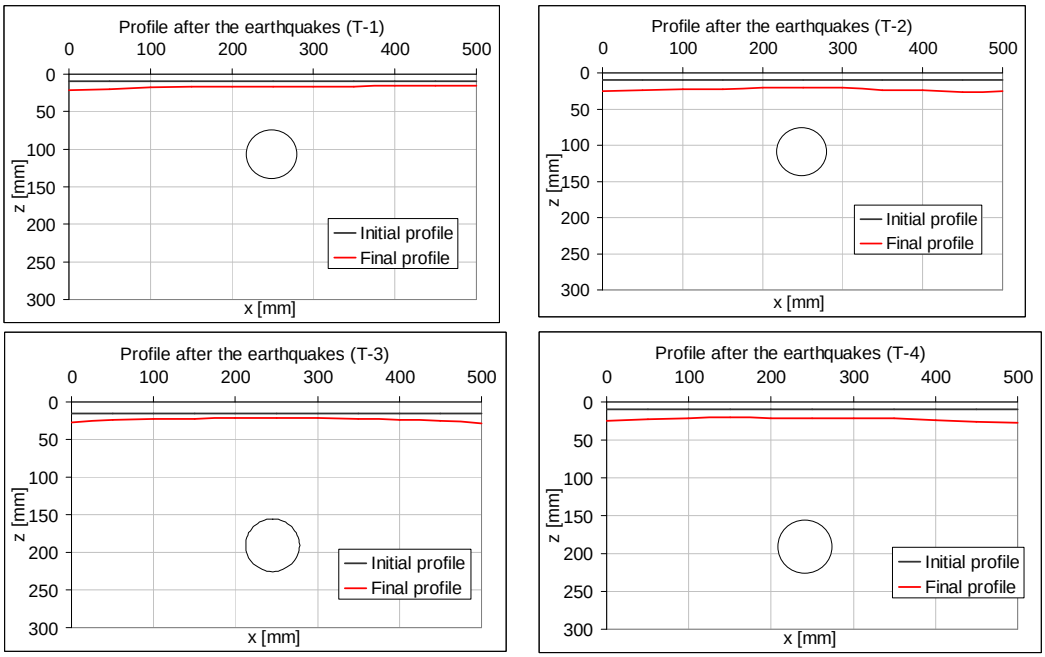

Fig. 5.27: Settlements of soil surface after the tests

Table 5.14: Physical parameters evaluated from the volume variation

Test	**m** [kg]	**Δz_{av}** [mm]	**e_i**	**e_f**	**$D_{r,i}$** [%]	**$D_{r,f}$** [%]	**γ_i** [kg/m^3]	**γ_f** [kg/m^3]
T1	52.4	8	0.71	0.68	75.3	86.5	15.16	15.46
T2	48.52	11	0.85	0.77	41.2	62.3	14.04	14.65
T3	51.5	7	0.71	0.67	75.9	89.5	15.22	15.56
T4	48.48	12	0.85	0.78	40.8	61.2	14.03	14.61

A first order approximation of initial shear modulus could be obtained from the average value of void ratio reached in each test, using the expression suggested by Hardin & Drnevich (1972):

$$G_0 = 100\left(\frac{(3-e)^2}{1+e}\right)\sqrt{p'} \quad [\text{MPa}] \tag{5.20}$$

In which p' is the average effective stress expressed in kPa. The values of initial shear modulus with depth were showed in the fig.5.28.

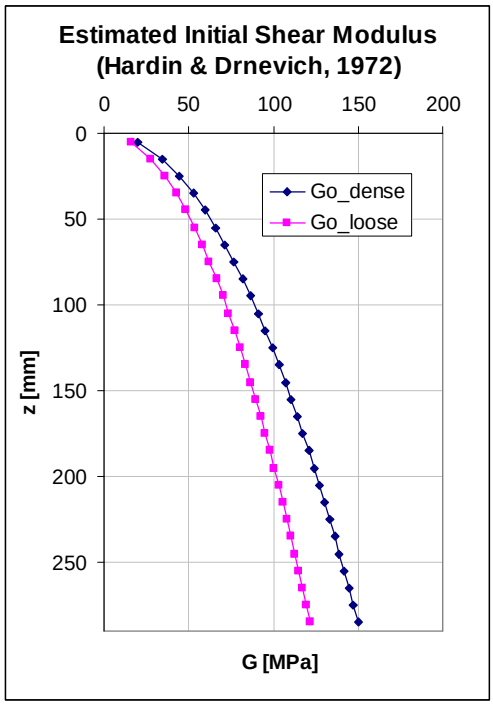

Fig.5.28: Initial shear modulus

The estimated value was variable from about 15MPa on soil surface to 120MPa for loose models or 150MPa for dense model at box bottom. After the visual observation and measurement of the sand surface, the box was carefully empted in order to conserve the positions of the accelerometers and the tunnel. During the empting phase at every level in which instruments was found the depth was measured and some photos were done. The pictures, released at the tunnel depth for every model, were shown in the fig.5.29.

5.11 FINAL CONSIDERATION

This chapter described the procedure of centrifuge testing, showing all the facilities, materials and instruments features. From simple consideration of the physical parameters, a first approximation interpretation on the initial shear stiffness of the soil were obtained from the void ratio measured

during the test preparation and at the end of the flight. In the next chapter, the obtained results from the installed instruments was showed, considering the possible interpretations of the acquired data, in order to perform in the last chapter, a back-analysis of the tests.

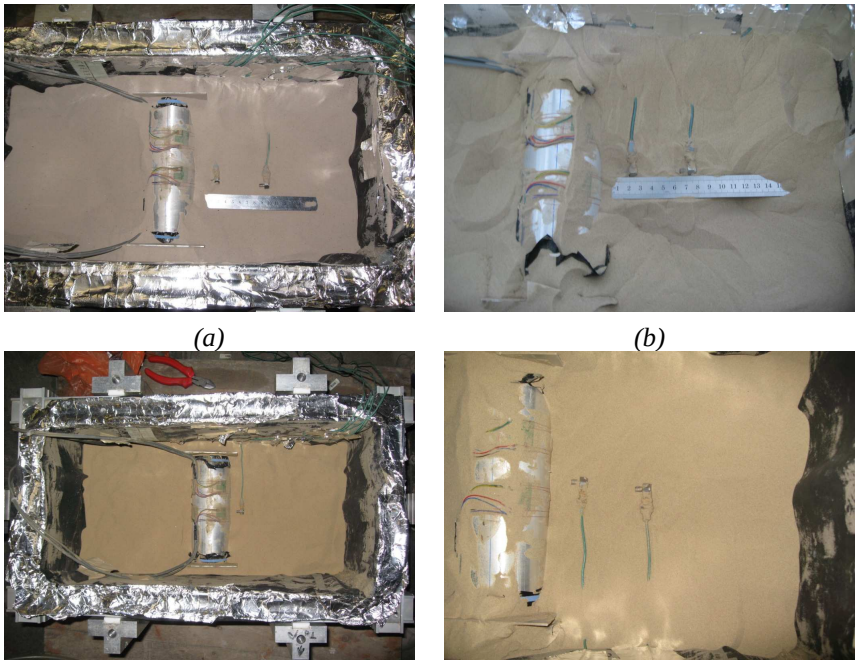

(a) *(b)*

© *(d)*

Fig.5.29: Model empting at tunnel level a) T-1; b) T-2; c) T-3; d) T-4)

REFERENCE

Coelho P.A., (2007), *In situ densification as a liquefaction resistance measure for bridge foundations*, PhD Thesis, University of Cambridge.

Hardin B.O. & Drnevich V.P., (1972), Shear modulus and damping in soils: design equations and curves, Journal of the Soil Mechanics and Foundation Division, ASCE, July 1972, pp.667-692.

Jeyatharan, K., (1991), *Partial liquefaction of sand fill in a mobile arctic caisson under ice loading*, PhD Thesis, University of Cambridge

Lanzano G. & Madabhushi S.P.G., (2007), *DYNAMIC CENTRIFUGE TESTS, ReLUIS Project – Tunnels, Data Report, (Tests T-2 &T-4)*, Internal Report, University of Cambridge, October 2007

Lanzano G. & Madabhushi S.P.G., (2007), *DYNAMIC CENTRIFUGE TESTS, ReLUIS Project – Tunnels, Data Report, (Tests T-1 &T-3)*, Internal Report, University of Cambridge, November 2007

Madabhushi S.P.G., Schofield A.N., Lesley S., (1998), *A new Stored Angular Momentum (SAM) based earthquake actuator*, Centrifuge 98, Balkema, Rotterdam

Madabhushi S.P.G., Houghton N.E., Haigh S.K., (2006), *A new automatic sand pourer for model preparation at University of Cambridge*, Physical Modelling in Geotechnics – 6ICPMG'06

Ramberg W., Osgood W.R. (1943). *Description of stress strain curves by three parameters.* Technical Note 902, National Advisory Committee for Aeronautics, Washington, D.C.

Roark R.J., 2002, *Roark's formulas for stress and strain.* McGraw-Hill.

Schofield A.N., (1980), *Cambridge Geotechnical Centrifuge Operations*, Geotechnique 30, No.3, 227-268

Tan F.S.C. 1990. *Centrifuge and theoretical modelling of conical footings on sand*, PhD Thesis, University of Cambridge.

Timoshenko S.P., (1961), *Theory of elastic stability*, McGraw-Hill, chap.7 pp.278-313.

Visone C. 2008. *Performance based design of embedded retaining walls*. PdD Thesis, University of Naples "Federico II".

Zhao Y., Gafar K., Elshafie M.Z.E.B., Deeks A.D., Knappett J.A., Madabhushi S.P.G., (2006), *Calibration and use of a new automatic sand pourer,* Physical Modelling in Geotechnics – 6ICPMG'06

Zeng X., (1992), *Dynamic Centrifuge tests on Quay Wall Models*, Internal Report, University of Cambridge.

Chapter 6
Interpretation of the experimental results

6.1 INTRODUCTION

The data obtained from the instruments located in the model was given both in the swing up and in the dynamic phase. During the swing up the sampling frequency for the recordings was 4Hz, instead during the dynamic phase changed in 4000Hz, because the earthquake time was very short (0,4s) and the frequency was high (30-60Hz), according with the centrifuge scaling factors. In this chapter all the data recorded by the instruments were reported at model scale. The recordings was given in bit by the acquisition system and, in order to obtain the measure in mV, the value was calculated as:

$$l[mV] = l[bit]\frac{10}{2^{15}} \tag{6.1}$$

This relation were checked with readings carried out during the models flight both for the swing up and the dynamic phases. The instruments installed in the models were:

- LVDTs
- Accelerometers
- Strain Gauges

In the next sections from the instruments recordings a possible interpretation of the results were carried out, in order to obtain a complete view of the models behaviour during the dynamic tests.

6.2 LVDT

The LVDT readings were available only for three tests: T1, T3 and T4, because in the test T2, which was carried out as first one, all the Junction Box acquisition channels were used for the strain gauges recordings. Therefore the Junction Box for the LVDT and the strain gauges was the same and the values given by the measurements were red both in the swing up step and during the earthquakes fired. The swing up data were obtained both from monitor readings and recordings sampled at 4Hz. The measuring points were in the top surface of the model, transversally placed in the middle section. Instead longitudinally the LVDTs were positioned at 140mm from the tunnel axis both on left and right side (layout figs. 5.24-28). The data given from the swing up readings were showed in the fig.6.1 for the T1 model, in the fig.6.2 for the T3 model and in the fig.6.3 for the T4 model.

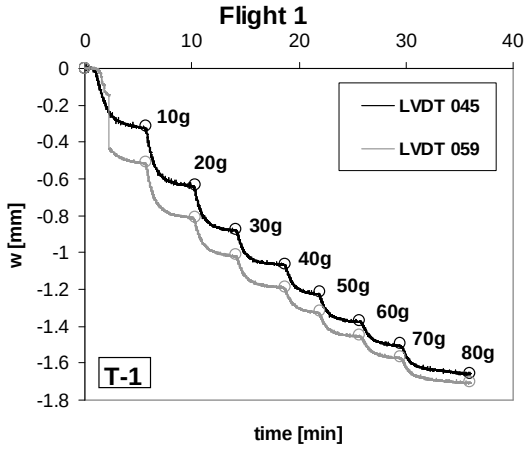

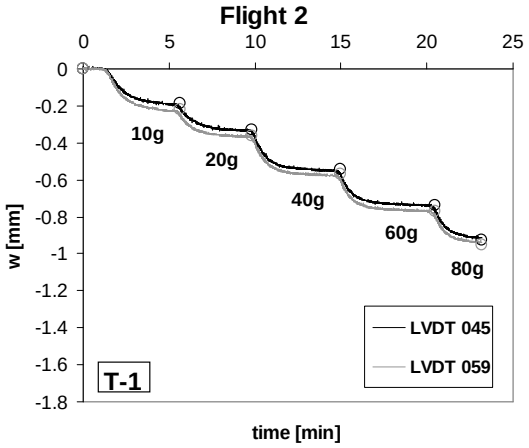

Fig.6.1: LVDTs readings during the swing up step (T1)

The model T1 was subjected to two different flight: both in the first and second flight the LVDTs showed a similar behaviour, having similar displacement in each acceleration level, both for the readings and the recordings. The total settlement was 1,7mm during the first flight and 0,9mm during the second one. Considering the flights were sequential, the densification observed in the second flight, due to the settlement of the soil surface, was smaller due to higher value of initial density.

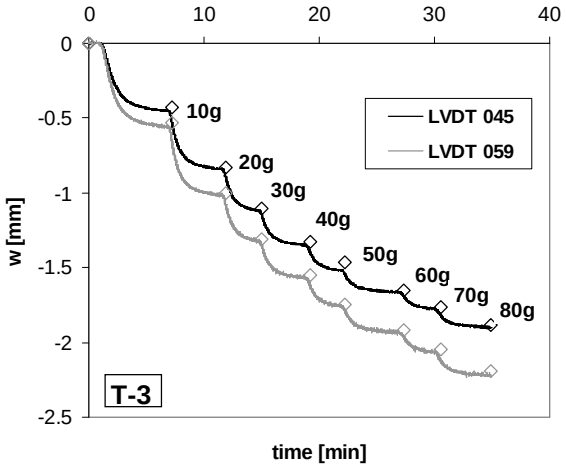

Fig.6.2: LVDTs readings during the swing up step (T3)

The top surface of the model T3 settled during the swing up step slightly more compared to the first flight of the T1 model. The LVDTs had similar value in each levels of “g” and performed a total average displacement of around 2mm. The T1 and T3 tests exhibited similar behaviour due to same initial density.

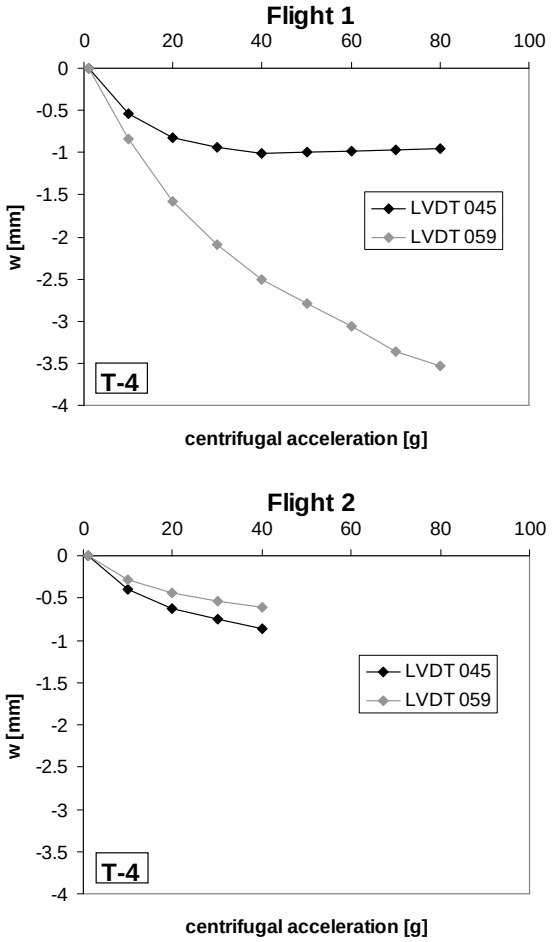

Fig.6.3: LVDTs readings during the swing up step (T4)

During the T4 test, four earthquakes were fired after the first flight, and only one after the second flight. Therefore the SAM actuator had autonomy only for five earthquake: the model was slowed down to 1g and the motor was recharged in order to perform the sixth earthquake in a second flight.

Clearly the T4 model exhibited larger deformations compared to T1 and T3 models: therefore the initial density was smaller compared to the other tests. The data concerning the LVDTs measurements during the swing up was available only from the readings, because the swing up recordings were missed for a malfunctioning. The two LVDTs had different behaviour during the first flight: the LVDT 059 had large displacement until 3,5mm; the LVDT 045 maintained constant value of 1mm from 40g to 80g.

The data recorded during the dynamic step were plotted in order to show both the partial and the total displacement measured. In the fig.6.4 an example of the output recordings during different earthquakes were showed (model T3, LVDT 045).

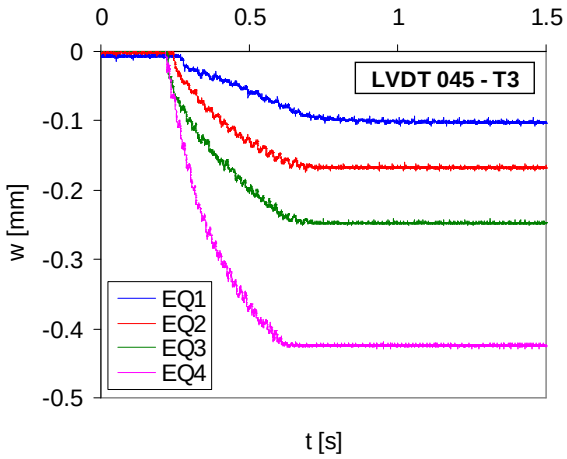

Fig.6.4: Comparison between the displacements of the 80g earthquakes

The dynamic recordings exhibited a different behaviour during the different input motion: therefore the settlement increased from the EQ1 to EQ4 with a more than linear law. The total value of the displacement in each earthquake was a combined effect of the increasing both of the input amplitude and the frequency, which contemporarily changed from EQ1 to EQ4. Moreover the displacement took place only during the earthquake time, showing both an average increase of the settlement and an oscillation until a constant value when the motion ended.

In the figs.6.5, 6.6 and 6.7 the displacement were sequentially reported against the time, pointing out the time range relative to each earthquake. In

order to check the values of the recordings, in the graphs the readings were reported, showing in all the cases a good agreement with the data obtained by the acquisition system. From the readings a significant information was obtained for all the tests, concerning the negative displacement (uplift) between the last earthquake at high "g" and the centrifuge slowing down, due to the elastic part of the settlement.

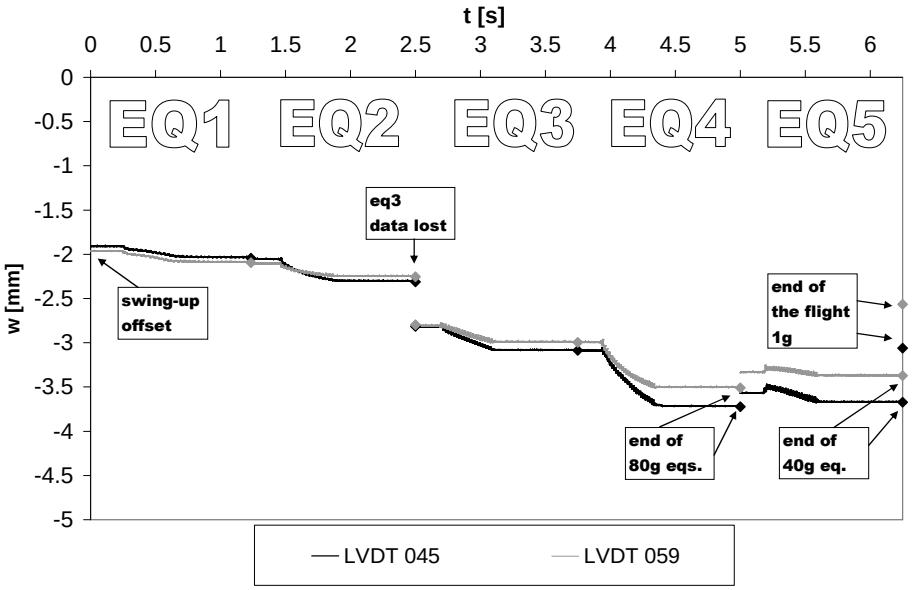

Fig.6.5: LVDTs measurements during the dynamic phase (T1)

The dynamic displacements of T1 model were reported in fig.6.5. For the 80g earthquakes the displacement increased with the severity of the input motion, while the 40g earthquake had a very small displacements, almost negligible. After the second earthquake, the data relative to an earthquake fired, with same features of earthquake 3, was missed, but the top surface suffered a permanent displacement of 0.5mm. When the model was slowed down until 40g the sand surface was subjected to negative settlement, probably due to slighter stress field suffered by the model. The total settlement relative to T1 test was around 1,6mm, considering the different behaviour of the two LVDTs: therefore the LVDT 059 had a smaller displacement (1,4mm) compared to the LVDT 045 (1,8mm).

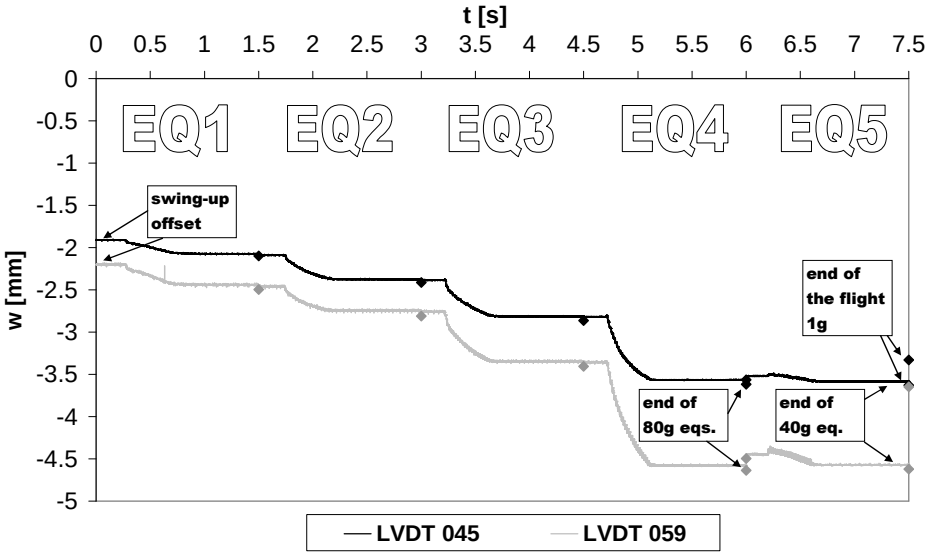

Fig.6.6: LVDTs measurements during the dynamic phase (T3)

Similar consideration can be done for the T3 (fig.6.6) and T4 (fig.6.7-6.8) test, relative to the increasing displacement at 80g and the negligible displacement at 40g. The T3 model exhibited an average deformation larger compared to T1 model, despite of the additional displacement of the missed T1 earthquake. The two LVDTs had different behaviour: the LVDT 045 gave total displacements similar to T1 values (1,7mm); instead the LVDT 059 showed bigger value of settlement until 2,4mm. The LVDT recordings of the test T4 were plotted in two different graphs relative to the two flights subjected by the model: in the first graph were reported 5 of the 6 earthquake fired, 4 at 80g and 1 at 40g. The two installed LVDT exhibited a very different behaviour: therefore the LVDT 045, as happened in the swing up phase, registered settlements which were strongly smaller compared to the LVDT 059, which exhibited more realistic values. Considering the LVDT 059, the settlement in the dynamic phase was larger compared to the displacements observed in the dense model, around two times larger, both in the static (3,5mm) and dynamic phase (4,5mm). In the second flight the two transducers gave consistent results, which had values very slighter compared to the settlements registered in the first flight.

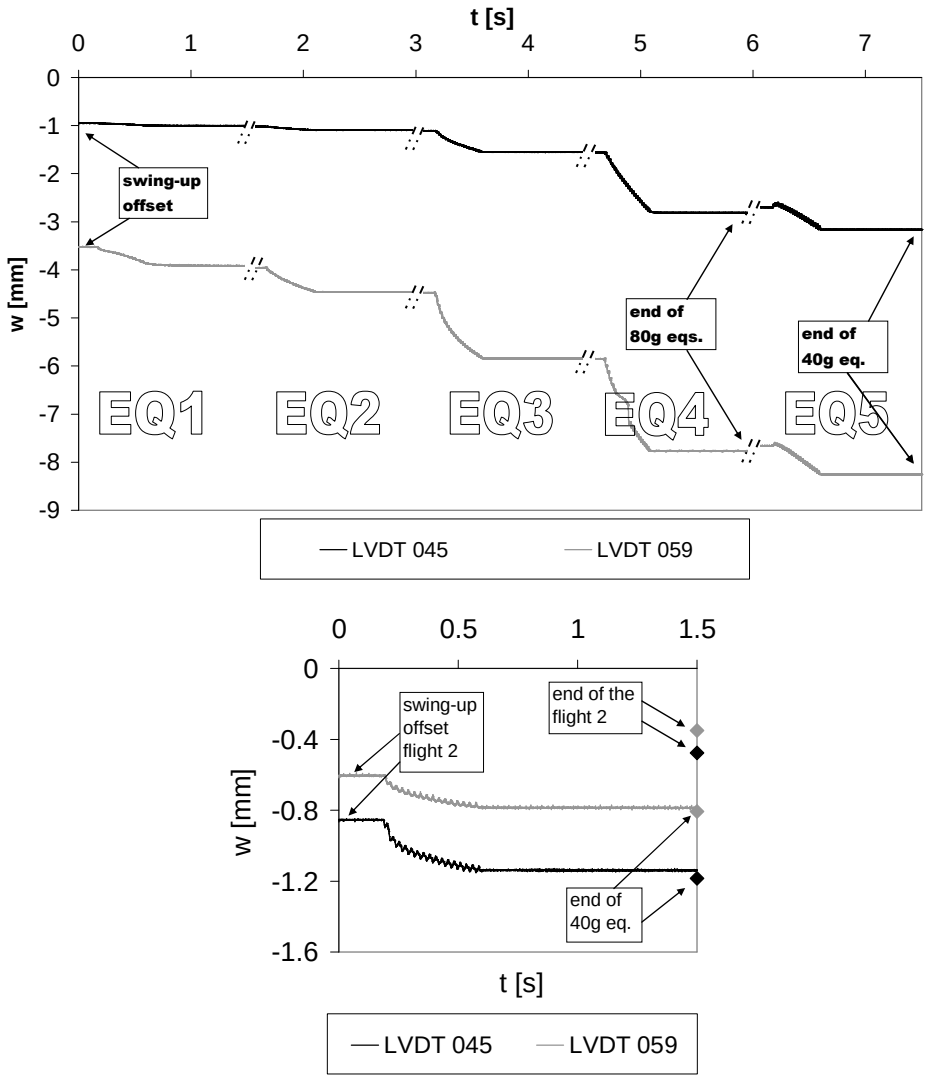

Fig.6.7: LVDTs measurements during the dynamic phase (T4)

In order to summarize the variation of sand properties both in static and dynamic phases, the total displacement and the density variation were showed in the table 6.1. The permanent densification was stronger during the first flight compared to the second flight, due to higher value of initial density. The density variation in the dynamic phase is generally lower compared to the swing up steps: in other words most of the mechanical properties variation happened during the static phase. The observed

displacement is generally higher to the measured one, probably due to settlements accumulated when the model was unloaded from the centrifuge.

Table 6.1: Overview of the maximum displacement and densification

Test	Instrument	Flight 1		Flight 2		Dynamic phase	
		u [mm]	ΔD [%]	u [mm]	ΔD [%]	u [mm]	ΔD [%]
T1	*LVDT 045*	1.65	5.43	0.91	1.50	1.76	2.90
	LVDT 059	1.7	5.52	0.95	1.56	1.41	2.32
T3	*LVDT 045*	1.89	6.86	---	---	1.75	2.93
	LVDT 059	2.19	7.36	---	---	2.4	4.02
T4	*LVDT 045*	0.95	2.81	0.87	1.55	2.48	4.41
	LVDT 059	3.53	7.40	0.62	1.10	4.92	8.75

6.3 HORIZONTAL ACCELEROMETERS

6.3.1 Output signals

In the performed tests, 3 columns in the models were instrumented by 3 or more accelerometers: the first column was instrumented along the vertical passing through the tunnel axis (*tunnel*); the second column was located at 125mm from the central vertical (*free-field*); the third column of accelerometers were placed on the box on the external side (*reference*). One of the external instruments, who was located on the base-plate, measured the input motion from the SAM actuator. In the Fig.6.8 the acceleration time histories of the model T1, recorded at the base of the box, and the Fourier spectra are shown for the 4 different frequencies investigated in the tests. The graphs clarified that the signals applied at the model base was not exactly harmonic: therefore the fig. clearly showed that the signals had not constant amplitude and in some cases the signal was not symmetric to the time axis. The frequency content was extended and larger compared to the design frequency, because some subsequent frequencies were present until around 400Hz.

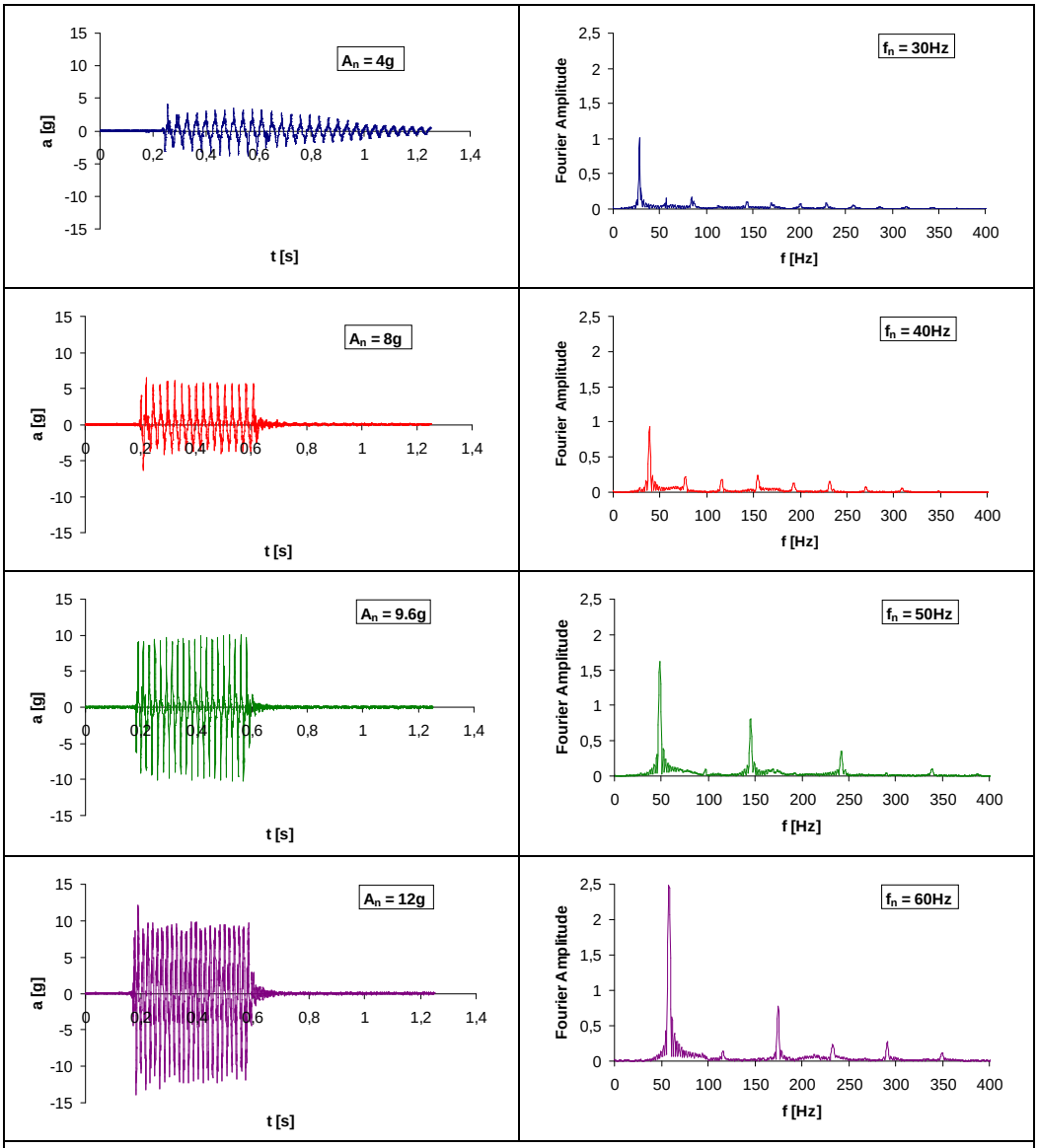

Figura 6.8: Input signal of the model T1(recorded on the base-plate)

Brennan *et al.* (2004) observed that this extended frequency content was not a noise recorded by the instruments, but was an effective energetic content and must be not eliminated with a filtering. The 30Hz signals have a longer duration compared to design one, because at this frequency a wrong brake operation prevented an immediate oscillation block; instead in

the other time histories had a smaller duration, more or less equal to the design value, but had an extended zero recordings before and after the significant signal.

All the acceleration time histories were centred, neglecting the noising zero recordings before and after the significant signal, and filtered in a time domain: the filter was designed using a 4^{th} order Butterworth type, which was an infinite-impulse-response filter (IIR). The IIR filters have the advantage to perform filtering at lower order compared to finite-impulse-response filter (FIR), but have the disadvantage to be unstable in some cases and have a non linear phase compared to the FIR. The Butterworth filter is a IIR filter which have maximum flat magnitude in the interval of designed frequency, and zero over these range. The order of the filter determines the order of the curves which connect the limit frequencies at maximum magnitude to the zero magnitude ones. The digital filter was a typical “band pass” between the frequencies of 15Hz and 250Hz, in order to include all the meaningful frequency content of the Fourier spectrum of the input signal. The choice of the “band pass” filter was carried out in order to eliminate the low and the high frequency: the lowest frequency determined a drift of the signal during the integration of the acceleration time history; the highest frequencies were considered only a recording noise, because had an almost zero spectral ordinates. Moreover a base-line correction with a linear law was applied to the input signal: this correction was useful to obtain a zero trend value and the end of the time histories of integrated velocity and displacement. In order perform a correct integration, the initial acceleration time histories was both filtered at low frequency and subjected to a linear base line correction; moreover the integrated signal was filtered again in order to eliminate the phase distortion introduced by the integration.

The fig.6.9 showed a comparison between the same signal (EQ1), relative to T4 model, but filtered with different frequency range: first time history was unfiltered; the second one is relative to a large band pass (15Hz -250Hz); the third one considered only a narrow interval around the main frequency of 30Hz (20Hz -40Hz).

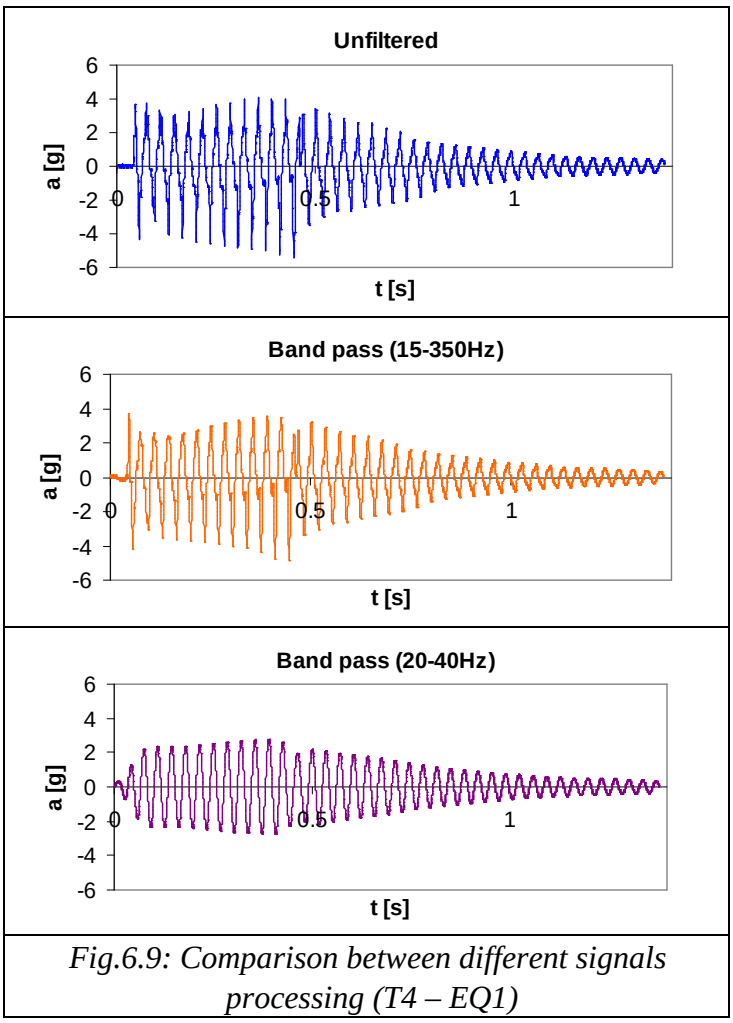

Fig.6.9: Comparison between different signals processing (T4 – EQ1)

The effect of filtering is the reduction of maximum acceleration: of course for the large band pass the reduction is smaller, but for the narrow band pass the variation is too strong and could simulate a false response of the soil at the wave passage. Moreover Brennan et al. (2004) observed that an over-filtering determined an underestimation of the shear modulus and damping ratio obtained by the shear stress-strain cycles.

Once all the signals were filtered, all the acceleration measurements given by the instruments were reported in the figs.6.10-6.13 for the four model tests carried out. In each figure the normalized horizontal and vertically profile of the maximum acceleration were showed. All the data

was normalized by the maximum acceleration of the input signal, which was reported for all the earthquake fired. The vertical profiles of the average values were given for the three instrumented columns, instead the horizontal profile were referred to three different depths. Moreover the comparison between the nominal amplitude and the maximum value of the input time histories were showed in order to check the difference between the design and the real value.

The vertical profiles of maximum acceleration showed same behaviour during the different earthquakes, because the normalized values were systematically overlapped. The profiles of the reference and free-field vertical exhibited a slight amplification of the base acceleration ($S = a_{max,s}/a_{max,b}<1.5$). Both in the free-field and in the tunnel vertical the profiles showed a reduction of acceleration at tunnel depth, considering that in the central alignment, the accelerometers was located laterally to the lining. The base accelerometer under the tunnel always measured a larger value of acceleration compared to the other base instruments, which were generally similar with the lower value of the free-field one. The accelerometers located near the soil surface gave a slightly higher value of the maximum acceleration for the reference instrument, compared to the internal ones. In many cases the value of the maximum amplitude of the input signal was substantially lower than the design amplitude, especially for the earthquakes at 40Hz at 80g and the 50Hz at 40g.

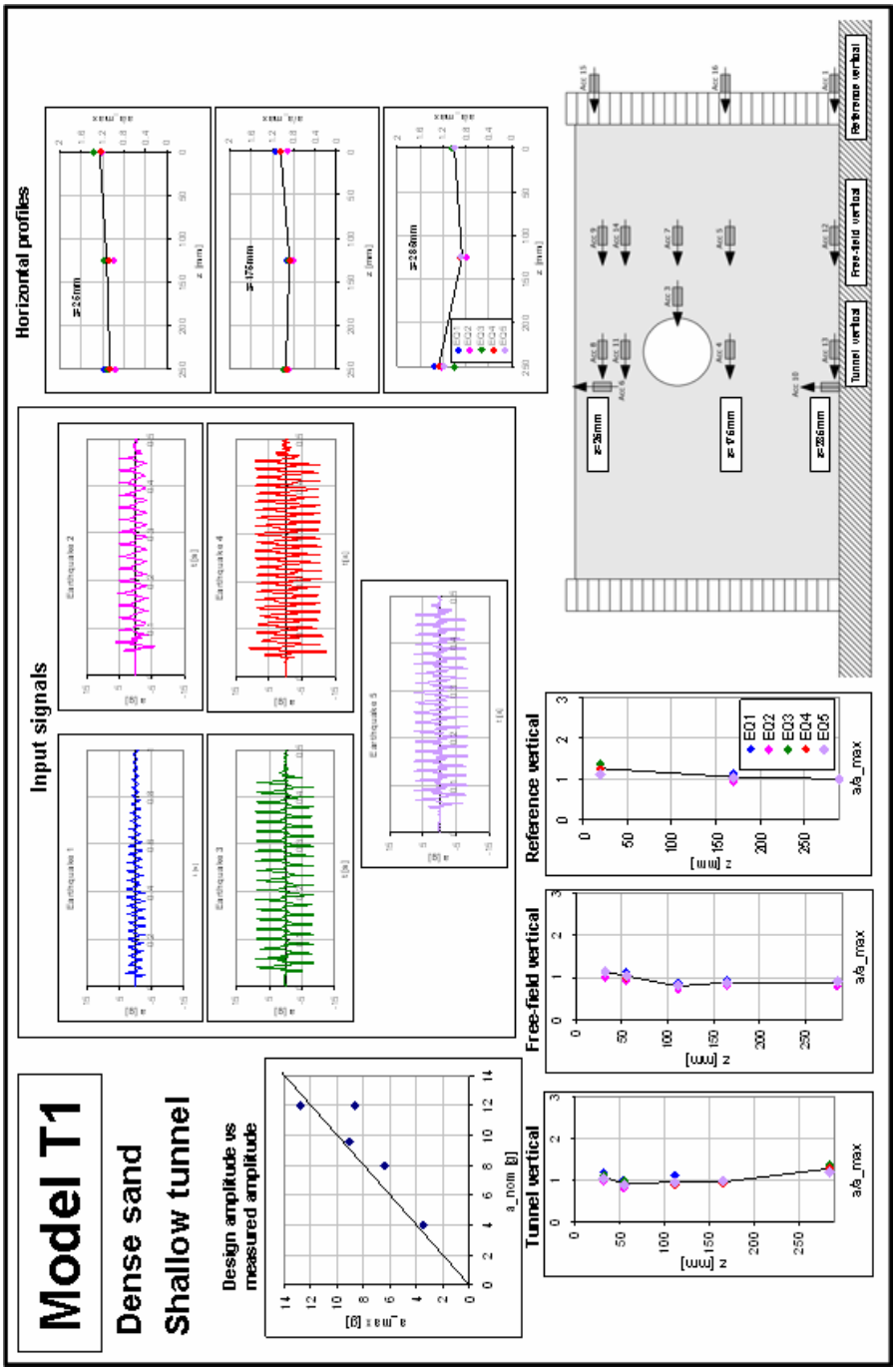

Fig.6.10: Profile of peak ground acceleration (T1)

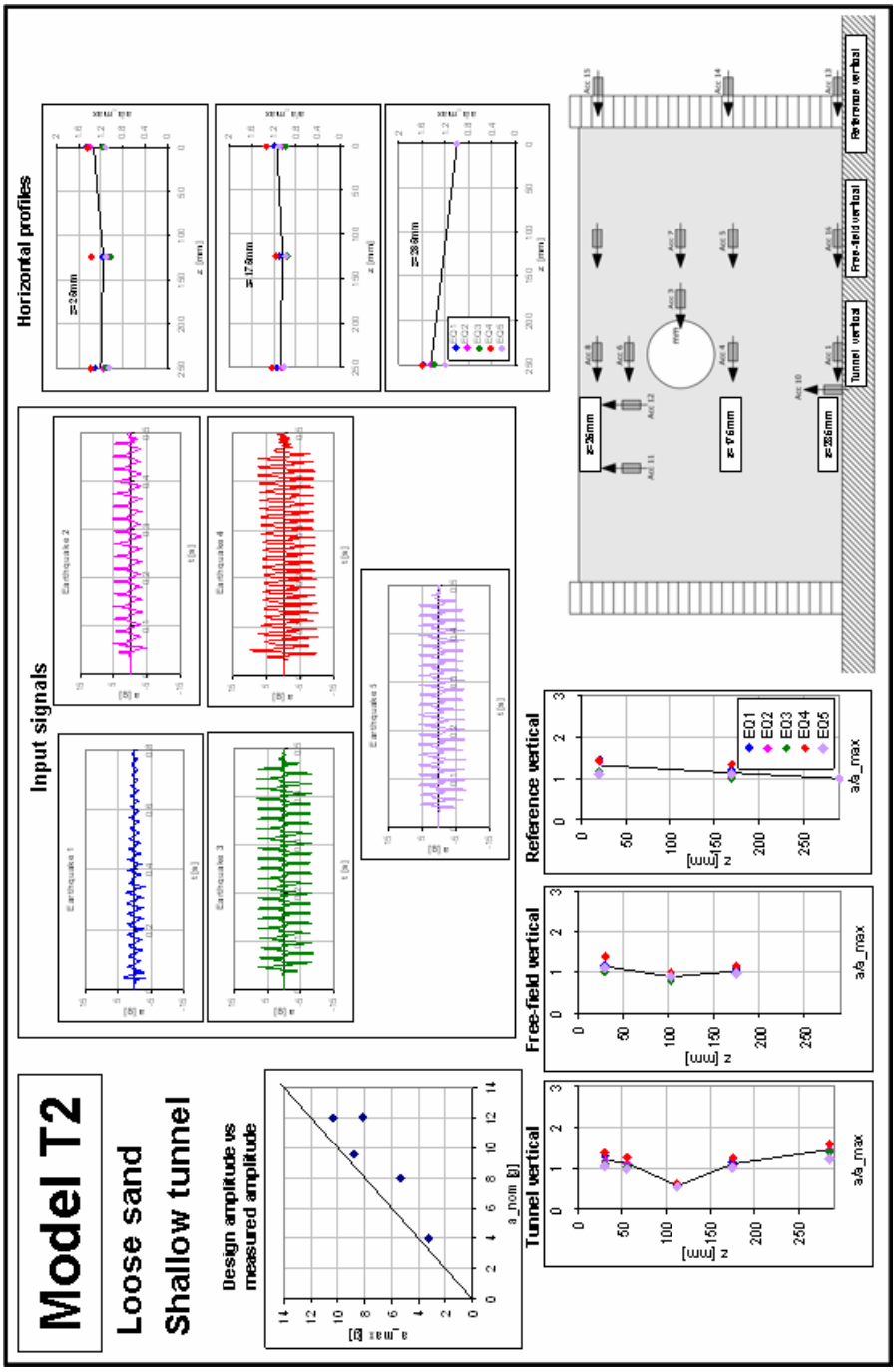

Fig.6.11: Profile of peak ground acceleration (T2)

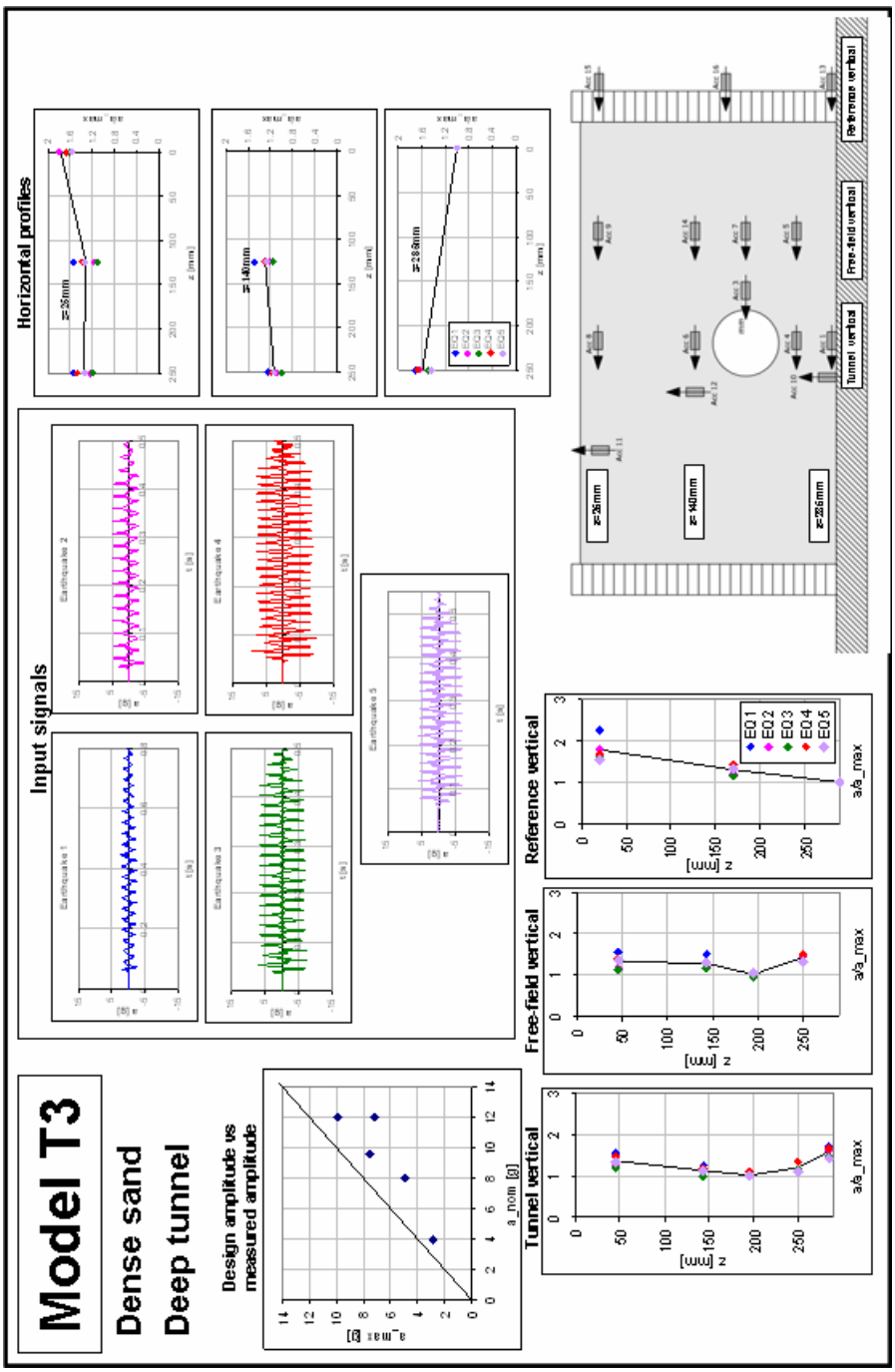

Fig.6.12: Profile of peak ground acceleration (T3)

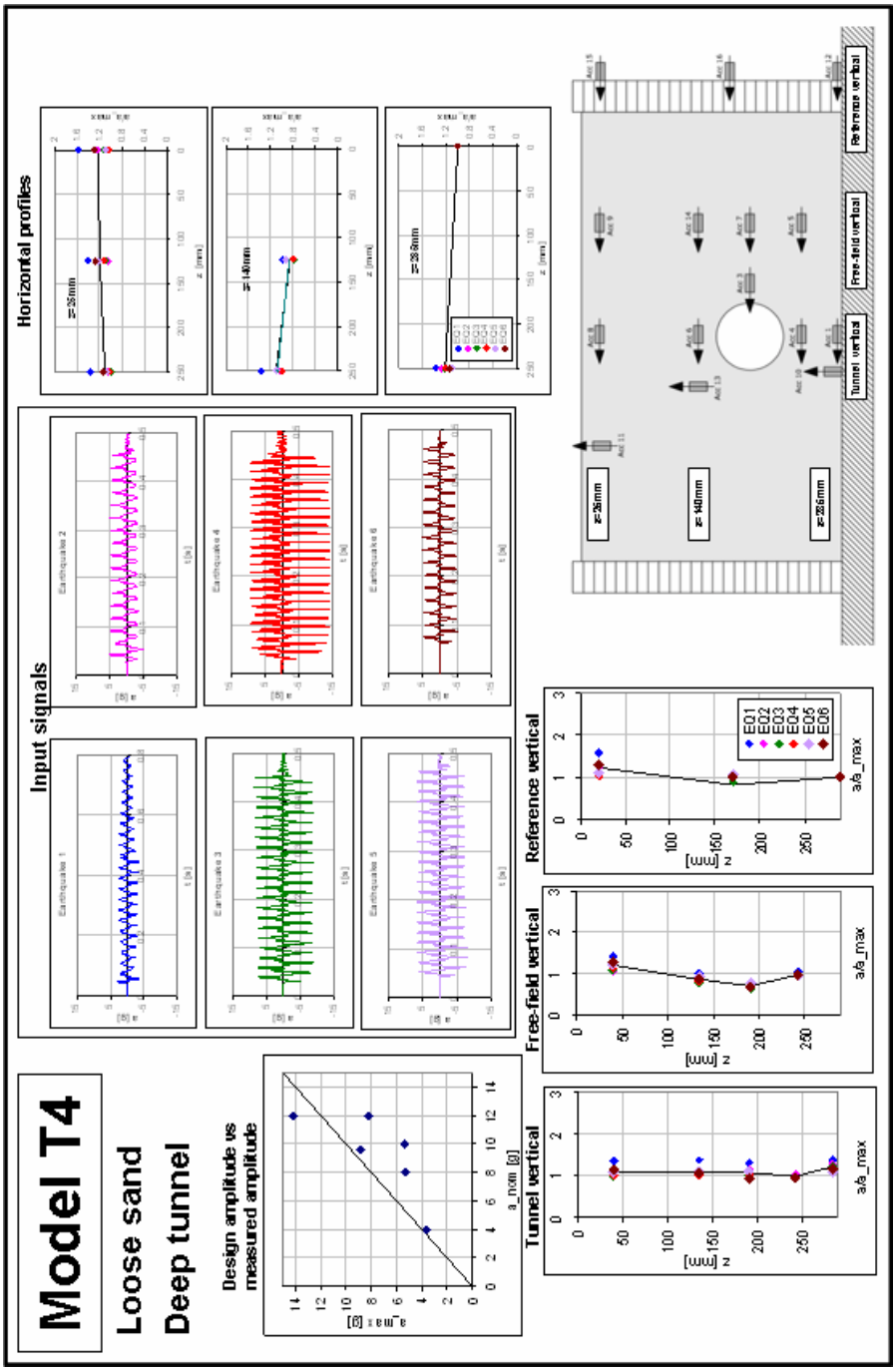

Fig.6.13: Profile of peak ground acceleration (T4)

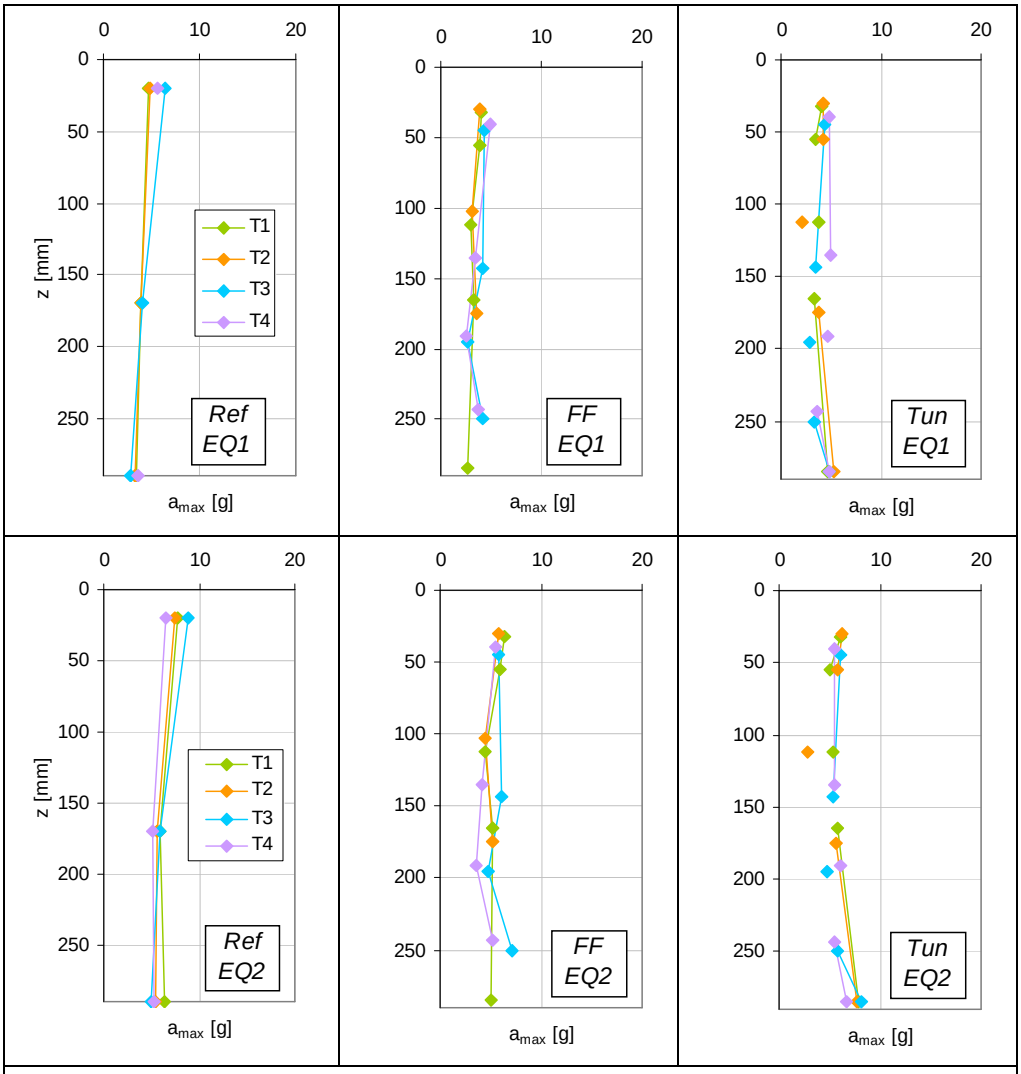

Fig.6.14:Profile of maximum acceleration for different models (EQ1 – EQ2)

The comparison between the maximum acceleration profile was also carried out considering the behaviour of different model during the same earthquake. In the figs.6.14-6.15 the values of acceleration were showed for the same vertical alignment of accelerometers. The measurements, referred to the reference alignment, were located at the same depth in different models, because the instruments were allocated in fixed lodging on the external wall of the box.

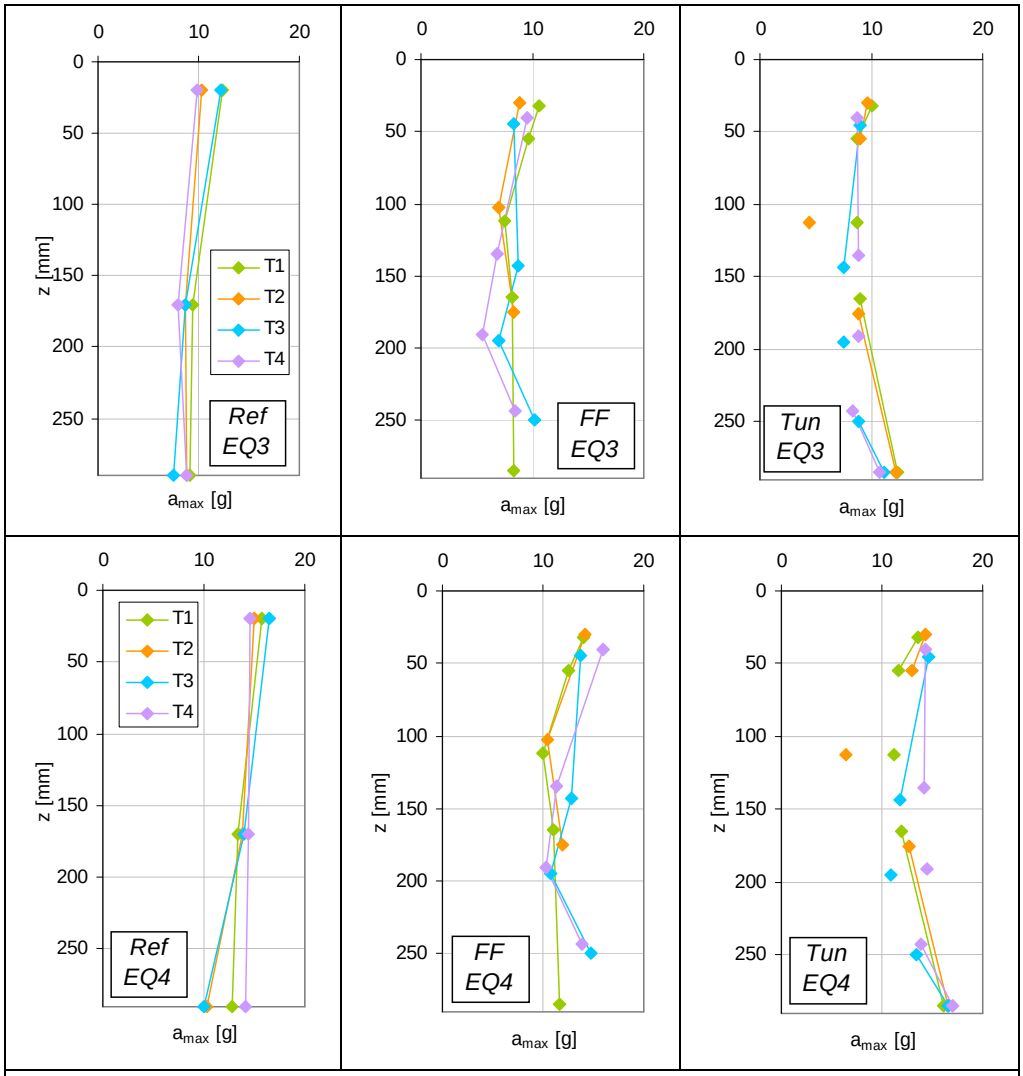

Fig.6.15:Profile of maximum acceleration for different models (EQ3 – EQ4)

The tunnel profiles contained an accelerometer not exactly aligned to the others, but located laterally at the tunnel depth and for simplicity included in the graphs. In the figs.6.14-6.15 only the profiles relative to the 80g earthquakes were considered.

The reference profiles showed a slight difference between the values obtained in the different tests: the test T3, which was relative to the deep tunnel in dense sand, showed in all the earthquakes a higher amplification

from the base to the top instruments; on contrary the test of deep tunnel in loose sand exhibited in each case the lower amplification. The reference profiles relative to shallow tunnel were generally similar, showing an intermediate behaviour compared to the previous described ones. The free-field profiles showed a good agreements between dense and loose model both for shallow and deep tunnel. Therefore the free-field profiles of the T1 and T2 tests showed very similar behaviour; in the case of the T3 and T4 free-field profile the difference was larger, but generally exhibit a typical acceleration reduction at tunnel depth. The values of maximum acceleration along the tunnel vertical registered a drastic reduction of the tunnel acceleration for the model with shallow tunnel, especially for the dense sample; the other points for tunnel profiles are generally overlapped for the shallow tunnel models and had some differences but similar behaviour for deep tunnel models. The results of maximum acceleration seemed to explain that, despite of the different preparation procedure in order to obtain different sand density, the values of soil stiffness of loose and dense models should be similar.

6.3.2 Spatial variability of the ground motion

In order to study the spatial variability of the ground motion, some significant parameters could be introduced, obtained from the acceleration time histories. The similarity between two time histories of signals measured in different points can be represented by the cross covariance (Kramer):

$$CCov_{jk}(\tau) = \sum_{i=1}^{N} a_j(t_i) a_k(t_i + \tau) \tag{6.2}$$

Where t is the time increment and N is the samples number. When the cross covariance is used to analyze an acceleration time histories against itself, a function called auto-covariance is obtained. The coherency is a possible description of the frequency content between different signals. Therefore the coherence function measures the similarity between two different time histories in the frequency domain:

$$Coh_{jk}(\omega) = \frac{S_{jk}(\omega)}{\sqrt{S_{jj}(\omega) S_{kk}(\omega)}} \tag{6.2}$$

Where S_{jk} is the Fourier transform of the cross covariance and S_{jj} and S_{kk} are the auto-spectra of the Fourier transform of the auto-covariance. The coherency has a value (for each frequency) included between 0 and 1: the 1 value indicates a perfect correlation between the two signals, while a 0 value gives a total incoherency.

The transfer function is an other possible representation of the ground motion variability due to the wave propagation inside a medium. This function is defined as the ratio between the Fourier Spectra of two different signals. The absolute value of the transfer function represents the amplification factor, which is defined as:

$$A(\omega) = |H(\omega)| = \frac{X(\omega)}{Y(\omega)} \tag{6.4}$$

In the (6.4) X(ω) and Y(ω) are the Fourier Spectra of two different signals.

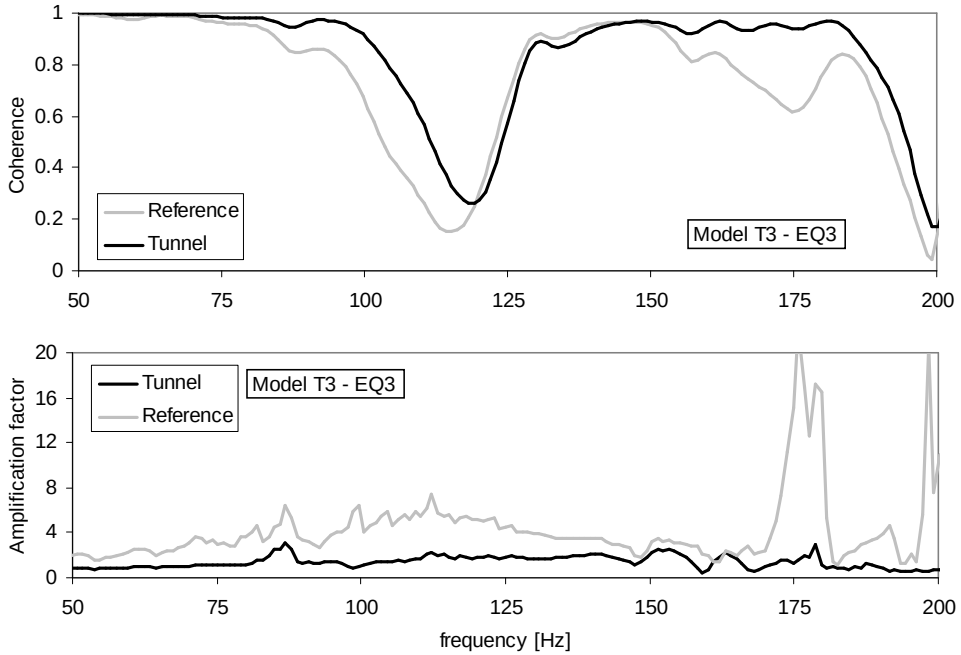

Fig.6.16 Comparison between amplification function and coherence

The amplification function cold be used to recognize which frequencies were amplified when the waves propagate thought the medium from the first to the second accelerometers. The interpretation of the transfer function should be always combined with the coherency analysis: therefore an extraneous peak in the amplification function could be attributed to a very low value of the coherence function and couldn't be considered realistic. An example of compared values of coherence and amplification factor in the same frequency range were showed in the fig. 6.16: the instruments were located in the same alignment, the first at the model base and the second near the top surface.

The comparison of fig.6.16 was carried out for all the instrument alignment of the models. In the fig. 6.17 the transfer function were calculated along the three instrumented verticals located in the model (*reference*, *free-field* and *tunnel*). The experimental amplification function were plotted together with the theoretical function for a damped scheme. Therefore the experimental data could be given an approximate value of the natural frequency of the soil layer between the two instruments. The expression of the analytical plotted function is:

$$A(\omega) = \frac{1}{\sqrt{\cos^2 F + (DF)^2}} \tag{6.5}$$

In the eq.(6.5), the parameter F is the frequency ratio, which is defined as $F=kH=\omega H/C_S$ (H is the soil layer thickness and C_S is the shear wave velocity).

The experimental curve was best-fitted with the analytical expression, obtaining an average reasonable value of the amplified frequency and the damping ratio.

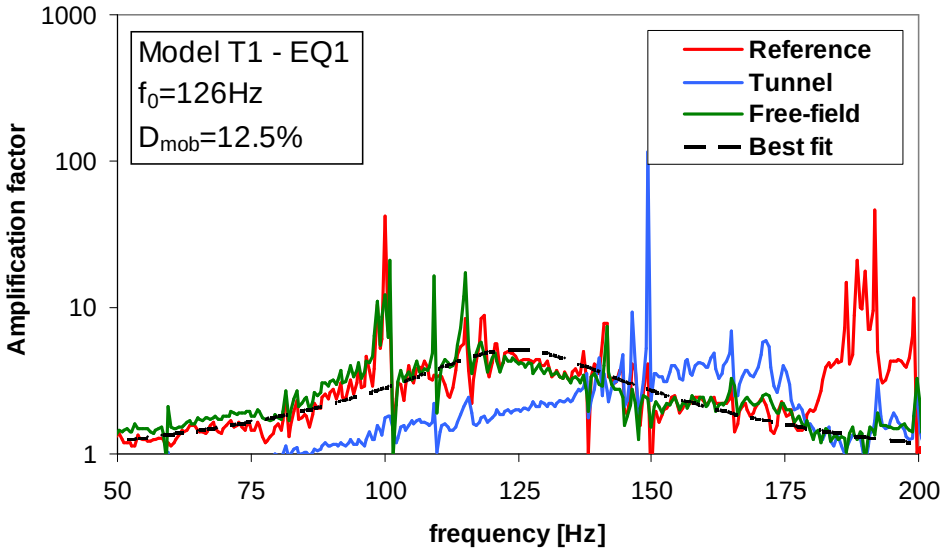

Figura.6.17: Amplification function of the model T1

The experimental curves showed that the amplified frequencies of the reference and free-field verticals were very similar and the tunnel vertical exhibited higher values. The presence of the tunnel modified the first natural frequency of the soil, increasing its stiffness. Figure 6.17 also shows that, along the tunnel vertical, the surface amplification appeared significantly reduced, especially around the resonant peak observed at the reference vertical. This is a clear evidence of the wave-screening effect of the tunnel structure.

The transversal modulus of elasticity G, which was the average mobilized value in the whole soil layer, could be approximately evaluated from the transfer functions. For the smaller motions the strain level was so low that the modulus G was practically equal to maximum value G_0. Instead in the other cases the value of mobilized G was directly connected to the strain level reached during the fired earthquake. From the transfer functions evaluate along the free-field verticals, the first natural frequency f_0 was given and the shear modulus was obtained from the expression:

$$G_0 = V_s^2 \rho = (4Hf_0)^2 \rho \qquad (6.6)$$

Considering the experimental data of the fig.6.17, the first natural frequency of the model deposit was included between 100Hz and 120Hz,

which corresponded to a mobilized shear modulus of 20-30MPa. Along the central vertical the resonant frequency is modified by the presence of tunnel, until the range values between 150Hz and 170Hz.

In the table 6.2 the average values of the mobilized shear stiffness were reported, evaluated from the reference columns of accelerometers. Through the best-fitting curves an estimation of the mobilized damping ratio was carried out, obtaining for each test the values showed in the table 6.3.

Table 6.2: Evaluation of the shear stiffness from the transfer function

Estimated mobilized shear stiffness [MPa]				
Model	*Earthquakes fired*			
	EQ1	EQ2	EQ3	EQ4
T1	29,4	26,5	26	-
T2	24,4	18,3	22,5	-
T3	26,8	27,9	24,8	17,1
T4	29,3	25	19,7	8

Table 6.3: Evaluation of the damping ratio from the transfer function

Estimated mobilized damping ratio [%]				
Model	*Earthquakes fired*			
	EQ1	EQ2	EQ3	EQ4
T1	12,5	15,2	13	-
T2	13,2	14,8	32	-
T3	7,6	5,5	10	9
T4	18,6	17,8	16,4	31

The values range for the mobilized shear stiffness was between 10Hz and 30Hz, confirming that the stiffness of the soil was relatively low. The difference between the dense and the loose sand models was generally small, showing that the dense sand models were generally stiffer compared to the loose one, considering the same tunnel position. Moreover, according to the increasing energy of the successive earthquakes, the strain level should be increased from EQ1 to EQ4, because of the decreasing mobilized stiffness. The values of the damping ratio were extremely affected by the false amplification peak, due to very low coherence at same frequency, and could give a overestimation or underestimation of the real value. Despite of this limit, the damping level was generally very high between 5,5% to 30%.

The average damping ratio value was 15%, showing the lower values during the earthquakes of the model T3 and the higher values for the model T4.

6.3.3 Stress-strain loops

Brennan *et al.* (2004) reported a procedure to evaluate the shear modulus and the damping ratio using the centrifuge data. They proposed a way to understand soil behaviour when a set of laboratory test using cyclic triaxial and resonant column is not available. In order to estimate well the G modulus and the D ratio a set of 3 or more accelerometers should be positioned in every column.

Zeghal & Elgamal (1994) and Brennan *et al.* (2005) suggested a procedure to calculate the shear strain along the instrumented verticals with two or more accelerometers. From the time histories of acceleration, the displacements u(t) were obtained for double integration. In order to avoid annoying effects and integration errors like the unreal linear variation of the displacement after the shaking, the signal was filtered two times, first like acceleration before the first integration and secondly like velocity before the second integration. Moreover the filter eliminated the phase distortion due to the integration procedure. The shear strain could be evaluated using a first order approximation between two instruments positioned in the same vertical:

$$\gamma = \frac{(u_2 - u_1)}{(z_2 - z_1)} \tag{6.7}$$

Moreover when three or more accelerometer were vertically aligned, the shear strain is calculated using a second order approximation:

$$\gamma(z_i) = \frac{\left[(u_{i+1} - u_i)\frac{(z_i - z_{i-1})}{(z_{i+1} - z_i)} + (u_i - u_{i-1})\frac{(z_{i+1} - z_i)}{(z_i - z_{i-1})}\right]}{(z_{i+1} - z_{i-1})} \tag{6.8}$$

in which the index *i* was relative to the position of the central instruments and *i*-1 and *i*+1 to the top and bottom accelerometers. For every instrumented columns installed in the model, the shear strains were

calculated using the (6.7) and (6.8). In the figs.6.18-21 the profile of maximum shear strain was reported considering all the test performed.

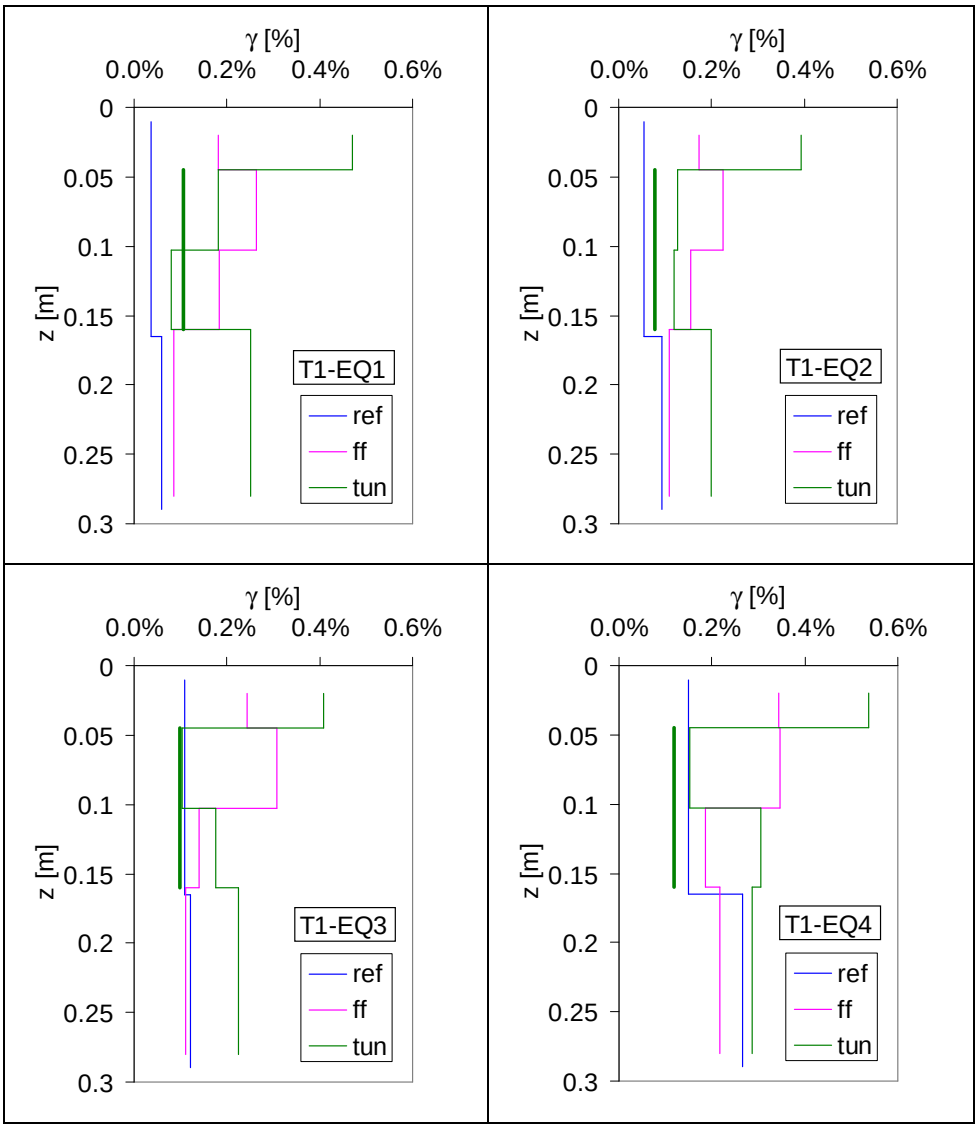

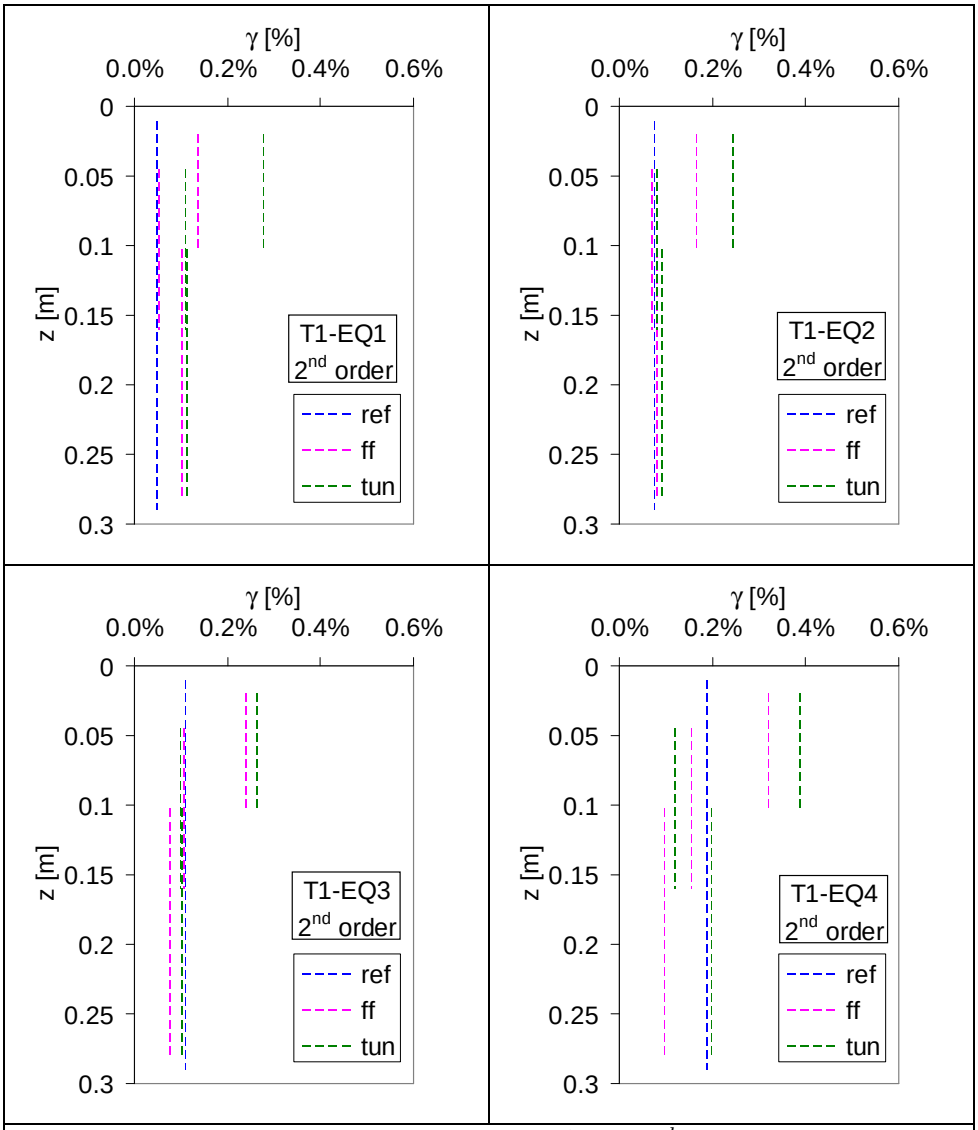

Fig 6.18: Shear strains of the model T1 (1st and 2nd order approximation)

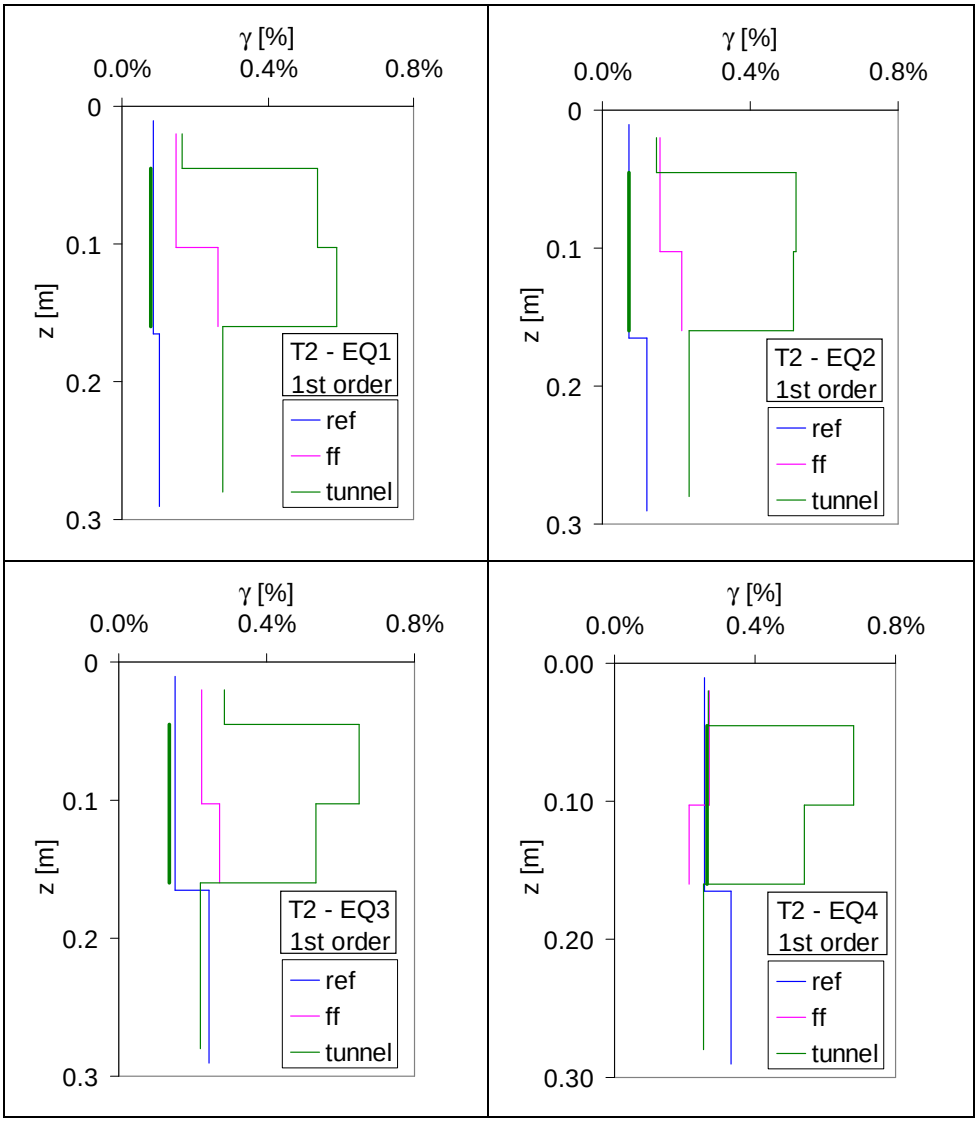
γ [%]
0.0%
0.4%
0.8%
z [m]
0
0.1
0.2
0.3
T2 - EQ1
1st order
ref
ff
tunnel
γ [%]
0.0%
0.4%
0.8%
z [m]
0
0.1
0.2
0.3
T2 - EQ2
1st order
ref
ff
tunnel
γ [%]
0.0%
0.4%
0.8%
z [m]
0
0.1
0.2
0.3
T2 - EQ3
1st order
ref
ff
tunnel
γ [%]
0.0%
0.4%
0.8%
z [m]
0.00
0.10
0.20
0.30
T2 - EQ4
1st order
ref
ff
tunnel

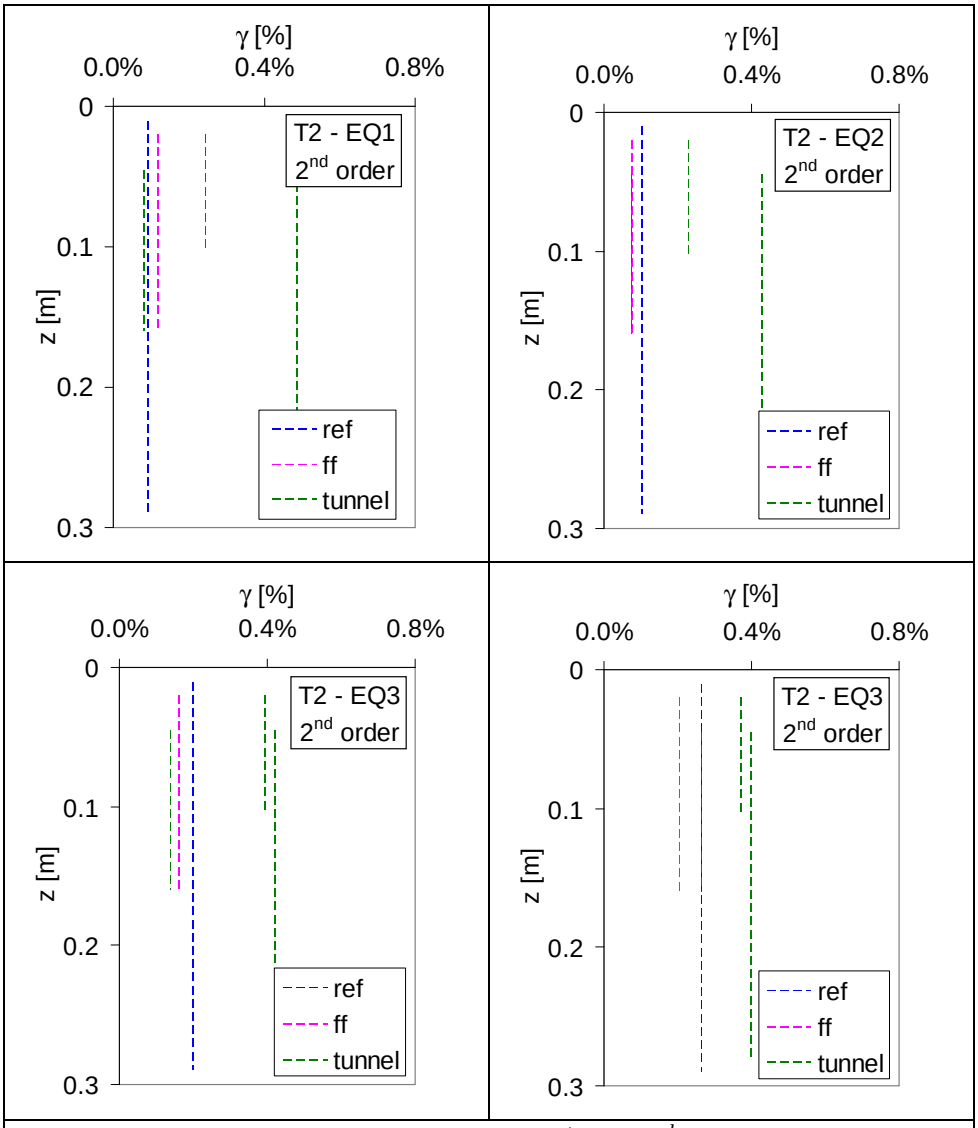

Fig 6.19: Shear strains of the model T2 (1st and 2nd order approximation)

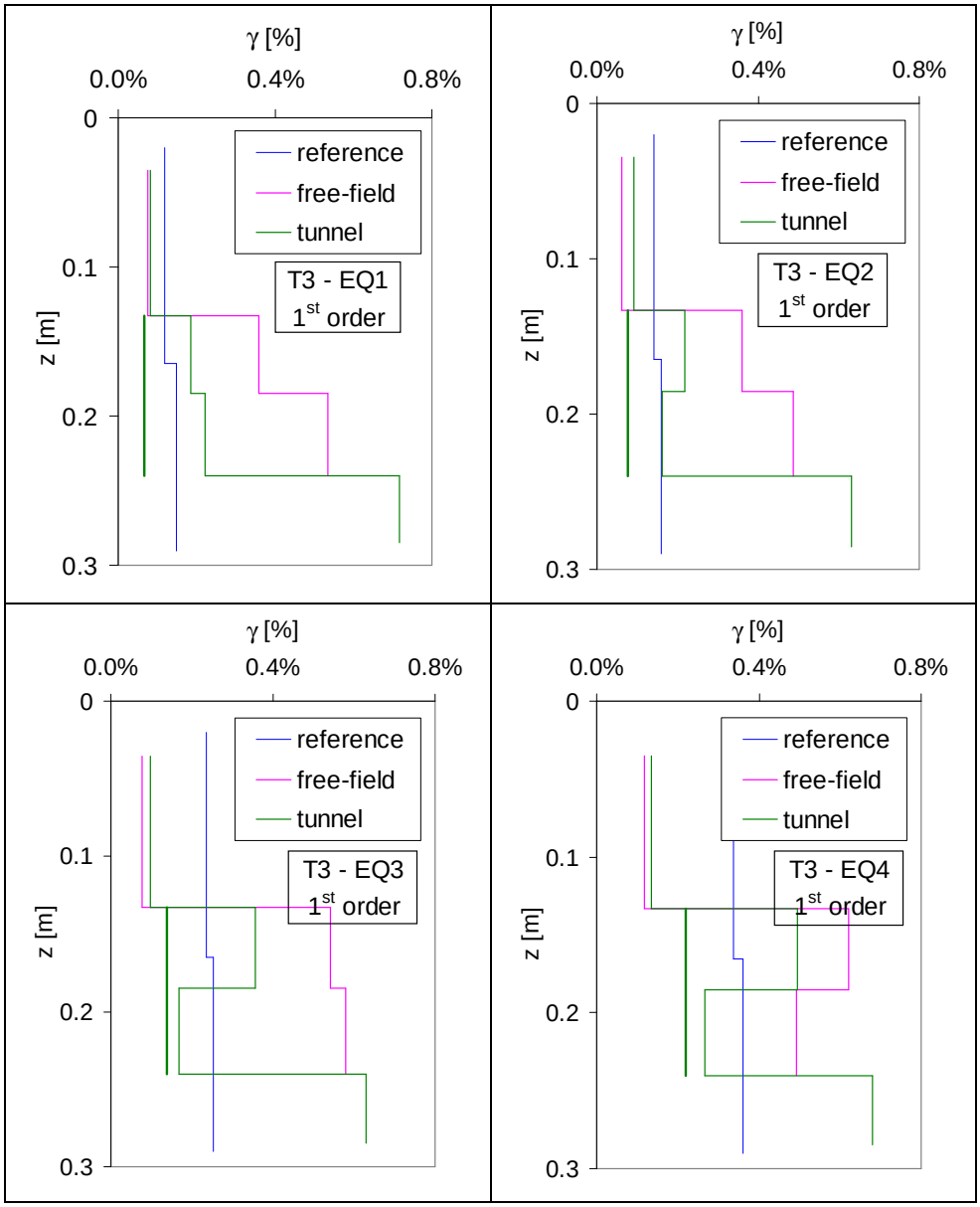
γ [%]
0.0%
0.4%
0.8%
0
0.1
0.2
0.3
z [m]
reference
free-field
tunnel
T3 - EQ1
1st order
T3 - EQ2
1st order
T3 - EQ3
1st order
T3 - EQ4
1st order

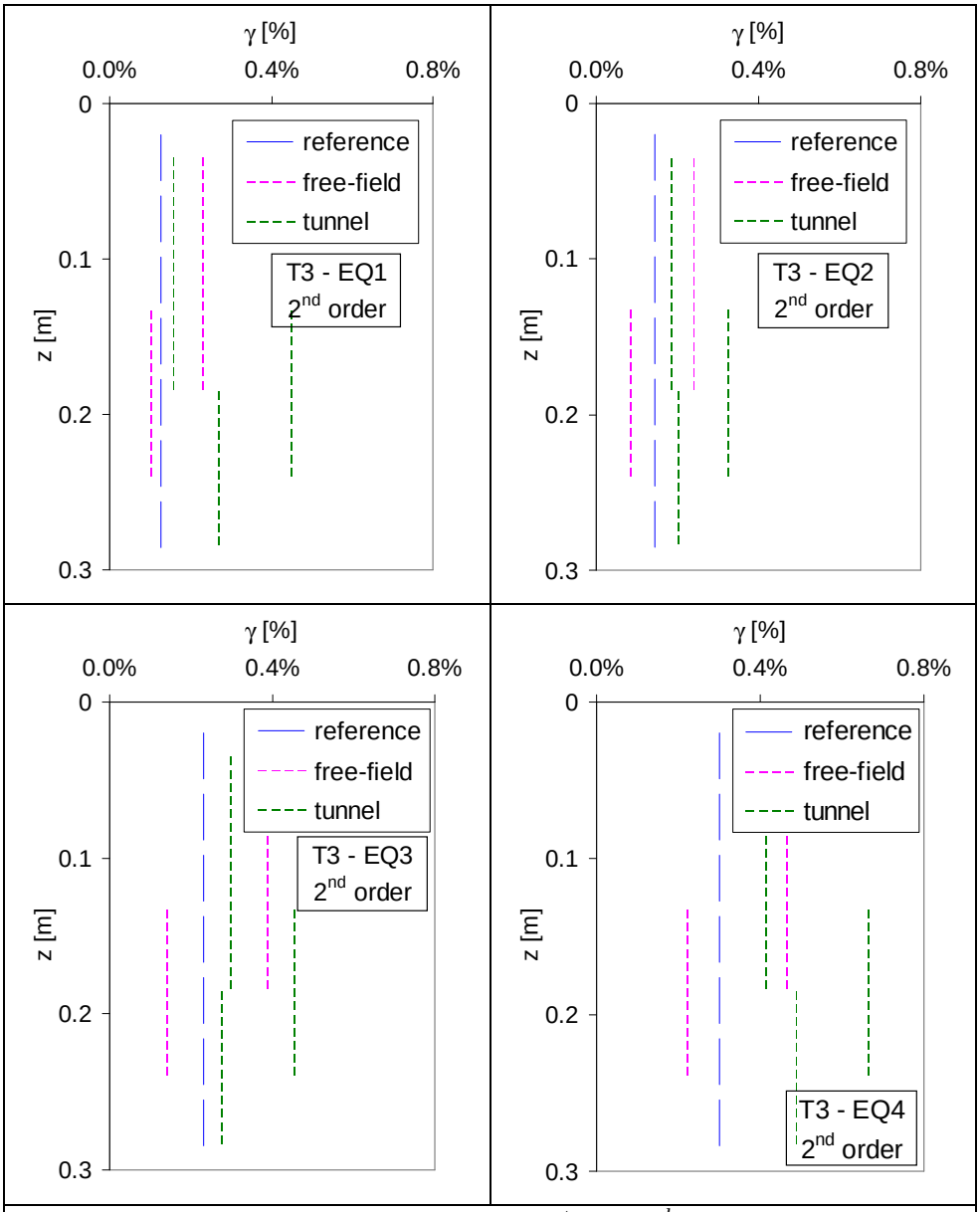

Fig 6.20: Shear strains of the model T3 (1st and 2nd order approximation)

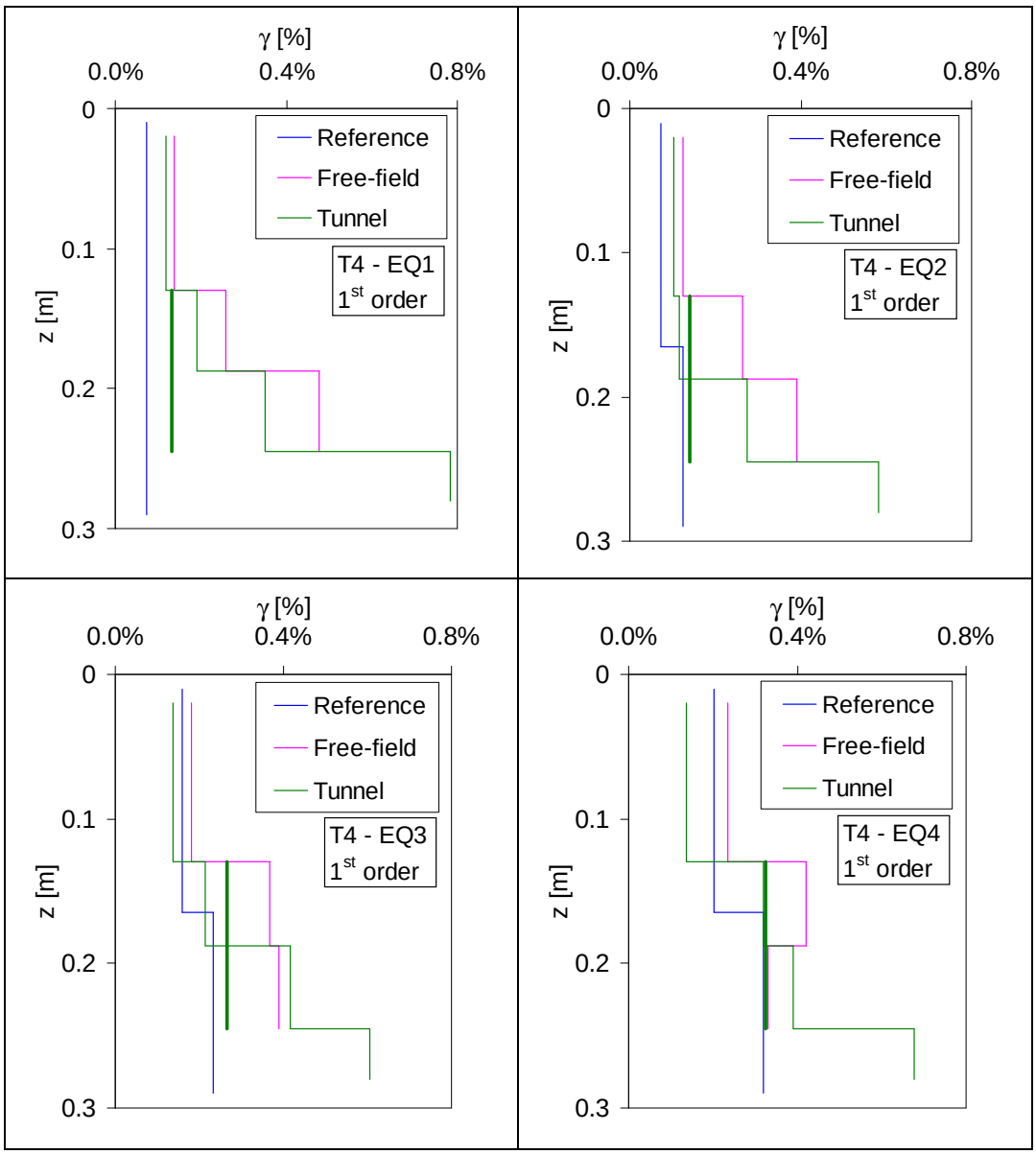
γ [%]
0.0%
0.4%
0.8%
0
0.1
0.2
0.3
z [m]
Reference
Free-field
Tunnel
T4 - EQ1
1st order
T4 - EQ2
1st order
T4 - EQ3
1st order
T4 - EQ4
1st order

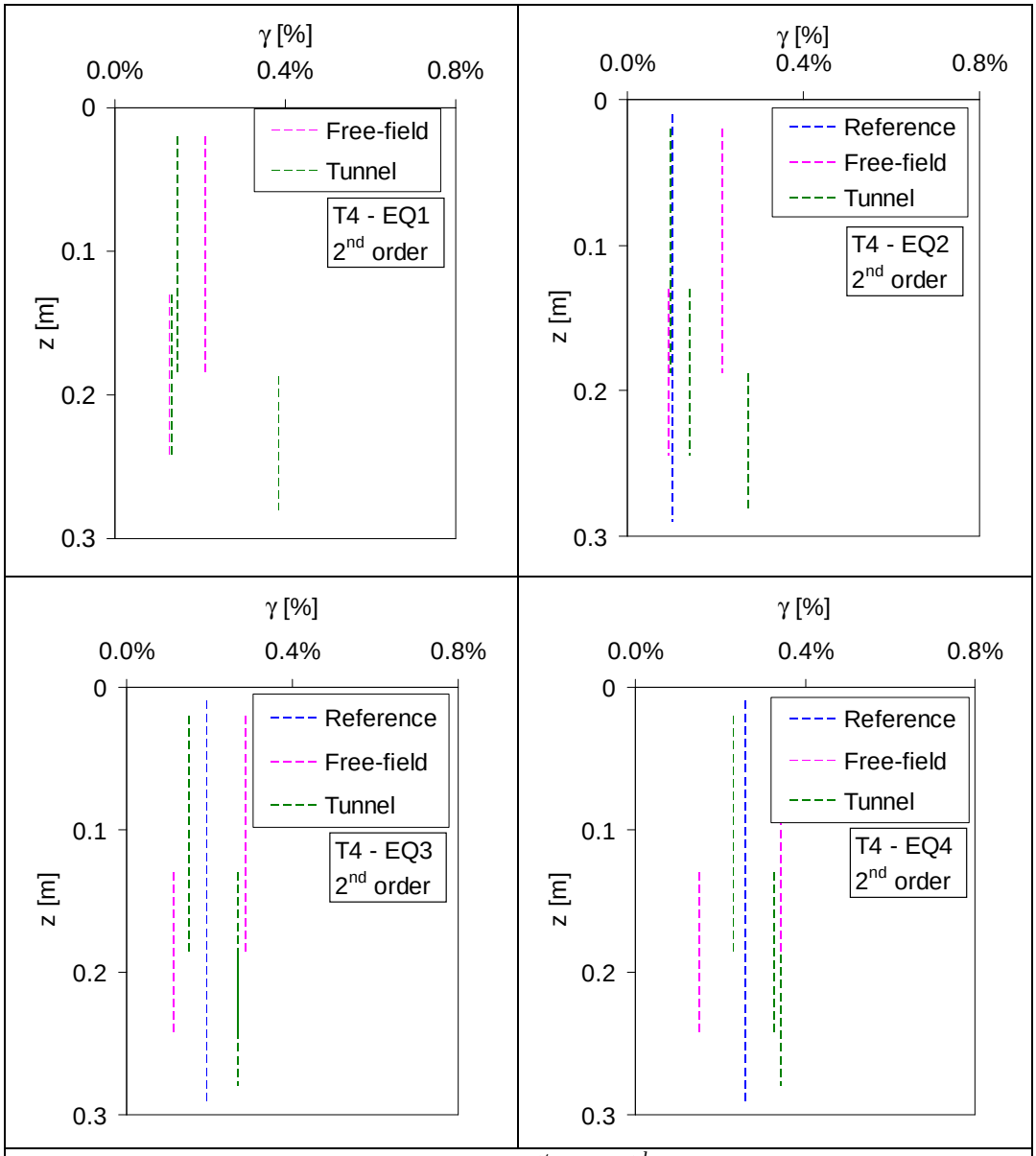

Fig 6.21: Shear strains of the model T4 (1st and 2nd order approximation)

The plotted shear strain in the figs.6.18-21 were generally high, greater than 0,05%, which corresponded to a strain level in which the mobilized shear stiffness was lower than the initial value. The strain level reached in the reference column always increased with depth and was generally lower

than the free field and tunnel alignment, especially around the tunnel depth. Therefore the calculated shear strains registered high variation both for the 1st and 2nd order evaluation. The ovaling of the tunnel was evaluated, using a 1st order approximation, from the accelerometers above and under the tunnel; the ovaling deformation value (plotted in bold green) was generally lower than the calculated values of the free-field and tunnel alignments. Instead the shear strain of the tunnel vertical were obtained considering also the ACC3 which was located in every test laterally to the tunnel. The shear strains evaluated with the 2nd order approximation were generally lower (0.4%) than the corresponding 1st order ones (0.8%), giving a probable overestimation of the real value. Moreover the strains calculated from two instruments located at very closed distance were generally higher, due probably to an underestimation of the distance between the accelerometers. Therefore during the test phase the model suffered settlement that could change the reciprocating positions of the instruments. The shear strain obtained in the first two earthquakes were generally similar and increased with the successive earthquakes, especially for the values which were initially lower.

Starting from the acceleration records, the shear stress value was given using the equation of shear beam. Considering the equilibrium of deformable column τ was obtained from the integration of the acceleration time histories in the space domain (Zeghal & Elgamal, 1994):

$$\tau(z) = \int_0^z \rho a dz \tag{6.9}$$

In order to maintain the exact location of accelerometers during the flight the instruments were buried of 20mm. For this reason a measurement of surface acceleration was not available. A linear fit was performed in order to evaluate the surface acceleration using the adjacent pair of instruments:

$$a(z) = a_1 + \frac{(a_2 - a_1)}{(z_2 - z_1)}(z - z_1) \tag{6.10}$$

The eq.(6.10) was used to fit the acceleration at a generic depth z, in which z_1 and z_2 were the depths of two adjacent instruments, for which the recorded time histories were a_1 and a_2. The profiles of the calculated shear

stresses for each fired earthquake of the centrifuge models were reported in the fig 6.22-25.

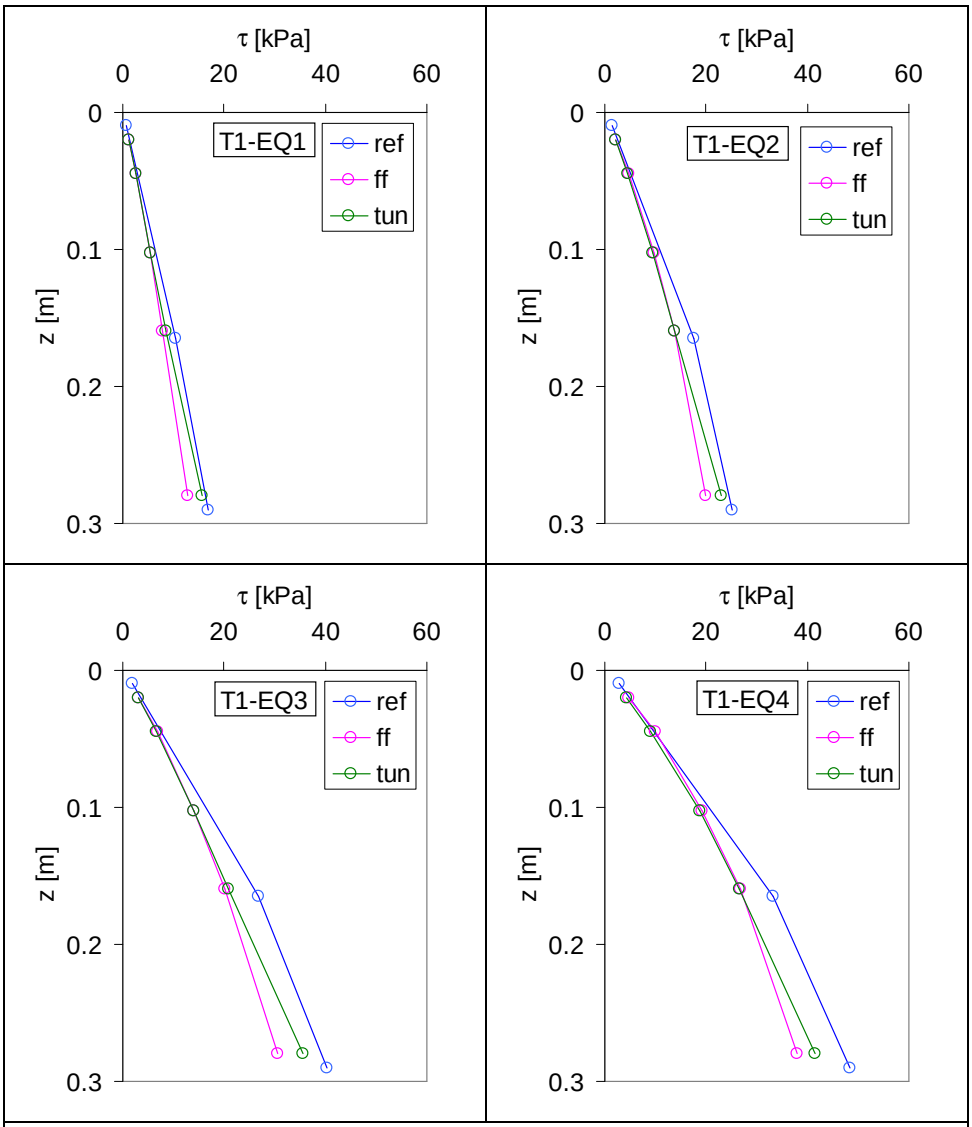

Fig 6.22: Shear stresses of the model T1

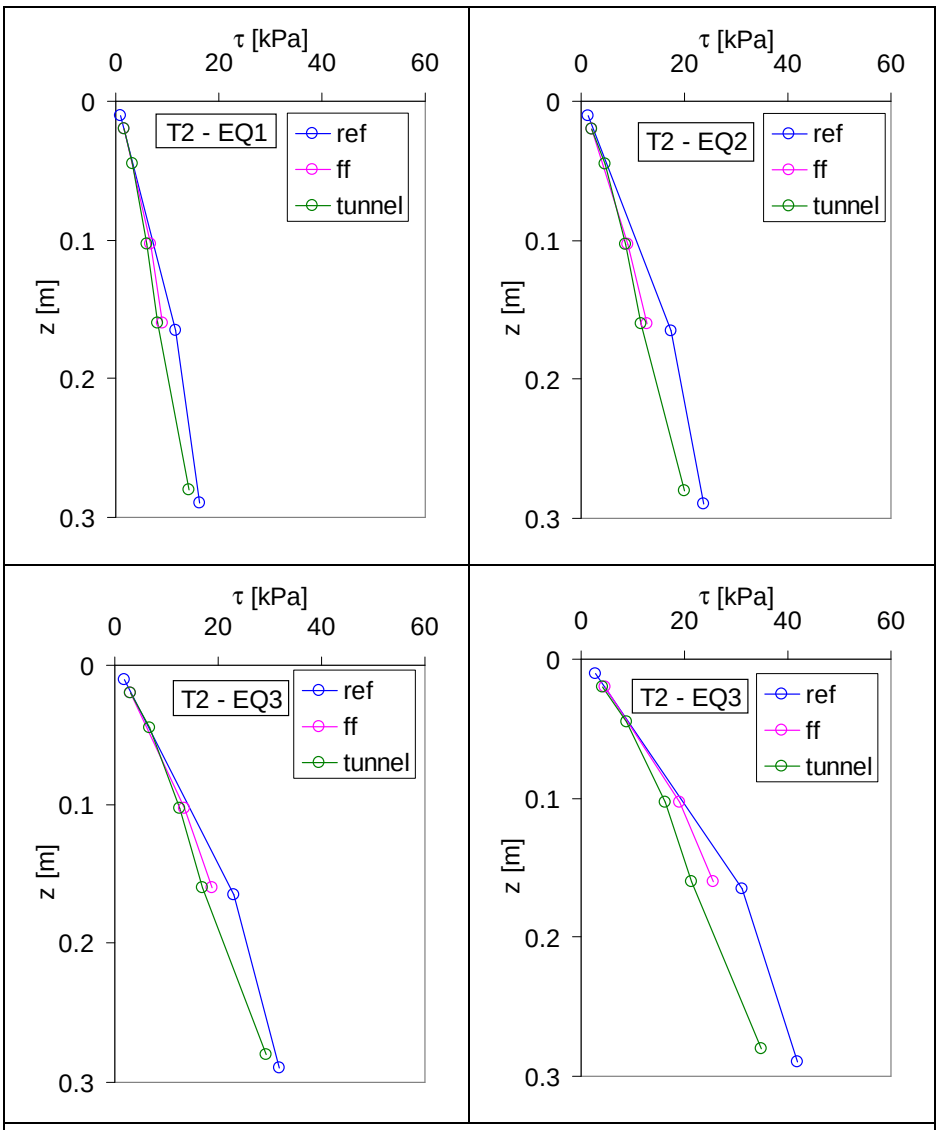

Fig 6.23: Shear stresses of the model T2

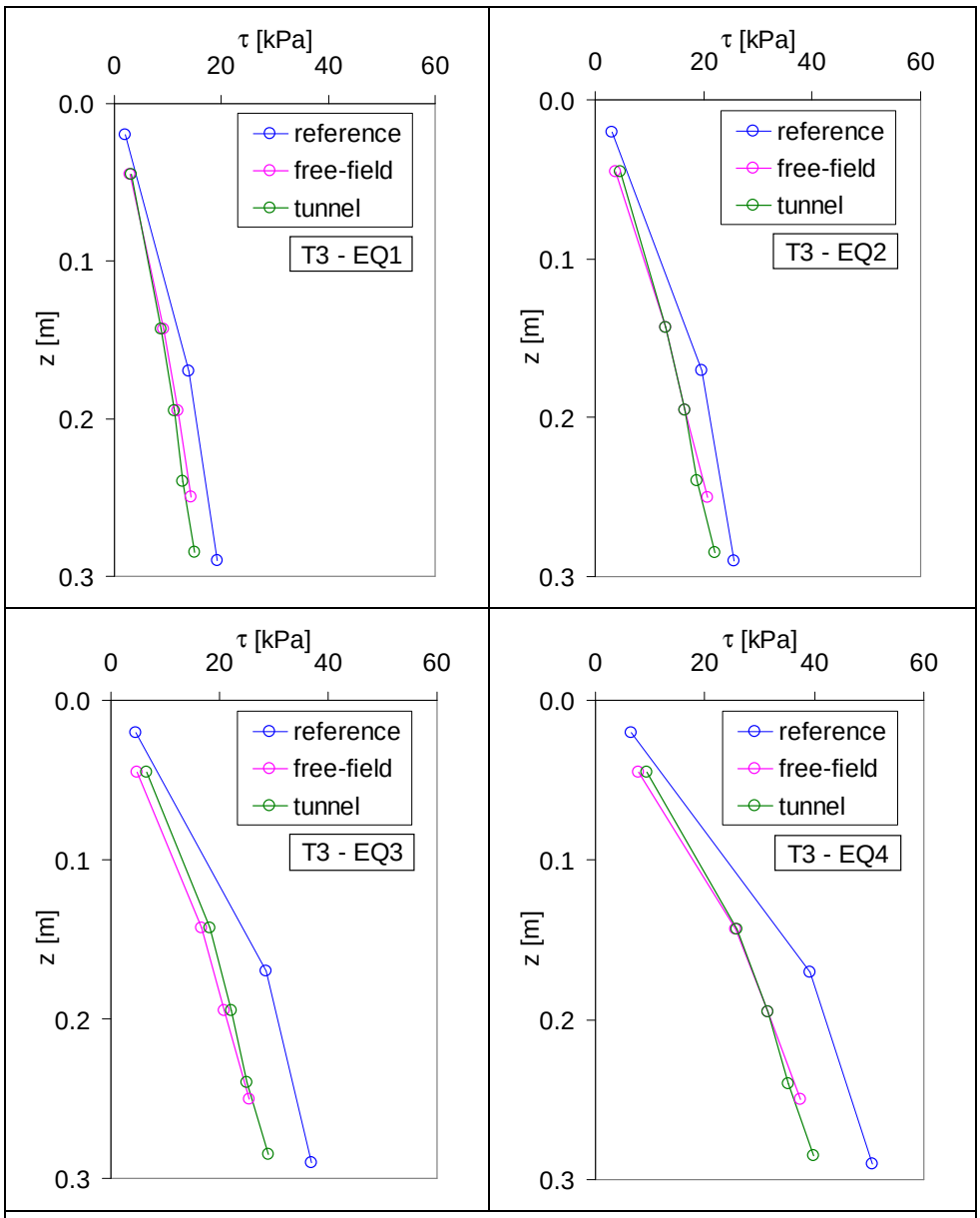

Fig 6.24: Shear stresses of the model T3

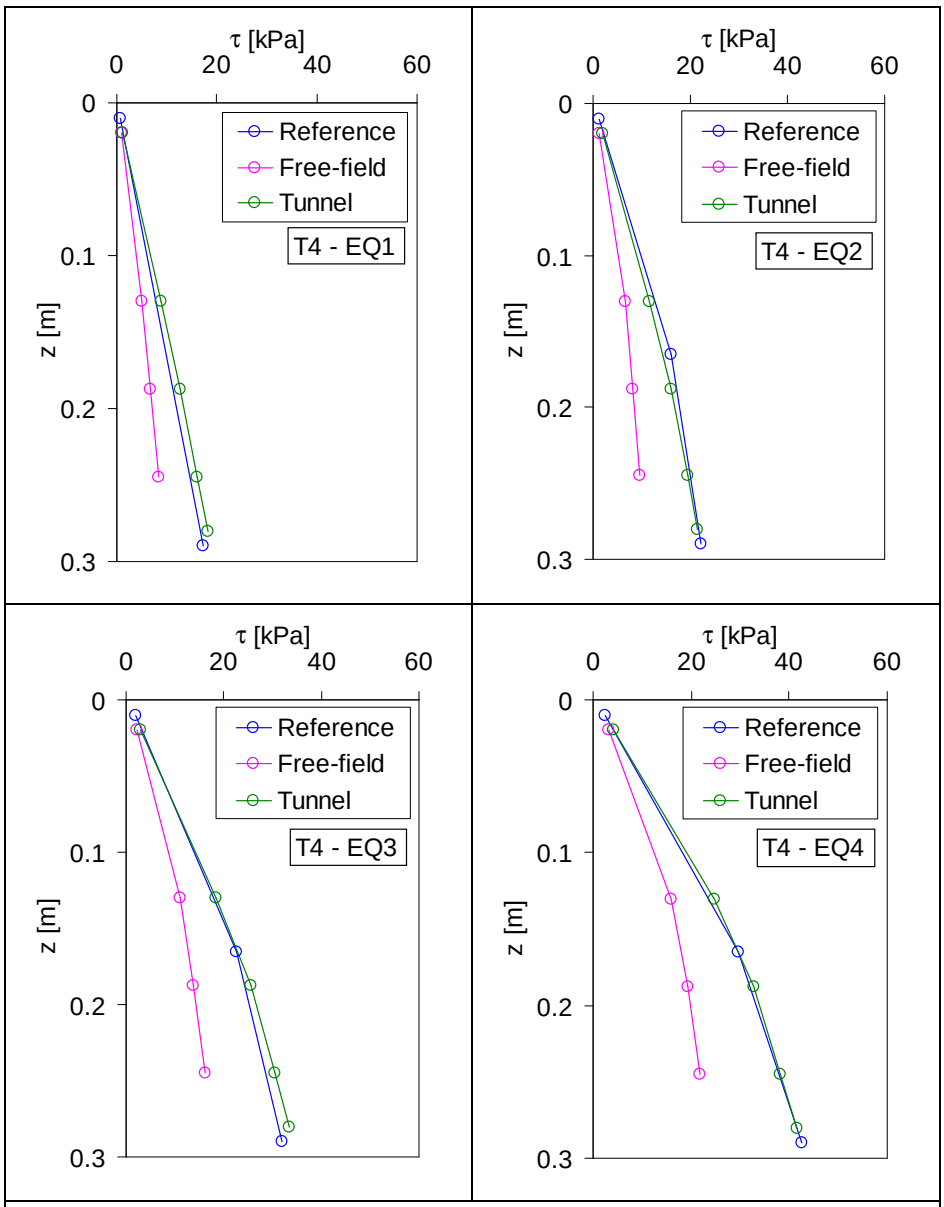

Fig 6.25: Shear stresses of the model T4

The profiles of shear stresses were generally regular, showing in all the cases an increasing of values with depth, which was lower than linear. The stresses obtained by the acceleration recordings of the reference verticals were generally higher compared to the free-field and tunnel verticals. The

maximum value in each vertical were included in the range 10-60kPa for the reference verticals; instead the free-field vertical was always lower than 40kPa.

Once the shear stresses and the shear strain were evaluated from the accelerometers outputs, all the data were put in a graph of shear strain against shear stress, in order to evaluate the loops. An example of the stress-strain cycles was reported in the fig.6.26, considering the same position in different earthquakes.

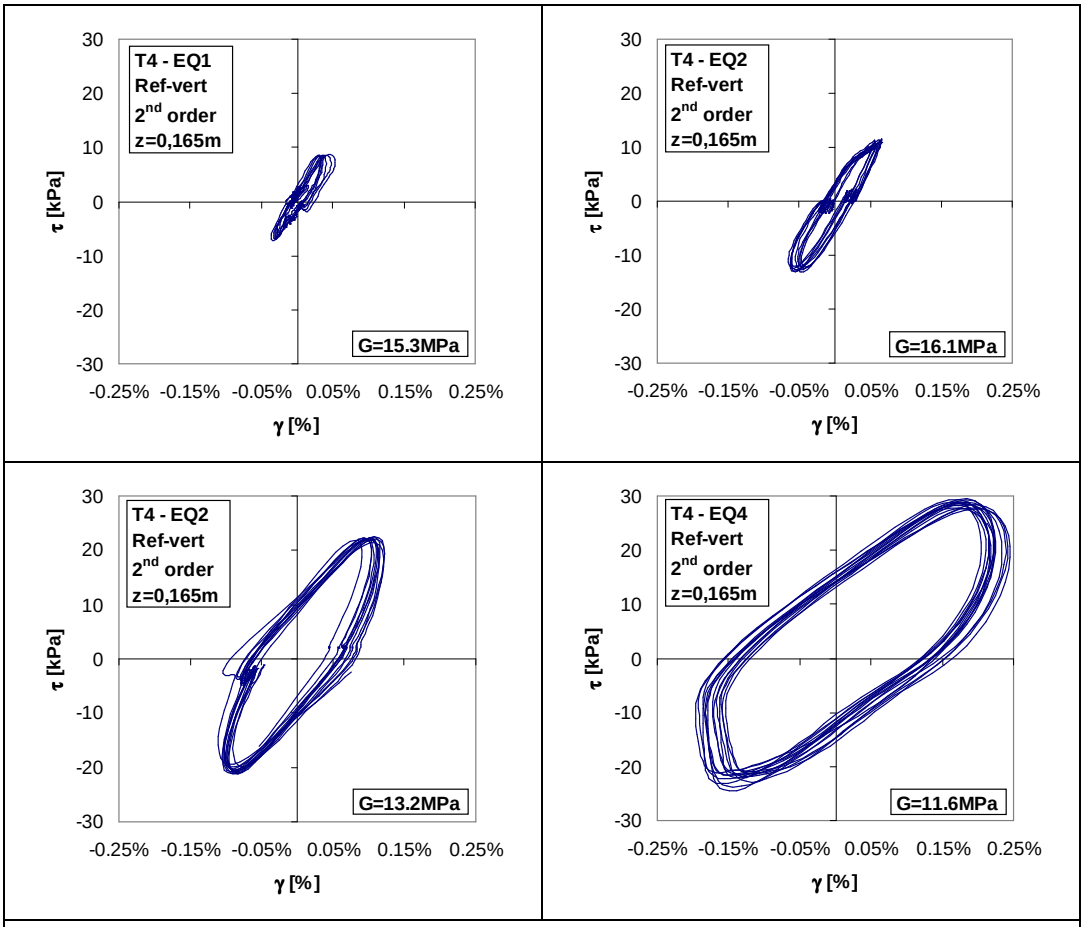

Fig 6.26: Stress-Strain cycles

The signals were not a single frequency motion, and the cycles were affected to the higher frequency, showing many tangent changes in the

curve. Moreover the shear stresses derived from the acceleration, which were filtered one time; instead the shear strains were obtained by the displacements which were filtered two times, causing a cleaning of the signal by the higher frequencies. Despite of this irregular shape, the estimation of shear stiffness by the cycles generally gave a reliable value of G_{mob}, compared to over-filtered signals, in which only the signal main frequency was considered. The mobilized shear stiffness was calculated in each cycle as:

$$G_{mob} = \frac{\tau_{max} - \tau_{min}}{\gamma_{max} - \gamma_{min}} \tag{6.11}$$

Using the eq,(6.11) the profiles of mobilized stiffness for the three instrumented verticals was showed in the fig.6.27-30, considering both the shear stains obtained from 1st and 2nd order approximation calculation.

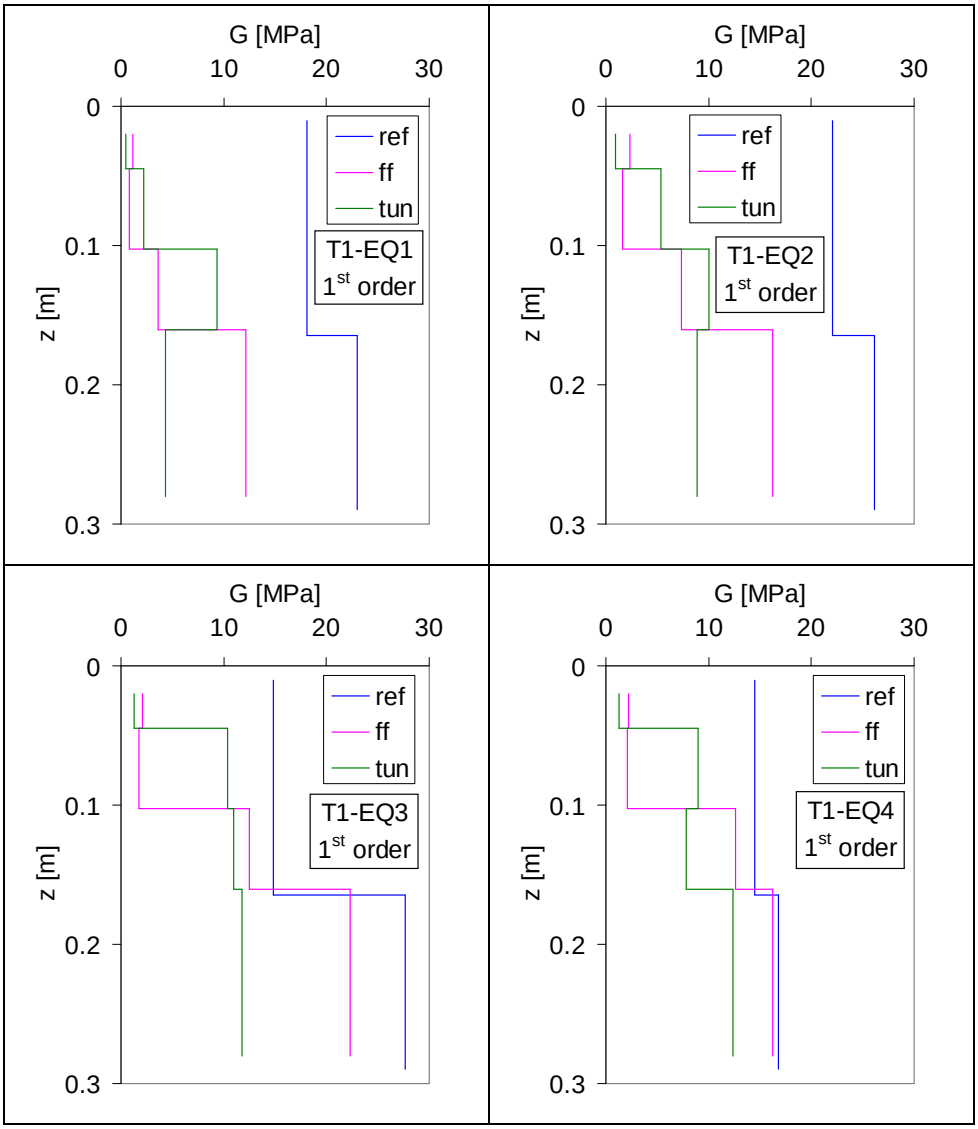
G [MPa]
0
10
20
30
z [m]
0
0.1
0.2
0.3
ref
ff
tun
T1-EQ1
1st order
T1-EQ2
1st order
T1-EQ3
1st order
T1-EQ4
1st order

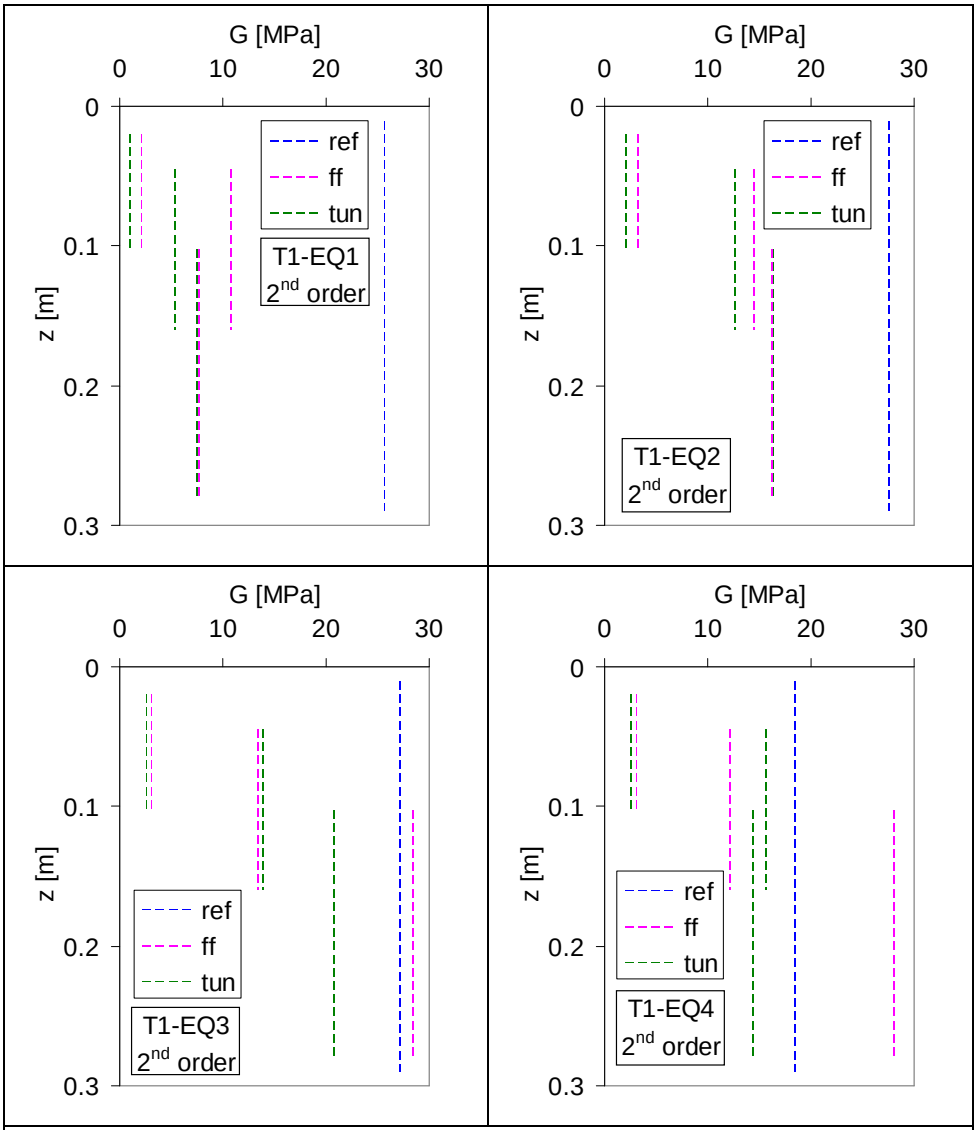

Fig 6.27: Mobilized shear stiffness of the model T1 (1^{st} and 2^{nd} order approximation)

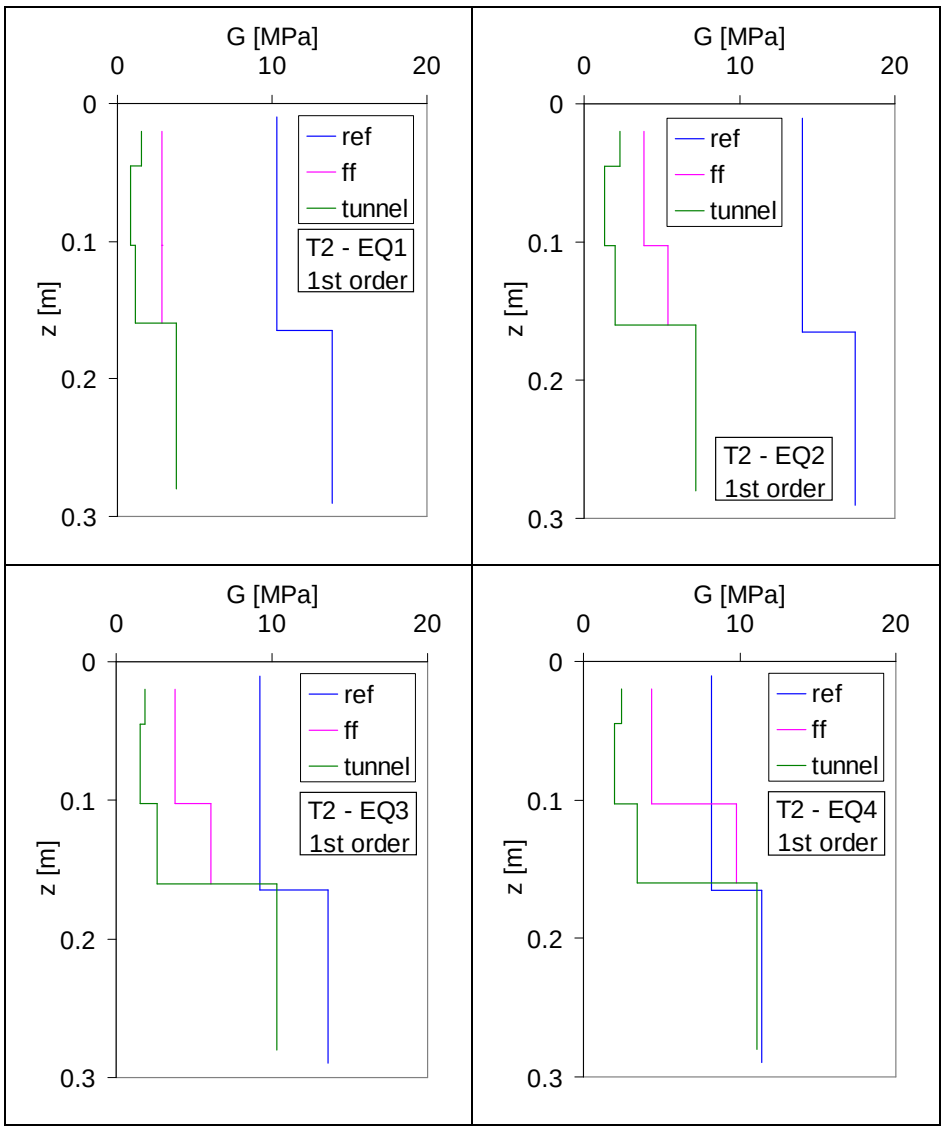
G [MPa]
0
10
20
z [m]
0
0.1
0.2
0.3
ref
ff
tunnel
T2 - EQ1
1st order
T2 - EQ2
1st order
T2 - EQ3
1st order
T2 - EQ4
1st order

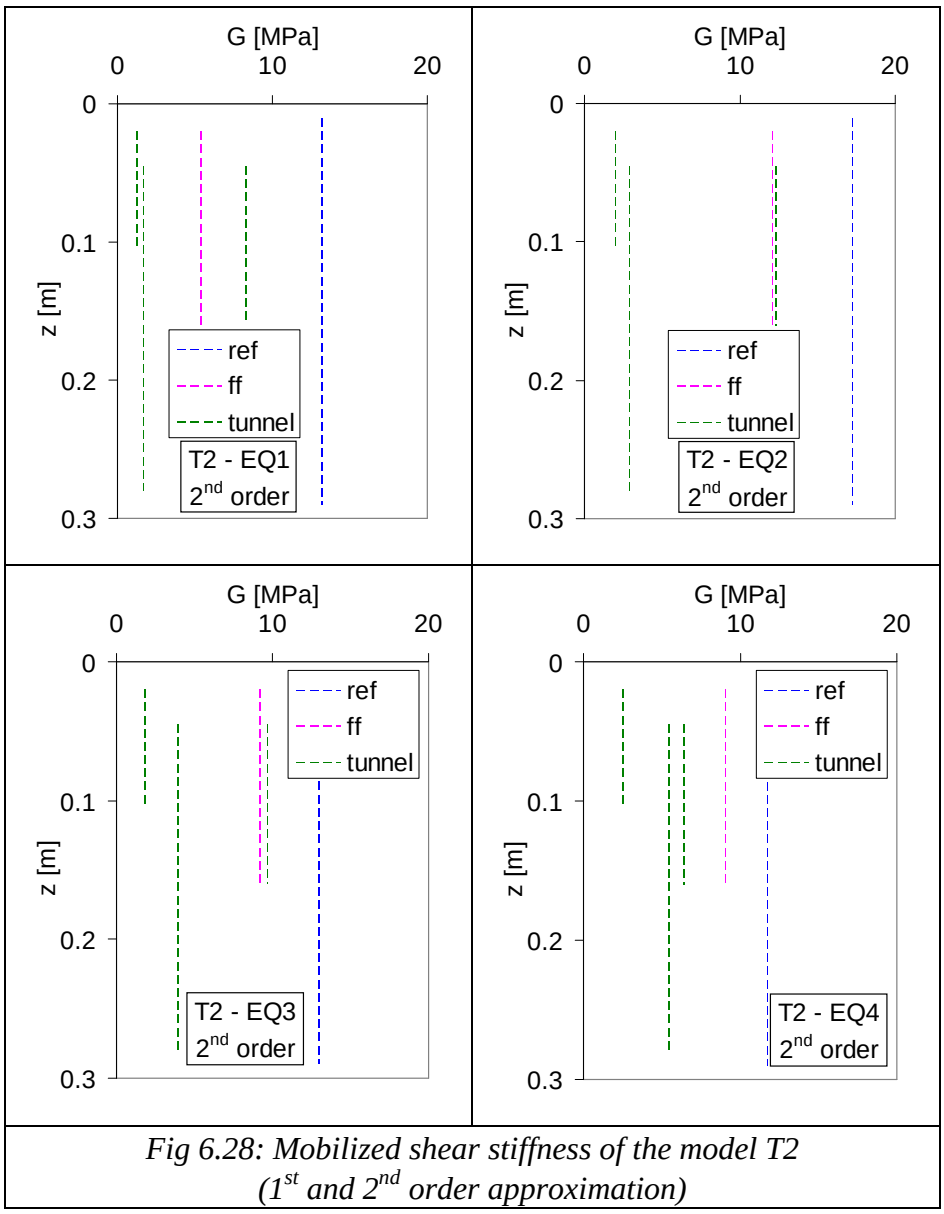

Fig 6.28: Mobilized shear stiffness of the model T2 (1^{st} and 2^{nd} order approximation)

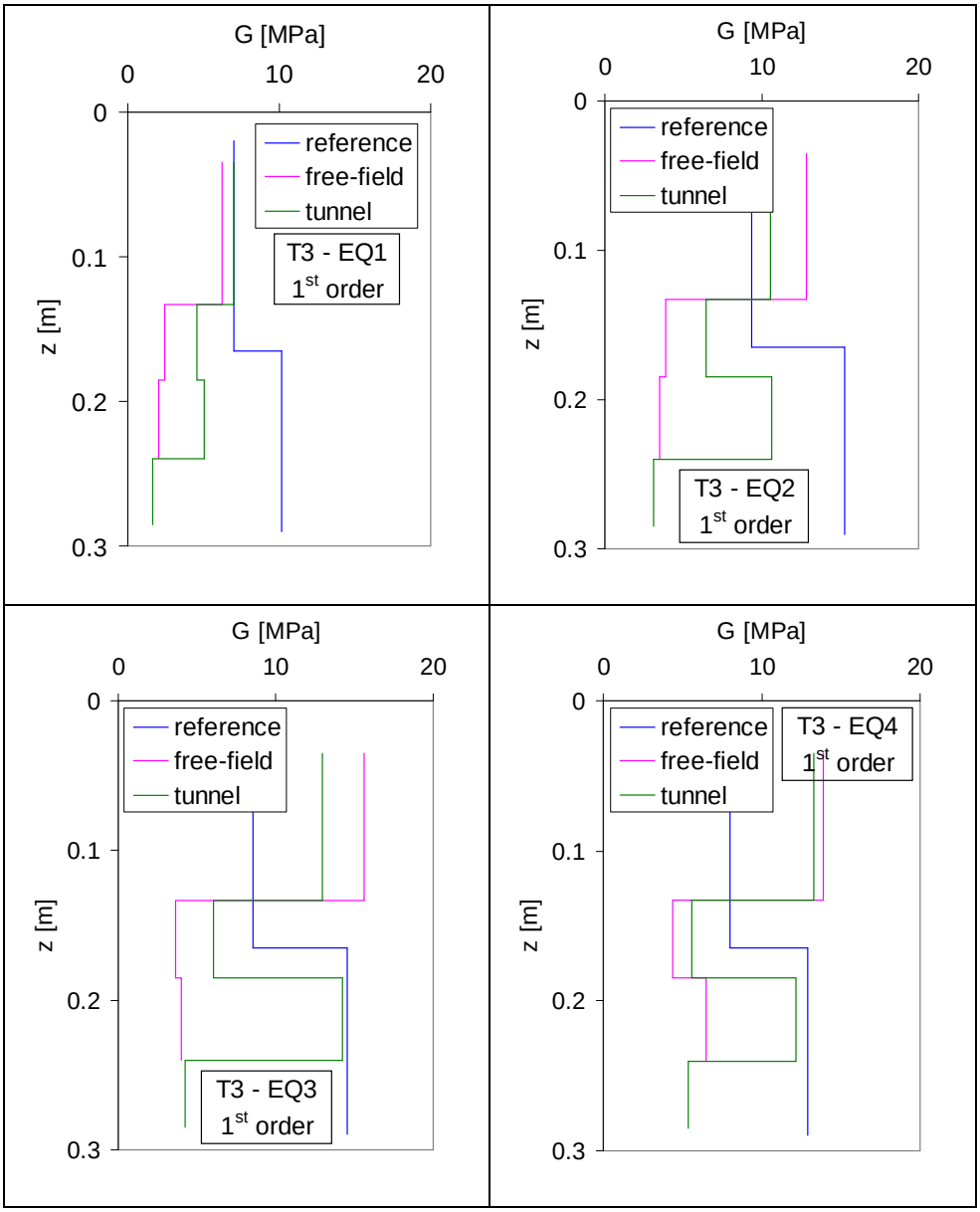
G [MPa]
0
10
20
z [m]
0
0.1
0.2
0.3
reference
free-field
tunnel
T3 - EQ1
1st order
T3 - EQ2
1st order
T3 - EQ3
1st order
T3 - EQ4
1st order

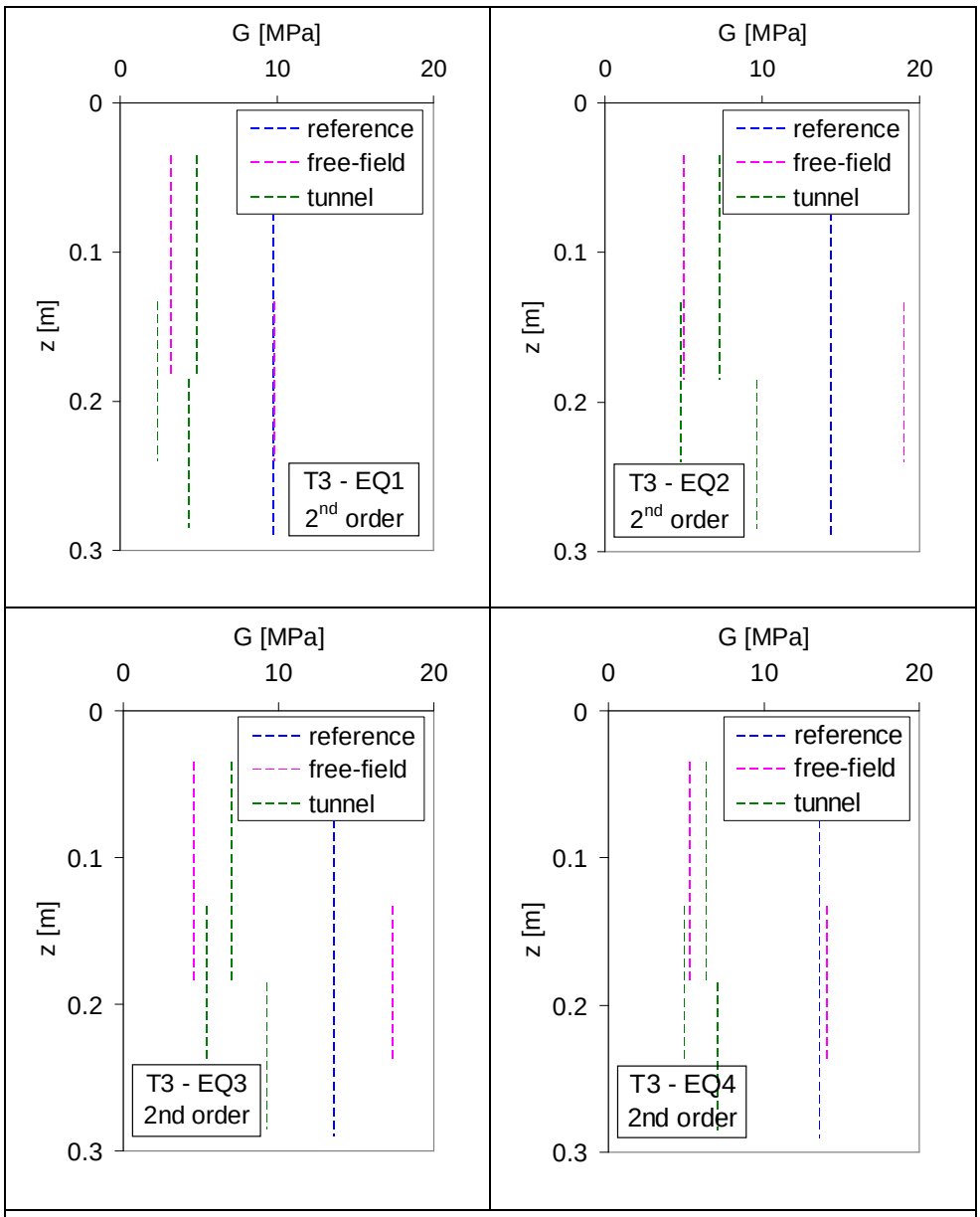

Fig 6.29: Mobilized shear stiffness of the model T3 (1^{st} and 2^{nd} order approximation)

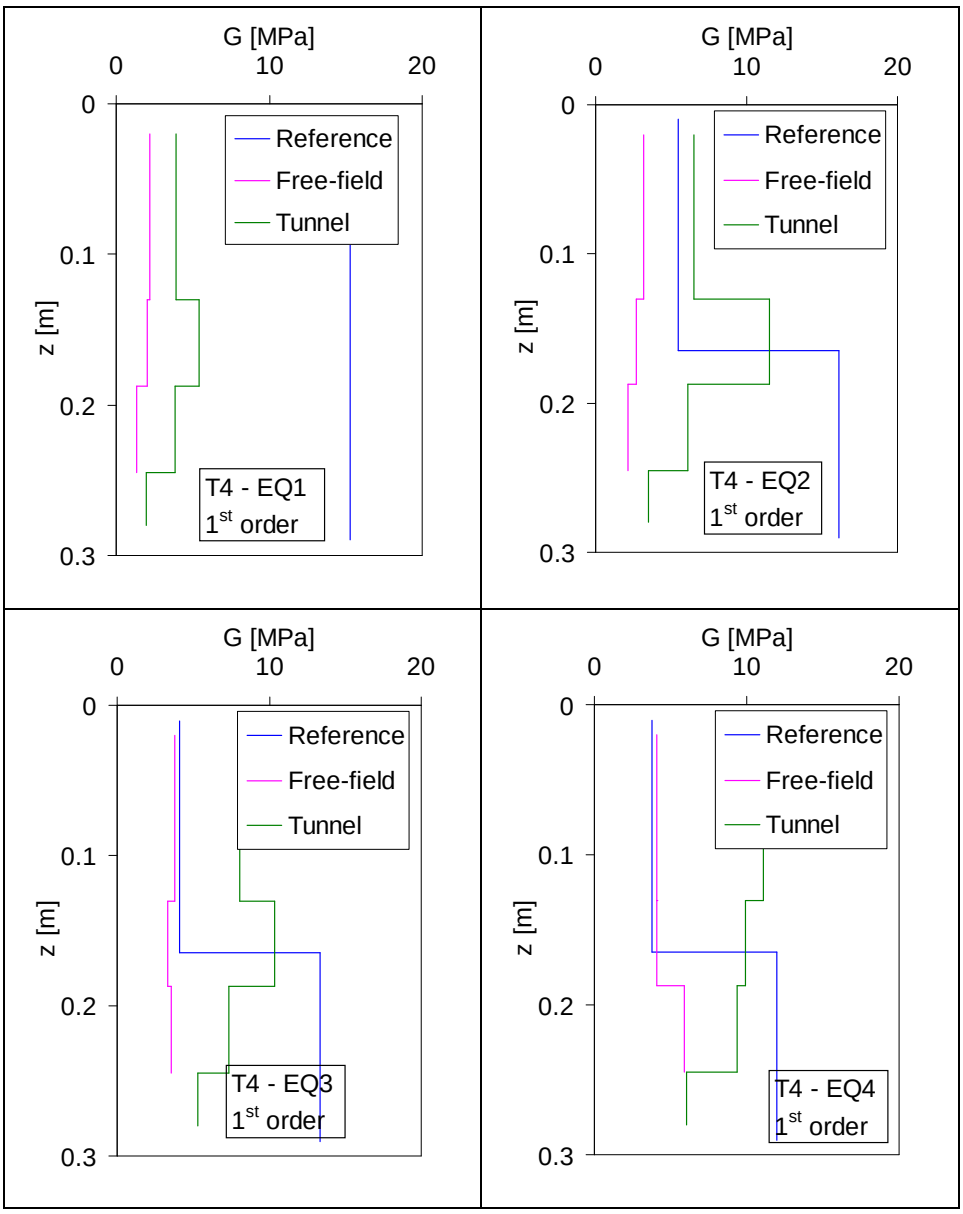
G [MPa]
0
10
20
z [m]
0
0.1
0.2
0.3
Reference
Free-field
Tunnel
T4 - EQ1
1st order
T4 - EQ2
1st order
T4 - EQ3
1st order
T4 - EQ4
1st order

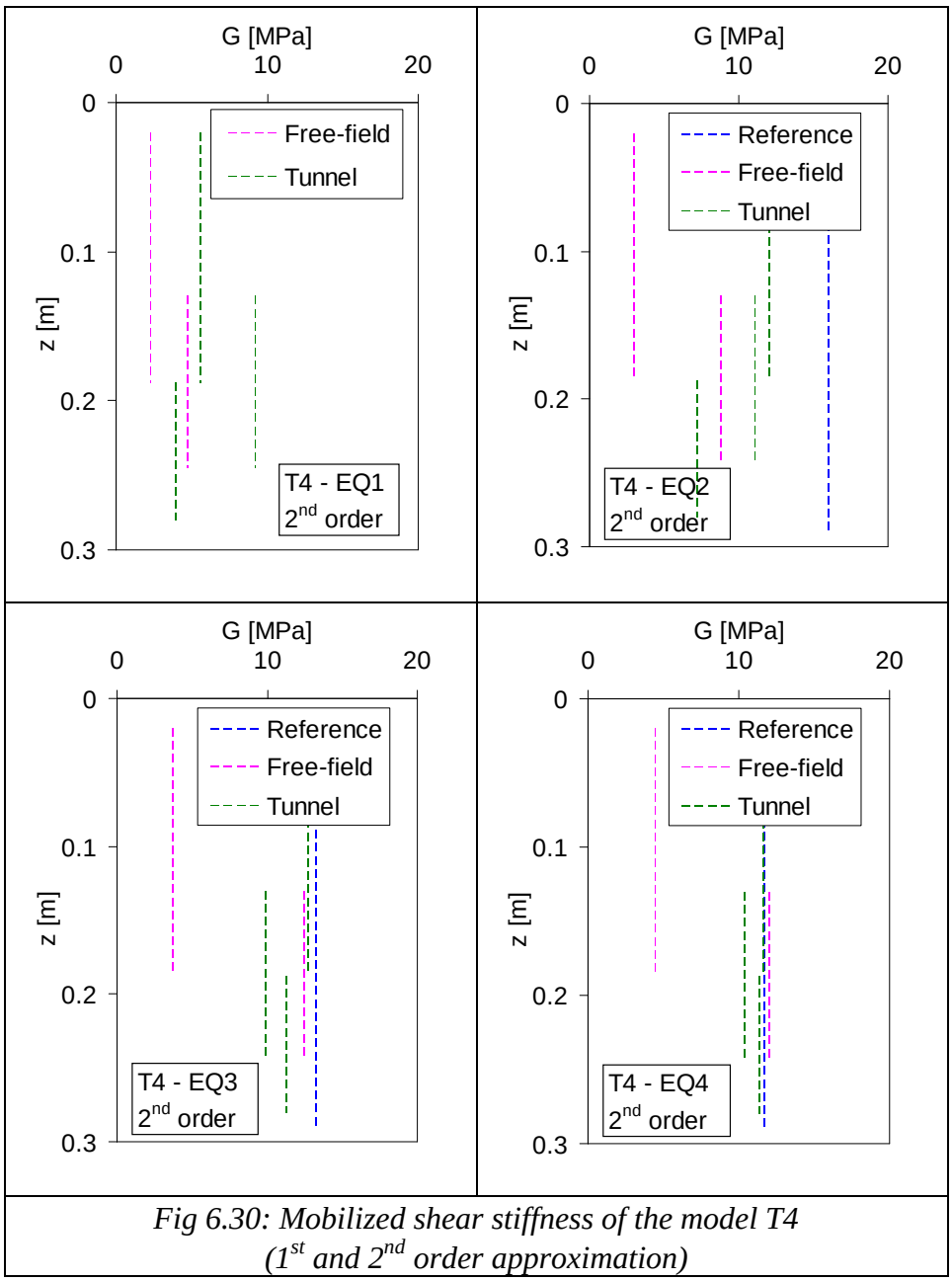

Fig 6.30: Mobilized shear stiffness of the model T4 (1^{st} and 2^{nd} order approximation)

The profiles of mobilized shear stiffness gave value always lower than 20MPa and registered maximum during the EQ2 event, despite this earthquake was not the less strong. Considering a first order approximation

for the calculation of the shear strains, the value of the shear stiffness of the reference vertical was always increasing with depth for all the fired earthquakes and was generally higher compared to the corresponding value of the free-field and tunnel verticals. Moreover also the mobilized shear stiffness of the internal verticals (free-field and tunnels) increased with depth for the shallow tunnel models; instead for the deep tunnel models the values of the profiles decreased or had not a monotonic trend. Similar consideration were obtained by the shear stiffness evaluated with a second order of approximation on the calculation of the shear strain: the mobilized G of the reference vertical was generally higher compared to the other verticals value; in some cases, however, the free-field deformation at tunnel depth registered the highest values. Also in these cases the profile of G was not always increasing with depth.

6.4 STRAIN GAUGES

6.4.1 Output signals

The measurements of bending moment and hoop force from the strain gauges transducers was directly given, expressed as a time histories of stress for each earthquake applied. The typical dynamic time histories given from both the bending moment and hoop force transducers were showed in fig.6.31: in every stress cases the final value was different from the initial value and the graph had an oscillation during the dynamic phase.

As observed also from the LVDT measurements, during the model shaking permanent deformations in the model occurred. The internal forces result was an increasing stress during the dynamic phase, which caused, close to the tunnel surface, a residual stress at the end of the earthquake. The entity of residual component was not negligible compared to oscillation entity, because in some cases the trend was 4-5 times larger compared to the deviation to the average value.

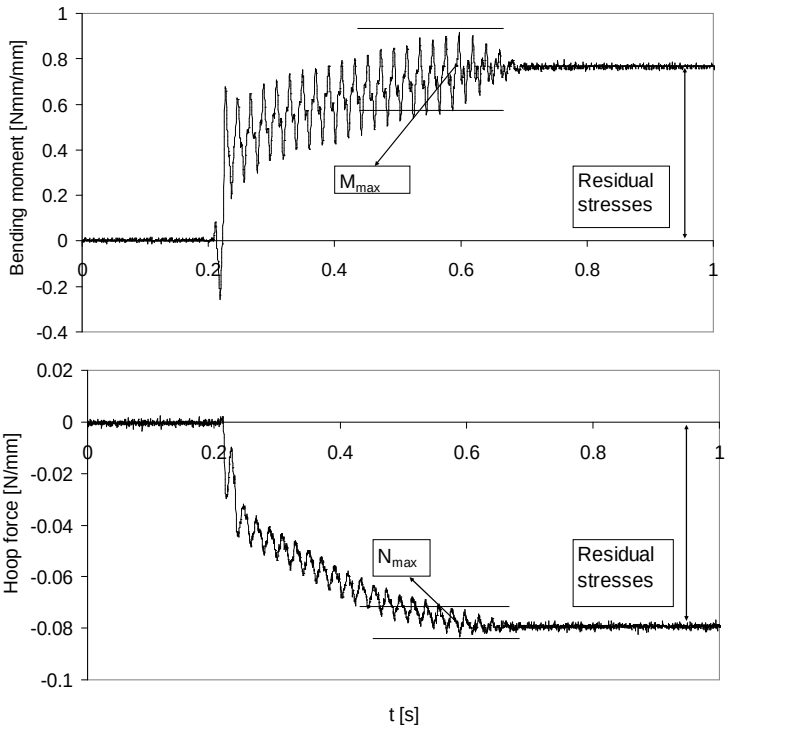

Fig.6.31: Recordings of the bending moments and hoop forces

This transducer response was probably due to a densification of the sand during the soil shaking. This condition was confirmed from the visual measurements of soil surface before and after the flight: in every model cases a settlement from the initial height was found. In the next sections the stain gauges data, registered by the acquisition system, were reported for the swing up and the dynamic phase, in order to consider the values both of the oscillation and the permanent components.

6.4.2 Swing up data

During the swing up phases the model was subjected to increasing levels of gravity acceleration, corresponding to higher values of angular velocity of the centrifuge arms. The results for the internal forces were an absolute increasing of the hoop forces and bending moments, because the increment of gravity forces determined and weight of the soil column above the tunnel. The data of the swing-up phase was given both through Junction

Box recordings and video readings during the test. The scaling factor at every level of g was clearly different and for this reason the swing up data were reported at the model scale.

In the figs. 6.33-36 the bending moments in the swing up phase were plotted for the four models, considering the two instrumented section. Same representation were carried out for the hoop forces (fig. 6.37-40). The location of the transducers were represented by the numbers of the strain gauges reported in the fig. 6.32.

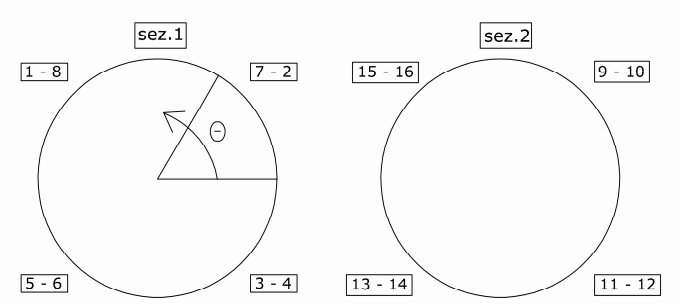

Fig.6.32: Location of the strain gauges in the cross section

The plotted data were obtained from the recordings of the acquisition system, except for the model T4, in which the swing up data were not saved after the tests (fig. 6.41). Similar problem exhibits the swing up recordings of the T2, which were incomplete, but, considering the coincidence with the readings, were completed with these last checking values. Moreover for the T1 test two swing up were performed until the earthquakes were fired: the data of the first swing up were reported in order to check the difference between the measurements. Therefore the comparison showed that the internal forces data were generally consistent, reaching values slightly higher during the first flight.

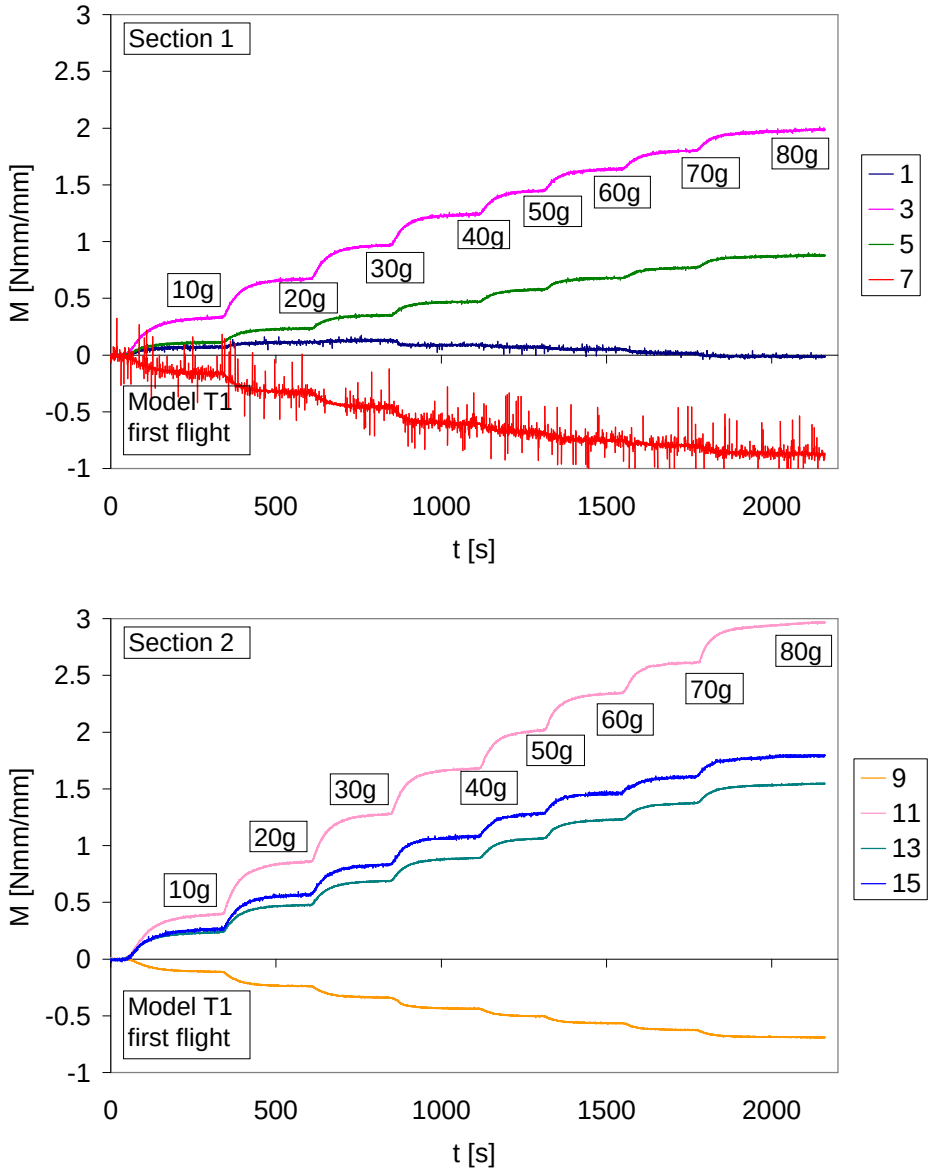

Fig.6.33: Bending moments measurements in the swing up phase (model T1 - first flight)

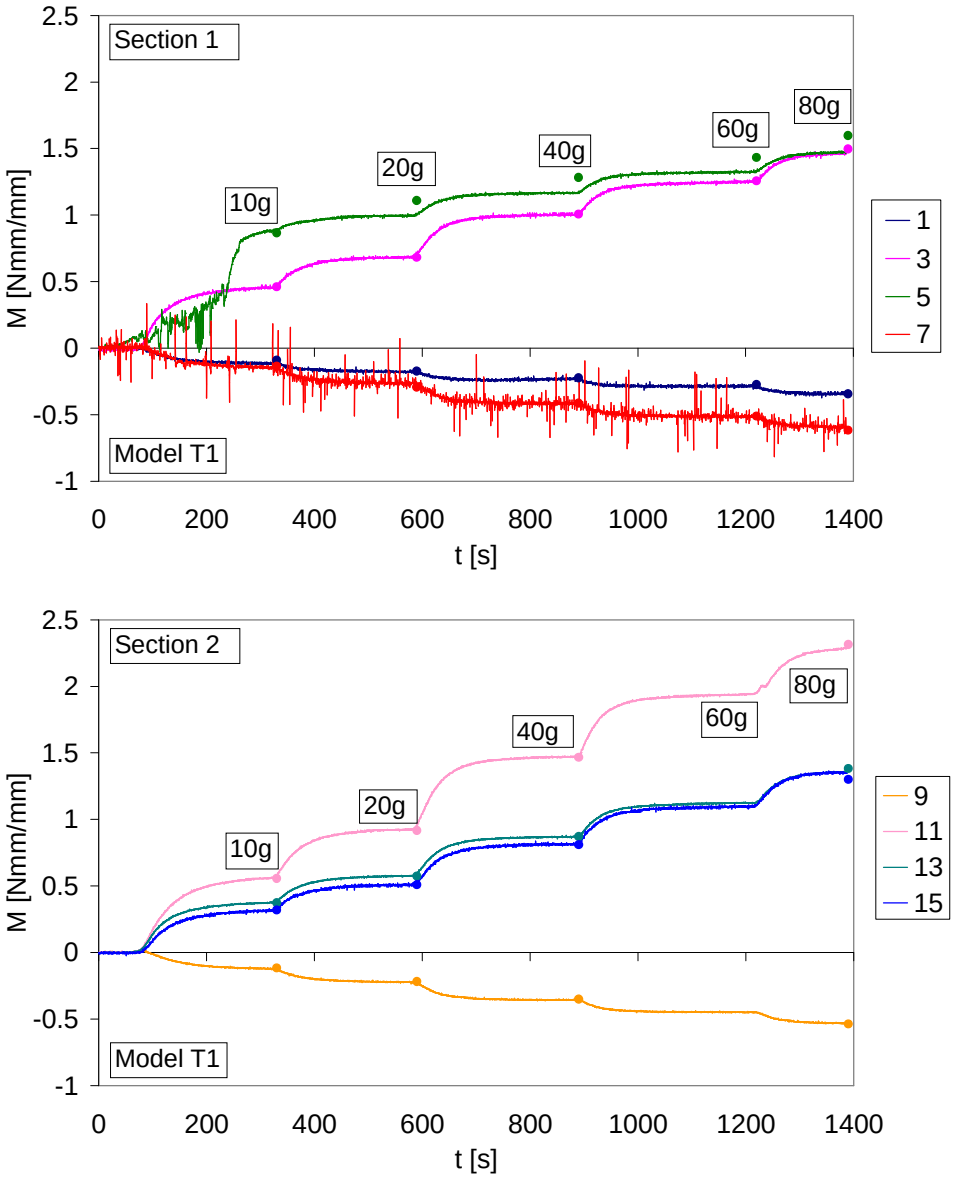

Fig.6.34: Bending moments measurements in the swing up phase (model T1 - second flight)

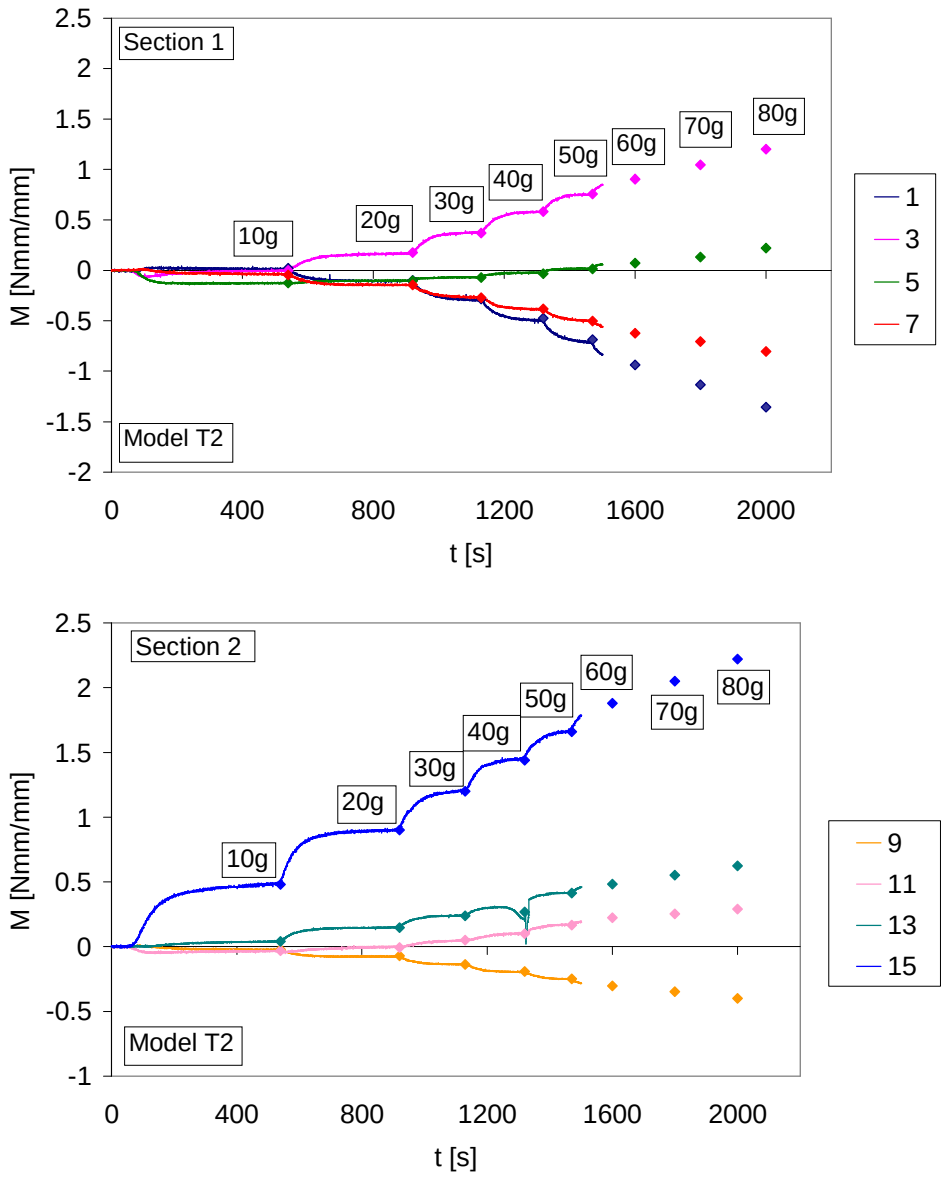

Fig.6.35: Bending moments measurements in the swing up phase (model T2)

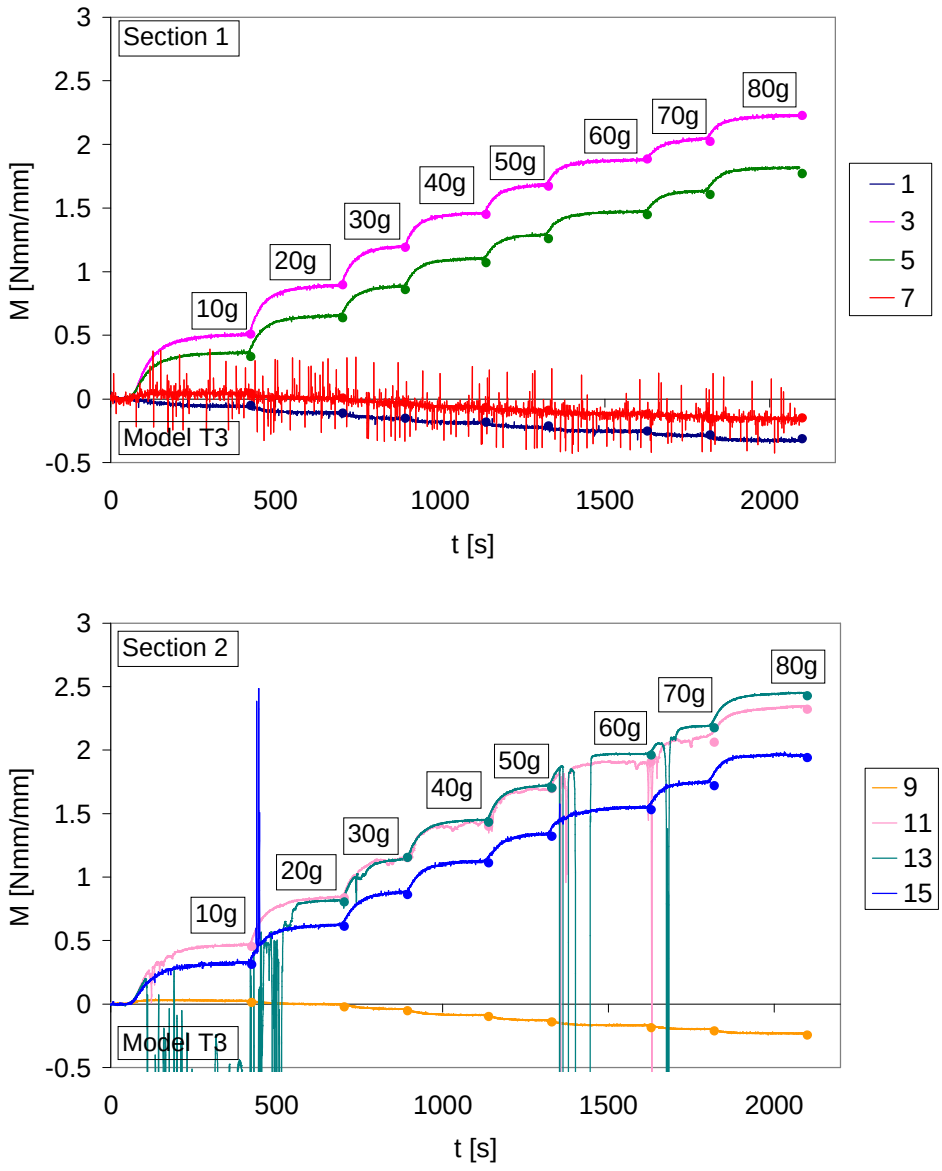

Fig.6.36: Bending moments measurements in the swing up phase (model T3)

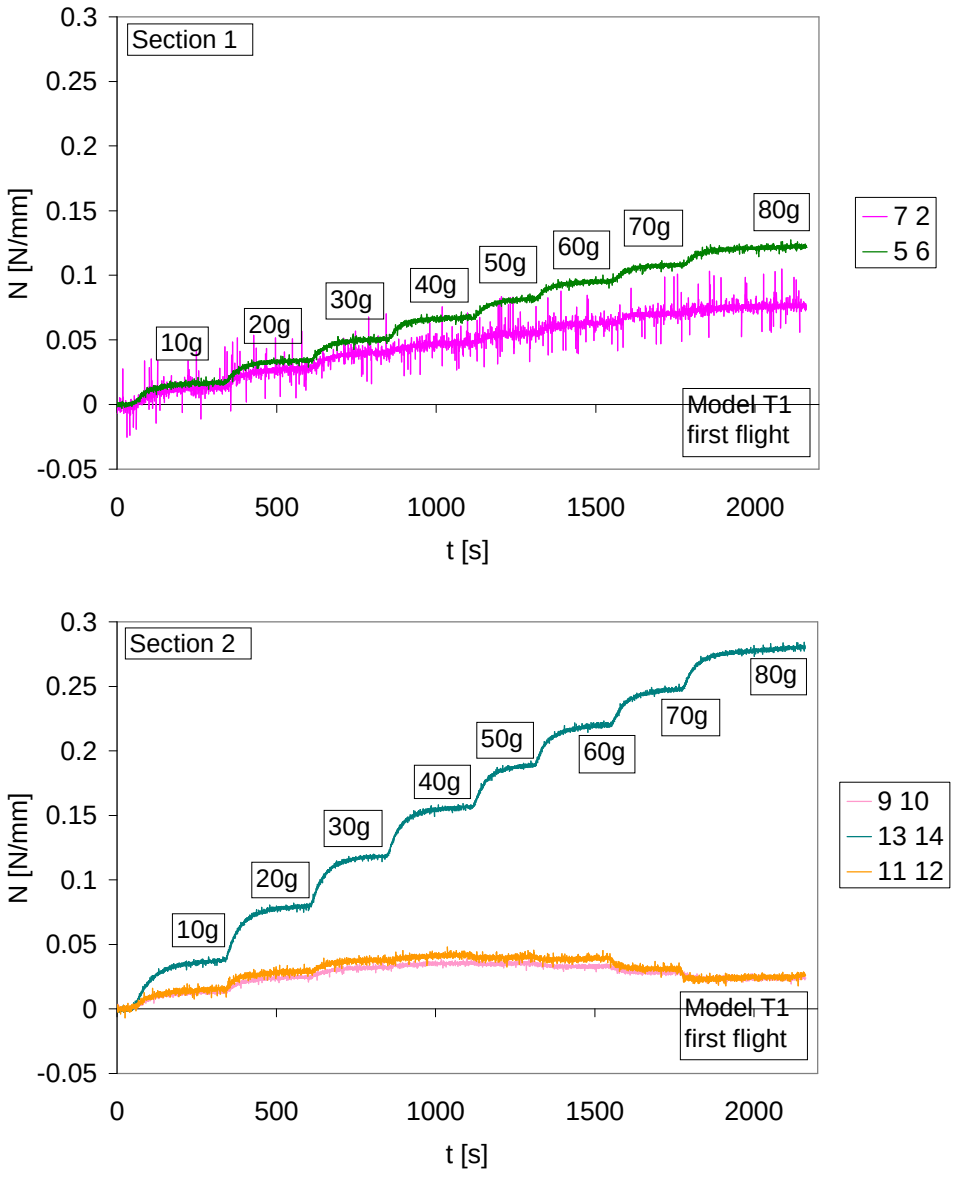

Fig.6.37: Hoop forces measurements in the swing up phase (model T1 - first flight)

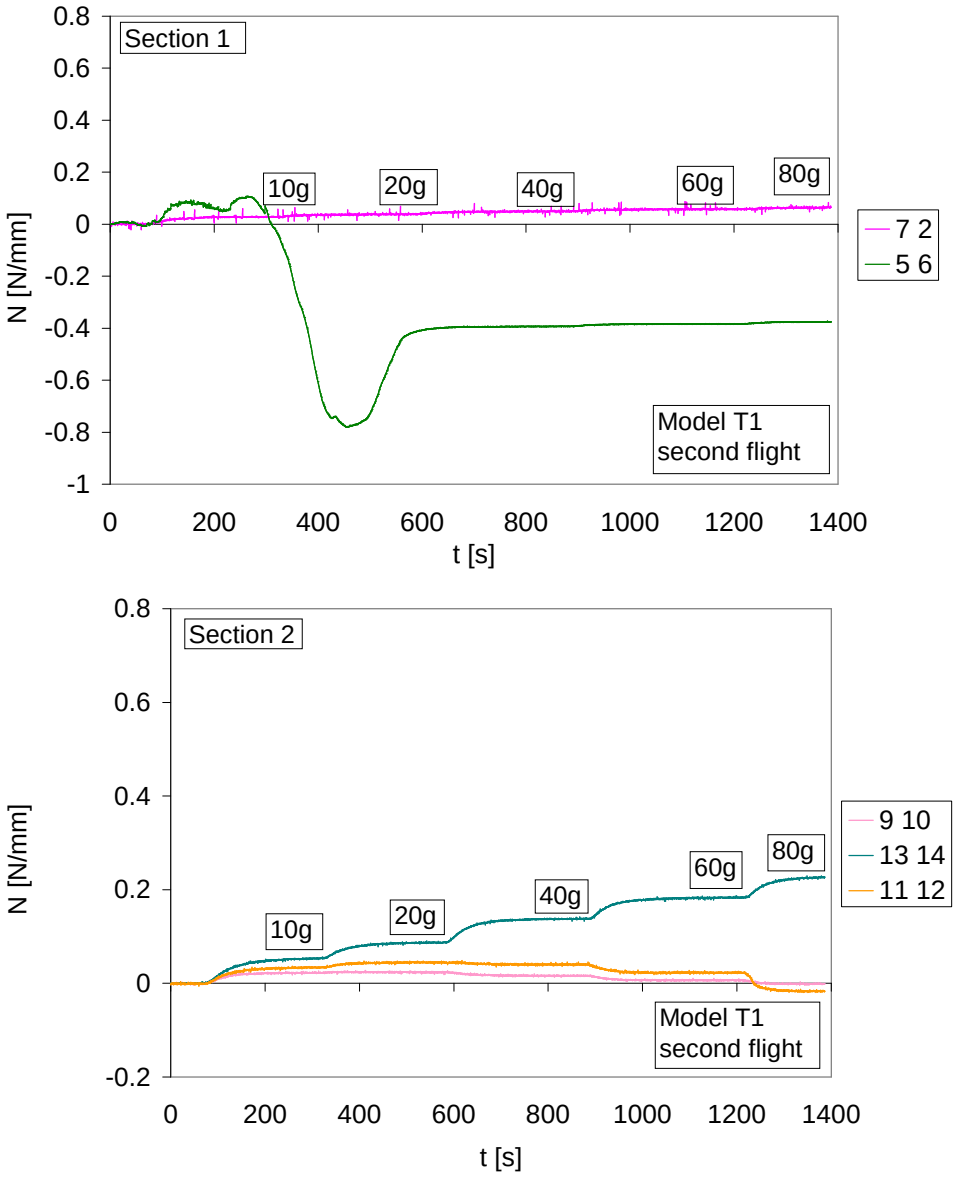

Fig.6.38: Hoop forces measurements in the swing up phase (model T1 – second flight)

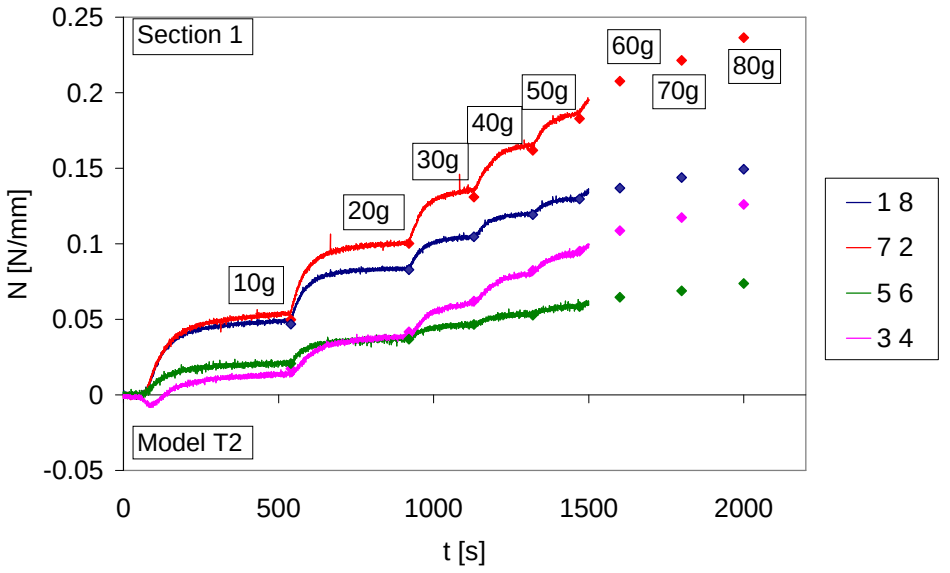

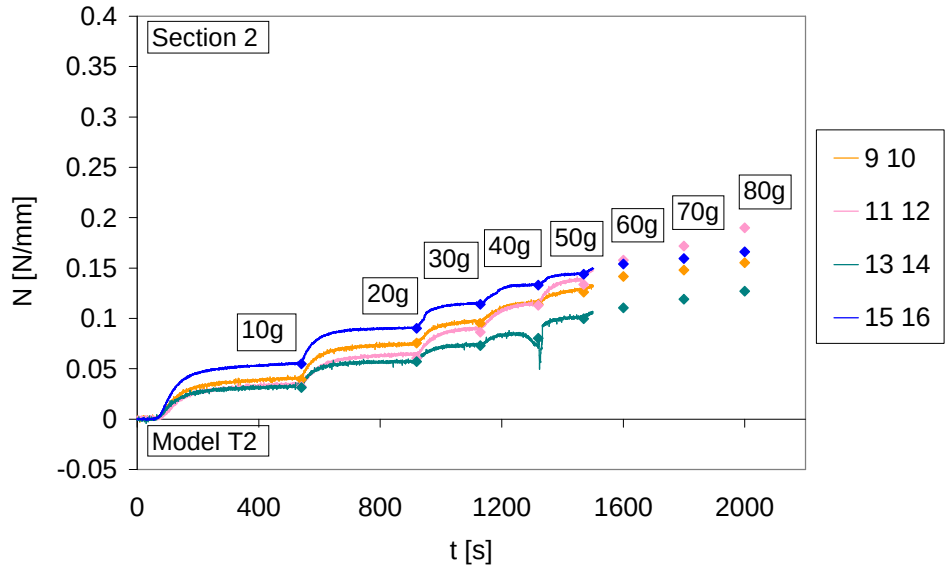

Fig.6.39: Hoop forces measurements in the swing up phase (model T2)

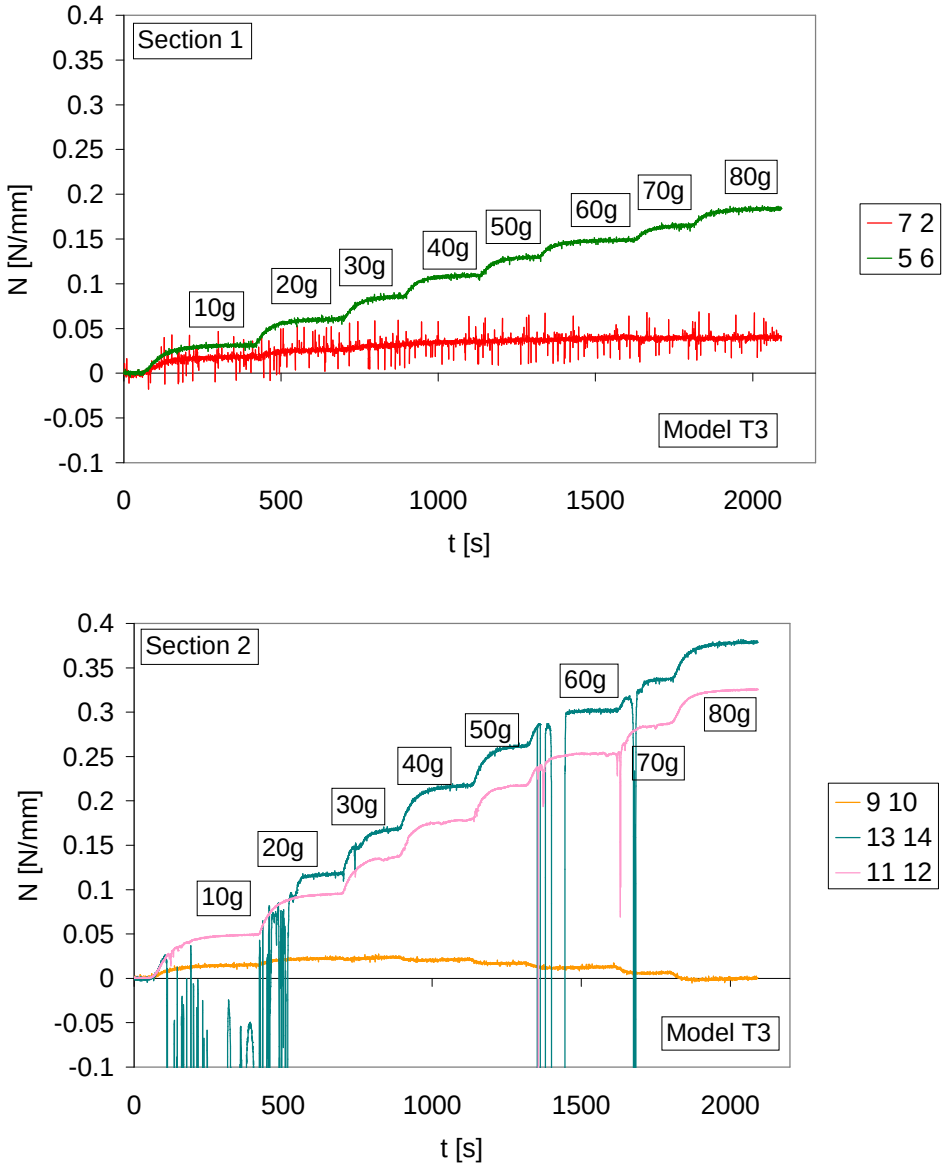

Fig.6.40: Hoop forces measurements in the swing up phase (model T2)

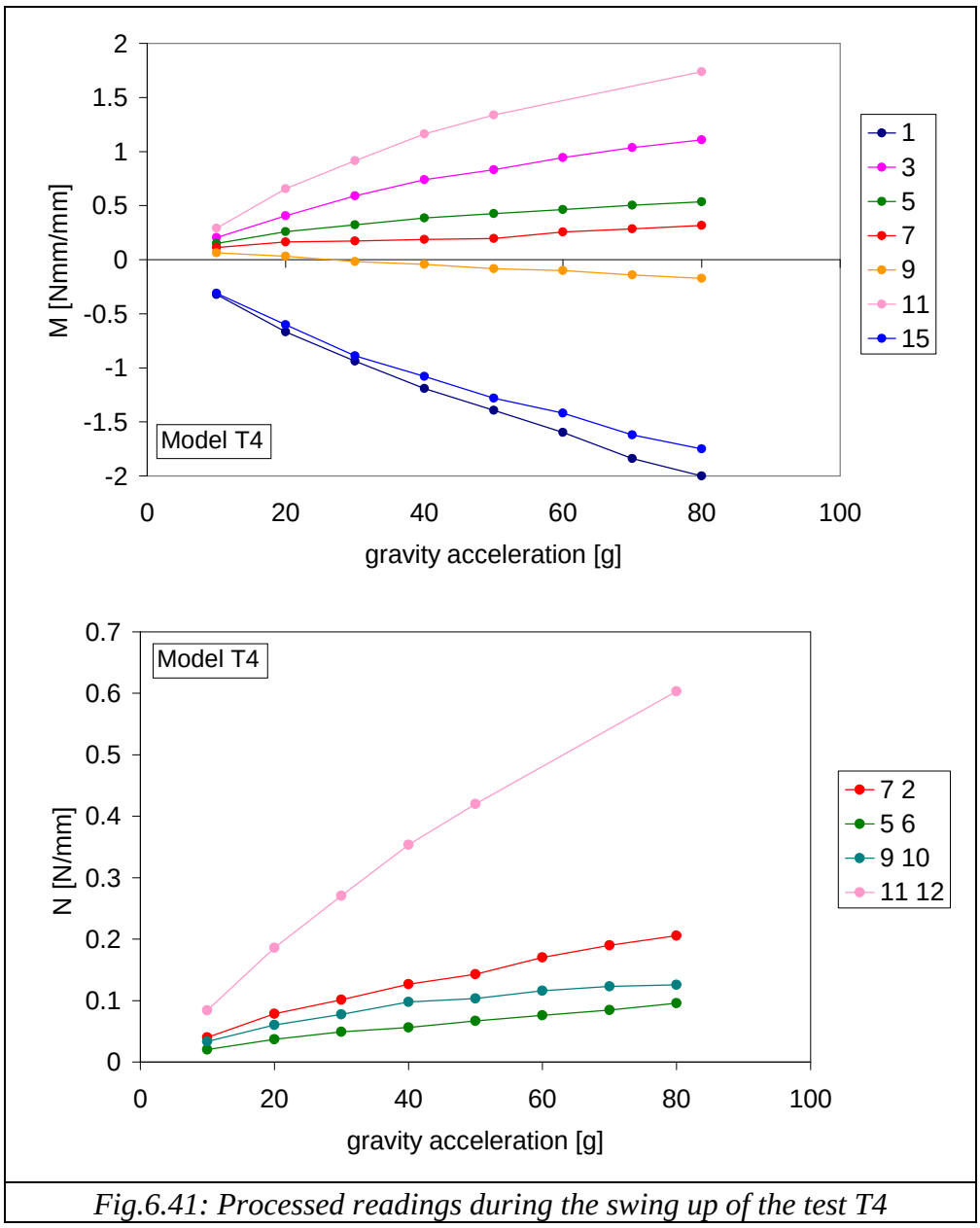

Fig.6.41: Processed readings during the swing up of the test T4

The bending moments exhibited both positive and negative values: the positive value corresponded to the extension of the inner fibres. In most of the cases the positive bending moment corresponded to the transducers located on bottom positions; instead the negative values were relative to the

strain gauges located on the top side, except for the case of the transducer 15. Therefore this instrument didn't give a reliable value of the calibration factor and the assumed constant were assumed from the corresponded instruments in the other section. For these reason the transducer 15 could give a false value of the bending moment in that cross section. The maximum positive value was included in a range between 2-3Nmm/mm, instead the negative value did not exceed the 1Nmm/mm.

The hoop forces are always positive, corresponding to a compression stresses state in the lining. In some cases the value were close to zero, as happened to the transducers 9-10 and 11-12 in the test of dense sand model. The transducers 5-6 in the second flight of the test T1 exhibited an anomaly of working, probably due to a change of the offset during the swing up of the model: for this reason, when the dynamic internal force of 5-6 were considered, the initial value of the hoop force were offset by the value of the corresponded transducer in the other section (13-14). The maximum value did not exceed the value of 0.4N/mm, except for the transducer 11 12 of the model T4. In the next section, starting from the value of the static forces obtained in the swing up phase, the evolution of the internal forces in the dynamic phase was obtained.

6.4.3 Dynamic internal forces

In the figs 6.42-49 the dynamic time histories of the bending moment and hoop forces in the two instrumented sections were showed, considering as the earthquake was happened in sequence. In reality between two earthquakes the time to save the previous event data was passed.

The experimental data showed that generally recorded data relative to corresponding position in the different section exhibited similar trend. In most of the cases the earthquakes determined a positive increase of the internal forces, both for the bending moment and the hoop forces.

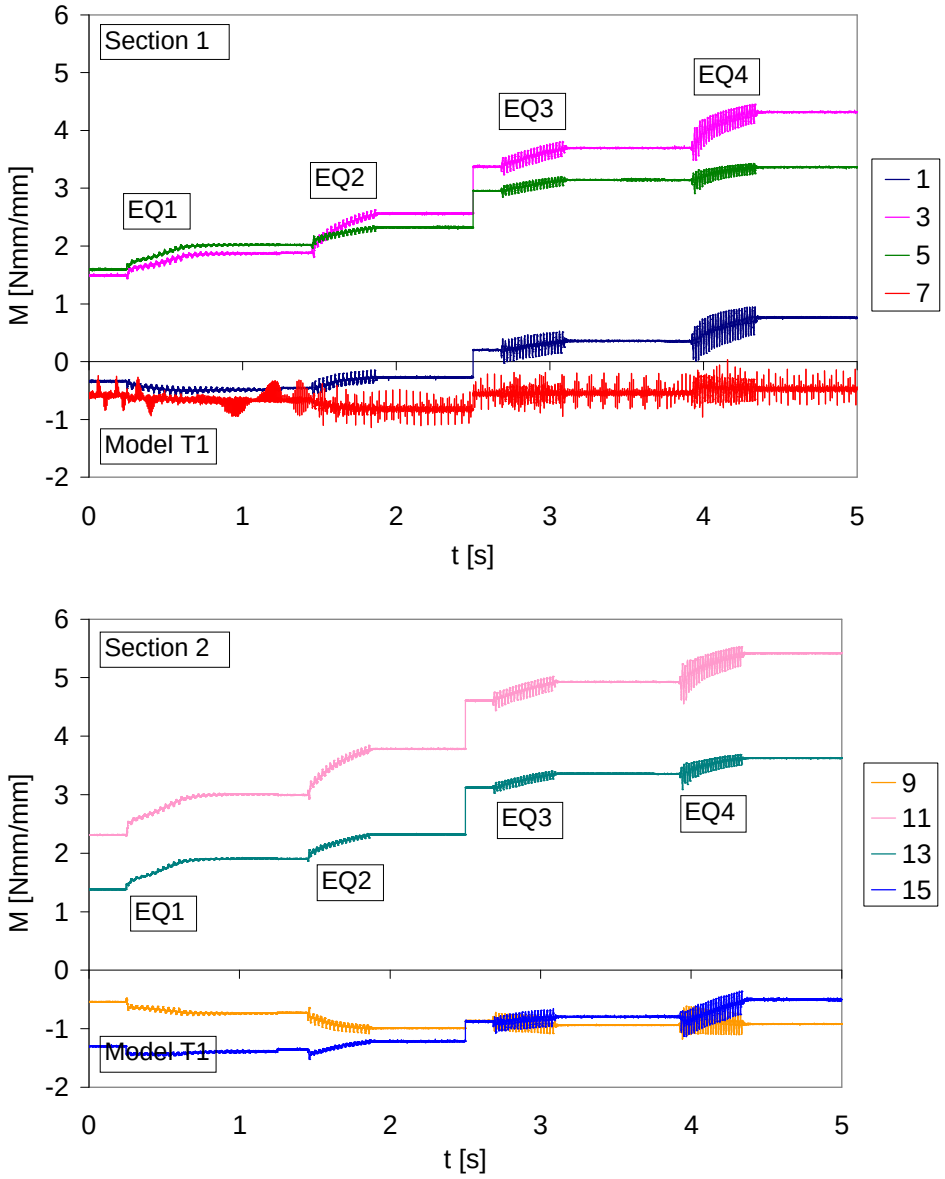

Fig.6.42: Time histories of the bending moment of the model T1

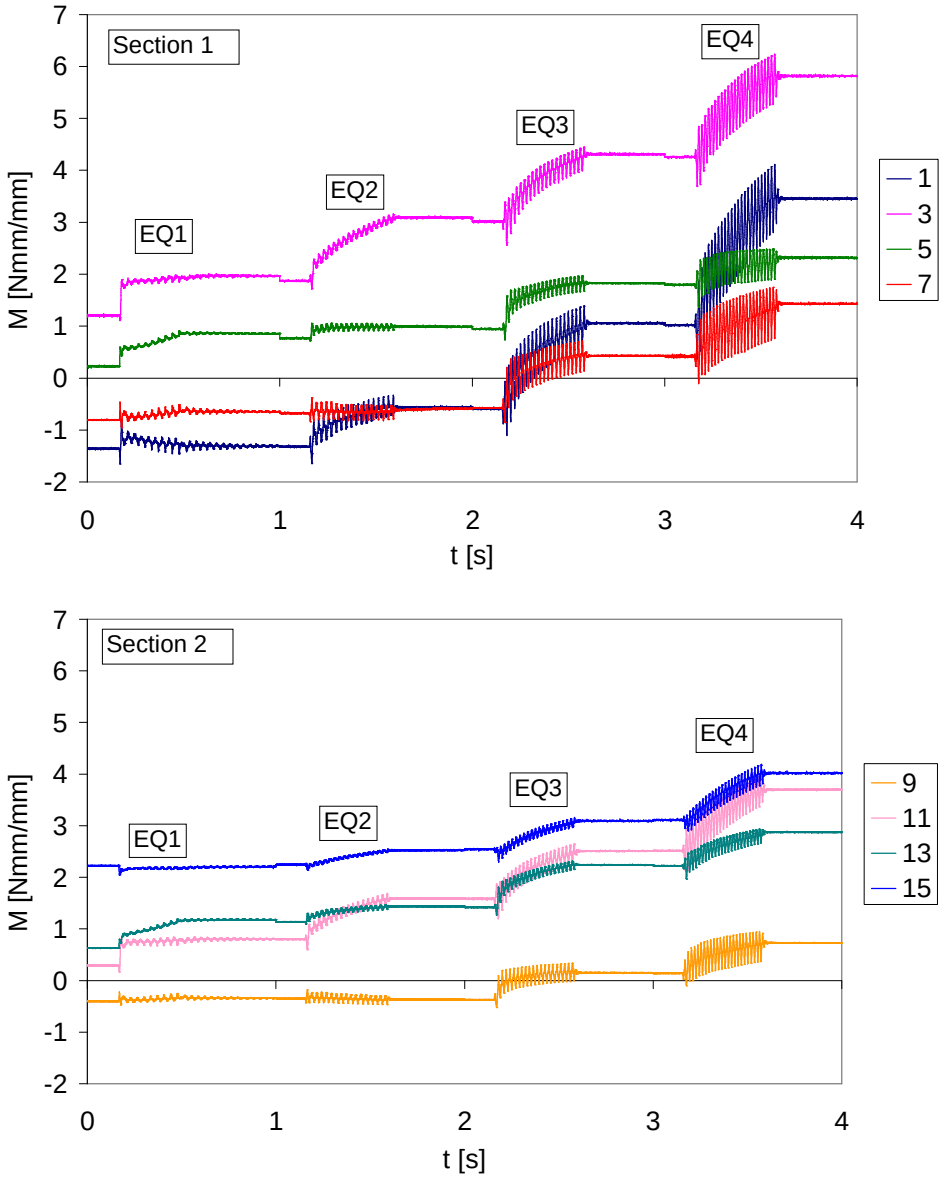

Fig.6.43: Time histories of the bending moment of the model T2

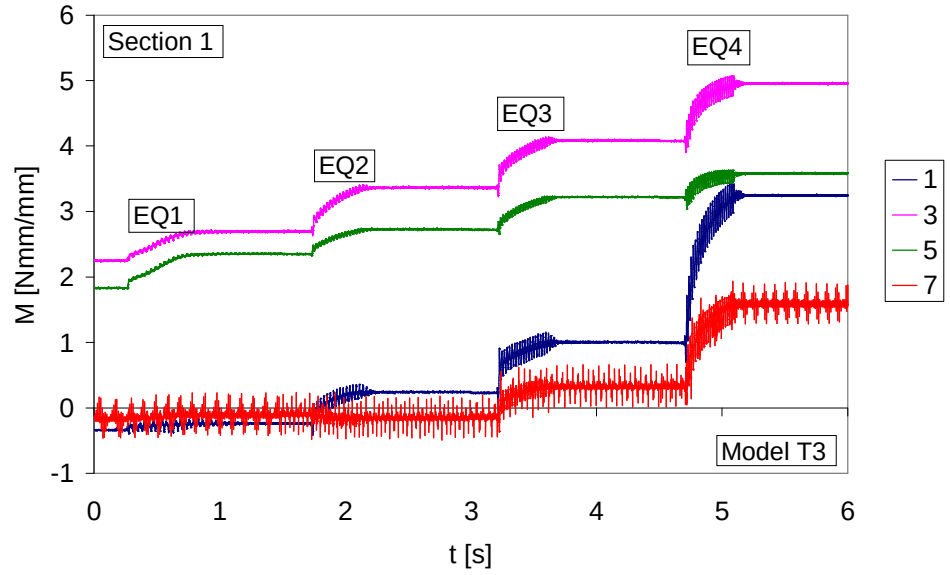

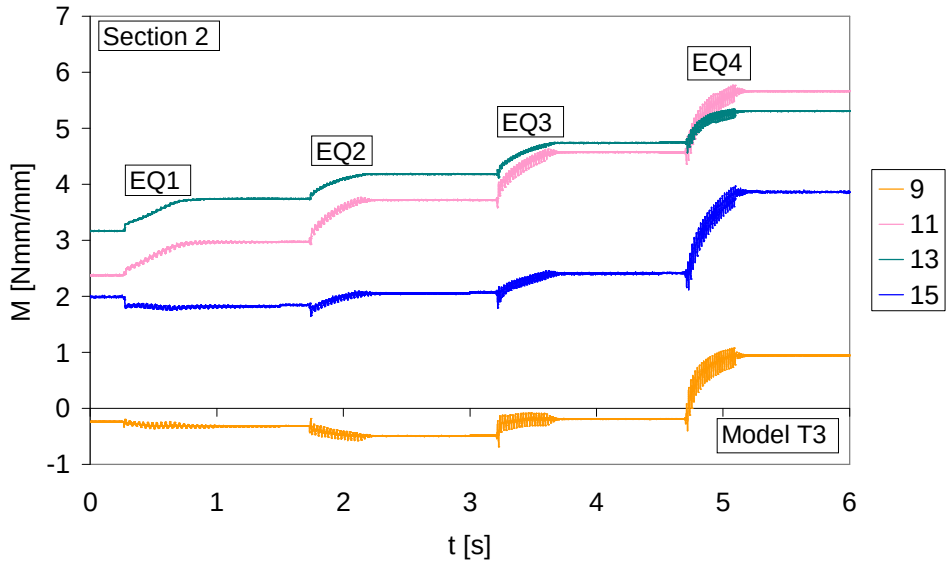

Fig.6.44: Time histories of the bending moment of the model T3

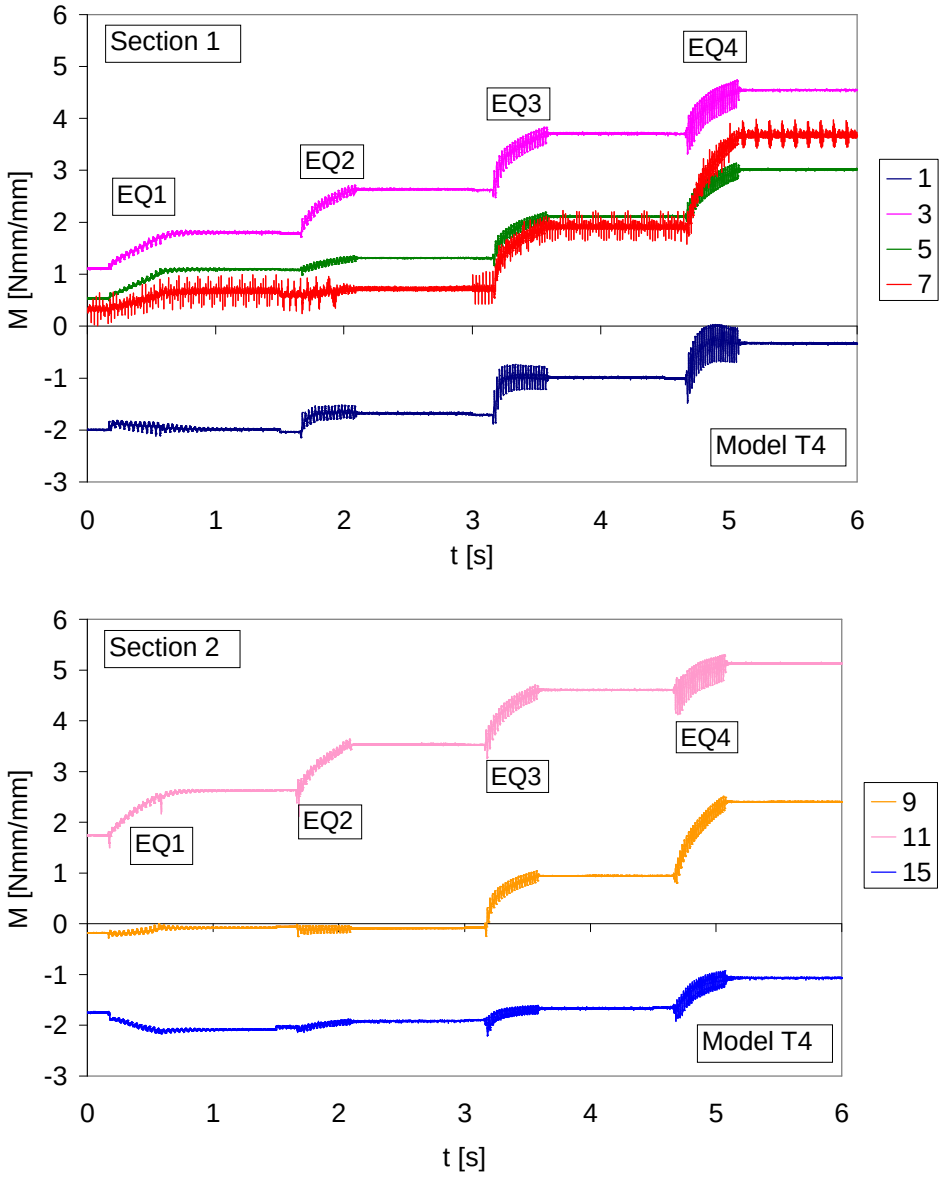

Fig.6.45: Time histories of the bending moment of the model T4

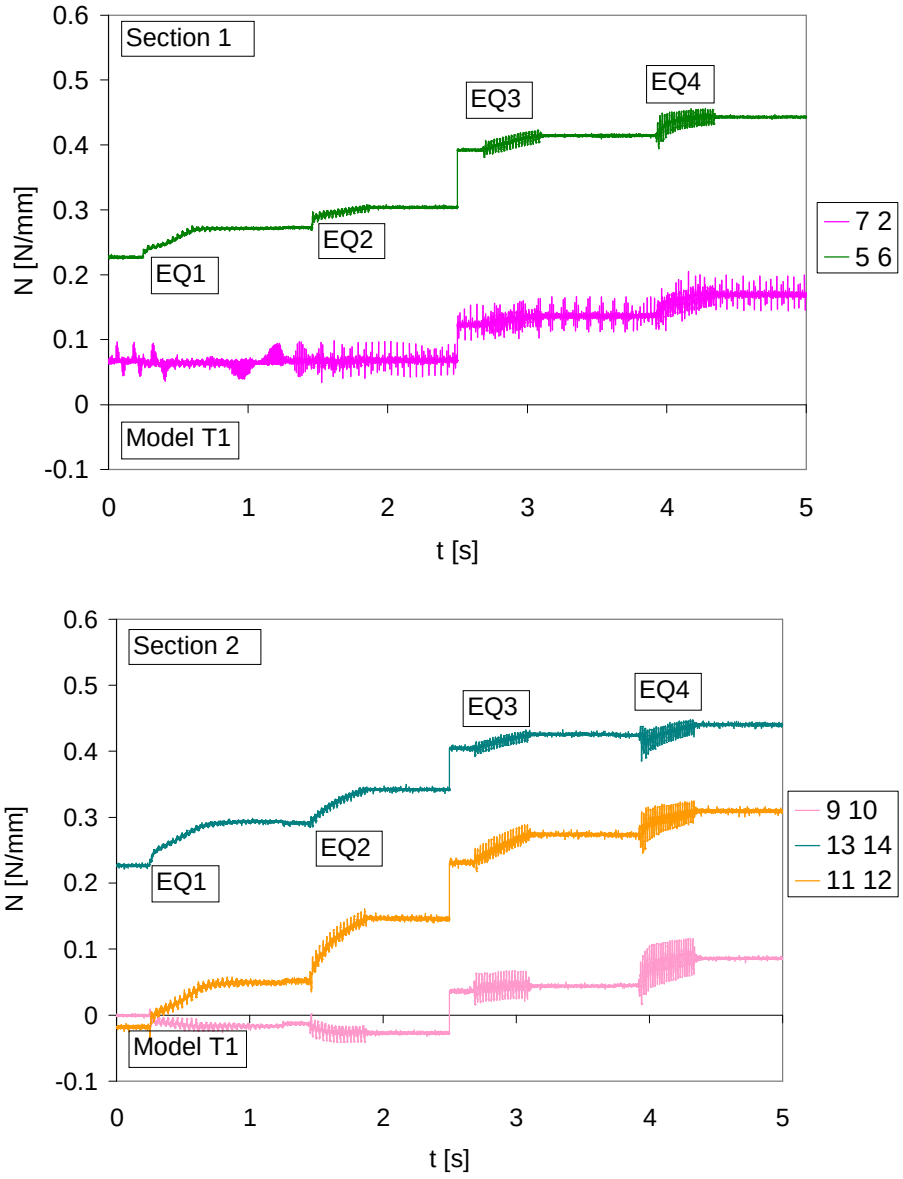

Fig.6.46: Time histories of the hoop forces of the model T1

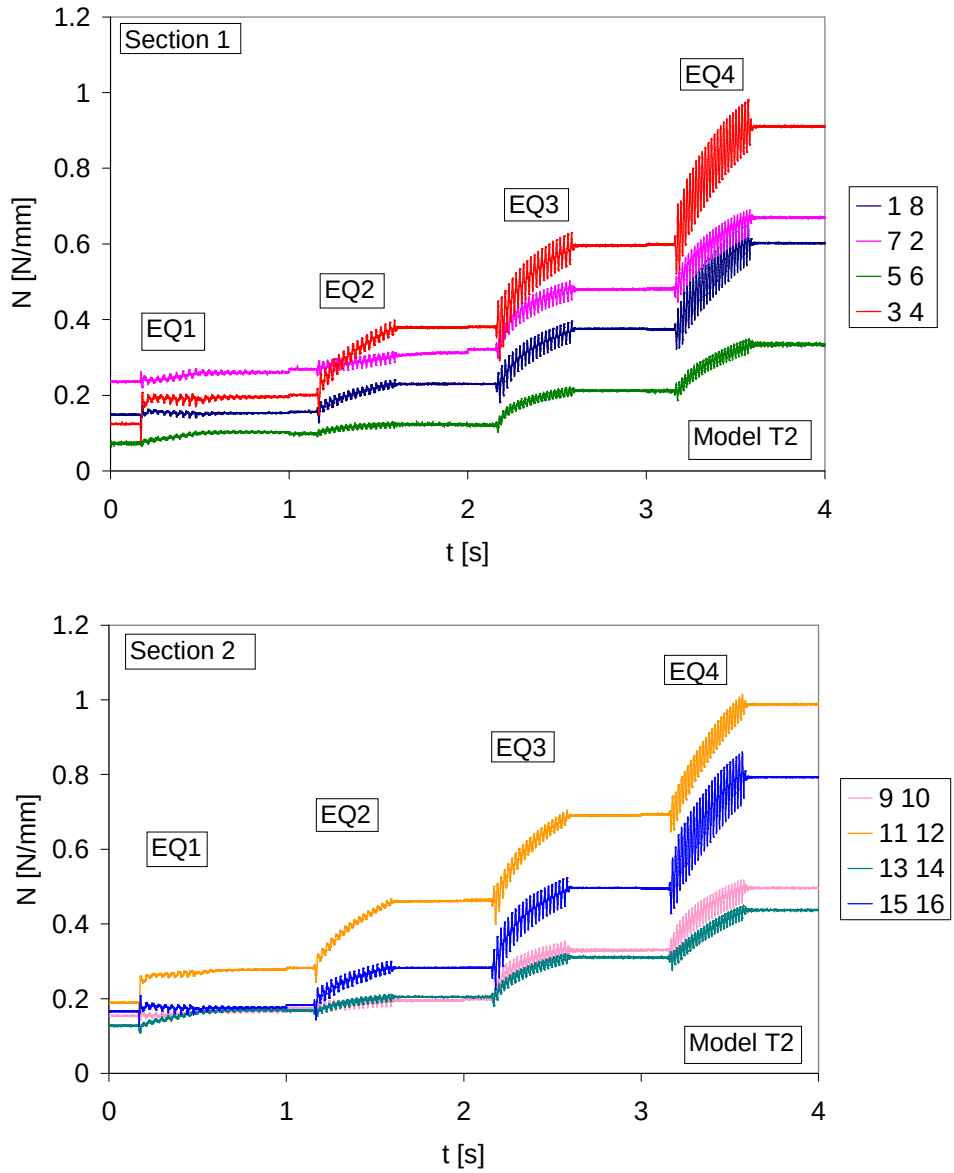

Fig.6.47: Time histories of the hoop forces of the model T2

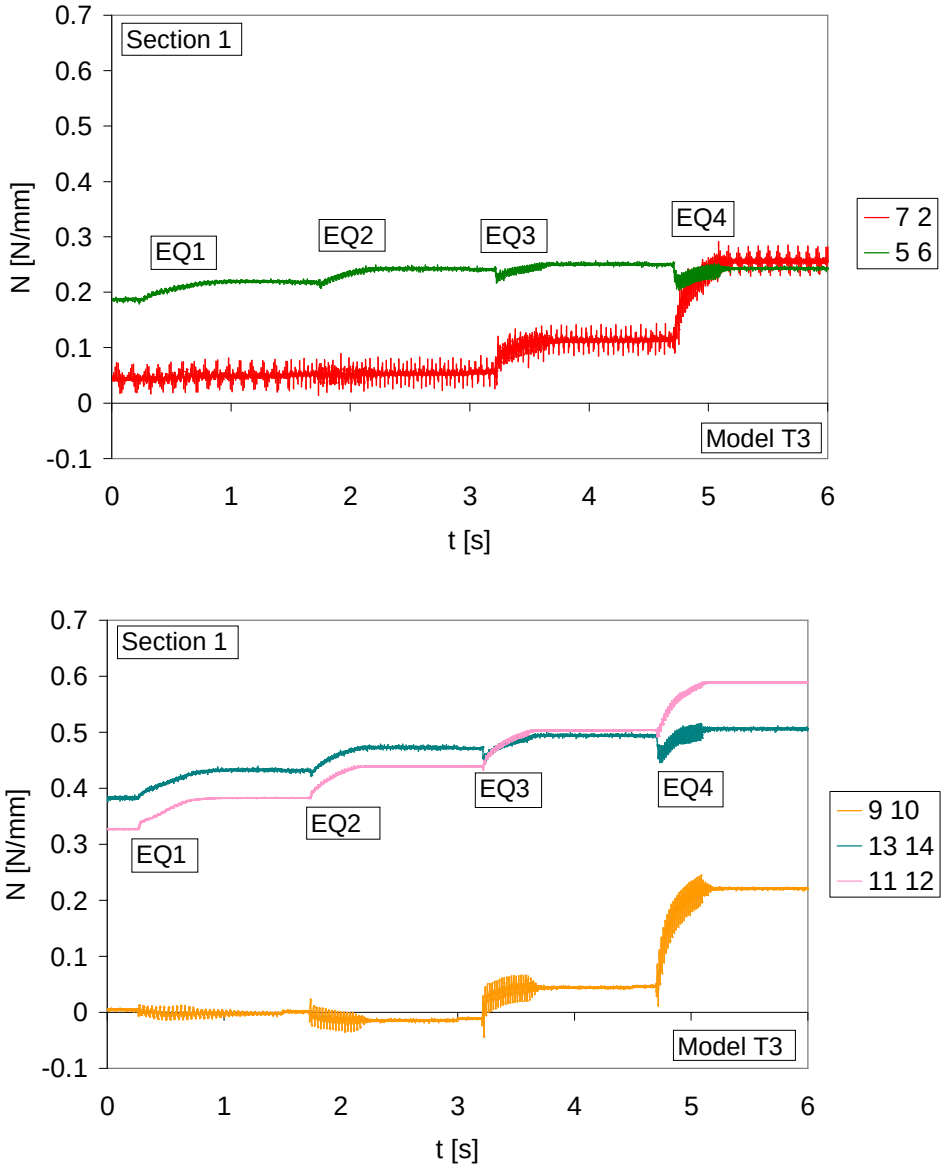

Fig.6.48: Time histories of the hoop forces of the model T3

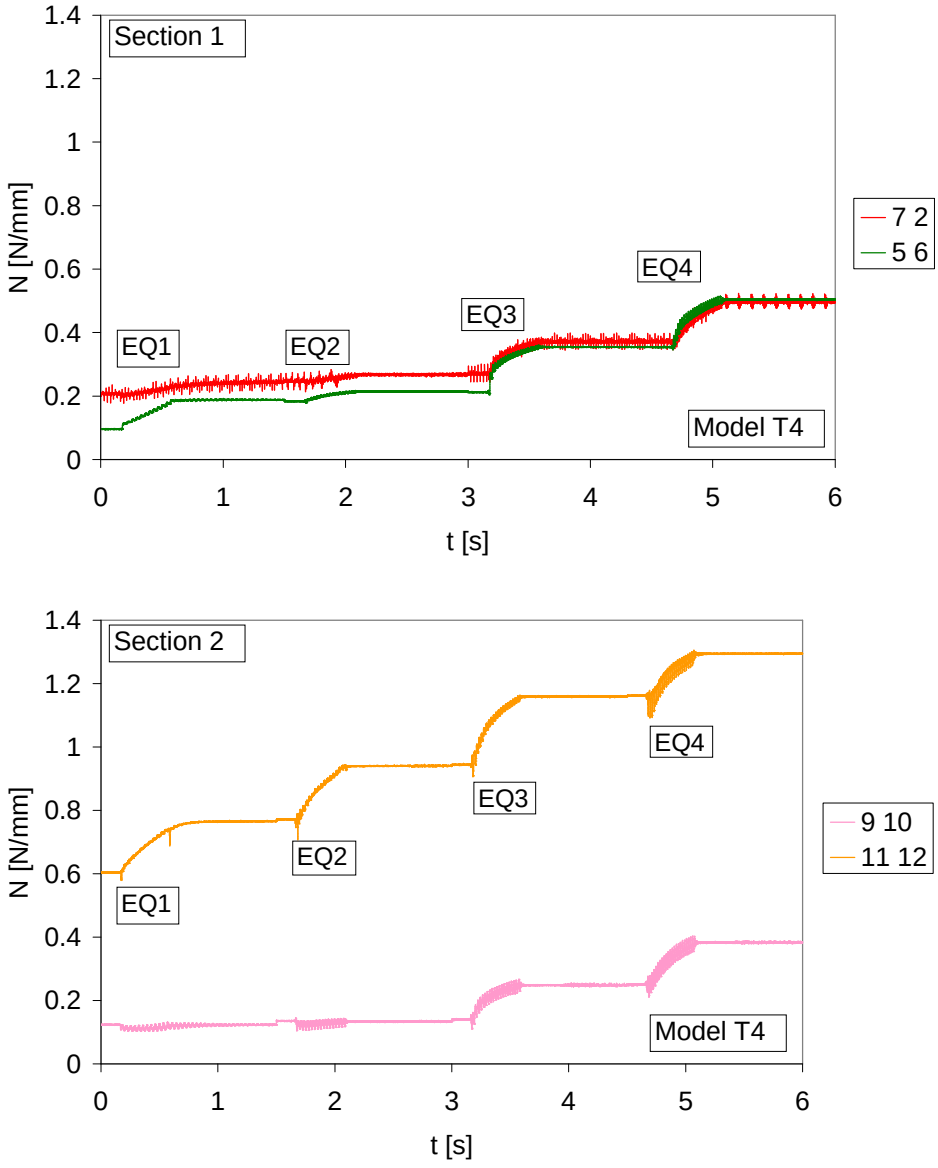

Fig.6.49: Time histories of the hoop forces of the model T4

The values of the bending moment located in the top side, as in the swing up phase, were higher than the corresponding in the bottom side, which were negative or positive close to zero. The maximum value obtained were around 5-6Nmm/mm, two times larger compared to the static value. The negative reached values were around 1-2Nmm/mm.

The hoop forces were generally always positive, except some case of null or slightly negative values. The increment of hoop forces was more clear in the loose sand test (1-1.2 N/mm), which were two times larger compared to the values of the dense sand models (0.5-0.6N/mm).

6.4.3 Experimental dynamic forces vs analytical pseudo-static forces

The average oscillation relative to the stress trend in the stationary phase was evaluated and compared to the bending moment and hoop load calculated from the analytical formulas of Wang (1993) considering full slip conditions. In the figs. 6.50-6.52 the comparison between the bending moments and hoop forces values for the models is shown: on the abscissa axis the stress measured by the gauges was reported against the ordinate values, calculated from the Wang's expressions (1993) using a free field shear strain. From the stress comparison between coupled and uncoupled analysis, it's clear that the values obtained from the Wang's formulas overestimate the stresses given by the test measuring instruments for the dense models; instead the closed-form expressions tend to underestimate the internal forces obtained by the transducers of the loose sand model. In the figs.6.51-53 a similar comparison of figs.6.50-52 is showed: differently from the previous graphs, the stresses calculated using the closed form formulas was found using the lining ovaling measurements as an input data. The stresses in figs.6.51-53 are consistent with the measured ones, except for two fired earthquakes of the model T1: this behaviour should be an effect of cinematic interaction on the stresses evaluation.

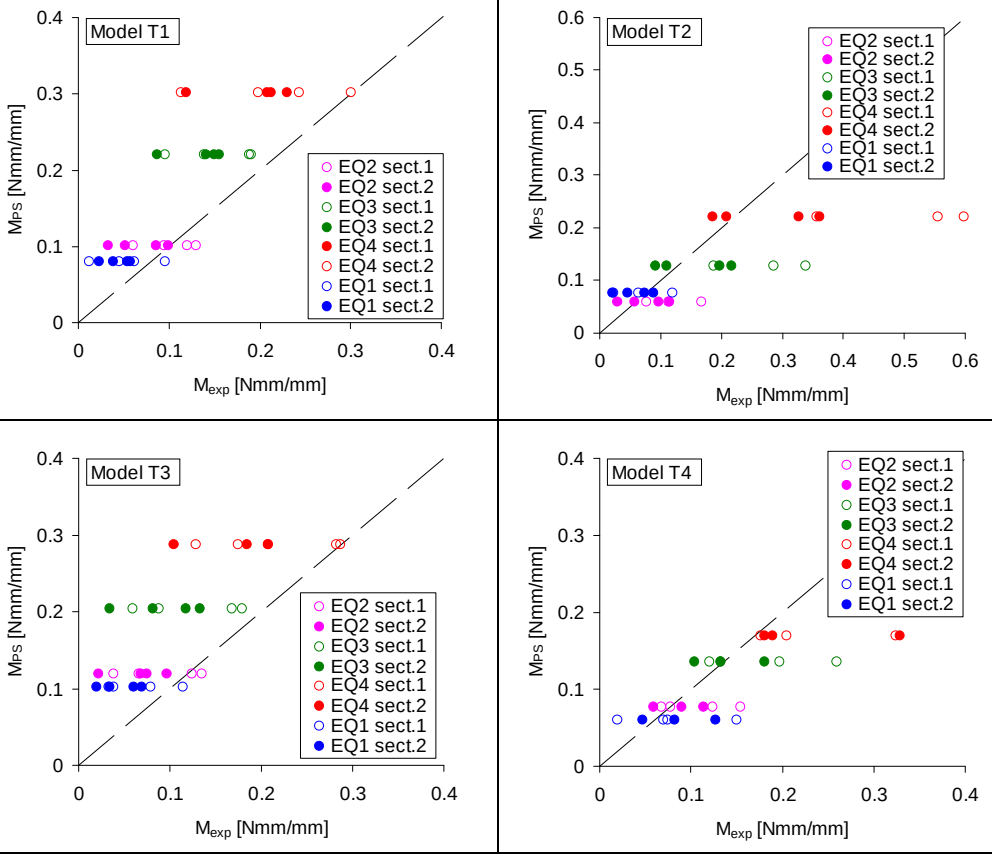

Fig. 6.50: Dynamic bending moment: experimental vs pseudo-static (Wang 1993) (experimental "free-field" shear strains)

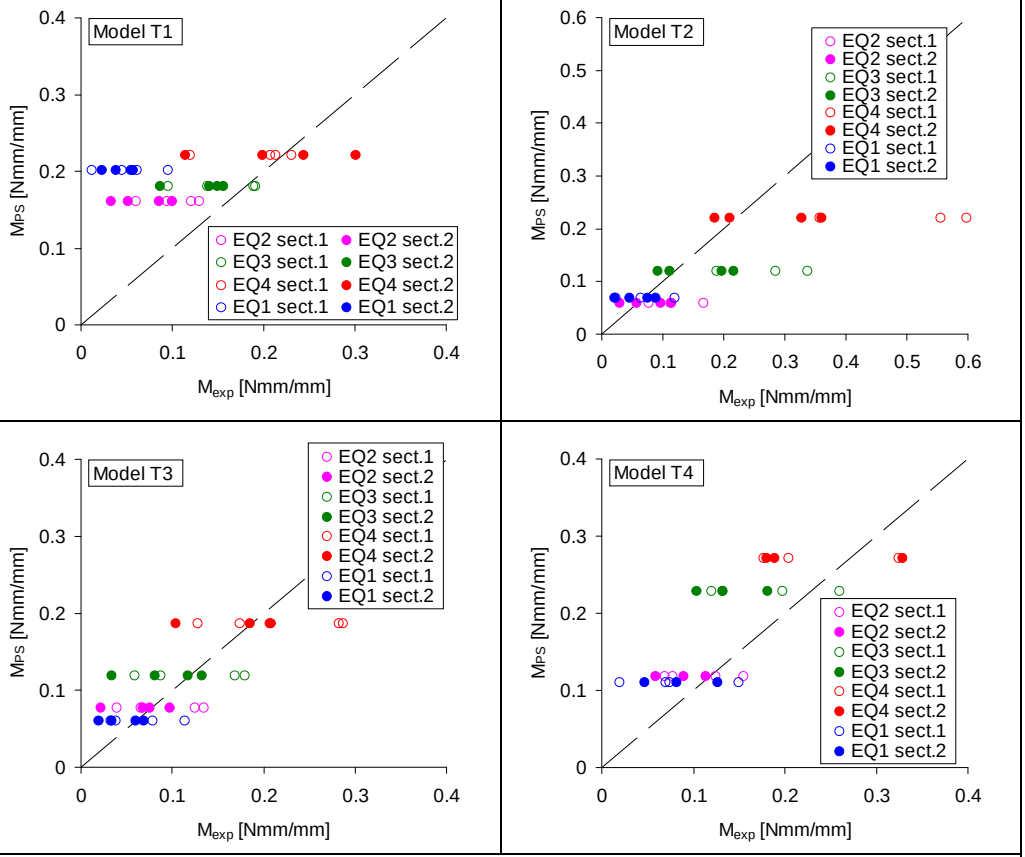

Fig.6.51: Dynamic bending moment: experimental vs pseudostatic (Wang 1993) (experimental "tunnel" shear strains)

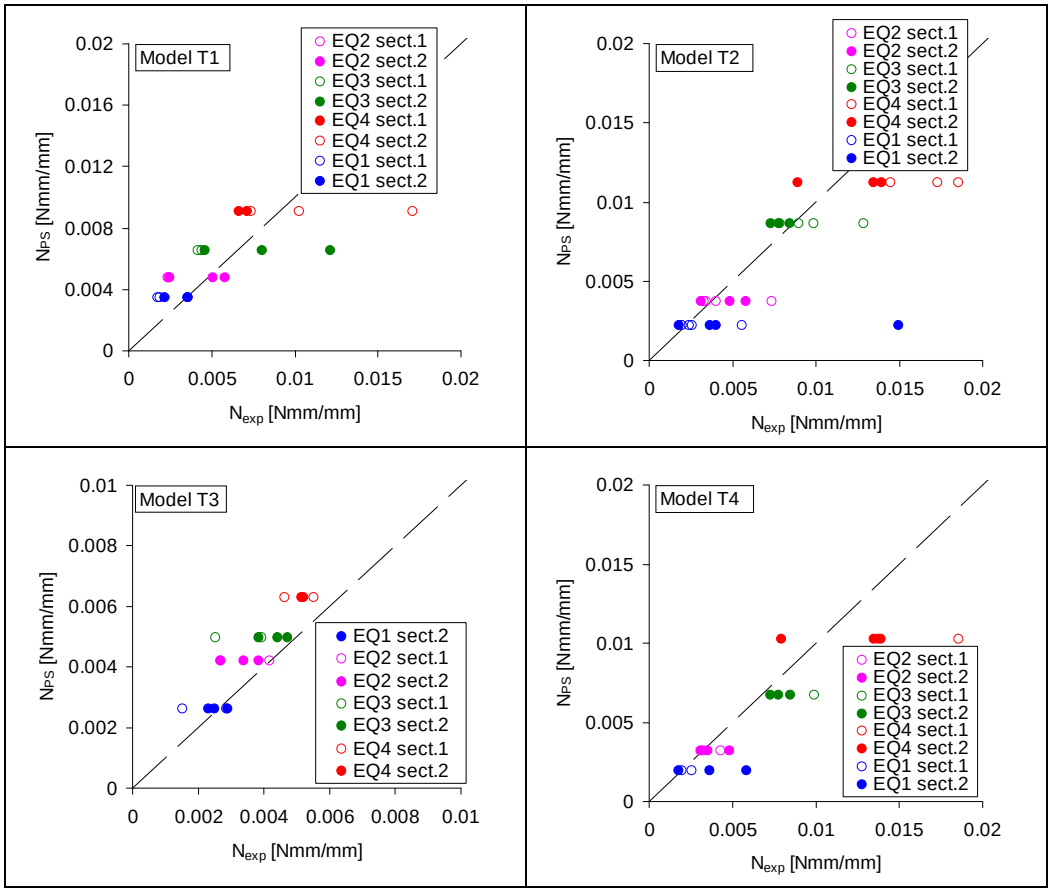

Fig.6.52: Dynamic hoop forces: experimental vs pseudo-static (Wang 1993) (experimental "free-field" shear strains – full slip conditions)

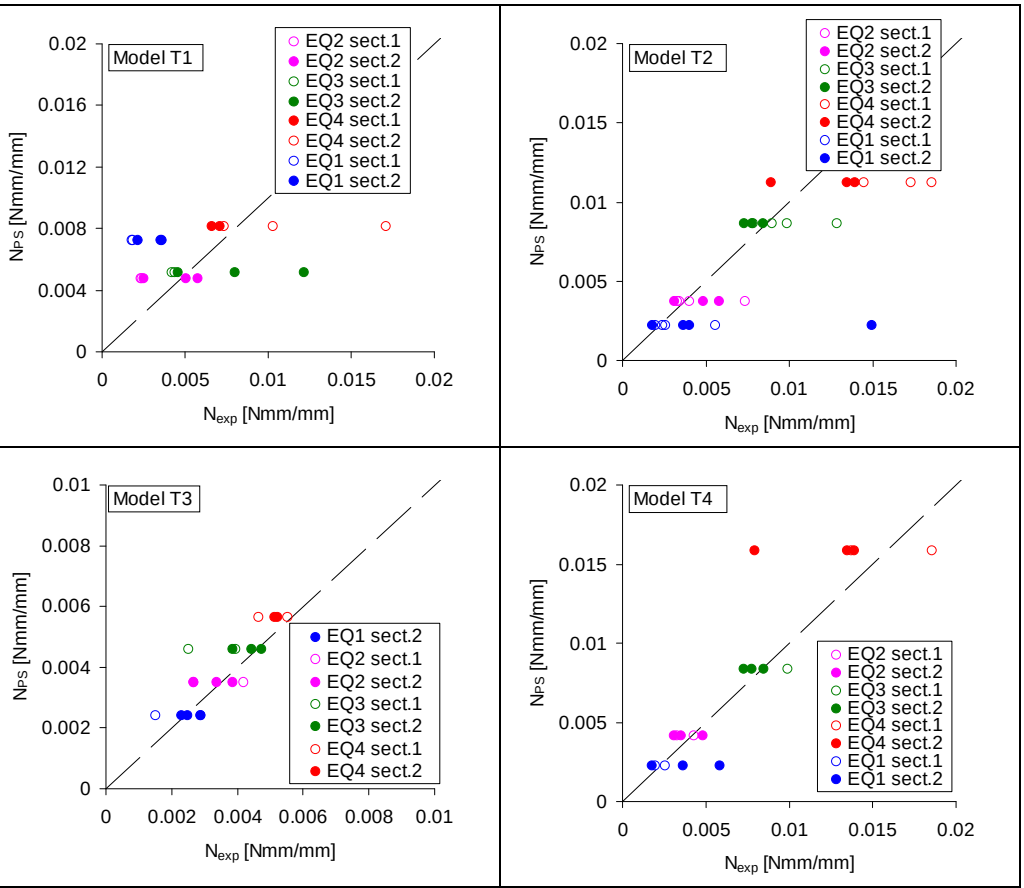

Fig.6.53: Dynamic bending moment: experimental vs pseudo-static (Wang 1993) (experimental "free-field" shear strains – full slip conditions)

FINAL REMARKS

The centrifuge models were instrumented using transducers in order to measure displacements, acceleration and deformation during the fired earthquakes of each tests. In this chapters the measurements were widely showed at the model scale, without considering the scaling factors for the experimental sample depending on the gravity level. Therefore the soil layer thickness at the prototype scale corresponded to around 23m and the dimension of the tunnel were D=6m and d=0.04m. Considering all the

scaling factors, the interpretation of the transducers measurements gives the following considerations:

- The LVDTs measurements show in all the tests the settlement of the model surface, both in the swing up and dynamic phase. The loose sand models exhibited displacements which were around two times larger (6.5cm) compared to the dense sand models (3.2cm). The swing up settlement were around the half part of the total displacement, as the measured displacement in the dynamic phase;
- The accelerometers measured time histories of pseudo-sinusoidal motions: therefore the acceleration amplitude was not constant and non symmetric around the time axis; the frequency content was larger compared to the design frequency and was not due to annoying effects. For this reason the acquired signals were filtered in a large band pass of frequencies (0.2-3.124Hz at prototype scale);
- The three verticals, instrumented with horizontal accelerometers, showed the amplification of the peak ground acceleration from the base registration to the top accelerometers. The amplification was generally low ($S<1.5$), especially for the internal alignments. Moreover the tunnel in the model determined the reduction of the acceleration of the free-field column at the structure depth and the increase of the peak ground acceleration for the instrument located at the bottom of the box under the tunnel;
- The variability of the ground motion was represented using the coherence and the transfer functions. The natural frequency of the soil layer was obtained from the amplification function between the base and the top accelerometers, in order to obtain an average value of the mobilized shear stiffness. Considering, therefore, a best-fitting curve gave an evaluation of the damping ratio, which were generally quite high. The calculated stiffness was fairly low, around 20MPa;
- The strain-stress cycles were plotted in order to obtain an evaluation of the shear stiffness layer by layer; the shear strain was calculated from the displacements time histories, obtained from the double integration of the instruments measurements; the shear stresses was evaluated from an integration of the acceleration with depth. The

corresponding shear stresses and strains, plotted in a graphs, gave a lower values of the mobilised shear stiffness compared to the results of the amplification functions (under 20MPa);

- The strain gauges measurements gave a direct measurement of the internal forces in the lining, showing, for each earthquake recordings, an oscillation during the motion and a residual value at the end of the earthquake; the variation of the static forces were probably due to a densification of the soil during the shaking, confirmed by the LVDTs measurements;
- In order to check the experimental data with analytical formulas, the maximum dynamic oscillation of the internal forces were compared to the results of the closed-form expressions of Wang (1993), considering full slip conditions; the results were consistent especially when the shear deformation of the tunnel was used as a input data in the Wang's expression;

REFERENCES

Brennan A.J. Thusyanthan N.I., Madabhushi S.P.G. 2005. Evaluation of shear modulus and damping in dynamic centrifuge tests, ASCE – Journal of Geotechnical and Geo-environmental Engineering, n°1488

Kramer S:L. Geotechnical earthquake engineering. Prentice Hall

Wang J-N. 1993. Seismic Design of Tunnels, Parson Brinckerhoff Inc.

Zeghal M., Elgamal A-W. 1994. Analysis of site liquefaction using earthquake records, ASCE - Journal of Geotechnical and Geo-environmental Engineering, n°120.

Chapter 7
Numerical simulation of the centrifuge tests

7.1 INTRODUCTION

The centrifuge tests carried out on the scaled models gave an extended quantity of data, which included measurements of settlements, accelerations and lining deformation. In the previous chapter, the acceleration data were integrated in time and space to obtain shear strain, stress and stiffness, considering the spatial variability of the ground motion. From the deformation recorded by the strain gauges stuck on the lining surface, the measurements of the internal forces were derived, both in the static and in the dynamic phase.

Simplified and full dynamic interaction analyses were performed, to simulate both ground motion and dynamic increments of the internal forces induced by the centrifuge earthquake. The procedure implemented for the interaction analyses (Amorosi et al. 2007; Bilotta et al. 2007) was already used for the pilot full dynamic analyses, previously described in Chapter 3. This procedure was followed for all the earthquakes fired on all the models realized, but it is hereafter reported for a single example case.

7.2 INPUT DATA

The seismic centrifuge test on the dense sand model T3 (EQ2) was taken as reference for the preliminary calibrations of prediction models with different complexity. In Fig. 7.1 the input acceleration time history of the reference earthquake is plotted: the signal was filtered considering a large band-pass range of frequency (at prototype scale 15-250Hz), compared to the nominal frequency of 40Hz; also, the peak-to-peak amplitude was not constant and was lower than the nominal value (8g).

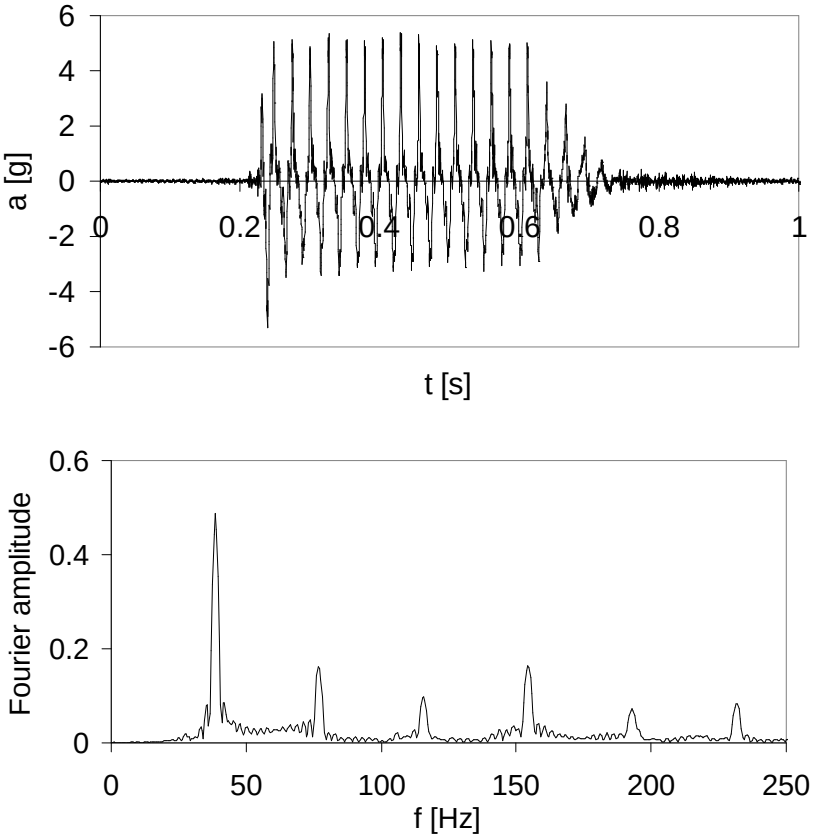

Figure 7.1. Input signal (model T3, EQ2).

The surface/base transfer functions along the vertical alignments were calculated as the ratio between the Fourier spectra of the recorded accelerograms. Figure 7.2 shows the comparison between the surface/base

amplification factor at the reference accelerometer array (black solid line) and that along the tunnel axis (black gray line).

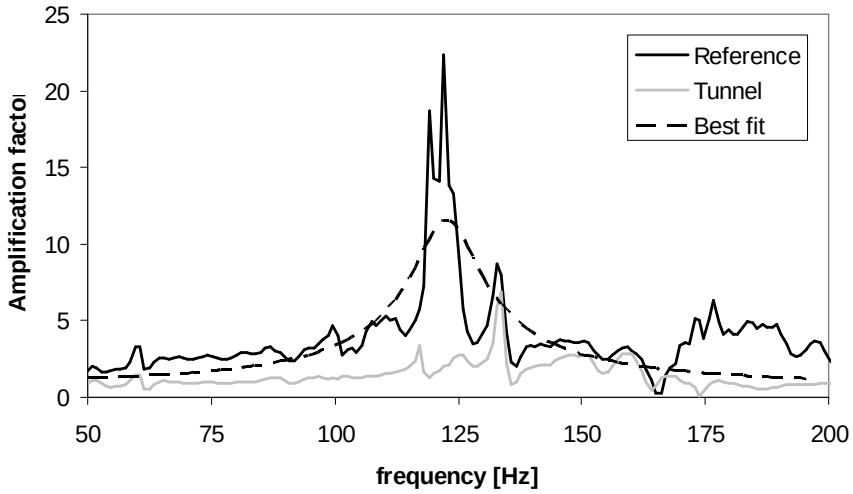

Figure 7.2. Surface/base transfer functions (model T3, EQ2).

The transfer function at the reference vertical (black solid line in Fig. 7.2) was back-analysed to derive the equivalent stiffness and damping parameters of the sand model mobilised during the centrifuge test. The experimental curve was best-fitted with the analytical expression of the amplification factor of a visco-elastic soil column (dashed line in Fig. 7.2). Following such procedure, an equivalent shear modulus G equal to 27 MPa and a damping ratio D equal to 5.5 % were back-calculated.

The application of the same procedure to all tests on both dense sand models (T1 and T3) resulted into values of the equivalent stiffness ranging between 18 and 30 MPa; instead, the shear stiffness values for the loose models were slightly lower.

Figure 2 also shows that, along the tunnel vertical, the surface amplification appears significantly reduced (grey solid line), especially around the resonant peak (≈ 125 Hz) observed at the reference vertical. This is a clear evidence of the wave-screening effect of the tunnel structure.

The shear stiffness and the damping ratio of the Leighton Buzzard Sand fraction E were also assumed on the basis of resonant column (RC) tests carried out at the University of Napoli Federico II (Visone 2008). Figure 7.3a shows, at the prototype scale, the variation with depth of the initial

shear stiffness, G_0, obtained from RC tests on a dense sand specimen with D_r = 71%. Such values (open circles and dash-dot line) plot significantly higher than the initial stiffness (G_0 = 45 MPa) back-figured from the frequency response curve in the centrifuge test. This latter value results from the mobilized stiffness of G=27 MPa, obtained by the transfer function, multiplied by a factor of about 1.6, to account for the average shear strain level (0.1%) measured in this test (§6.3.2). In the same figure, a constant profile of G, representing the average value with depth of the secant stiffness exhibited during experimental cycles (§6.3.3), is also shown (thick line).

The variation with depth of the initial damping, D_0, was taken by curve-fitting the experimental values resulting from the RC tests (Fig. 7.3b, open circles and dash-dot line). In the same figure, a constant profile of the equivalent damping ratio, D (=5.5%), is also shown, again estimated on the basis of the best fitting of the transfer function.

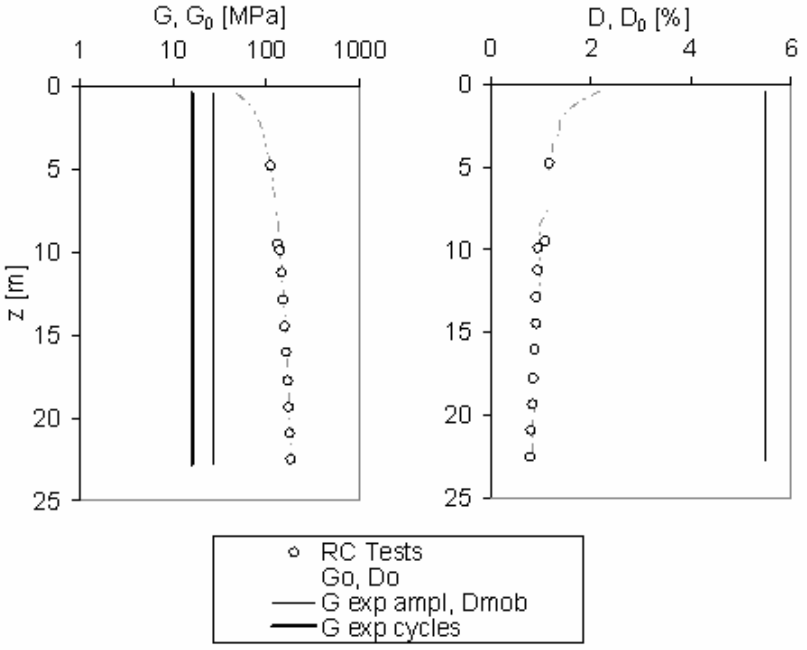

Figure 7.3. Profiles of initial shear modulus (a) and damping ratio (b) with depth (model T3, prototype scale).

Fig. 7.4 reports the RC test results in terms of dependency on shear strain of both stiffness and damping ratio, respectively normalised ($\overline{G} = G / G_0$) and scaled ($\overline{D} = D - D_0$) to their initial values. The laboratory results were best-fitted by the Ramberg-Osgood curves (Fig. 7.4):

The model parameters obtained by the interpolation of the laboratory results in a bi-logarithmic plane, were R=7291 and C=2.227.

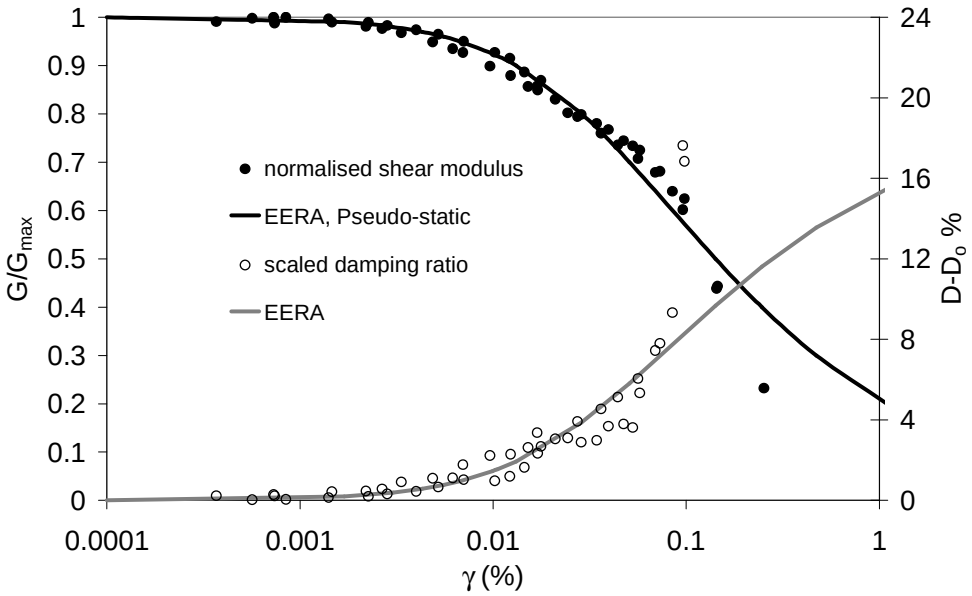

Figure 7.4. Variation of shear modulus and damping ratio with shear strain (experimental data after Visone, 2008)

7.3 PSEUDO-STATIC ANALYSES

In the pseudo-static analyses, the seismic increment of internal forces in the lining was evaluated by the formulas by Wang (1993) in full slip conditions, reported in the §2.5.2. The maximum dynamic increments of the bending moment and the hoop force were calculated from the average value at the tunnel depth of the maximum shear strain, γ_{max}, computed in

free-field conditions. Two different methods, based on the equilibrium of a deformable soil column from the surface to a given depth z, were used (§2.5.2).

In the former method, γ_{max} was calculated "down-up", from the value of the reference peak acceleration $a_{r,max}$, by assuming a linear profile of amplification from the base to the surface. The latter method followed an approach "up-down", by reducing with depth the maximum value of surface acceleration $a_{s,max}$. In both methods, the peak acceleration at surface was computed as:

$$a_{s,\max} = S \cdot a_{r,\max} \quad (1)$$

where *S* was taken equal to 1.6, being the prototype soil profile of 'class E' according to EC8 (CEN 2003) and the new Italian code (D.M. 14.01.2008). The experimental evaluation of the shear modulus from RC tests was used in the calculations (dash-dot line in Fig. 3a combined with the curve in Fig. 4). The values of γ_{max}, computed by both methods for all T3 tests, are reported in Table 7.1. They resulted about one order of magnitude lower than those measured in the centrifuge tests (see Fig. 5).

T*able 7.1. Results of pseudo-static analyses at prototype scale*.

Input signal	$a_{r,max}$ [g]	$a_{s,max}$ [g]	γ_{max} (down-up) [%]	γ_{max} (up-down) [%]
EQ1	0.035	0.06	0.008%	0.007%
EQ2	0.062	0.10	0.014%	0.012%
EQ3	0.094	0.15	0.023%	0.020%
EQ4	0.120	0.19	0.031%	0.026%

7.4 SIMPLIFIED DYNAMIC ANALYSES

An alternative way to calculate the free-field shear strain γ_{max}, to be introduced in Wang's formulas, was carried out by one-dimensional dynamic response analysis by EERA (§ 3.3.1). The input acceleration time history for the analyses was considered equal to the record taken by the accelerometer located at the base of the reference array. Therefore, the base

boundary conditions correspond to those of a very stiff outcropping bedrock.

The code EERA performed a frequency domain analyses (Bardet *et al.* 2000), modelling an equivalent linear layered subsoil. Both linear and linear equivalent analyses were carried out. The curves adopted for the normalised stiffness, $G(\gamma)/G_0$, and the scaled damping, $D(\gamma)$-D_0, are shown in Fig. 7.4. Figure 7.5 reports the comparison at prototype scale between experimental and EERA profiles of both accelerations and shear strains with depth. Two experimental profiles are plotted: one is derived from the reference array while the other is obtained by the free-field array. It should be kept in mind that while the accelerations are truly measured the experimental shear strains are indeed derived by the computed displacements obtained by double integration of the accelerations.

The solid lines plotted on the left side graphs result from linear analyses, carried out assuming constant profiles for the shear stiffness and the damping ratio. Like in Fig.7.2, the thin and thick lines correspond to the two different back-analysis procedures of the centrifuge tests (amplification curve and stress-strain cycles, respectively). In terms of accelerations, the former approach fits the experimental results better than the latter. The opposite is true for the shear strains. Attempts to introduce a variation of stiffness with depth (not reported here) did not produce any significant variation of the results of such linear analyses.

In the plots on the left side constant profiles for the shear stiffness and the damping ratio were used (thin and thick lines in Fig. 7.2) and linear analysis was carried out. The plots on the right side contains the results of linear equivalent analysis carried out with the profile of $G_0(z)$ and $D_0(z)$ obtained by laboratory tests (dash-dot line in Fig. 2).

In terms of accelerations both curves fit reasonably the experimental results, the former case performing slightly better than the latter. The opposite is true for the shear strains. The plots on the right side show that the use of the laboratory results in linear equivalent analysis is still satisfactory in terms of accelerations profiles, the result being similar to those obtained by the latter case of the plots on left side. On the contrary a substantial underestimation of the experimental strains is obtained by using the laboratory stiffness profiles. It is worthy mentioning that attempts to

introduce a variation with the depth for the cases analysed in the plots on the left side did not produce any significant variation of the predictions.

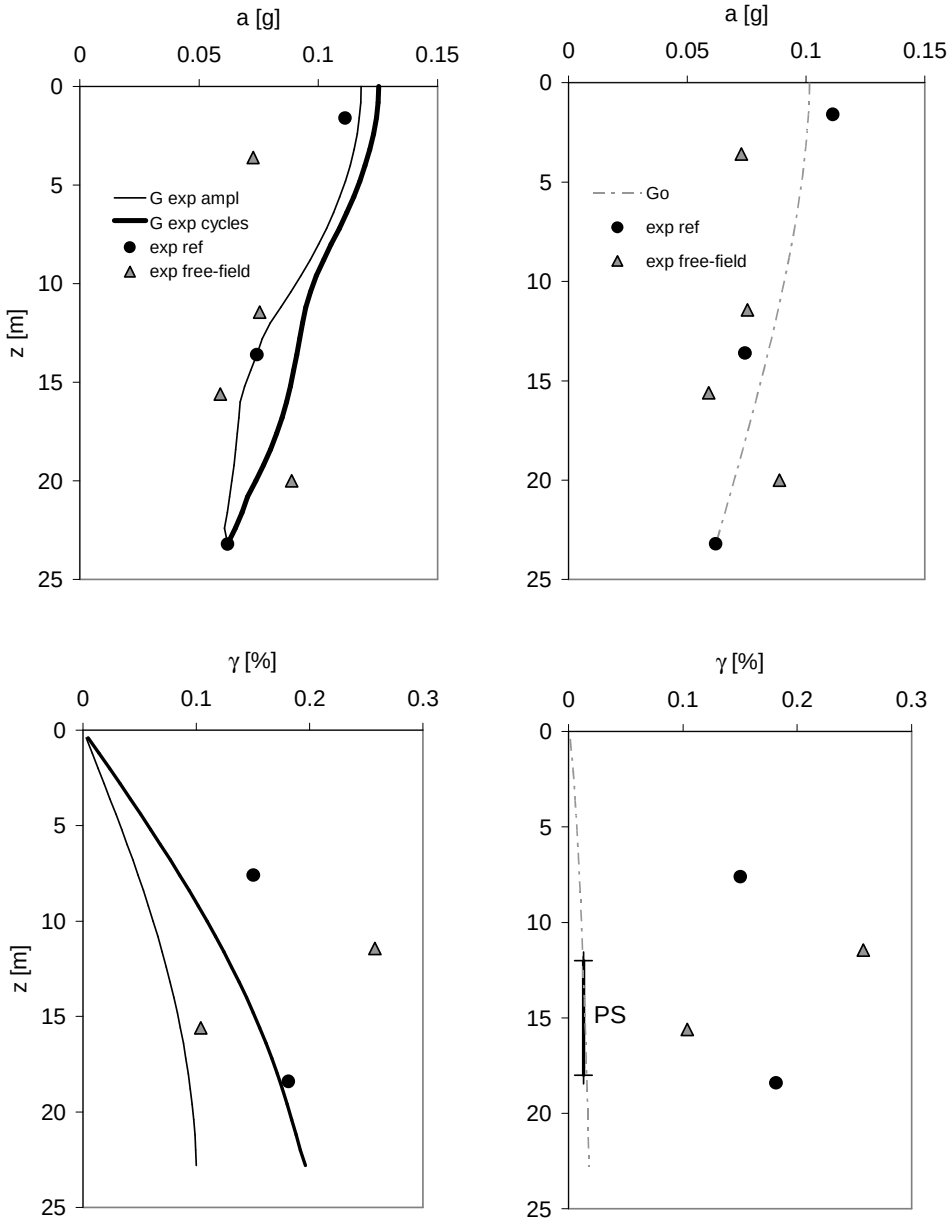

Figure 5. Comparison between measured and predicted profiles of a_{max} and γ_{max} (model T3, EQ2).

In the same figure, the average of the pseudo-static values of γ_{max} shown in Table 7.1 for EQ2 are also plotted as a constant line between 12m and 18m (tunnel position). Such value overlaps those computed by EERA linear equivalent analysis.

7.5 FULL DYNAMIC ANALYSES

Full dynamic linear visco-elastic analyses of the coupled ground-tunnel system undergoing shaking were performed by the FE code Plaxis v8 (Brinkgreve, 2002; § 3.3.2).

Two different profiles of shear stiffness and damping ratio with depth were used. In the first case (class A prediction) the profiles of G(z) and D(z) were derived from the last iterations of the 1D linear equivalent analysis by EERA (G_0 and D_0 according to the RC tests and the dash-dot profile in Fig. 2) (Amorosi & Boldini 2007).

In the second case (class C prediction) G and D were assumed constant with depth and corresponding to the thin lines in Fig. 7.2.

The geometry of the centrifuge model was reproduced by the finite element mesh shown in Figure 7.6 (test T3). The two vertical boundaries were linked by rigid *node-to-node* anchors, forcing them to have identical horizontal displacements. The input signal of the acceleration was applied to the base. The analyses were carried out at model scale, considering an increment of the gravity acceleration until 80g. The soil damping was modelled through a Rayleigh formulation using double frequency approach (Park & Hashash 2004).

Two different profiles of shear stiffness and damping ratio with depth were used. In the first case, following Amorosi & Boldini (2007), the profiles of G(z) and D(z) were derived from the last iterations of the 1D linear equivalent analysis by EERA, with G0 and D0 introduced according to the RC tests and the dash-dot profile in Fig. 7.2. This corresponds to a truly blind (class A) prediction. In the second case class C prediction, the vertical profiles of G and D were assumed constant with depth, and corresponding to the values back-analysed from the experimental amplification curve (thin solid lines in Fig. 7.2).

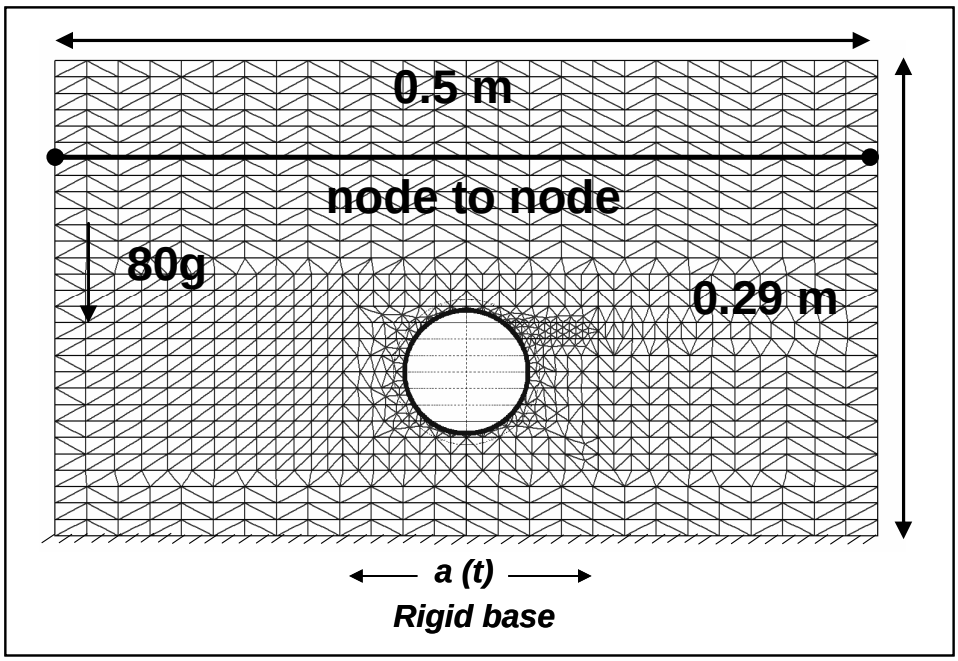

Figure 7.6. Finite element mesh (test T3)

The comparison between the predicted profiles of a_{max} and γ_{max} by EERA and Plaxis are shown in Fig. 7.7. The profiles computed by Plaxis along the reference vertical alignment overlap those computed by EERA in 1D conditions using the laboratory results. The difference computed by Plaxis between the free field alignment and vertical line passing trough the centreline of the tunnel are practically negligible. The use in Plaxis code of the stiffness derived by experimental amplification produce little difference in terms of accelerations while significant differences arise in terms of shear strains.

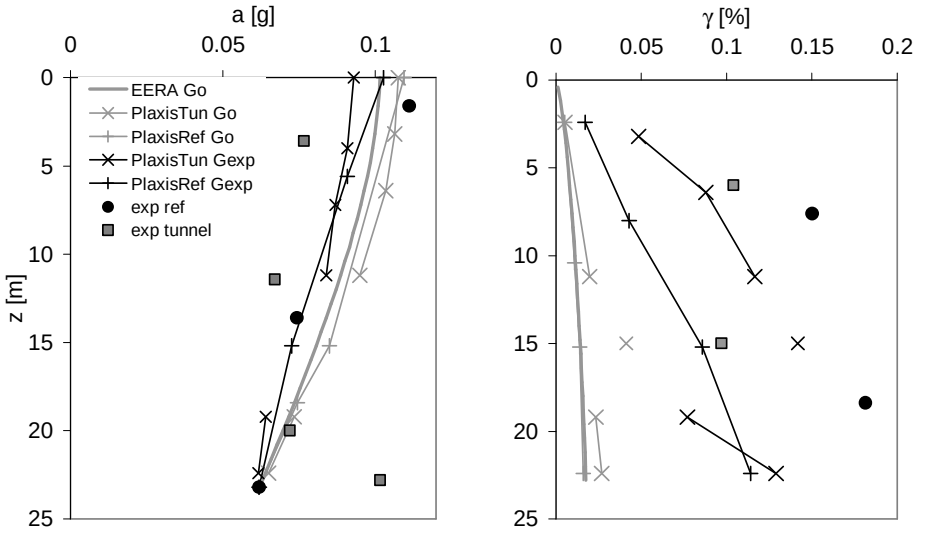

Figure 7.7. Comparison between measured and predicted profiles of a_{max} and γ_{max}

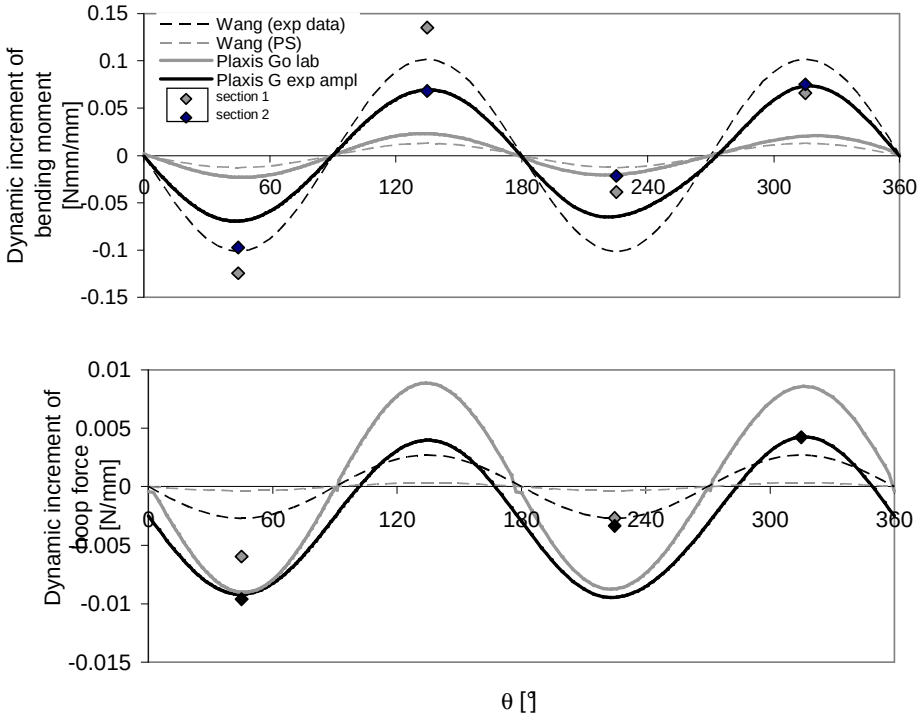

Figure 7.8. Increments of bending moment M and hoop forces N

The finite element analyses allowed the increments of bending moment M and hoop forces N to be computed along the tunnel lining as shown in Figure 7.8 for the earthquake EQ2 of the model T3.

In the same figure the corresponding measured values are shown for comparison together with the values obtained by the straightforward application of Wang's formulas using both the experimental shear strains (class C prediction) and their pseudo-static estimation (class A prediction).

The increments of hoop forces and bending moments calculated by the full dynamic analysis based on the stiffness deduced by the experimental amplifications are in substantial agreement with the measured values. The use of the stiffness deduced by the laboratory tests cause the bending moments to be underestimated and hoop forces to be overestimated.

7.6 CONCLUSIONS

The time histories of both bending moment and hoop forces revealed that significant residual forces accumulated in the lining during the seismic events, presumably due to soil densification. A progressive accumulation of surface settlement was measured at the same time by the displacement transducers.

Such behaviour cannot be predicted by the usual closed-form solutions adopted in design (i.e. Wang et al. 1993; Penzien & Wu 1998; Penzien 2000) as they assume reversible behaviour for soil. Therefore, in these simplified analyses only the reversible part of both bending moments and hoop forces was considered.

The experimental results were compared to the prediction of simplified design methods suggested by the national and European codes and to those of full dynamic numerical simulations, based on the soil characterisation provided by a separate campaign of laboratory tests on the used Leighton Buzzard sand. In addition, the soil parameters were back-figured directly from the results of the centrifuge tests.

The two classes of prediction (class A from the laboratory soil characterisation, class C from the interpretation of the centrifuge results) were compared each other in terms of profiles of maximum acceleration a_{max}, maximum shear strain γ_{max} and maximum values of internal forces.

The comparison highlighted that, while the acceleration values are hardly affected by the soil characterisation and the numerical modelling, the prediction of the shear strains and, accordingly, the internal forces are significantly conditioned from the assumption of a reliable small strain stiffness profile.

In the future the performed tests should be back analyzed in order to consider also the residual value of the internal forces due to a densification of the medium during the tests. A more complex material model should be implemented in a full dynamic analyses, in order to consider the effect of the earthquakes on the static internal forces observed at the end of the motion. This model should be accounted for non- linearity and coupling between shear and volumetric straining.

REFERENCES

Amorosi A. Boldini D. 2007. *Modellazione numerica del comportamento sismico trasversale di gallerie superficiali in terreni argillosi,* Memorie in ricordo di Renato Ribacchi, pp.207-217.

Bardet J. P., Ichii K., Lin C. H. (2000). *EERA a Computer Program for Equivalent-linear Earthquake site Response Analyses of Layered Soil Deposits*. Univ. of Southern California, Dep. of Civil Eng.

Bilotta E., Lanzano G., Russo G., Santucci de Magistris F., Silvestri F. 2007. *Methods for the seismic analysis of transverse section of circular tunnels in soft ground*. ISSMGE-ERTC12 Workshop at XIV ECSMGE "Geotechnical Aspects of EC8", Chapter 22, Patron Editore

Brinkgreve R.B.J., *Plaxis 2D version8*. A.A. Balkema Publisher, Lisse, 2002NTC, 2008

CEN 2003. prEN 1998-1, Eurocode 8: *Design of structure for earthquake resistance,. Part 1: General rules, seismic actions and rules for buildings*. CEN European Committee for Standardisation, Bruxelles, Belgium

D.M. 14.01.2008. *Nuove Norme Tecniche per le Costruzioni*, (in italian)

Park D. & Hashash Y.M.A. 2004. *Soil Damping Formulation in Nonlinear Time Domain Site Response Analysis*, Journal of Earthquake Engineering, 8(2), 249-274.

Penzien J. & Wu C.L. 1998. *Stresses in linings of bored tunnels*, Earthquake engineering and structural dynamics, 27:283-300.

Penzien J. 2000, *Seismically induced racking of tunnel linings*, Int. J. Earthquake Eng. Struct. Dynamics 29, pp. 683–691.

Visone C. 2008. *Performance based design of embedded retaining walls*. PdD Thesis, University of Naples “Federico II”.

Wang J-N. 1993. *Seismic Design of Tunnels*, Parson Brinckerhoff Inc.

Conclusions

FINAL CONSIDERATIONS

The thesis was addressed to calibrate design procedures of tunnels under seismic loads. The motivation of the research was the observation of the damage suffered by the tunnels under strong earthquakes, mainly consisting of extended cracking and collapse of the lining sections. The most significant example was the wide cracking occurred in the tunnel sections of the Kobe Metro during the catastrophic event in the 1995 (Yoshida, 1999). On the other hand, in the traditional practice, the importance of an accurate seismic design of the tunnels was often underestimated, because of the lower vulnerability of the underground structure, compared to the aboveground structures.

The simplest design method consists of quasi-static analysis; indeed, this should be considered a kinematic approach, since the seismic action is taken equivalent to a shear strain assigned at the tunnel depth. Such assumption is supported by field observations suggesting that the damage of the tunnel under seismic loads was strongly influenced by the deformation of the surrounding ground (Okamoto *et al.* 1973). The simplified methods adopt analytical closed-form expressions to calculate the seismic increments of internal forces, using as input data the maximum shear strain in the subsoil evaluated in free-field conditions by pseudo-static

or dynamic one-dimensional site response analysis (Wang 1993, Penzien & Wu 1998, Penzien 2000). This assumption corresponds to an uncoupled approach, neglecting the kinematical interaction occurring between the soil and the structure.

Full dynamic methods involve the use of 2D FEM or FDM codes, which simulate both wave propagation and dynamic interaction between the tunnel and the soil. The predictions of these numerical instruments are expected to act as a benchmark in order to check the validity of the simplified design methods.

In this work, full dynamic analyses were performed using the finite element code Plaxis 8.0 (Brinkgreve 2002), which integrates the motion equations in the time domain. The correct use of the software required the calibration of the subsoil model, including the dimensions (H x L) of the calculation domain, the size of the mesh and the factors for the material damping.

To validate all the input settings, the results of the Plaxis dynamic analyses in free-field conditions were compared with one-dimensional analyses, carried out by the EERA code (Bardet *et al.* 2000), with identical input motions and soil properties. The best agreement was reached for a very extended FE domain (L=16H), showing that the lateral boundaries, modelled as viscous dampers, had a strong influence on the results.

To account for soil non-linearity, a two-stage calculation procedure was used (Amorosi & Boldini 2007), consisting of the execution of:

- preliminary 1D linear equivalent visco-elastic analyses performed by EERA, accounting for the degradation of initial shear stiffness and damping ratio with the shear strain level;
- subsequent 2D linear visco-elastic analyses by Plaxis, using as input parameters the mobilised values of shear stiffness and damping ratio computed as above.

The above procedures were preliminary calibrated on a set of virtual subsoil profiles representative of the classes B, C, D specified by Eurocode 8 and the National Technical Code. The profiles of the shear wave velocity were typical of a medium dense gravel (class B), a medium dense sand

(class C) and a soft clay (class D). The input motions were selected from a database of Italian seismic records among those pertaining to strong-motion earthquakes, with peak ground acceleration higher than 0.3g.

The results of the full dynamic analyses confirmed that the distribution of the peak dynamic increments of internal forces with the anomaly θ exhibited maximum bending moments and hoop forces at $\theta=\pi/4+n\pi$ (n=0,1,2,3). The results of the full dynamic analyses were compared to those of simplified pseudo-static and dynamic uncoupled approaches. The analytical closed-form solutions to evaluate the seismic internal forces were seen to overestimate the maximum values of hoop forces and bending moments, which resulted higher for the pseudo-static evaluation of shear strains. In other words, the comparison showed the effect of the kinematic interaction on the calculation of the internal forces, since the presence of the tunnel usually reduces the free-field strains. This reduction is simulated by full dynamic analyses, but neglected when using the simplified (pseudo-static and dynamic) uncoupled design approaches.

A set of centrifuge tests on physical models of a shallow tunnel deployed in a sand layer was planned in the framework of the research project ReLUIS. The usefulness of the small scale experiments derives from the lack of instrumented test sites or well-documented case histories with records of the seismic motion and tunnel lining forces. Therefore, the centrifuge tests were carried out to provide ‘artificial case histories’ allowing to calibrate simplified to advanced numerical analyses of the behaviour of tunnels under seismic conditions.

A research agreement between the ReLUIS consortium and the Cambridge University (CUTS) was addressed to perform the centrifuge tests at the Schofield Centre laboratory, equipped with geotechnical centrifuges to run dynamic tests.

The tests were addressed to simulate the plane strain behaviour of a tunnel section in a dry sand deposit built in a laminar box (500x250x300 mm^3). The actual sequence of a tunnel construction process could not be physically modelled, but the procedures to create the centrifuge models

were specified in order to include them in the numerical models of the experiments.

Since soil stiffness and strength are strongly dependent on the overburden stress, a realistic reproduction of the in situ state is needed to correctly evaluate the dynamic interaction between the structure and the surrounding ground. The reason why centrifuge model testing was preferred to shaking table testing was that the scaling factor, N, between model and prototype (equal to the centrifuge acceleration level) allows to reproduce the same mechanical properties of a real subsoil.

In order to define the centrifuge testing programme, a set of full dynamic analyses was preliminarily performed. The input motions were sinusoidal time histories of accelerations, simulating the dynamic load shape fired in the centrifuge tests. The signals had constant amplitude and variable frequency. The soil profile was assumed as typical of a medium dense sand subsoil and the lining thickness was varied. The results showed that the soil/structure stiffness ratio had a great influence on the dynamic response of the tunnel. Therefore, a specific stiffness ratio, corresponding to a particular value of the lining thickness, reproduces the free-field conditions, dividing the range of lining thickness into two classes: rigid and flexible.

The centrifuge programme included four physical models, in which both the soil density and the tunnel cover (C) were varied. The models were prepared with dry sand (Leighton Buzzard), poured at two different values of relative density (D_r), and spinned up to N = 80 g and 40g. Table 1 shows the centrifuge testing programme.

Table 1: Centrifuge tunnel tests

model	D [mm]	C [mm]	D_r	N
T1	75	75	~75%	80-40
T2	75	75	~40%	80-40
T3	75	150	~75%	80-40
T4	75	150	~40%	80-40

The tunnel lining model was an aluminium tube having an external diameter D = 75mm and a thickness t = 0.5mm. This is equivalent to a very flexible concrete lining (0.06m) with a diameter of 3.0 (N=40) to 6.0 m

(N=80). Such a small dimension for the lining was selected to rely upon a better resolution of the measurement of the seismic load increments during the dynamic step.

The models were instrumented using accelerometers, strain gauges and displacement transducers (LVDT). The accelerometers were placed both in the sand and on the walls of the laminar box, in order to record the acceleration time histories at significant locations. The tube was instrumented with pairs of strain gauges, in order to measure bending moments (BM) and hoop stresses (HS) at 4 locations along 2 transverse sections. The main instrumented section was located at the mid-span of the tube, and a second section at 50mm aside. The surface displacement during the whole test duration was measured by a couple of linear variable differential transformers (LVDTs).

All the instruments were carefully calibrated, especially the strain gauges, which were subjected to different loading series in order to obtain reliable values of the calibration factors. To obtain the different degree of density desired, the sand was poured manually for the loose models (T2, T4) and automatically for the dense models (T1, T3).

The instrumental recordings, taken both in the swing-up and in the dynamic phase, provided a clear interpretation of the test results. The swing-up data were obtained both from monitor readings and recordings sampled at 4Hz; the dynamic data, instead, were sampled at 4000Hz, according to the scaling factors of the dynamic test (very short duration and high frequency).

The LVDT readings were available only for three tests: T1, T3 and T4, because in the test T2, which was the first one of the sequence, all the acquisition channels were used for the strain gauges recordings. The LVDTs measurements show the settlement of the model surface in all the tests, both in the swing up and dynamic phase. The loose sand models exhibited displacements about twice larger (6.5cm) than those of the dense sand models (3.2cm). The swing-up settlements were, on average, about equal the displacement increment measured in the dynamic phase.

In all the sand-tunnel models, three soil columns were instrumented by at least three accelerometers each: the first column was instrumented along the vertical passing through the tunnel axis (*tunnel*); the second column was located at 125mm from the central vertical (*free-field*); the third column of accelerometers was placed along the external wall of the laminar box (*reference*). Hence, the lowest reference sensor, located on the base-plate, was supposed to measure the input motion from the SAM actuator.

The accelerometers measured time histories of pseudo-sinusoidal motions, being the peak acceleration amplitude not constant and non-symmetric around the time axis. The actual frequency content was larger compared to the nominal frequency, but this was not attributable to annoying effects. For this reason, the acquired signals were centred and filtered in a large band-pass frequency range (0.2-3.124Hz at prototype scale).

The verticals instrumented with horizontal accelerometers showed the amplification of the peak ground acceleration from the base to the top of the sand layers. The amplification was generally low (<1.5), especially for the internal alignments. The tunnel in the model determined the reduction of the acceleration along the free-field column at the structure depth, as well as the increase of the peak ground acceleration for the instrument located at the bottom of the sand layer under the tunnel.

The variability of the ground motion was represented using the coherence and the transfer functions. The best-fitting of the amplification function between the base and the top accelerometers allowed to obtain average values of the mobilized shear stiffness and damping ratio of the sand layer. The back-calculated stiffness was fairly low (around 20MPa) and, consistently, the damping ratio resulted generally quite high.

The shear stress-strain cycles were analysed to obtain an evaluation of the equivalent shear stiffness layer by layer. The different values computed in this way resulted as low as 1-2MPa, and on the average of the order of 10 MPa, about one half the overall shear stiffness back-calculated from the amplification functions.

The strain gauge arrangements gave a direct measurement of the internal forces in the lining. Generally, the experimental records relative to corresponding positions in the two different sections exhibited similar trend. In every case, the final value was different from the initial reading, and the record showed oscillation during the dynamic phase. As observed also from the LVDT measurements, during the model shaking likely permanent deformations of the sand occurred. In most cases, the earthquakes determined an increase of the internal forces, for both the bending moment and the hoop forces.

As in the swing up phase, the seismic increments of the bending moment in the top positions were higher than the corresponding in the bottom side, which were negative, but close to zero. Therefore, it appears that the final non-zero internal forces resulted from plastic straining during the dynamic phase, which caused, especially close to the tunnel surface, a residual stress at the end of the earthquake. The maximum measured value was around 5-6Nmm/mm, twice larger compared to the static conditions. The negative amplitudes resulted around 1-2Nmm/mm.

The hoop forces were generally positive (compression), except some case of values close to zero. The seismic increment was more apparent in the loose sand test (1-1.2 N/mm), two times larger compared to the dense sand models (0.5-0.6N/mm).

To check the experimental data with analytical formulations, the maximum dynamic oscillation of the internal forces were compared to the predictions of the closed-form expressions by Wang (1993), considering full slip conditions; the results were consistent, especially when the measured shear deformation of the tunnel was directly introduced in the Wang's expression.

The experimental results were also compared to the predictions of simplified methods and full dynamic numerical simulations, based on the soil characterisation provided by a separate campaign of laboratory tests on the Leighton Buzzard sand. In addition, the soil parameters were back-figured directly from the results of the centrifuge tests.

The two classes of prediction (class A from the laboratory soil characterisation, class C from the interpretation of the centrifuge results)

were compared each other in terms of profiles of peak acceleration, a_{max}, shear strain, γ_{max}, and internal forces. The comparison showed a good agreement between the numerical and experimental results in terms of acceleration, for which the Class A and Class C analyses profiles were quite similar. On the contrary a substantial underestimation of the experimental strains is obtained by using the laboratory stiffness profiles, which were agreed with the pseudo-static evaluation. The Class C analyses gave a slighter underestimation in terms of maximum shear stiffness compared to the Class A analyses. The increments of hoop forces and bending moments calculated by the full dynamic analysis based on the stiffness deduced by the experimental amplifications are in substantial agreement with the measured values; instead The use of the stiffness deduced by the laboratory tests cause the bending moments to be underestimated and hoop forces to be overestimated.

In the future, it is expected that the tests might be interpreted with higher detail, to better simulate also the occurrence of residual internal forces due to the accumulation of soil plastic straining during the earthquake. A more complex material model should be implemented in the full dynamic analyses, in order to account for soil non-linearity and coupling between shear and volumetric straining.